



HAL
open science

A preliminary theoretical and experimental study of a photo-electrochemical cell for solar hydrogen production.

Azin Eskandari

► To cite this version:

Azin Eskandari. A preliminary theoretical and experimental study of a photo-electrochemical cell for solar hydrogen production.. Chemical and Process Engineering. Université Clermont Auvergne [2017-2020], 2019. English. NNT : 2019CLFAC104 . tel-03071710

HAL Id: tel-03071710

<https://theses.hal.science/tel-03071710>

Submitted on 16 Dec 2020

HAL is a multi-disciplinary open access archive for the deposit and dissemination of scientific research documents, whether they are published or not. The documents may come from teaching and research institutions in France or abroad, or from public or private research centers.

L'archive ouverte pluridisciplinaire **HAL**, est destinée au dépôt et à la diffusion de documents scientifiques de niveau recherche, publiés ou non, émanant des établissements d'enseignement et de recherche français ou étrangers, des laboratoires publics ou privés.

UNIVERSITE CLERMONT AUVERGNE

ECOLE DOCTORALE
SCIENCES POUR L'INGENIEUR DE CLERMONT-FERRAND

Thèse

Présentée par

Azin Eskandari

pour obtenir le grade de

DOCTEUR D'UNIVERSITÉ

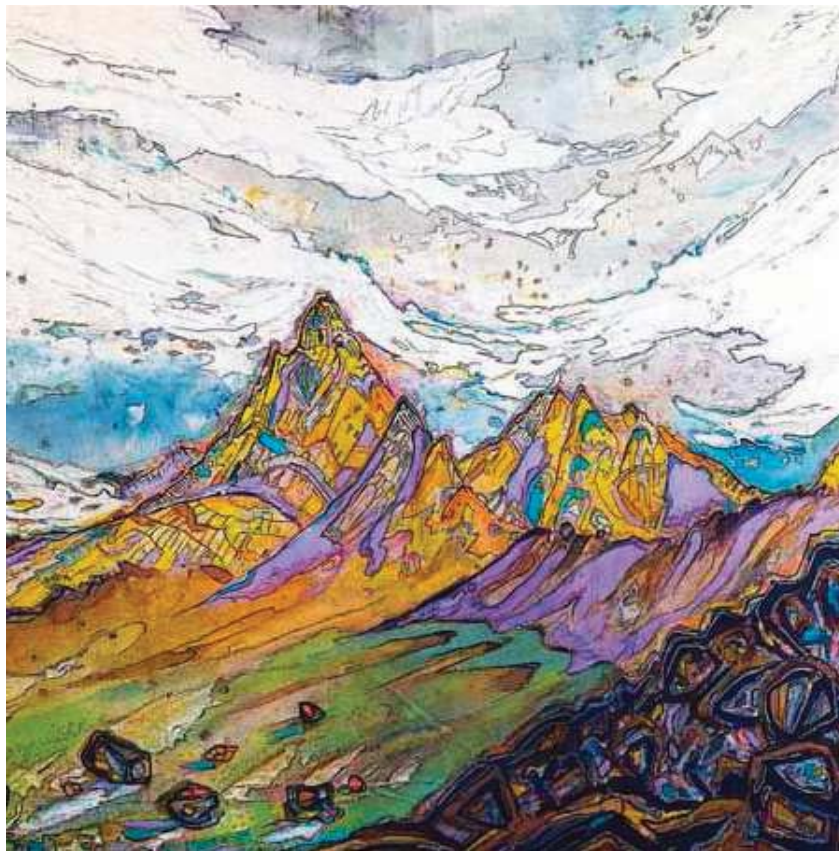
SPECIALITE : GENIE DES PROCEDES

A preliminary theoretical and experimental study of a photo-electrochemical cell for solar hydrogen production

Soutenue publiquement le 5 novembre 2019 devant le jury :

M. Frédéric GLOAGUEN	Rapporteur	Directeur de recherche CNRS, UBO Brest
M. Jack LEGRAND	Rapporteur	Professeur, Université de Nantes, Nantes
M. Marc AUROUSSEAU	Examineur	Professeur, Grenoble INP, Grenoble
Mme Florence DRUART	Examineur	Maître de conférences, Grenoble INP, Grenoble
M. Winfried LEIBL	Examineur	Directeur de recherche, Institut Joliot, CEA Saclay
M. Fabrice GROS	Examineur	Professeur, SIGMA Clermont, Clermont Ferrand
M. Jean-François CORNET	Directeur de thèse	Professeur, SIGMA Clermont, Clermont Ferrand

In search of Adventure; The Mountain appears



Himalayas, Renan Azturk

Contents

Chapter 1	Hydrogen and methods of production	1
1.1	Energetic issue	1
1.2	Renewable methods of hydrogen production	6
1.2.1	Water electrolysis.....	6
1.2.2	Water photolysis.....	10
1.3	Photoelectrochemical cells	16
1.3.1	Photoelectrochemical cell and material aspects	17
1.3.2	Key functional properties of photoelectrodes.....	18
1.3.3	PEC structure	21
1.3.4	Dye-sensitized solar cell.....	22
1.3.5	Photoelectrochemical Hydrogen production	24
1.4	A personal view of this thesis outlines	28

Chapter 1

Hydrogen and methods of production

1.1 Energetic issue

Fossil fuels are subsiding because of their finite resources and environmental damages. Although fossil fuels resources are renewable via natural processes, they are commonly considered as non-renewable resources because it takes millions of years for the Nature to regenerate them. Consequently, they are being depleted faster than they can be regenerated to comply with the future energy demand. The world energy consumption in 2013 was reported about 17.7 TW for 7 billion world population while this amount is potentially supposed to reach to 30 TW for 9.5 billion people by 2050 (Figure 1.1 and 1.2). Besides the increasing demand, all actual coal reserves are estimated to last 150-400 years while oil reservoirs are sufficient for 40–80 years and finally we have 60–160 years of natural gas supply (Krol, 2012).

It is therefore unavoidable to play down the role of fossil resources and move faster toward renewable energy alternatives. Today the specific term of “renewable energies” is defined as energies derived from natural processes (e.g. sunlight and wind) which are renewed at a faster rate than they are consumed. Solar, wind, geothermal, hydro, and some forms of biomass are common sources of renewable energy (IEA PUBLICATIONS 2015).

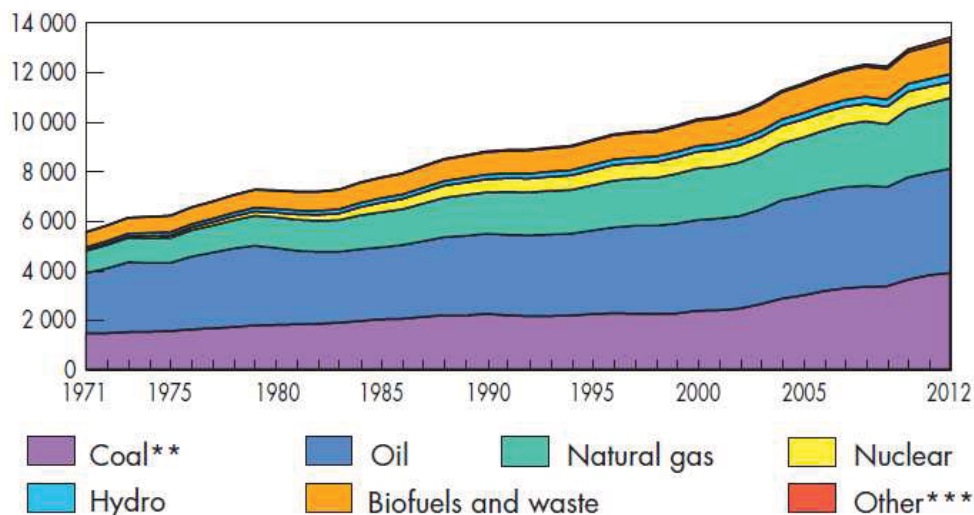


Figure 1.1 World* total primary energy supply from 1971 to 2013 by fuel (Million toe) (PUBLICATIONS, 2014). Note that toe stands for ton of oil equivalent and 1 toe =1.63 megawatt-hours (MWh) (PUBLICATIONS, 2015b).
 * Excludes electricity trade.
 ** In these graphs, peat and oil shale are aggregated with coal.
 *** Includes geothermal, solar, wind, heat, etc.

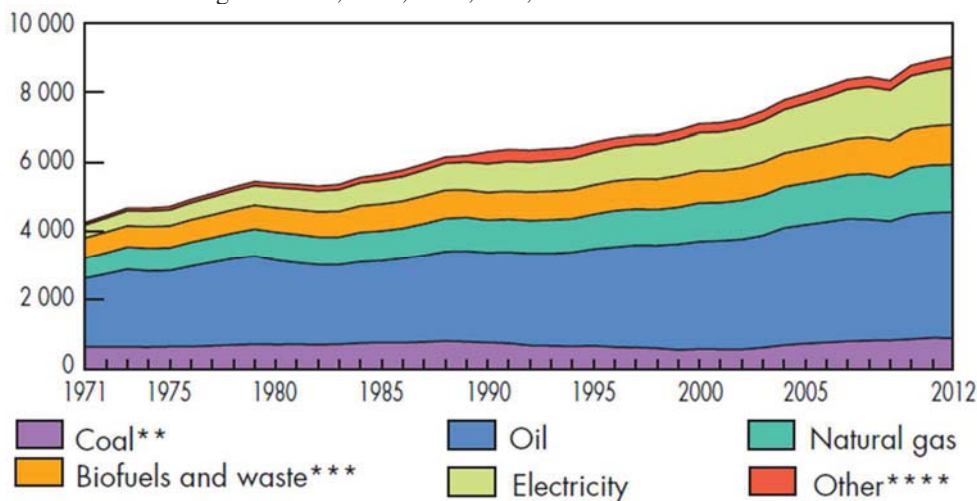


Figure 1.2 World* total primary energy consumption from 1971 to 2012 by fuel (Million toe) (PUBLICATIONS, 2014). Note that toe stands for ton of oil equivalent and 1 toe =1.63 megawatt-hours (MWh) (PUBLICATIONS, 2015b).
 * World includes international aviation and international marine bunkers.
 ** In these graphs, peat and oil shale are aggregated with coal.
 *** Data for biofuels and waste final consumption have been estimated for a number of countries.
 **** Includes geothermal, solar, wind, heat, etc.

According to Renewable Energy Policy Network (Renewables Global Status Report, 2014), the world produced 19% of global final energy consumption through primary renewable resources and in 2013 renewable energies contribution raised to 22% of overall electricity generation which had 5% increase comparing to 2012.

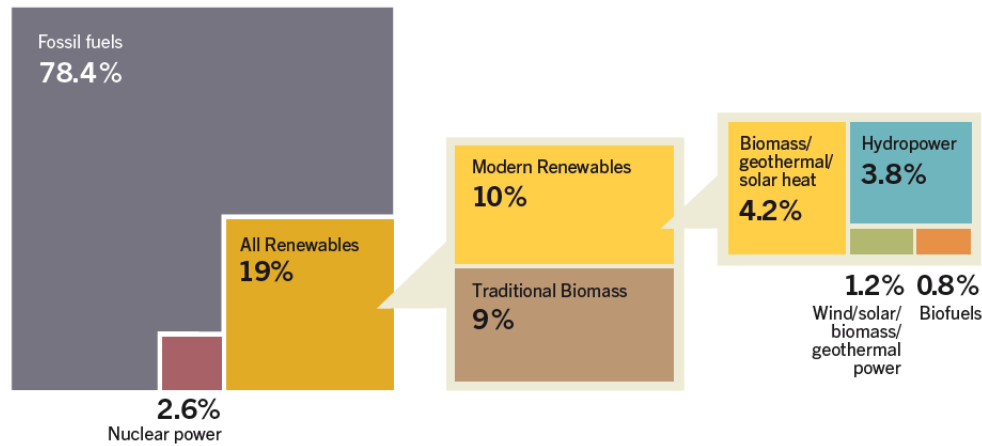


Figure 1.3 Renewable energy contribution to final overall energy consumption in 2012 (Adrian and Agency, 2013; BP, 2013; Renewables Global Status Report, 2014).

Figure 1.2 presents the diagram of global energy consumption and the share of renewable energy for 2012. Except the 9% of traditional biomass the rest of renewable energy production comes from modern renewable energies (hydropower, solar). Furthermore the contribution of solar PV in global electricity production is reported to be 0.7% in 2013 (Adrian and Agency, 2013; Renewables Global Status Report, 2014) while the fossil fuel contribution remains equal to 77.9%.

Although they are still under development, the most credible technologies are dependent on either fossil fuels or nuclear industry which is not renewable and whose pollution concerns are not negligible. However the most aggravating circumstance of using fossil fuels is environmental hazards. The greenhouse gases emission, in particular CO₂, and their role in global warming are the main concerns of energy issues. Referring to the International Panel on Climate Change (IPCC) reports, carbon dioxide concentrations have increased by 40% after pre-industrial times (Figure 1.3), mainly due to fossil fuel emissions and land-use and forestry sector emissions since land-use changed and impacts the carbon cycle. In the event that the CO₂ level reaches to 450 ppm, it puts a high risk on global warming by more than 2°C when the actual CO₂ level is increasing 2 ppm each year.

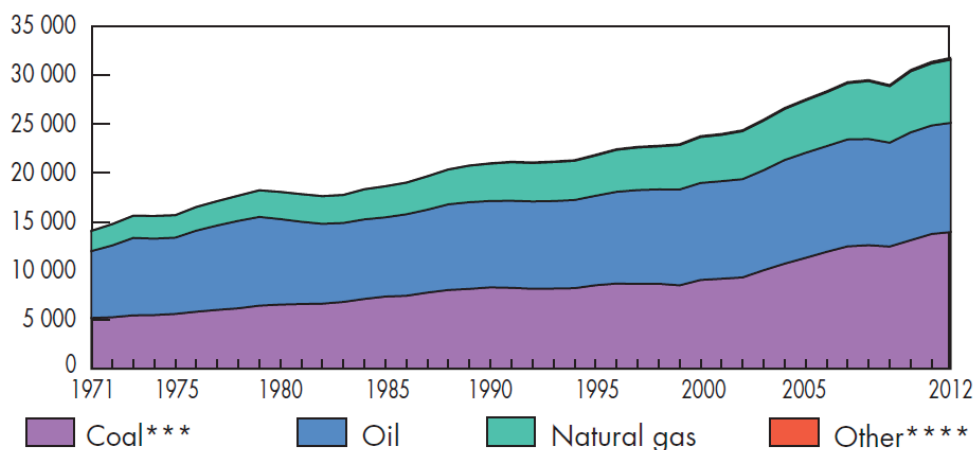


Figure 1.4 World CO₂ emissions from 1971 to 2012 by fuel (Mt of CO₂). Note that Mt stands for metric tons of carbon dioxide equivalent, where: Total Emissions (Mt CO₂) = Emissions Mt CO₂ + CH₄ Emissions (Mt CO₂ Eq.) + N₂O Emissions (Mt CO₂ Eq.) (PUBLICATIONS, 2014).

* World includes international aviation and international marine bunkers.

** Calculated using the IEA's energy balances and the Revised 1996 IPCC Guidelines. CO₂ emissions are from fuel combustion only.

*** In these graphs, peat and oil shale are aggregated with coal.

**** Includes industrial waste and non-renewable municipal waste.

This augmentation causes several irreparable devastation on ecosystems and human society such as season shifting, decreasing northern hemisphere snow cover, rising sea levels, ocean acidifications and increasing the frequency of violent weather events (Allison et al., 2009; IPCC, 2013).

Today, considering all mentioned energetic concerns, it is inevitable to dedicate a large effort to move toward sustainable energy sources. Between different renewable sources of energy and different methods of production, the efficiency and cost-effectiveness are important factors for scientists and industrialists. From an economical point of view some methods are on priority, but they confront technical obstacles and also the cost concerns remain a decisive factor in future energy supply (Hoffert, 2010). An overview of sustainable sources and their capacity of power supply is presented in Table 1.1. Accordingly solar energy seems to have more potential to meet the future energy demand (Krol, 2012). Most renewable energies are directly or indirectly related to the sun and the sunlight can be used directly for generating electricity and lightening via photovoltaic.

Energy source	Power (TW)	Remarks
Wind	4	Represents 10–15% of global technical potential for on- and off-shore installations
Hydroelectric	1–2	Remaining untapped potential is 0.5 TW
Tidal and ocean currents	<2	
Geothermal	12	Only a small fraction of this can be exploited
Biomass	10	Requires 10% of earth's land surface to be covered with switchgrass
Nuclear	10	Requires construction of a 1-GWpeak power plant every 35 h for the next 40 years. Finite uranium supplies imply need for fast breeder or thorium reactors.
Solar	>20	Requires 0.16% of the Earth's surface to be covered with 10% efficient solar cells. Total solar power reaching the Earth's surface is 120,000 TW

Table 1.1 Overview of sustainable energy sources and power generation capacities (Krol, 2012).

It is clear that the sunlight is not available permanently, but its energy can be stored. As a result, efficient storage systems have to be planned for a large scale power generation to overcome natural solar energy shortcomings such as intermittency. Another possibility to energy storage is to store it in chemical forms such as hydrogen, methane, methanol, gasoline, and diesel. Among several chemical fuels, hydrogen is the only one which can be produced without carbon source contribution. Hydrogen does not represent an energy source but it is an energy carrier, which can store and convey the required energy. However, hydrogen exists mostly in the nature in molecular form such as water or organic compounds and not much in gas form (H_2). So it would be necessary to produce it from the compounds which are composed of hydrogen element such as natural gas, coal, nuclear, biomass, water, etc... . This hydrogen can be used in the fuel cells to produce electricity, with water and heat as by-product (CEA, 2004; Krol, 2012; Lewis and Nocera, 2006) or directly burnt to produce heat.

Several methods have been presented for hydrogen generation including thermal processes, for instance “natural gas reforming or biomass gasification”; electrolytic as water splitting using a variety of energy resources and photolytic like water splitting using sunlight via biological and mineral materials. Today in France 95% of hydrogen production is carried out by reforming of hydrocarbons and natural gas, and the other 5% is provided by electrolysis. Today steam methane reforming, with an industrial efficiency of 65-70% is the most prevalent method, whereas 10 to 12 tons of CO_2 would be generated as by-product per ton of produced hydrogen (CEA, 2004).

It comes to conclusion that hydrogen can be a future energy carrier if and only if it can be produced within renewable methods. Otherwise, it would be more reasonable to keep actual

methods based on methane direct usage or reforming because their processes and the required facilities are thoroughly developed with a satisfying efficiency.

1.2 Renewable methods of hydrogen production

Hence we are confronting two process categories with different methodologies. The processes with remarkable efficiency and less renewability; and those based on more renewable technologies but with modest efficiency comparing with actual leading methods. In the following we present renewable methods of hydrogen production and we put the accent on the solar technologies and their contributions to renewable hydrogen production because of the notable available solar power (Table 1.1).

1.2.1 Water electrolysis

Water splitting into hydrogen and oxygen can be achieved through an electric current passage as a result of an electrical potential difference, applied between two electrodes. This process named electrolysis established for the first time in 1800 by William Nicholson and Anthony Carlisle (Laguna-Bercero, 2012) which is the reverse of fuel cell mechanism. It has been developed in two principal methods of separation classified by the operation temperature, low temperature and high temperature water electrolysis.

1.2.1.1 Low temperature electrolysis

Low temperature electrolysis is mainly about two commercial technologies; alkaline electrolysis which relies on low temperature (80 to 90°C) and liquid electrolyte on the one hand and polymer electrolyte membrane (PEM) electrolysis based on low temperature (40 to 80 °C) solid electrolyte on the other hand. Alkaline electrolysis proceeds in an aqueous KOH solution, generally with electrolyte circulation within the cell. The process operates from atmospheric pressure up to 25 bars. Alkaline electrolysis is a mature process with significant output purity. The concept is carried out by following reactions:



Although alkaline electrolysis has notable industrial record, lowering the electricity cost is still a major challenge to be investigated.

Contrary to the alkaline electrolysis, polymer electrolyte membrane (PEM) electrolysis implies no liquid as electrolyte since an acidic polymer membrane is used as the electrolyte. The process pressure in this case can vary up to hundreds of bars.



The most important privilege of PEM to alkaline electrolysis is higher turndown ratio¹, more safety because of the absence of KOH electrolytes, more compact system and higher operating pressure. However due to the high cost, poor efficiency and short life time of membrane, PEM is not a fully developed process like alkaline electrolyser. PEM process can be revised by additional investigation on material improvement and cell stack design (IEA PUBLICATIONS 2006).

1.2.1.2 High temperature electrolysis

High temperature electrolysis is a prominent method of hydrogen production inspired by high temperature fuel cell (IEA PUBLICATIONS 2006). The technology relies on the idea that H_2O can be dissociate to H_2 and O_2 in an efficient way if the system is associated with a heat source like solar, geothermal or nuclear. One typical commercial example is solid oxide electrolyser cell (SOEC) based on solid oxide fuel cell as well, with the operation temperature of 700 up to 1000 °C. The necessary energy estimated by the enthalpy variation (ΔH) for hydrogen production in this method is calculated by:

$$\Delta H = \Delta G + T\Delta S \quad (1.7)$$

Where ΔG , the free energy variation is the required electrical energy for the reaction and $T\Delta S$ is the thermal energy need.

This method is more beneficial than electrolysis at ambient temperature, as Gibbs free energy for water splitting reduces with rising temperature. This means that an increase in operating temperature reduces the required electrical energy but it also raises the thermal energy requirement. However, the total energy consumption does not change significantly with temperature variation but, supplying a large amount of this energy demand with heat sources

¹ Operating ratio of part load to full load.

cheaper than electricity is affordable. Furthermore, at very high temperature (2500°C), electrical work comes unnecessary because water decomposition goes through thermolysis. The efficiency of this technology with use of several heat sources increases to 40-50% and the cost evaluation is about 2.0 to 3.5 €/ kg H₂ for nuclear heat source, which still remains non-renewable and has environmental pollution issues in some cases (Grimes et al., 2008; Hoffert, 2010; Laguna-Bercero, 2012; Lewis and Nocera, 2006).

1.2.1.3 Photovoltaic and water electrolysis combination

Taking into consideration all photovoltaic (PV) plants and installations around the world and their large capacity to produce renewable low cost electricity, the combination of photovoltaic and water electrolysis systems may develop a path through renewable methods to produce clean hydrogen (Grimes et al., 2008; Zoulias and Varkaraki, 2004). The system applies a PV system into a commercial water electrolyser in order to supply required electricity for water dissociation.

Theoretically it seems to be simple to replace a usual power supply by a solar source of electricity in a water electrolyser system and turn it to a renewable system but nearly all of these systems are confronted with PV defects. The main deficiency of PV systems in this case is the discontinuity and the fluctuation in output yield, because PV's functioning is inevitably influenced by daylight and weather condition. The main components of such a system are PV panels, water electrolyser and hydrogen storage system. In some cases a transportation system should be also taken into account, because of the distance between the areas with solar energy potential and the zones of request.

There is two typical industrial way to combine PV system to a water electrolyser. The simplest one is the direct combination, as it is shown in Figure 1.4. Although it is quite a simple assembly, but there are some drawbacks such as; power loss owing to solar intensity changes.



Figure 1.5 Direct coupling of photovoltaic and water electrolysis system.

PV system and electrolyser have different type of voltage-current curves. In the other words, the maximum power point of PV (MPP) changes with the variation of solar energy input; and this derives the whole system out of its optimum point. The entire system thence should works at appropriate voltage and current to adapt the electrolyser with PV and keeps PV working at

MPP point; nevertheless the solar energy variations can carry the system out of its MPP point. Consequently commercial systems have improvised an integration of PV with maximum power point tracking (MPPT) devices which leads to other methods of combination, represented in Figures 1.5 and 1.6. The water electrolyser and photovoltaic generator are coupled via a DC-DC converter device which permits both systems to operate at their efficient voltage and thus the maximum power can be obtained from PV system (Abe, 2009).



Figure 1.6 Indirect coupling of PV and water electrolysis system via DC-DC converter.

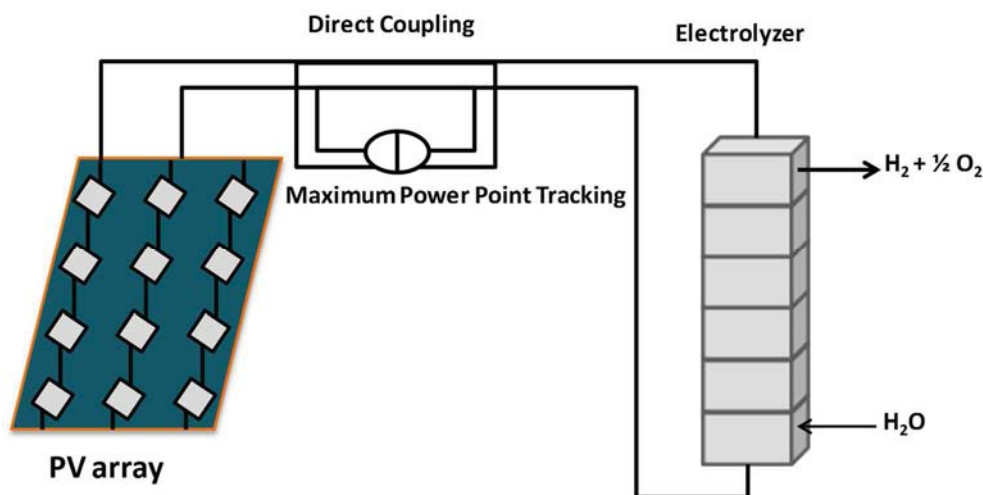


Figure 1.7 PV electrolyser system equipped with MPP tracker (Siegel, 1988).

Concerning photovoltaic generator, several PV cells has been implemented into the system in order to obtain the most efficient combination. There is also the possibility to replace the whole PV cell with a p-n junction semiconductor electrode. This system simplifies technical difficulties related to PV cells manufacturing, maintenance and mismatching problems between solar and electrochemical cells. The electrode can be directly immersed into the cell and exposed to solar radiation. Electrode stability in aqueous solution is an important concern.

Another alternative is the combination of multi-junction photovoltaic cells and PECs or dye sensitized solar cells (DSSC) and PECs which is known also as PEC-PEC combination. The DSSC-based system consists of two cells in sequence. The outer cell absorbs in ultraviolet and blue light ranges by means of nano-crystalline thin films and provides electron-hole pairs which results in water oxidation and H^+ generation. The DSSC cell based on nano-crystalline TiO_2

absorbs the green and red region of the light come from the first cell. Electrons are subsequently generated in the conduction band of the TiO₂ reduce H⁺ ions to hydrogen.

Both multi-junction photovoltaic cells and DSSC based systems as other PV-electrolyser combinations represent poor efficiency significantly below the other water electrolysis methods, since the ratio of power conversion from absorbed light to electricity has to be taken into account in overall efficiency calculation. Based on several publications, the overall efficiency of PV-water electrolysis system is reported about 10-11 %, and 6% for DSSC based systems whereas the efficiency of current commercial electrolysis methods are around 80% (Grimes et al., 2008; Jeon et al., 2012; Khaselev, 1998; Ni et al., 2008). Today PV electrolysis systems technology has been installed in several countries such as Germany, Saudi Arabia, Switzerland, Canada and US, as demonstration facilities (Abe, 2009; Sapru et al., 1998; Zoulias and Varkaraki, 2004).

Photoelectrochemical cells (PEC) and so DSSC will be discussed fully and inclusively in section 1.4.

1.2.2 Water photolysis

Another interesting method of hydrogen production is water photolysis. The term defines a chemical reaction in which water molecule is broken into hydrogen and oxygen by photon contribution the process is named water photolysis; where the global reaction is:



There has been many ways to achieve water photolysis in order to produce hydrogen, but hereafter we subdivide all methods into two simple categories; direct and indirect water photolysis.

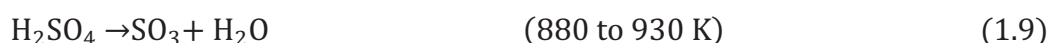
1.2.2.1 Indirect water photolysis

If the reaction (1.8) takes place in one step then it leads to direct photolysis. Hence, all photolysis reactions which come about in at least two steps or more represent indirect photolysis. Consequently, thermochemical cycles which carry out the reaction through multi powater photolysis.

1.2.2.1.1 Thermochemical cycles

The principle of thermochemical water splitting cycles (TCWSC) is to achieve water photolysis indirectly by associating one or more reactions, at least one of which is occurring at high temperature (800-900°C) but still less than the temperature of water dissociation (4700 K).

For example the reaction (1.9) shows the general reaction of H_2SO_4 decomposition which can be achieved in multiples stages through the thermochemical cycles such as sulphur iodine (Figure 1.8) and Westinghouse cycles (Figure 1.9).



The interest in sulphur iodine cycle is that the cycle has the capacity to produce hydrogen in large amount. It consists of three step reactions which result to water dissociation.

The first reaction is the Bunsen reaction during which HI and H_2SO_4 are produced:

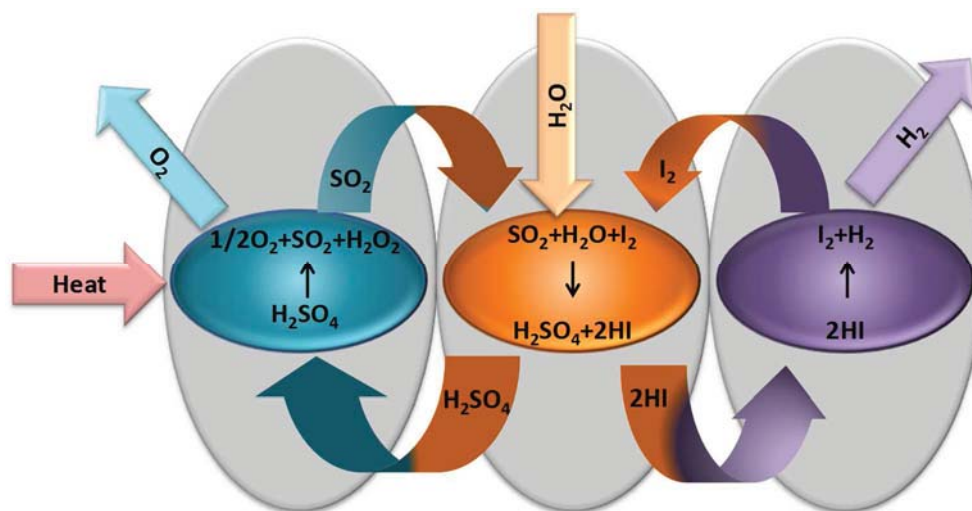
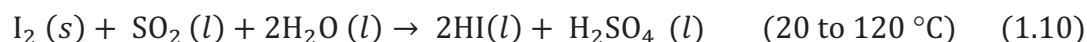
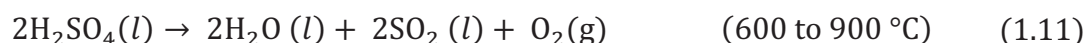


Figure 1.8 Overview of Sulphur-Iodine process. It shows the general reaction of H_2SO_4 decomposition which can be achieved in multiples stages through the thermochemical cycles such as sulphur iodine (I-S) and Westinghouse cycles.

The Bunsen section continues spontaneously and has a low operating temperature. The sulphuric acid decomposition takes place through the reaction (1.11):



The HI acid decomposition occurs, producing H_2 :



Sulphur iodine cycle achieve up to 40% of efficiency at 850°C (Schultz, 2003).

The Westinghouse Process is another thermochemical cycle based on sulphur and presenting two steps using both electrochemical and thermochemical process for decomposing water. The process is mostly comprised of two chemical reactions; one for producing oxygen and the other for hydrogen generation. The production of oxygen occurs via the thermal reduction of sulphur trioxide obtained from sulphuric acid (Brecher et al., 1977; Carty et al., 1977; Farbman, 1979; Lin and Flaherty, 1983).

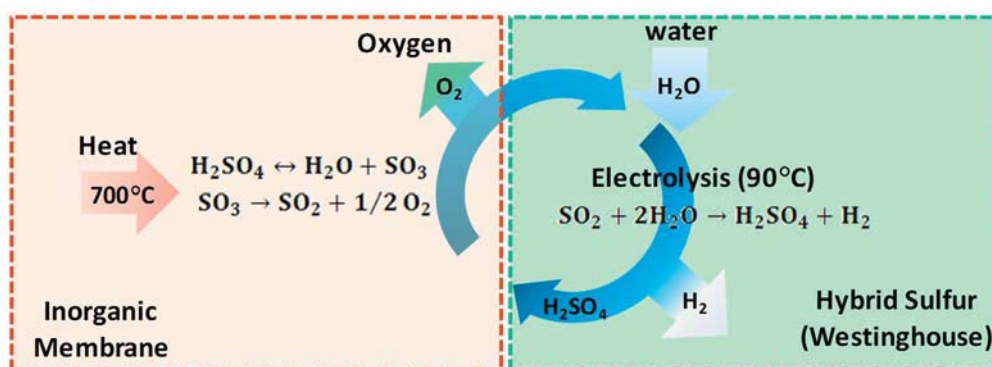
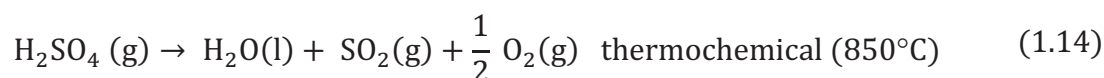
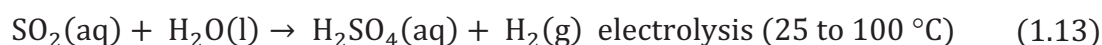
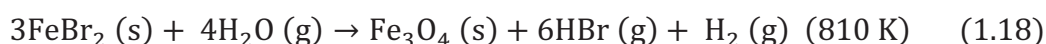
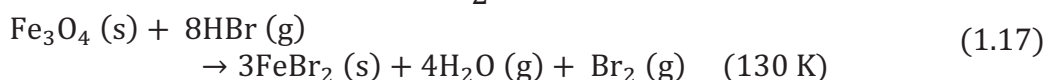
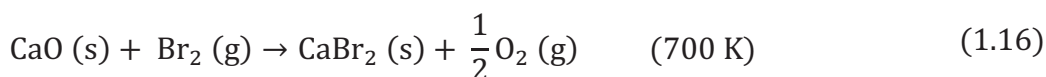


Figure 1.9 Diagram of Westinghouse sulphur cycle (Forsberg et al., 2003). It is a two-step sulphur cycle using both electrochemical and thermochemical process for decomposing water.

The UT-3 cycle has been developed firstly in Tokyo University is a thermochemical cycle also functioning at high temperature. It entails four adiabatic reactions consisting of two redox pairs, $\text{Br}_2|\text{HBr}$ and $\text{Fe}_3\text{O}_4|\text{Fe}_2\text{O}_3$ in a basic medium (Figure 1.10).



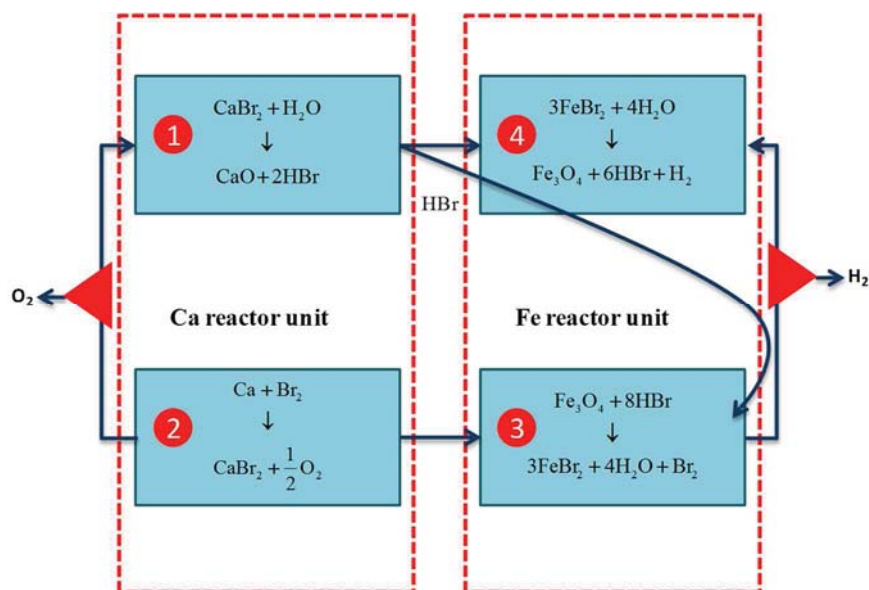


Figure 1.10 UT-3 flowsheet diagram of The UT-3 cycle developed in Tokyo University .

The yields of all thermochemical cycles are limited by the temperature of the heat source. For example, for sulphur iodine cycle the expected efficiency is about 50 %, but technically the attainable yield with preliminarily process improvement reaches to 45 %. On the other side, the optimal efficiency of Westinghouse cycle is 42 % which potentially can be raised up to 48.8 % if the electrolysis can be carried out in several steps. Also the NASA hybrid sulphur cycle has an overall thermal efficiency of 45.2 % (Farbman, 1976) while the ultimate efficiency of UT-3 cycle could reach to 53.2 % with nuclear reactor as heat source and to 49.5 % with solar source (Sakurai et al., 1996). It all concludes that to improve the efficiency of thermochemical cycles, the temperature of the heat source has to be increased cooperatively with a diminution in number of process steps. The major advantages of thermochemical cycles are the combination of heat and power and their considerable high efficiency. However, their main infirmities refer to the highly irreversible energy transformations, corrosive media in presence of aggressive compounds, strict selectivity of materials as a consequence of high temperature and the necessity of circulating and recycling involved components to ensure mass balance. Also, the common drawback of most of the high-temperature solar TCWSCs is that they only use the infrared portion of the solar spectrum, without considering the visible range. Therefore, the overall ratio of solar energy conversion to hydrogen of thermocycles is limited. As a matter of fact, more studies are required to develop new processes which involve solar energy and water as the only process inputs for hydrogen production. Today the studies show that to increase the efficiency and lower the process temperatures, the TCWSCs need a photochemical step (T-

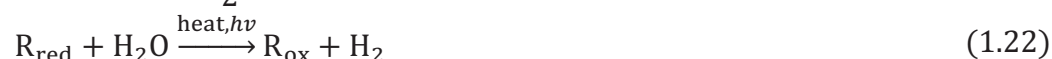
Raissi et al., 2007). However there is very limited information in the literature on the high-temperature water-splitting cycles involving such a photochemical step.

Here we introduce two solar based TCWSCs which have been investigated by (T-Raissi et al., 2007). The concept studied by this group is based on water splitting through multi step cycles at high temperature in which at least one step is driven by solar radiation. In a general form they can be presented as following:

Type 1:



Type 2:

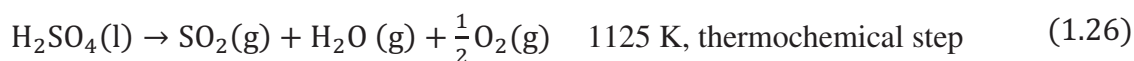
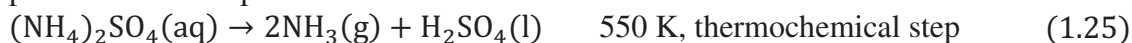
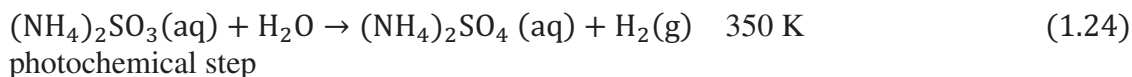


The example of the first type is carbon dioxide-carbon monoxide ($CO_2|CO$) cycle and for the second type a sulphur dioxide-sulphuric acid ($SO_2|H_2SO_4$) cycle can be mentioned. The first cycle relies on the fact that at high temperature (>1300 K), CO_2 becomes sensitive to a range of radiation between ultraviolet and even visible light. The second cycle is based on Westinghouse hybrid cycle with the modification that a photo-catalytic step takes the place of the electrochemical step.

Beside the low electricity consumption of Westinghouse cycle per unit of produced hydrogen, if the electricity is provided by using PV cells it may significantly increase the cost of hydrogen production. Another drawback of Westinghouse cycle is the pH issue : a low pH promotes the sulphur formation instead of hydrogen. To prevent sulphur formation, a high pH should be kept relatively high by reducing sulphuric acid concentration. While, high pH results in low hydrogen evolution rates besides the cost of acid separation in the outlet of reactor.

At the Florida Solar Energy Centre (FSEC), a novel hybrid photo-thermochemical sulphur ammonia (S-A) cycle has been developed which is not faced to the problems of sulphur dioxide-sulphuric acid cycle (Figure 1.11). The main reaction (unique to FSEC's S-A cycle) is the light-induced photo-catalytic production of hydrogen and ammonium sulphate from an aqueous ammonium sulphite solution. Ammonium sulphate product is processed to generate oxygen and

recover ammonia and SO_2 that are then recycled and reacted with water to regenerate the ammonium sulphite. Experimental data for verification of the concept are provided.



Reactions (1.23) to (1.25) belong exclusively to the FSEC's S-A cycle, but reaction (1.26) is similar to all sulphur family cycles and has been widely studied (Farbman, 1979).

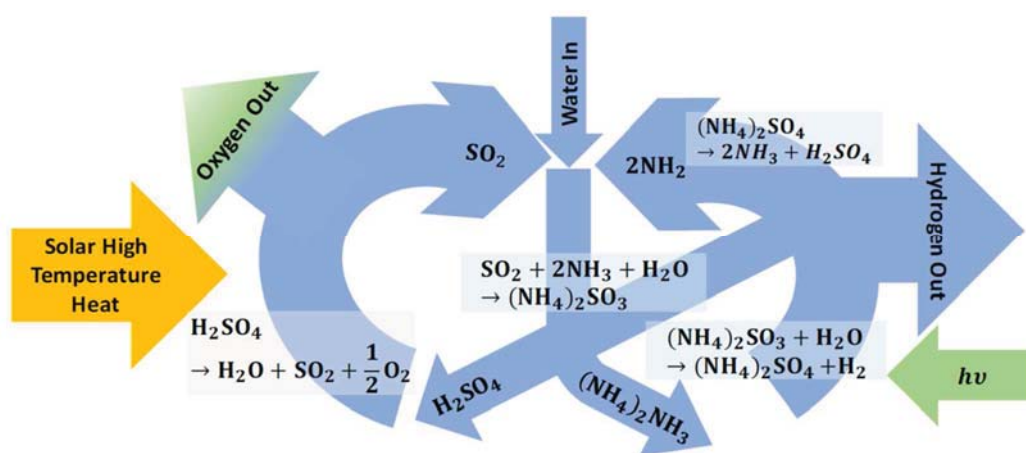


Figure 1.11 Descriptive diagram of energy and mass flow for the FSEC's sulfur-ammonia (S-A) cycle.

The process is composed of 4 units. First in a low temperature solar reactor sulphite ions of ammonium sulphite are oxidized to sulphate ions and water is reduced to H_2 (Eq 1.24). The second unit is gas liquid separator in which hydrogen is withdrawn. Then in a heat exchanger the ammonium sulphate solution is heated with heat from the sulphuric acid decomposition and produces sulphuric acid and NH_3 in an ammonia recovery unit. Most of the water evaporates off at the same time. H_2SO_4 in liquid form is then thermally decomposed in the decomposition unit by the concentrated radiation from a solar dish, and form SO_2 and O_2 . This SO_2 and O_2 are afterward mixed with NH_3 and chemically absorbed in water to regenerate ammonium sulphite. In this stage oxygen is separated from the mixture because of the significant difference in its solubility in water with other components.

Thermal efficiency of sulphuric acid decomposition process can be as high as 75% (Huang and T-Raissi, 2005), meaning that 75 kW of thermal energy out of 100 kW delivered by a solar concentrator will be available for splitting H_2SO_4 .

The S-A cycle has a step in which the solar energy of photon is directly converted into the chemical energy of hydrogen and this is without using intermediate devices such as photovoltaic cells. The other specification of S-A is that no electrical energy is necessary and maximum temperature of the cycle remains under 1170 K which reduces the materials cost of process. Moreover, the thermochemical step of the process such as decomposition of sulphuric acid is a common process to all sulphur cycles which is very well developed. As a result, the S-A cycle has the potential to achieve higher solar energy to hydrogen conversion efficiencies, comparing to solar concentrator turbine electrolyser systems.

1.2.2.2 Direct water photolysis

After photoelectrochemical water splitting was firstly achieved by (Fujishima and Honda, 1972) using TiO₂ photoelectrochemical cell (PEC), direct water photolysis via semiconductor photoelectrodes or photocatalysts have been largely investigated as a potential novelty in renewable hydrogen production challenge. The whole system is based on converting light energy to chemical energy through the reaction



Photocatalytic water splitting mechanism in a photoreactor or photoelectrochemical cell is very similar to the photosynthesis in plants (photon absorption, charge transport, reactions are occurring) ; hence it has been mostly mentioned as artificial photosynthesis. Photocatalysis as all catalytic processes can happen in heterogeneous or homogeneous phases. Even though both photoelectrochemical water splitting and photocatalytic are interesting, heterogeneous photocatalytic (HPC) systems which utilize semiconductor powder suspended in reaction phase, have some superiority over PEC systems because of their lower cost and less complexity. Hence, many studies have been devoted to studying new semiconductor materials in order to develop and optimize efficient HPC systems.

The second method of direct photochemical water splitting is photoelectrochemical water decomposition. The principle is the same as other photocatalytic process, which here means the light conversion into electricity or chemical energy through an photoelectrochemical cell.

1.3 Photoelectrochemical cells

Photoelectrochemical cells (PEC) have become a considerable point of interest of researchers during last decades because of their ability of splitting water in separate compartments. They

are mostly categorized according to their structures, materials and their outputs. As a brief introduction, a photoelectrochemical cell (PEC) is an electrochemical device in which the light energy is converted into electricity or chemical compounds through a light driven reaction. In a photoelectrochemical cell a potential difference and subsequently an electric current can be generated following light absorption by one or more semiconductor electrodes. The most important part of a photoelectrochemical cell is the semiconductor which enables a photoelectrode to accomplish different key processes including; light absorption, charge separation and transport. Furthermore, it should operate and be stable in aqueous solution and brings down cost of fabrication. Since the first publication of (Fujishima and Honda, 1972) many articles have been focused on different materials and the impact of their structures on PECs' performance since the properties of used materials is a determinant factor to the energy conversion efficiency of water splitting process. Hence discovering more effective materials has a crucial role in PEC development.

1.3.1 Photoelectrochemical cell and material aspects

In general, there are three possible combinations of photoelectrode in PECs setup. A very common arrangement is the photoelectrochemical cell consisted of an n-type semiconductor photoanode and a metal as cathode both immersed in an aqueous electrolyte (Figure 1.12). In this case illuminating an n-type photoanode makes oxygen evolution in photoanode and hydrogen evolution in cathode. Another possibility is to either of n-type and p-type materials as photoanode and photocathode respectively. Thereupon the n-type semiconductor as photoanode enforces water oxidation which results in H^+ generation and this H^+ will be reduced by the p-type photocathode (Bak et al., 2002; Grimes et al., 2008).

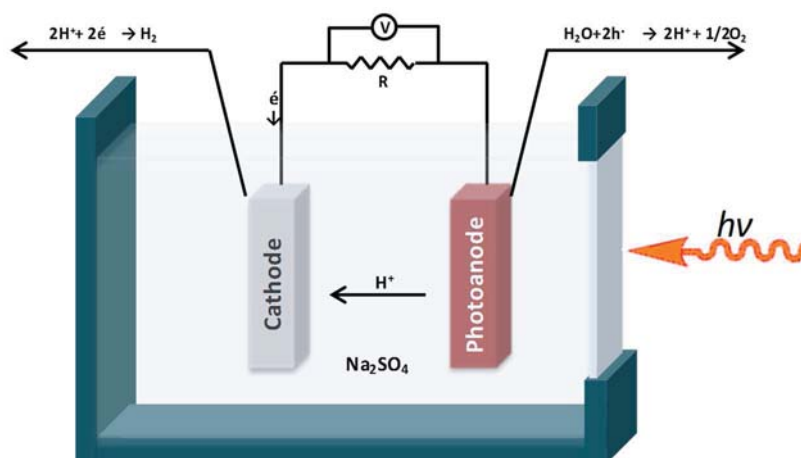


Figure 1.12 Scheme of photoelectrochemical cell for water photo electrolysis (Bak et al., 2002).

The last combination can be a p-type photocathode coupled with a metal anode; protons can be reduced to H_2 from the p-type photocathode exposure to the light which entails oxygen formation at metal anode.

Note that for all photoelectrochemical cell combinations; a third electrode (Ag/AgCl or saturated calomel electrode) can be used as a reference in order to define the contribution of both anode and cathode in global PEC functioning.

Setting aside the PEC electrodes combination based on material types the required materials for PEC fabrication have to fulfil two major factors: optical properties to realize maximal light intensity absorption and catalytic characteristics to split water. Semiconductors are widely used as photoelectrode material in PEC fabrication process.

1.3.2 Key functional properties of photoelectrodes

Photoelectrodes material should meet different specifications such as: appropriate band gap, flat band potential, Schottky barrier, electrical resistance, Helmholtz potential, corrosion resistance and microstructure.

1.3.2.1 Band gap

The minimum energy difference between the highest energy level in valence band and the lowest energy level in conduction band is defined as the band gap. This amount is important for photoelectrode materials because it defines the necessary energy for an electron issued from photon-ionization, to arrive to the conduction band. It means, only the photons of energy equal to or larger than that of the band gap may be absorbed and used for conversion. The maximal conversion efficiency of photovoltaic devices may be achieved at band gaps in the range 1.0–1.4 eV.

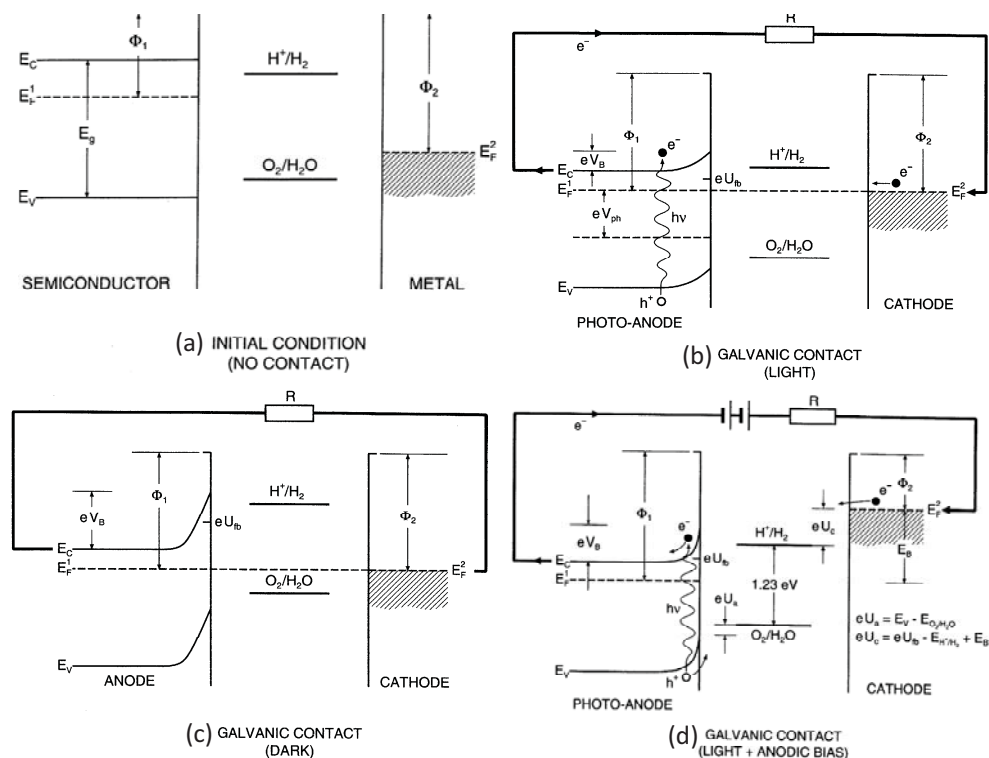


Figure 1.13 (a) Energy diagram of PEC components before galvanic contact: anode (semiconductor), electrolyte, and cathode (metal). (b) Energy diagram of PEC components after galvanic contact between anode and cathode. (c) Effect of light on electronic structure of PEC components. (d) Effect of light on energy diagram of PEC with externally applied bias (Bak et al., 2002).

Most of the commercial oxide materials do not benefit of both optimal band gap and the corrosion stability and so material processing has been become a crucial step in photoelectrode fabrication. The band gap of most of oxide materials is between 2.3 and 3.7 eV. Furthermore they demonstrate better absorption in ultraviolet (UV) region ($\lambda < 400\text{ nm}$) whereas almost half of the sun light is visible light and it compromise only about 3% of UV. Among all studied systems with different semiconductor materials, TiO_2 based systems are commonly used because of TiO_2 non toxicity, chemical stability and cheap cost. However the main disadvantage of TiO_2 is its large band gap of around 3.2 eV, which makes it unable to absorb visible light. According to (Bak et al., 2002) one method to extend the photoactive range of TiO_2 is heavy doping with ions such as V^{4+}/V^{5+} . In spite of the band gap reduction to 1.99 eV this modification is nevertheless not pertinent as the formation of O_2 is destructive to the photoactivity of material because of increasing the flat band potential up to 1 eV which entails the application an external bias (Phillips et al., 1982). However since TiO_2 is one of the most stable materials in water the photoelectrode photonic properties might be enhanced by using a low band gap material such as "Si" in the inner part of photoelectrode so that the total energy absorption be improved comparing to TiO_2 by itself (Morisaki et al., 1976).

1.3.2.2 Flat band potential

The flat band potential is the necessary potential to be applied to the electrode-electrolyte interface to flatten the bands (Figure 1.13). The flat band potential U_{fb} is important because for example in water photo-electrolysis the reaction within the cell starts when the flat band potential is higher than the redox couple potential in the electrolyte ($H^+|H_2$ in case of water electrolysis). Accordingly only the photoanodes with negative flat band potentials vs. redox potential of $H^+|H_2$ can accomplish the water decomposition without applying an external bias. Otherwise all materials are able to split water only in presence of bias. The flat band potential varies with pH values of electrolyte because the redox couple potential is dependent on pH (Seraphin, 1979).

1.3.2.3 Schottky barrier

Schottky barrier is a potential drop in the potential in the interface layer of the solid, which is formed because of concentration gradients, surface states, or adsorption states. The existence of Schottky barrier prevents the recombination of the charge formed due to photo-ionization because an electrical potential barrier across the surface layer can be formed as a result of several phenomena. The most common one can be structural deformations within the layer near surface layer because of a surface energy excess and chemical potential gradients of aliovalent ions across the surface layer imposed as a result of surface processing. Therefore, the formation of these gradients may be used for the modification of the Schottky barrier in a controlled manner (Bak et al., 2002; Kozuka et al., 2000)

1.3.2.4 Electrical resistance

Electrical resistance is a general term used in literature to discuss the electrical conductivity of each part of the system, electrodes, electrolyte and electrical connections. The discussion and definition of these resistances will be largely developed later in chapter 2.

1.3.2.5 Helmholtz potential barrier

The charge transfers at the interface of electrode|electrolyte charges the surface layer of the electrode and so changes the potential level of the semiconductor which is known as band bending. This leads to the formation of a potential barrier whose height is recognized as Helmholtz barrier. The surface charging is followed by accumulation of opposite charges at the electrode surface within the electrolyte. This layer of adsorbed electrolyte ions on the electrode

surface is named Helmholtz layer. A significant part of photoelectrode performance can depend on the height of Helmholtz barrier (Chandra et al., 1986; Gerischer, 1979; Lewerenz, 1989).

1.3.3 PEC structure

So many different categories have been defined for PECs. Some of the significant classifications are as following:

- Single photoelectrode system which is simply the combination of one photo-sensible electrode (photoelectrode) with another non light sensitive electrode;
- Hybrid photoelectrode is established by two n-type semiconductor which results to a heterogeneous system for example hybrid photoelectrode reported by (Morisaki et al., 1976). The photoelectrode as it was mentioned earlier is made up of TiO_2 thin film under which a Si photovoltaic cell is implemented. Using the Si cell provides a photovoltage acting as an internal bias (Gerischer, 1979).

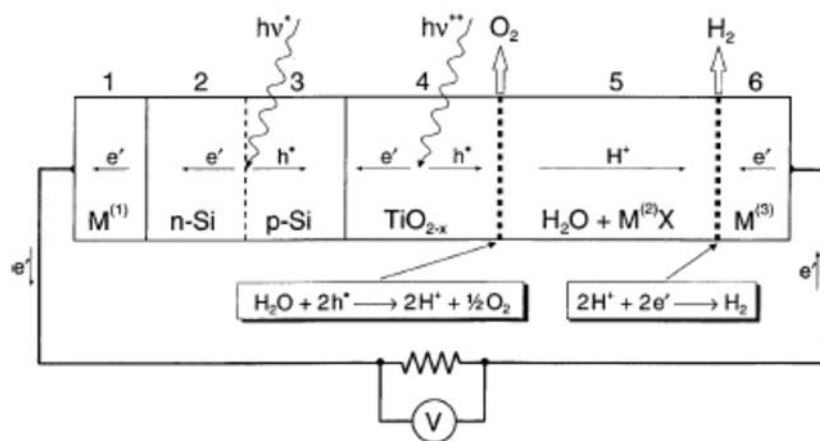


Figure 1.14 Hybrid photoelectrode PEC consisting of TiO_2 layer and Si solar cell as a sublayer in photoanode. Only the TiO_2 film is contact with the electrolyte (Bak et al., 2002).

- Bi-photoelectrode cells are composed of two photoelectrodes made of n-type and p-type semiconductors as photoanode and photocathode respectively. The positive point of this system does not need a bias application for water photolysis because the net photo-voltage produced by both photoelectrodes is enough for water photolysis (Nozik, 1976).
- Photoelectrode sensitized through doping by foreign ions (Ghosh and Maruska, 1977; Zhao et al., 1999).

- Photoelectrode sensitized through incorporation of particles of noble metals, is another method of sensitizing TiO_2 by dispersing noble metals e.g. Ag and Pt on semiconductor film (plasmonic effect) (Liao et al., 1998).
- Photoelectrode sensitized through dye deposition, which is about the sensitization of semiconductor thin film with dye molecules directly attached on the surface of semiconductor layer (Krol, 2012).

All above categories are mentioned and studied largely in literatures. In this work we dedicate a large part to the study of Dye Sensitized Solar Cell (DSSC) systems because our PEC development is conceptually inspired by DSSC principles.

1.3.4 Dye-sensitized solar cell

An important classification of photoelectrochemical devices based on n-type semiconductors relies on their outputs, which points to two categories. The first class represents regenerative cells, in which the input light energy gives electric power as output but in overall process no global chemical change happens. In the case of a photoelectrode only constituted of a semiconductor, photons with greater energy than the semiconductor's band gap develop electron-hole pairs which lead to electron transfer from the valence band into the conduction band of the semiconductor. This transfer is ensured by the electric field issues from the space-charge layer which keeps pushing holes to the electrode-electrolyte interface and driving the electrons within the semiconductor film toward the external circuit. These electrons will re-enter the cell from the cathode side to reduce an oxidizing agent O in the electrolyte; $\text{O} + \text{e}^- \rightarrow \text{R}$. The reducing agent R after travelling through the electrolyte will be regenerated by positive holes at the photoanode electrolyte interface (Grätzel, 2001).

Regenerative cells have been studied on many aspects but mostly on the n-type doped semiconductor (II/IV, II/V) together with mesoscopic semiconductor materials and nanocrystalline junctions. Several redox couples in electrolytes have been tested as well; such as sulphide/polysulphide, vanadium (II)/vanadium (III) or Iodide (I_2) | Iodine (I^-). A famous example of regenerative cells group is Dye-Sensitized Solar Cell (DSSC) also known as Grätzel

cell which was co invented by Brien O'Regan and Michael Grätzel in 1988² (Bach et al., 1998; Grätzel, 2005).

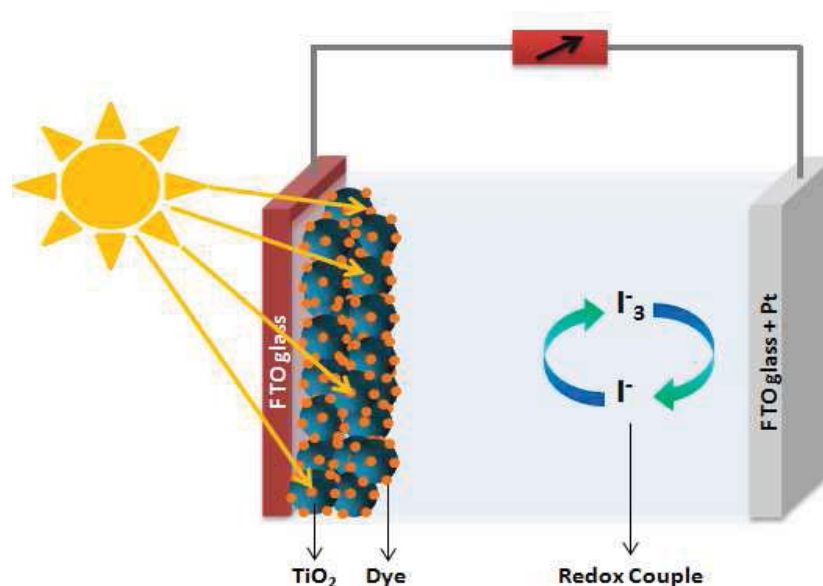


Figure 1.15 Dye-sensitized solar cell (DSSC) also known as Grätzel cell. The electrolyte consists of iodide/triiodide redox couple; the iodide (I^-) regenerates the oxidized dye by injecting an electron in dye's conduction band and will be oxidized into triiodide (I_3^-). This triiodide (I_3^-) will be reduced to iodide by electrons arriving at counter electrode via the external circuit.

The advantage of DSSC to other types of this family refers to its light absorption and charge separation aspects which are enormously developed by adsorbing a dye sensitizer molecule to a wide band gap semiconductor such as TiO_2 (Grätzel, 2005; Somani et al., 2006).

A dye sensitizer is an organic or inorganic molecule which absorbs the light efficiently. As it is shown in Figure 1.15, the photoanode is composed of a nanocrystalline thin layer film of a semiconductor, here TiO_2 (anatase), associated with a layer of dye sensitizer molecules all attached on the surface of a conducting glassy electrode (e.g. FTO). Both photoanode and cathode are in contact with an organic or redox electrolyte. The dye absorbs a photon and injects an electron in the conduction band of the semiconductor. This electron travels through the semiconductor film and reaches to the conducting glass. This dye will be regenerated afterward through electron exchange with the electrolyte. In the case of the electrolyte containing iodide/triiodide redox couple; the iodide (I^-) regenerates the oxidized dye by injecting an electron in dye's conduction band and will be oxidized into triiodide (I_3^-). This triiodide (I_3^-)

² The work was developed subsequently by Michael Grätzel at the Ecole Polytechnique Fédérale de Lausanne up till the first publication of high efficiency DSSC in 1991.

will be reduced to iodide by electrons arriving at counter electrode via the external circuit. Consequently, the whole device generates electric power while no chemical changes happen in overall process. The efficiency of dye sensitized solar cells is about 4-5% for commercial versions but the efficiency of laboratory prototypes can reach up to 10-11% (Grätzel, 2001; Grimes et al., 2008; Krol, 2012; Lewis et al., 2005) .

1.3.5 Photoelectrochemical Hydrogen production

The second class of PECs are photosynthetic cells. They operate in a similar way to regenerative cells with the difference that two redox systems are present in the electrolyte. One is engaged in the oxidation reaction with holes in semiconductor photoelectrode at the semiconductor|electrolyte interface while the other couple runs the reduction reaction with electrons arriving to the counter electrode side.



As it is shown in Figure 1.12 the output of this system is oxygen gas evolution issued from water oxidation at the photoanode and the hydrogen gas generation by the reduction of ionized water at the cathode. Therefore, the global reaction in the cell is solar water splitting (Eq 1.30). Photoelectrochemical water splitting has the simplicity of producing hydrogen and oxygen separately at room temperature which reduce significantly the explosion risk of hydrogen and oxygen gas mixture. Subsequently there would be no extra charge for separating the gases.

Other important aspect of photoelectrochemical splitting is about device fabrication and process materials. The entire photoelectrochemical process could be fully implemented with inorganic materials, which shows more stability and process viability in comparison to organic materials.

In photocatalytic systems the solar radiation after an electron excitation generates electron-hole pairs in a photoactive site that could be a semiconductor or a chromophore and converts solar energy into electromotive force which gives result to water oxidation into oxygen and proton reduction into hydrogen. As already explained in PEC structure part (1.3.3), titanium dioxide is an interesting semiconductor for photoelectrochemical cells' studies but because of its large band gap (3.0-3.2 eV); TiO₂ does not absorb the visible part of the solar spectre. It can only

absorb in the ultraviolet range and yet it shows low conversion efficiencies. Accordingly this limitation can be compensated by coupling chromophores with TiO_2 .

Using chromophores as photoactive site on the semiconductor film enables the system to absorb as much as possible in visible range. The chromophore is an intermediate which builds a shortcut for transferring electron into the conduction band of TiO_2 .

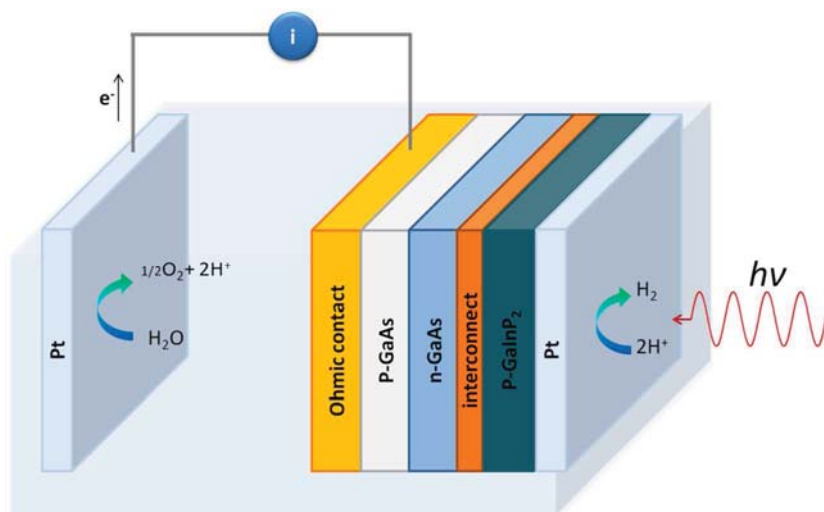


Figure 1.16 Schema of monolithic PV-PEC system (Tran et al., 2010). A monolithic PEC system represented by a p-type photocathode (GaInP_2) which can present a notable efficiency in hydrogen production (12.4%).

Other alternative is to choose another semiconductor material such as ZnO , SnO_2 , CdS and Fe_2O_3 that have been also investigated.

Therefore we can presume three approaches for photoelectrochemical water splitting. Owing to previous discussion about PV-PEC combination (Figure 1.16), a monolithic PEC system represented by a p-type photocathode (GaInP_2) (Khaselev, 1998) can present a notable efficiency in hydrogen production (12.4%) (Khaselev et al., 2001; Krol, 2012). The major drawbacks of the system are the high cost and the lack of durability of GaInP_2 and GaAs in aqueous solution. Other researches are focused on using metal oxide semiconductors; such as Fe_2O_3 (hematite) and WO_3 who's chromatic properties permit to act as the photoactive site in the system. The system has to be coupled with cobalt based complexes or iridium dioxide (IrO_2) for catalysing the oxygen evolution reaction (OER) at photoanode (Figure 1.17) (Sivula et al., 2009; Zhong and Gamelin, 2010). Contrary to PV-PEC systems, metal oxides have remarkable stability in aqueous solution and low costs of manufacturing as well. Many effort has been dedicated to improve hematite photoanodes but even at their very best operating point they are

far from the optimum comparing to similar materials like WO_3 and TiO_2 (Tilley et al., 2010). Nevertheless in addition to correct stability and high light absorption, the semiconductor should be also abundant and this keeps hematite still interesting as photoanode material. Another major problem of Fe_2O_3 and WO_3 remains poor light absorption and limited charge transfer properties. Several solutions such as mesoporous materials, guest–host nanostructures, tandem junctions has been introduced in literature to improve these systems (Krol, 2012; Youngblood et al., 2009).

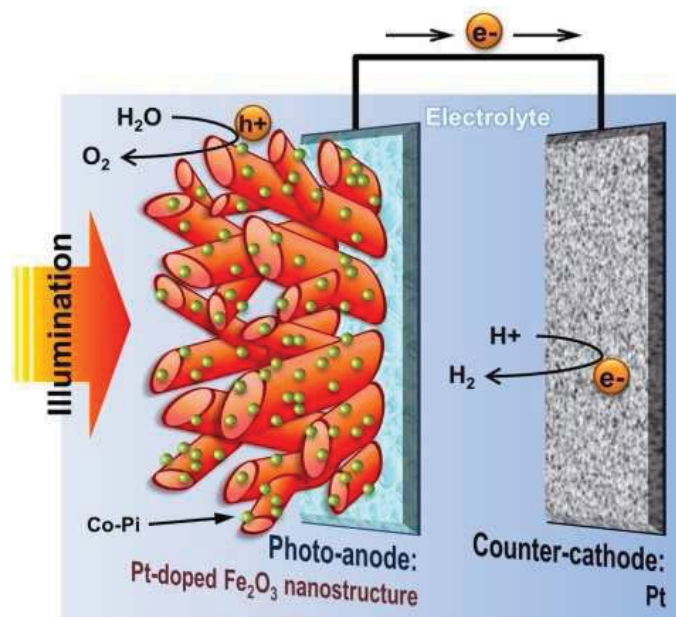


Figure 1.17 Metal oxide (hematite thin film) based photoelectrochemical cell coupled up to cobalt complex as catalyst (Kim et al., 2013). The OER is limited by light absorption and charge transfer properties of the photoanode. However it shows satisfying stability depending on the operating pH.

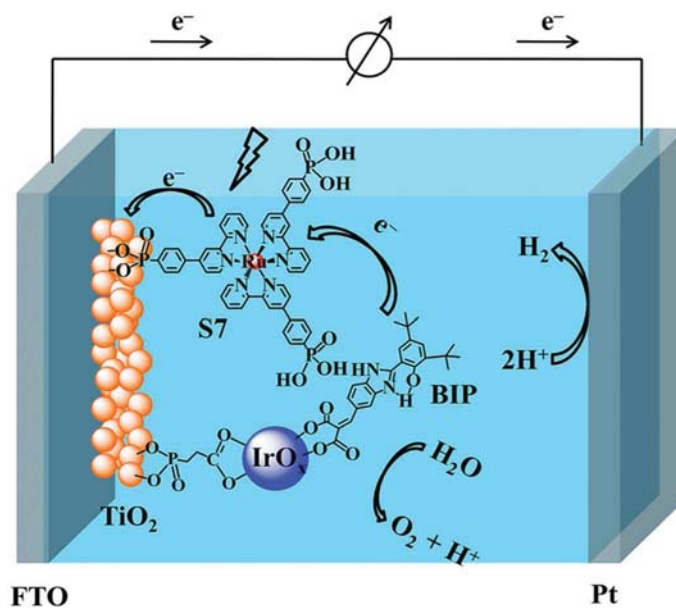


Figure 1.18 Example of molecular PEC device with ruthenium based chromophore (Sun et al., 2014).

Another approach investigated largely during last decade is molecular approach which suggests an inexpensive method of photocatalytic water splitting in a similar fashion as photosynthesis. The system is based on a nanoporous TiO_2 and the semiconductor film is covered by ruthenium complexes as dye molecule. The process is catalysed by an efficient catalyst like IrO_2 nanoparticle linked directly to the dye (Figure 1.18). The combination of ruthenium complex and TiO_2 accomplishes the light absorption and charge separation processes. The main concern of molecular approach is about the efficiency. Today the system performance is less than 1%.

1.4 A personal view of this thesis outlines

Da Vinci says “Nature is the source of all true knowledge. She has her own logic, her own laws; she has neither effect without cause nor invention without necessity”. Any simple logic in the nature can be linked to a necessity to our world running out of time to discover them. It can be a simple tiny reflection about what a flower pot behind our window does every minute. It absorbs the sunlight by chlorophyll and splits water and carbon dioxide to sugar and oxygen gas. This inspiration is followed by vast investigations on water and solar energy combination as two most abundant and potential sources and puts hydrogen production through photosynthetic cells in the centre of recent research. Between many hydrogen production methods what concerns this work is a direct inspiration of photosynthesis and moving toward water splitting within photo-electrochemical cells (PEC) through two approaches. The main approach is the molecular water splitting through cheap materials by remaining faithful to the main elements of the process. Hence a Ruthenium molecular dye complex named chromophore plays the role of chlorophyll and absorbs the light into the system. This photon absorption gives result to the charge separation and charge transfer within the semiconductor film and so within the photoanode (Figure 1.19). The objective is to complete the process with a ruthenium molecular catalyst which regenerates the chromophore and make the process renewable.

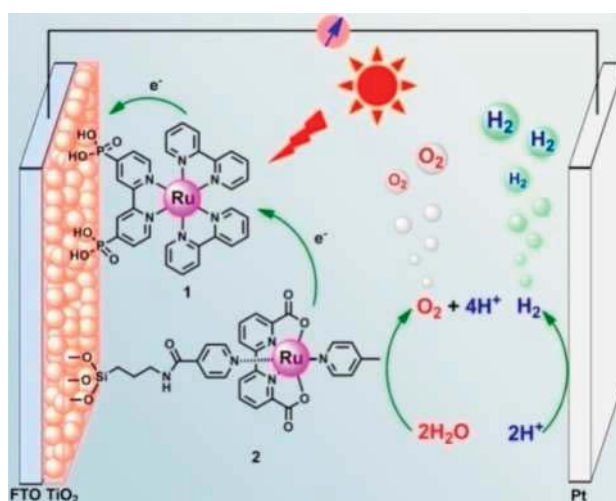


Figure 1.19 water oxidation by ruthenium synthesiser complexes and ruthenium catalyst attached on titanium dioxide electrode in a photoelectrochemical cell. The water reduction reaction takes place at the platinum counter electrode which results to evolution of hydrogen gas³.

³ TechBio'Phyb project, ANR 2011.

This thesis intends to incept a path toward photoelectrochemical hydrogen production by considering radiative transfer as a main limiting step to photo processes. After years of fundamental research in modelling of radiative transfer in photoreactors and developing several devices such as photobioreactor and torus photoreactor by photoreactive process engineering group in Institut Pascal, GePEB; the group started its work on photo-electrochemical cells by collaborating in TECBIO'PHYP project an acronym for Toward Efficient and Cheap BIO-inspired cells for Photo-electrochemical HYdrogen Production. This research project is a subject funded by «Agence Nationale de la Recherche (ANR)». As its name implies, it is dedicated to the solar hydrogen production from water in photo-electrochemical systems by bioinspired catalysts.

Our task includes the development of a comprehensive knowledge model of photo-electrochemical cells (PEC) taking into account the main limiting steps of photoprocess as a major key for simulation, design and optimization of PECs. Thereupon the main block of our approach lays on modelling of radiative transfer in photoanodes. For this, our work has been concentrated on two photoanodes systems. First, hematite photoanode coupled with iridium oxide as a catalyst. This system which has been briefly explained earlier is a photocatalytic system in which hematite oxide is used as photosensitive material and iridium oxide is used as catalyst for oxidation reaction. In fact, this system was developed as a parallel to develop our knowledge model without being concerned about catalytic reaction limitation, the system is assumed to be limited by radiative transfer. The other system concerns using molecules developed by TECHBIO'PHYP photoanode group. In this case the photoanode is made of a ruthenium molecular system attached on titanium dioxide layer. However, the molecular system has more complexity because the efficiency or chromophore regeneration should be taken into account and this makes the modelling of this system more difficult. So our group has decided to develop the knowledge model first for hematite photoanode and then adapt it to molecular system.

Another approach for PEC modelling which has been developed widely by several research groups is electrical modelling. In this case every phenomenon within the PEC will be analogically shown as an electrical element so the PEC can be thoroughly represented by an electrical circuit. This model will be presented and detailed in the first part of chapter 2. This approach has been used for the first time in the laboratory in the framework of this PhD and developed for our PEC device.

To understand better PEC functioning and perform photoelectrochemical measurements on different systems a PEC device was designed and fabricated by the Institut Pascal team in triplicate in order to give all collaborators the possibility to work with the same device under similar electrochemical conditions. The specifications and assembly details of this photoelectrochemical cell will be detailed in chapter 3. Fabricating and customizing our PEC device allow us to characterize every electrode under determined physical operating conditions.

To comprehend more about titanium dioxide photoanodes we started by studying and fabricating DyeSensitized Solar Cells (DSSC) which has many similarities to our ruthenium molecular system. Also most of the electrical models developed in recent decades are dedicated to DSSC which proves the necessity of understanding this system experimentally. Another interest of preparing DSSC setup is to perform prevalent tests of DSSC in our PEC device and compare our results to published results of DSSC and validate the performance of our PEC device. We also compared our DSSC results to the results obtained from a commercial version of DSSC fabricated by Solaronix. These results will be presented and discussed in chapter 4.

This thesis first brings a global and detailed view of theoretical and experimental developments of photoelectrochemical cells in published works especially on dyesensitized solar cells and hematite systems. It also presents the complete characterization of both photonic and electrochemical aspects of our PEC system and provides a complete data base which can be fitted and modelled by existing electrical models. It also enables us to present the accuracy of our knowledge and electrical models.

The objective of this thesis is not to achieve a replacement for actual energy vectors, with a debatable efficiency today, but to participate in putting all the possible solutions on the table and giving an understandable vision of renewable hydrogen production methods and photoelectrochemical cells developments in the near future. Indeed, this thesis will be the continuity of the work that has been started twenty years ago in study and modelling of photoreactors by photoreactive process engineering of Institut Pascal but it may add a new apex of the triangle of photobioreactor, photoreactor and photoelectrochemical cells in our group.

This thesis has benefited the collaboration of:

- Pr. Ally AUKAULOO, Laboratoire de Chimie Moléculaire et des Matériaux d'Orsay, Université Paris Sud, Orsay.
- Dr. Frédéric GLOAGUEN, Laboratoire de Chimie, Electrochimie Moléculaires et Chimie Analytique, Université de Bretagne Ouest, Brest.

- Dr. Winfried LEIBL, Institut de Biologie Intégrative de la cellule, CEA Saclay, Saclay.
- Dr. Boris VAUZEILLES, Institut de Chimie des Substances Naturelles, Université de Paris Saclay, Gif-sur-Yvette.

References

- Abe, I., 2009. Photovoltaic cell-water electrolysis system, in: Ohta, T. (Ed.), *Energy Carriers and Conversion Systems. Encyclopedia of Life Support Systems (EOLSS)*, Chiba, Japan.
- Adrian, G., Agency, I.E., 2013. *Key World Energy Statistics. Int. Energy Agency 2013*, 1–82. <https://doi.org/10.1201/b15566-3>
- Allison, I., Bindoff, N.L., Bindschadler, R. a, Cox, P.M., De Noblet, N., England, M.H., Francis, J.E., Gruber, N., Haywood, a M., Karoly, D.J., Kaser, G., Le Quere, C., Lenton, T.M., Mann, M.E., McNeil, B.I., Pitman, a J., Rahmstorf, S., Rignot, E., Schellnhuber, H.J., Schneider, S.H., Sherwood, S.C., Somerville, R.C.J., Steffen, K., Steig, E.J., Visbeck, M., Weaver, A.J., Noblet, N. De, Quéré, C. Le, 2009. *The Copenhagen Diagnosis: Updating the World on the Latest Climate Science 2009*, Provider.
- Bach, U., Lupo, D., Comte, P., Moser, J.E., Weissörtel, F., Salbeck, J., Spreitzer, H., Grätzel, M., 1998. Solid-state dye-sensitized mesoporous TiO₂ solar cells with high photon-to-electron conversion efficiencies. *Nature* 395, 583–585. <https://doi.org/10.1038/26936>
- Bak, T., Nowotny, J., Rekas, M., Sorrell, C.C., 2002. Photo-electrochemical hydrogen generation from water using solar energy. Materials-related aspects. *Int. J. Hydrogen Energy* 27, 991–1022. [https://doi.org/10.1016/S0360-3199\(02\)00022-8](https://doi.org/10.1016/S0360-3199(02)00022-8)
- BP, 2013. *BP Statistical Review of World Energy June 2013*. Br. Pet.
- Brecher, L.E., Spewock, S., Warde, C.J., 1977. The Westinghouse sulfur cycle for the thermochemical decomposition of water. *Int. J. Hydrogen Energy* 2, 7–15. [https://doi.org/10.1016/0360-3199\(77\)90061-1](https://doi.org/10.1016/0360-3199(77)90061-1)
- Carty, R., Cox, K., Funk, J., Soliman, M., Conger, W., Brecher, L., Spewock, S., 1977. Process sensitivity studies of the Westinghouse Sulfur Cycle for hydrogen generation☆. *Int. J. Hydrogen Energy* 2, 17–22. [https://doi.org/10.1016/0360-3199\(77\)90062-3](https://doi.org/10.1016/0360-3199(77)90062-3)
- CEA, 2004. *Livret Hydrogène. Gif-sur-Yvette*. <https://doi.org/ISSN 1637-5408>
- Chandra, S., Singh, S.L., Khare, N., 1986. A theoretical model of a photoelectrochemical solar cell. *J. Appl. Phys.* 59, 1570–1577. <https://doi.org/10.1063/1.336466>
- Farbman, G., 1979. Hydrogen production by the Westinghouse sulfur cycle process: program status. *Int. J. Hydrogen Energy* 4, 111–122. [https://doi.org/10.1016/0360-3199\(79\)90045-4](https://doi.org/10.1016/0360-3199(79)90045-4)
- Farbman, G.H., 1976. *Studies of the use of heat from high temperature nuclear sources for hydrogen production processes*.
- Forsberg, C., Bischoff, B., Mansur, L.K., Trowbridge, L., Tortorelli, P., 2003. *A Lower-Temperature Iodine–Westinghouse–Ispra Sulfur Process for Thermochemical Production of Hydrogen*, Submitted Manuscript to U.S Government (Global 2003 Manuscript number 87682) by Oak Ridge National Laboratory. <https://doi.org/DE-AC05-00OR22725>
- Fujishima, A., Honda, K., 1972. *Electrochemical Photolysis of Water at a Semiconductor*

- Electrode. *Nature* 238, 37–38. <https://doi.org/10.1038/238037a0>
- Gerischer, H., 1979. Solar photoelectrolysis with semiconductor electrodes. pp. 115–172. https://doi.org/10.1007/3-540-09224-2_4
- Ghosh, A.K., Maruska, H.P., 1977. Photoelectrolysis of Water in Sunlight with Sensitized Semiconductor Electrodes. *J. Electrochem. Soc.* 124, 1516. <https://doi.org/10.1149/1.2133104>
- Grätzel, M., 2005. Solar energy conversion by dye-sensitized photovoltaic cells. *Inorg. Chem.* <https://doi.org/10.1021/ic0508371>
- Grätzel, M., 2001. Photoelectrochemical cells. *Nature* 414, 338–344. <https://doi.org/10.1038/35104607>
- Grimes, C.A., Varghese, O.K., Ranjan, S., 2008. Light, water, hydrogen: The solar generation of hydrogen by water photoelectrolysis, *Light, Water, Hydrogen: The Solar Generation of Hydrogen by Water Photoelectrolysis.* <https://doi.org/10.1007/978-0-387-68238-9>
- Hoffert, M.I., 2010. Farewell to Fossil Fuels? *Science* (80-). <https://doi.org/10.1126/science.1195449>
- Huang, C., T-Raissi, A., 2005. Analysis of sulfur-iodine thermochemical cycle for solar hydrogen production. Part I: Decomposition of sulfuric acid. *Sol. Energy* 78, 632–646. <https://doi.org/10.1016/j.solener.2004.01.007>
- IPCC, 2013. IPCC, 2013: Summary for Policymakers., in: *Climate Change 2013: The Physical Science Basis. Contribution of Working Group I to the Fifth Assessment Report of the Intergovernmental Panel on Climate Change.* pp. 1–28.
- Jeon, H.S., Kim, J., Kim, H., Lee, S.D., Min, B.K., 2012. Design of an electrolytic cell for a monolytic photovoltaic-electrolytic hydrogen generation system: The electrode aspects. *Chem. Eng. Commun.* <https://doi.org/10.1080/00986445.2011.647137>
- Khaselev, O., 1998. A Monolithic Photovoltaic-Photoelectrochemical Device for Hydrogen Production via Water Splitting. *Science* (80-). <https://doi.org/10.1126/science.280.5362.425>
- Khaselev, O., Bansal, A., Turner, J.A., 2001. High-efficiency integrated multijunction photovoltaic/electrolysis systems for hydrogen production. *Int. J. Hydrogen Energy* 26, 127–132. [https://doi.org/10.1016/S0360-3199\(00\)00039-2](https://doi.org/10.1016/S0360-3199(00)00039-2)
- Kim, J.Y., Magesh, G., Youn, D.H., Jang, J.-W., Kubota, J., Domen, K., Lee, J.S., 2013. Single-crystalline, wormlike hematite photoanodes for efficient solar water splitting. *Sci. Rep.* 3, 2681. <https://doi.org/10.1038/srep02681>
- Kozuka, H., Takahashi, Y., Zhao, G., Yoko, T., 2000. Preparation and photoelectrochemical properties of porous thin films composed of submicron TiO₂ particles. *Thin Solid Films* 358, 172–179. [https://doi.org/10.1016/S0040-6090\(99\)00658-6](https://doi.org/10.1016/S0040-6090(99)00658-6)
- Krol, R. Van De, 2012. Photoelectrochemical Hydrogen Production, *Photoelectrochemical Hydrogen Production.* <https://doi.org/10.1007/978-1-4614-1380-6>
- Laguna-Bercero, M. a., 2012. Recent advances in high temperature electrolysis using solid oxide fuel cells: A review. *J. Power Sources* 203, 4–16. <https://doi.org/10.1016/j.jpowsour.2011.12.019>
- Lewerenz, H.-J., 1989. Semiconductor electrodes. *Adv. Mater.* 1, 96–97.

<https://doi.org/10.1002/adma.19890010316>

- Lewis, N.S., Crabtree, G., Nozik, A.J., Wasielewski, M.R., Alivisatos, P., 2005. Basic Research Needs for Solar Energy Utilization, in: Basic Energy Sciences Workshop on Solar Energy Utilization. p. 276.
- Lewis, N.S., Nocera, D.G., 2006. Powering the planet: chemical challenges in solar energy utilization. *Proc. Natl. Acad. Sci. U. S. A.* 103, 15729–15735. <https://doi.org/10.1073/pnas.0603395103>
- Liao, H.B., Xiao, R.F., Wang, H., Wong, K.S., Wong, G.K.L., 1998. Large third-order optical nonlinearity in Au:TiO₂ composite films measured on a femtosecond time scale. *Appl. Phys. Lett.* 72, 1817. <https://doi.org/10.1063/1.121193>
- Lin, S., Flaherty, R., 1983. Design studies of the sulfur trioxide decomposition reactor for the sulfur cycle hydrogen production process. *Int. J. Hydrogen Energy* 8, 589–596. [https://doi.org/10.1016/0360-3199\(83\)90226-4](https://doi.org/10.1016/0360-3199(83)90226-4)
- Morisaki, H., Watanabe, T., Iwase, M., Yazawa, K., 1976. Photoelectrolysis of water with TiO₂-covered solar-cell electrodes. *Appl. Phys. Lett.* 29, 338. <https://doi.org/10.1063/1.89088>
- Ni, M., Leung, M.K.H., Leung, D.Y.C., 2008. Technological development of hydrogen production by solid oxide electrolyzer cell (SOEC). *Int. J. Hydrogen Energy* 33, 2337–2354. <https://doi.org/10.1016/j.ijhydene.2008.02.048>
- Nozik, A.J., 1976. p-n photoelectrolysis cells. *Appl. Phys. Lett.* 29, 150–153. <https://doi.org/10.1063/1.89004>
- Phillips, T.E., Moorjani, K., Murphy, J.C., Poehler, T. O., 1982. TiO₂ -VO₂ Alloys, Reduced Randgap Effects in the Photoelectrolysis of Water. *Electrochem. Soc.* 129, 1210.
- PUBLICATIONS, I., 2015a. Renewable energy [WWW Document]. URL <http://www.iea.org/aboutus/faqs/renewableenergy/> (accessed 11.2.15).
- PUBLICATIONS, I., 2015b. IEA, Unit Converter [WWW Document]. URL <http://www.iea.org/statistics/resources/unitconverter/> (accessed 10.28.15).
- PUBLICATIONS, I., 2014. Key World Energy Statistics 2014.
- PUBLICATIONS, I., 2006. Hydrogen Production and Storage. *Energy* 13, 392. [https://doi.org/10.1016/0360-3199\(88\)90106-1](https://doi.org/10.1016/0360-3199(88)90106-1)
- Renewables Global Status Report, 2014. Renewables 2014 Global Status Report. <https://doi.org/ISBN 978-3-9815934-2-6>
- Sakurai, M., Bilgen, E., Tsutsumi, a., Yoshida, K., 1996. Solar UT-3 thermochemical cycle for hydrogen production. *Sol. Energy* 57, 51–58. [https://doi.org/10.1016/0038-092X\(96\)00034-5](https://doi.org/10.1016/0038-092X(96)00034-5)
- Sapru, K., Stetson, N.T., Ovshinsky, S.R., 1998. An integrated hydrogen production/storage system based on PV/electrolysis/metal hydrides for near-term applications, *Hydrogen Energy Progress Xii*, Vols 1-3.
- Schultz, K.R., 2003. Use of the Modular Helium Reactor for Hydrogen Production. *Symp. A Q. J. Mod. Foreign Lit.* 1–11.
- Seraphin, B.O., 1979. Solar Energy Conversion, Topics in Applied Physics. Springer Berlin Heidelberg, Berlin, Heidelberg. <https://doi.org/10.1007/3-540-09224-2>

- Siegel, A., 1988. Optimization of photovoltaic hydrogen production. *Int. J. Hydrogen Energy* 13, 659–675. [https://doi.org/10.1016/0360-3199\(88\)90076-6](https://doi.org/10.1016/0360-3199(88)90076-6)
- Sivula, K., Formal, F. Le, Grätzel, M., 2009. WO₃-Fe₂O₃ photoanodes for water splitting: A host scaffold, guest absorber approach. *Chem. Mater.* 21, 2862–2867. <https://doi.org/10.1021/cm900565a>
- Somani, P.R., Somani, S.P., Umeno, M., Sato, A., 2006. Concept and demonstration of all organic Gratzel solar cell (dye sensitized solar cell). *Appl. Phys. Lett.* 89. <https://doi.org/10.1063/1.2337563>
- Sun, L., Li, F., Yu, Z., 2014. Recent Advances in Dye-Sensitized Photoelectrochemical Cells for Solar Hydrogen Production Based on Molecular Components. *Energy Environ. Sci.* 8, 760–775. <https://doi.org/10.1039/C4EE03565H>
- T-Raissi, a., Muradov, N., Huang, C., Adebisi, O., 2007. Hydrogen From Solar Via Light-Assisted High-Temperature Water Splitting Cycles. *J. Sol. Energy Eng.* 129, 184. <https://doi.org/10.1115/1.2710493>
- Tilley, S.D., Cornuz, M., Sivula, K., Grätzel, M., 2010. Light-induced water splitting with hematite: Improved nanostructure and iridium oxide catalysis. *Angew. Chemie - Int. Ed.* 49, 6405–6408. <https://doi.org/10.1002/anie.201003110>
- Tran, P.D., Artero, V., Fontecave, M., 2010. Water electrolysis and photoelectrolysis on electrodes engineered using biological and bio-inspired molecular systems. *Energy Environ. Sci.* 3, 727. <https://doi.org/10.1039/b926749b>
- Youngblood, W.J., Lee, S.-H.A., Maeda, K., Mallouk, T.E., 2009. Visible light water splitting using dye-sensitized oxide semiconductors. *Acc. Chem. Res.* 42, 1966–1973. <https://doi.org/10.1021/ar9002398>
- Zhao, G., Kozuka, H., Lin, H., Yoko, T., 1999. Sol-gel preparation of Ti_{1-x}V_xO₂ solid solution film electrodes with conspicuous photoresponse in the visible region. *Thin Solid Films* 339, 123–128. [https://doi.org/10.1016/S0040-6090\(98\)01227-9](https://doi.org/10.1016/S0040-6090(98)01227-9)
- Zhong, D.K., Gamelin, D.R., 2010. Photoelectrochemical Water Oxidation by Cobalt Catalyst (“Co-Pi”)/ α -Fe₂O₃ Composite Photoanodes: Oxygen Evolution and Resolution of a Kinetic Bottleneck. *J. Am. Chem. Soc.* 132, 4202–4207. <https://doi.org/10.1021/ja908730h>
- Zoulias, E., Varkaraki, E., 2004. A review on water electrolysis, Centre for Renewable Energy Sources. Pikermi Greece , Nicosia Cyprus.

First lessons in climbing



Will knowledge safeguard freedom, by Uzo Egonu

Contents

Chapter 2	Modelling of Photo-electrochemical Cells	37
2.1	Photocurrent generation	39
2.2	Incident photon flux density q_0 and average density of absorbed radiant power $\langle A \rangle$	39
2.3	Electrochemical measurements	40
2.3.1	Polarization (jV curves) and basic diode model	40
2.3.2	Electrochemical Impedance Spectroscopy (EIS)	43
2.4	Analogical model	47
2.4.1	DS-PECs equivalent circuit	48
2.4.2	SC-PEC equivalent circuit	62
2.5	First elements toward a knowledge model	67
2.5.1	Radiative transfer in a photoanode (or photocathode)	68
2.5.2	Coupling radiative transfer and thermokinetic of charge generation and transport in photo-anodes	73
2.5.3	Stoichiometric and kinetic coupling at the cathode electrode	82
2.5.4	A summary on a possible comprehensive formulation, of nonlinear coupling with the radiation field	83
2.5.5	Thermodynamic efficiency of PEC	84
2.5.6	Conclusions about knowledge model developments	93

Chapter 2

Modelling of Photo-electrochemical Cells

Introduction

This chapter is focused on Photoelectrochemical cells (PEC) modelling through two approaches. First is the electrical approach (analogical model) which considers all phenomena in a PEC analogous to electrical elements. This approach, currently used in electrochemistry, is also known as equivalent circuit modelling and leads to practical information on PEC functioning. The other approach based on the development of knowledge model of the process with a refined radiative transfer analysis within the multilayer photoanode. This approach provides sufficient knowledge to determine the volumetric production rate of hydrogen as well as defining the thermodynamic efficiency of PEC which are key factors involved in PEC conception and optimization. In this chapter, we explain the basis of each approach but also we divide Photoelectrochemical cells (PEC) in this study in two different categories.

- (i) The first is PECs based on titanium dioxide. They use “molecular photo-catalysts” to absorb the radiation and “titanium dioxide nano-particles” to create specific surface area with a proper conduction band potential (same concept as Grätzel cells). They are

known as Dye Sensitized PEC. Here we name them this category, DS-PEC and it stands for Dye Sensitized PEC.

- (ii) The second is PECs based on semiconductor materials with reduced band gap (such as hematite) so they are photosensible and use noble metals (such as iridium oxide) to catalyse the process. Here we call them SC-PEC and it stands for semi-conductor based PECs.

In the following general subjects which are preliminary to PEC knowledge (both categories) are discussed in order to give basics information and the discussion in this chapter

2.1 Photocurrent generation

The main objective of this chapter is to understand the PEC functioning by mean of Electrochemical Impedance Spectroscopy (EIS) and the current-voltage (jV) curve results which will be used to formulate the cell efficiency. Electron-hole pairs resulted by light excitation in photoactive site of the cell (chromophore, hematite $\alpha\text{-Fe}_2\text{O}_3$) generate electric potential difference. This potential difference makes electrons travelling within the semiconductor's bulk which means an electrical current density generation $\langle j \rangle$, named photocurrent. As long as we have an electric potential difference (V) and an electrical current density $\langle j \rangle$, we can establish areal electrical power of the system P_E . So we can formulate the power conversion efficiency of a PEC as following:

$$\eta = \frac{P_E}{q_0} \quad (2.1)$$

Where $P_E = jV$ ($\text{W}\cdot\text{m}^{-2}$) and q_0 ($\text{W}\cdot\text{m}^{-2}$) is the incident photon flux density at PEC inlet. The Equation 2.1 explains that the efficiency of PEC can be investigated by analysis of jV curve and determination of the q_0 .

2.2 Incident photon flux density q_0 and average density of absorbed radiant power $\langle A \rangle$

The incident photon flux density q_0 is an important input parameter of PEC. It represents the number of photons emitted per unit of surface per second from the light source which arrive to the PEC entry and it can be measured directly by a flat detector. But the importance of q_0 is its relation with average density of absorbed radiant power $\langle A \rangle$. Since the local density of absorbed radiant power $\hat{\mathcal{A}}_\lambda$ is a crucial parameter to define the average volumetric production rate $\langle r_{\text{H}_2} \rangle$ if H_2 is produced. Establishing the relationship between $\hat{\mathcal{A}}_\lambda$ and $\langle r_{\text{H}_2} \rangle$ and how with simplification to the system geometry we can estimate the $\langle r_{\text{H}_2} \rangle$ from $\langle A \rangle$ will be largely explained in detail during development of knowledge model in this chapter but it should be kept in mind that $\langle A \rangle$ in a plane thin media can be obtained directly by measuring q_{in} and q_{out} . This part and how it is possible to consider this simplification will be also explained further in this chapter. But the interest of introducing q_0 and $\hat{\mathcal{A}}_\lambda$ in this part is that it has a direct impact on developing photocurrent relation since q_0 is the source of photocurrent generation and $\hat{\mathcal{A}}_\lambda$ explains how locally the radiant power is absorbed by photoactive site of

photoelectrode. Furthermore q_0 defines the power conversion efficiency while impacting simultaneously the current density as the only input of the system.

As we mentioned earlier efficiency analysis requires determining different aspects of jV curve. Photocurrent is major element of jV curve resulting from electron-holes separation and it is quantified by short circuit current j_{sc} in jV curve of a PEC but there is also some limitation about photocurrent generation such as absorption properties of photoactive materials which can be semiconductor (α - Fe_2O_3), chromophore or dye molecule. Each of these materials are specifically characterised and distinguished by their optical properties. In other word optical properties of absorber material determine \mathcal{A}_λ which gives along with other parameters a complete comprehension of photocurrent generation efficiency and also conversion efficiency of PEC. Here we continue firstly to interpret jV curves by impedance measurements and integrating an electrical model also named analogical model, which explains physical and electrochemical phenomena by establishing equivalence between a phenomenon and an electrical device.

2.3 Electrochemical measurements

Electrochemical measurements refers to a series of different measurement modes for a device in order to study different parameters of the system which can be determined during a measurement while it can be also obtained indirectly from other experiments. In the following we present typical electrochemical measurements used during this thesis experimental work.

2.3.1 Polarization (jV curves) and basic diode model

The jV curve of an electrical device typically represents the current flow evolution due to a corresponding potential difference. The jV graphs are mostly used to define and understand the systems components and parameters. For example, for an ohmic device the jV curve is linear but for other types of electrical devices the jV characteristic graph is not a linear. Semiconductor based devices such as diodes and transistors which are fabricated by using semiconductor p-n junctions show a non linear jV characterisation. Figure 2.1 shows a typical solar cell jV characteristics curve. The maximum current in a jV curve is where the voltage of the device at this point is zero, the system is at short circuit (SC) point and the current at this point is the short circuit current (j_{sc}) which is limited by the cell resistances. By increasing the

voltage the current decreases until it reaches to zero point. At this point the system is at open circuit (OC) operating state and the voltage at this point is open circuit voltage (V_{OC}) which is dependent of photon flux density (Fabregat-Santiago et al., 2007; Halme et al., 2010).

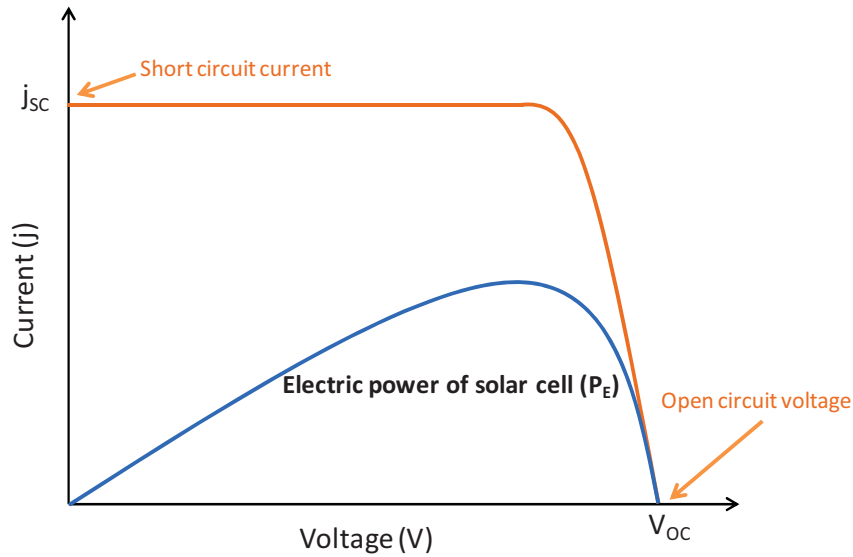


Figure 2.1 jV characteristic curve for a solar cell.

A photoelectrochemical cell jV curve can almost be represented by a photodiode model curve as well. If we consider a photodiode current voltage equation for a photoelectrochemical cell, as the Equation 2.2 formulates it;

$$i_{cell} = i_{ph} - i_0 \left(e^{\frac{-qe(V_{cell} + i_{cell}R_s)}{mk_B T}} - 1 \right) + \frac{V_{cell} + i_{cell}R_s}{R_{sh}} \tag{2.2}$$

Then the Figure 2.2 illustrates an electrical circuit which corresponds to the parameters forming the Equation 2.2.

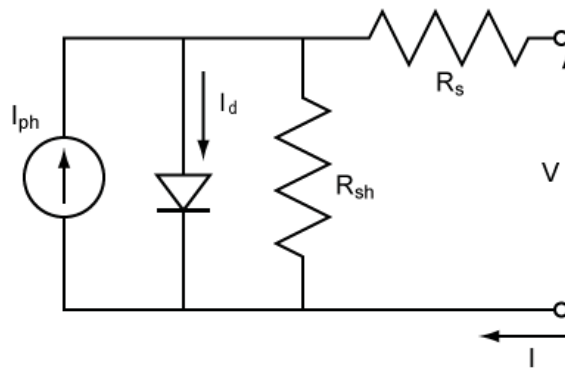


Figure 2.2 Diode equivalent circuit electrical model of solar cell (Koide et al., 2006)

A photocurrent (I_{ph} or in current density form j_{ph}) is produced when a photon with sufficient energy is absorbed in the p-n junction's depletion region of photodiode and generates electron-hole pair. Then these electron-holes pairs are carried away from the junction by the built-in electric field of the depletion region. This means the holes are swept to the anode while electrons move toward the cathode and this produces photocurrent. There is also the dark current (I_d) current that is generated in the absence of light resulting from photoconductive mode of diode (Tavernier, Steyaert, 2011). The total current through the photodiode is the sum of the dark current and the photocurrent. So it is favourable to minimize the dark current in order to maximize the sum of the current passing through the diode.

Figure 2.2 shows two resistance components, the series R_S and shunt resistance R_{sh} . The series resistance is in series with the photocurrent source, while the shunt resistance is considered in parallel with the photocurrent source. The shunt resistance of an ideal photodiode is infinite. In reality the value of shunt resistance is between 100 k Ω and 1 G Ω depending on the quality of the photodiode. This resistance is used to calculate the current leak or (noises) in photovoltaic mode means without any polarization of photodiode. The shunt resistance is defined to be the inverse slope of the jV curve at the 0 V point. To make the curve consistent with the theoretical model, the light input must be constant. The practice of industry is to measure the current I at $V = 10$ mV, and apply Ohm's law to find the shunt resistance (Tavernier and Steyaert, 2011).

Another important key factor of photocells is about the form of jV curve because it gives information about the operating point and at which voltage it is possible to extract electrons in form of electrical current. It is easier to extract the current at low voltage (near the short circuit point), from the cell, but putting overpotential on the cell (moving toward OC point) generates current within the cell which limits the photocurrent and brings a voltage loss to the system and consequently it diminishes the power of the cell. Hence the electrical power of PEC at its maximum power point is given as:

$$P_E = j_{SC} \times V_{OC} \times FF \quad (2.3)$$

Higher value of fill factor FF ¹ leads to higher value of power. For example for a diode increasing the shunt resistance, R_{sh} , and decreasing the series resistance, R_S , bring to a higher fill factor, resulting in greater efficiency, and bringing the cell's power closer to its theoretical maximum.

¹ Typical fill factors range from 50% to 82%. The fill factor for a normal silicon PV cell is 80%.

2.3.2 Electrochemical Impedance Spectroscopy (EIS)

The resistance in its well-known definition is the ability of circuit elements to resist the electrical current flow through Ohm's law.

$$R \equiv \frac{U}{j} \quad (2.4)$$

However the Ohm's law works only for ideal resistors and circuit elements. The non-ideal elements require a more complex definition of resistance which is impedance (Z). Impedance extends the notion of resistance to AC circuits, and includes both magnitude and phase, contrary to resistance, which includes only magnitude. In a circuit is driven with direct current (DC), there is no distinction between impedance and resistance. So the resistance can be thought of as the impedance with zero phase angles. Impedance is a complex number, with the SI unit ohm (Ω) same as resistance. It is usually symbolized by Z . In order to apply the concept to our system here we consider the electrochemical impedance and its measurement (Barsoukov, Macdonald, 2005). In Electrochemical Impedance Spectroscopy (EIS), an AC potential (E_t) at the time t with small amplitude (E_0) is applied to the electrochemical device as Equation 2.5:

$$E_t = E_0 \sin(\omega t) \quad (2.5)$$

Where ω , is the angular frequency expressed in radian per second, in Equation 2.6:

$$\omega = 2\pi f \quad (2.6)$$

And f is the temporal frequency with SI unit of Hertz.

In a linear system the response of E_t is j_t with a shifted phase of ϕ and the amplitude of j_0 :

$$j_t = j_0 \sin(\omega t + \phi) \quad (2.7)$$

Therefore the impedance can be formulated as below:

$$Z = \frac{E_t}{j_t} = \frac{E_0 \sin(\omega t)}{j_0 \sin(\omega t + \phi)} = Z_0 \frac{\sin(\omega t)}{\sin(\omega t + \phi)} \quad (2.8)$$

Where, the Z_0 is the magnitude of impedance. It is also possible to represent the impedance as a complex number from Euler relationship:

$$Z(\omega) = Z_0 (\cos\phi + i\sin\phi) \quad (2.9)$$

This last formulation of impedance includes a real $Z_0 \cos\phi$ and an imaginary part $Z_0 \sin\phi$.

There are several ways to present an impedance diagram. In a Nyquist diagram (Figure 2.3) the real part is presented on X axis and the opposite of the imaginary part is plotted on Y axis.

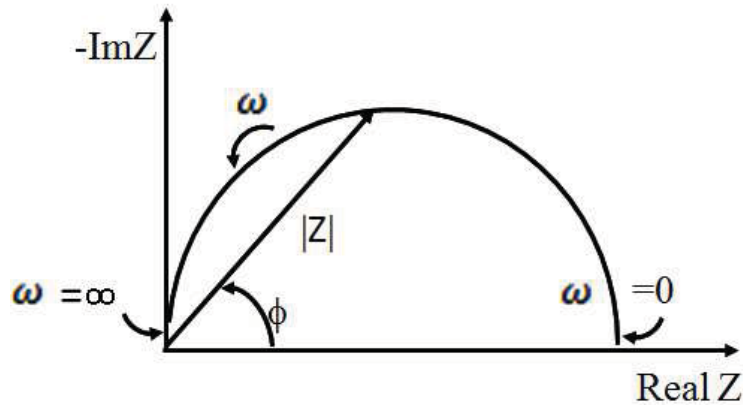


Figure 2.3 Nyquist diagram with impedance vector illustration.

On the Nyquist plot, impedance is represented by a vector with $|Z|$ magnitude which makes an angle ϕ with X axis, while ϕ is the phase angle. Each point on Nyquist diagram corresponds to impedance at a specific frequency; but the defect of the diagram is that it does not give directly any information about the frequency at which this point of impedance has been measured (Loveday, Peterson & Rodgers, 2004).

Other regular method of impedance plot illustration is Bode diagram (Figure 2.4 and Figure 2.5) in which the logarithm of frequency is plotted on abscissas axis and magnitude of the impedance $|Z|$ and phase shift on ordinate axis. In this work, we present all impedance diagrams on Nyquist plot. In Figure 2.5, the impedance data are the red points. Their projection onto the $Z'' - Z'$ plane is called the Nyquist plot while the projection onto the $Z'' - \nu$ plane is called the Cole Cole diagram and $Z' - \nu$ represents Bode plot.

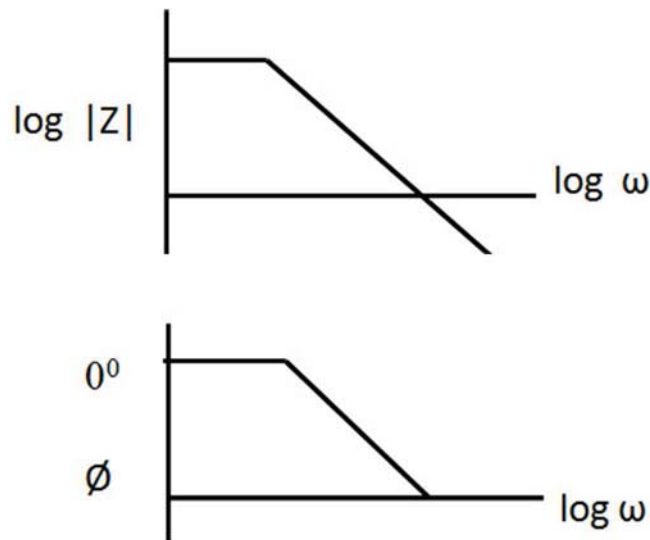


Figure 2.4 Bode diagram; another method of representing impedance during the same measurement.

Linearity or non-linearity of systems is an important factor in impedance analysis because linearity simplifies the EIS analysis of the system. By mathematical definition a system in which $y_1(t)$ is the output of $x_1(t)$ and $y_2(t)$ is the answer of input $x_2(t)$ is a linear system if it comes along a linear relation;

$$x_1(t) + x_2(t) \xrightarrow{\text{output}} y_1(t) + y_2(t) \tag{2.10}$$

$$x_1(t) \times x_2(t) \xrightarrow{\text{output}} y_1(t) \times y_2(t) \tag{2.11}$$

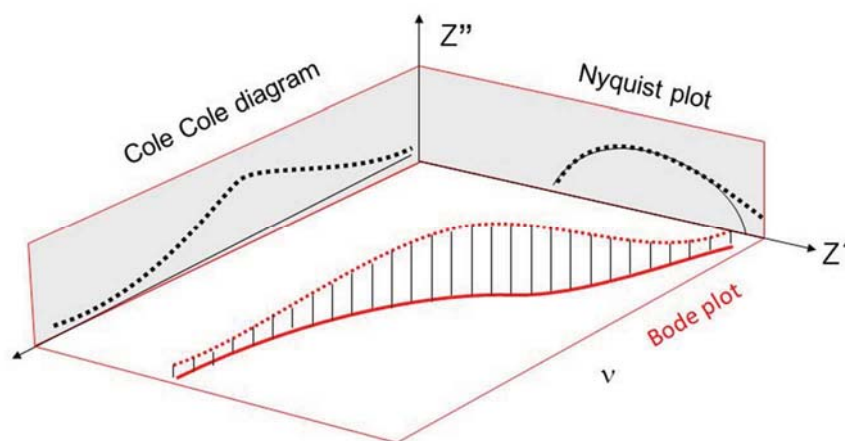


Figure 2.5 The impedance data are the red points. Their projection onto the $Z'' - Z'$ plane is called the Nyquist plot. The projection onto the $Z'' - \nu$ plane is called the Cole Cole diagram (Barsoukov and Macdonald, 2005).

In an electrochemical system controlled by a potentiostat, the input is the potential and the output is the current. Most of electrochemical device as electrochemical cells are not a linear system which means doubling the potential is not automatically going to double the current. This fact can be seen in a cell's current voltage curve.

The EIS under some specific condition of linearity can use existing analogies between phenomena taking place in an electrochemical device and an equivalent circuit composed of resistors and capacitors. This electrical circuit represents the electrochemical cell performance as an impedance response to a sinusoidal excitation in current flow (Bard and Faulkner, 2001) (Figure 2.6).

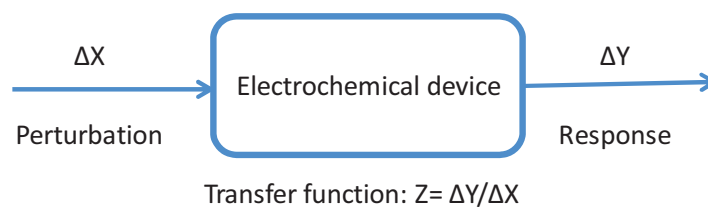


Figure 2.6 General diagram of impedance principle in electrochemical system.

Analytically this method consists in applying a sinusoidal voltage E with pulse of $2\pi f$ on electrochemical cell and measuring the current response j (Figure 2.7)

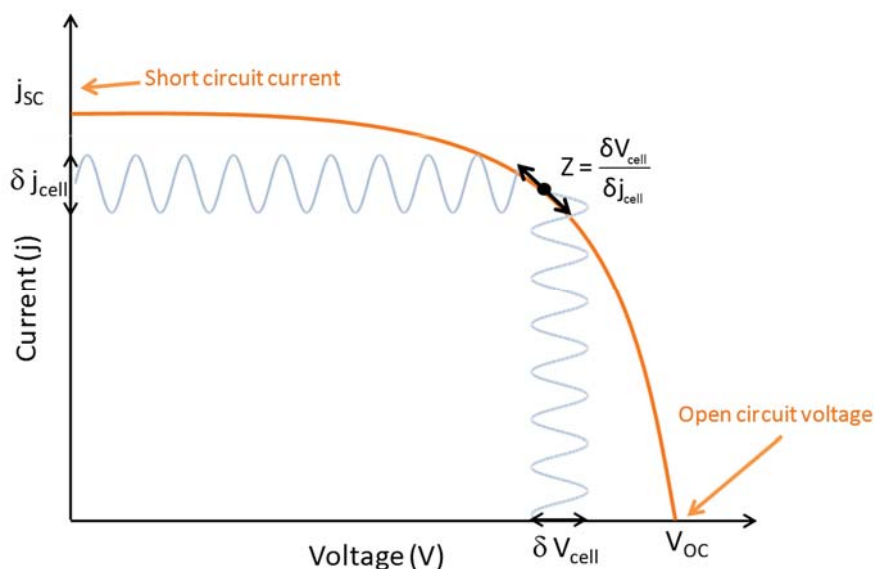


Figure 2.7 jV curve with sinusoidal signal perturbation in potential and the current response.

Consequently the impedance can be obtained from the slope of jV curve at the operation point. As the amplitude of applied voltage impedance can be considered the resistance of jV curve while it is a frequency function as well.

2.4 Analogical model

In the context of this work an analogical model represents an electrical model based on elements which can be linked to steady state empirical parameters measured during an electrochemical experience. We use a complete set of experimental measurements such as Electrochemical Impedance Spectroscopy (EIS), optical measurements such as transmission and optical properties measurements as well as jV curve characterization which permits to develop our equivalent circuit impedance model and verify it by fitting to experimental data.

As we discussed it above each component in equivalent circuit represents a phenomenon occurring in the system. Different cell components and their interfaces show resistance to charge transport across the cell. All these resistive phenomena are therefore illustrated by resistors in the circuit. The impedance of a resistor is independent of frequency so it shows no imaginary part. In the other hand accumulation of charge at cell components interfaces reveals capacitive currents, and is indicated by capacitors. Generally capacitor impedance reduces by increasing the frequency. As a result, capacitor impedance has only the imaginary part. Other type of component which may be mentioned in this work is Warburg element. Warburg element in a circuit is modelling semi-infinite linear diffusion.

Depending on the phenomena representing by impedance diagram, the circuit components and combinations can become more complex.

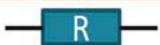
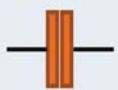
Component	Schematic	Defining relation	Impedance
Resistor		$E = I \times R$	$Z = R$
Capacitor		$I = C \frac{dV}{dt}$	$Z = \frac{1}{j\omega C}$
Warburg			$Z = \sigma(\omega)^{-1/2}(1 - j)$

Table 2.1 Equivalent Circuit components. The main elements are resistors and capacitors. Depending on the system and the phenomena we are experiencing (diffusion, etc.) other elements such as Warburg, inductor, etc. can be added.

If we consider a simple Nyquist impedance diagram as in Figure 2.3, the circuit equivalent to this diagram is composed of a resistor in parallel with a capacitor (Figure 2.8).

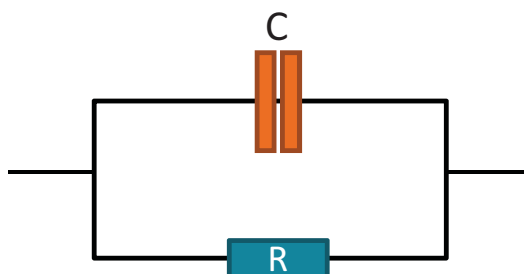


Figure 2.8 Equivalent circuit of Figure 2.3 impedance diagram.

Indeed, the parallel combination of a capacitor and a resistor constructs respectively the imaginary and real part of Nyquist diagram of Figure 2.3. Since we have: $|Z| = \frac{1}{\sqrt{(\frac{1}{R})^2 + (\omega C)^2}}$

Since the equivalent circuit for each case study in this work will be different, here we state to study each case separately and explain each contributing phenomena.

2.4.1 DS-PECs equivalent circuit

If we consider a typical EIS measurement of PEC as it is shown in Figure 2.9, we note that different impedance arcs present in the figure are generated by different component of the system. It means that each impedance arc presents the real and imaginary part of impedance of a cell component and appears at its characteristic frequency which depends on the operating point (j, V) on the jV curve. In typical Nyquist impedance diagram of a cell with a cathode, an anode and an electrolyte three major impedance arcs appear. First corresponds to the counter electrode resistance (R_{CE}), demonstrated in high frequency range (kHz), second is about TiO_2 resistance and photoanode electrolyte interface capacitance which comes into view in the range of 1Hz – 10Hz and finally the mass transport impedance at counter electrode which appears lately at low frequency region (0.01 – 1 Hz) (Koide et al., 2006).

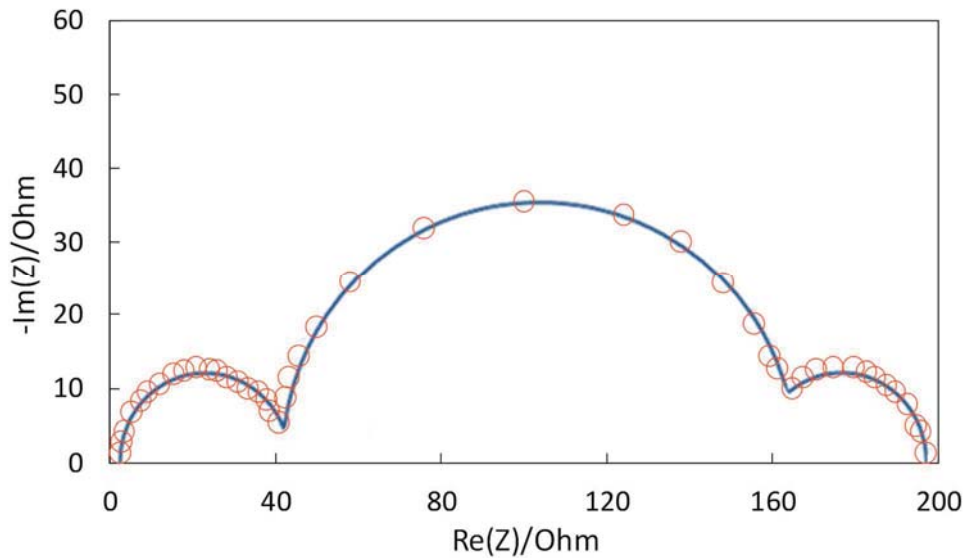


Figure 2.9 DSSC impedance diagram showing the relation between impedance arc and jV operating point.

The Figure 2.9 diagram can change by virtue of changes in value of resistors and capacitors attributed to phenomena within the cell. In other words, conform to phenomena occurring in the cell and their contribution in cell operation the Nyquist diagram of impedance can take a different shape.

Under dark condition and upon a forward bias, electrons are injected in the conduction band of TiO_2 from the FTO substrate and therefore the film will be charged by electrons where a part of these charges will be dissipated by reducing the present ions in the electrolyte such as I_3^- in the DSSC case (Wang et al., 2005).

Considering several works on Photoelectrochemical devices during two decades, principal phenomena can be summarized to:

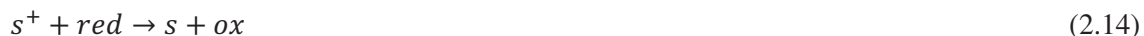
- Light harvesting (LH): light absorption by photosensitizer or chromophore (s), followed by electron excitation from low energy state (valence band) to a higher energy state (conduction band) which results to an excited electronic state.



- Injection (INJ): the injection of excited electron from conduction band in photosensitizer molecule to the TiO_2 molecule conduction band.



- Regeneration (RG): The oxidized photosensitizer (s^+) reduction by electrolyte redox couple.



- Collection (COL): the diffusion of electrons through the semiconductor nanoporous medium and arriving to the external circuit point.
- Electrolyte mass transport (EMT): the diffusion of electrolyte species between photoelectrode, electrolyte interface and counter electrode.



- Electrolyte regeneration (ERG): the oxidant species regeneration at counter electrode and their reduction to reducing agents which cross the electrolyte for photosensitizer regeneration at photoanode.



The equation (2.15) is the overall charge transfer reaction in the cell and by ionic transport of redox couple across the electrolyte, the electrical circuit of the cell will be closed.

Additionally, several phenomena can result in a decrease of efficiency of PEC, specially:

- Excited state degeneration (ED): the degeneration of excited state of photosensitizer molecule influences the injection step, these two phenomena are in competition.
- Electron-photosensitizer-recombination (EDR): The emitted electron can be recombined with oxidized photosensitizer and this is limiting for photosensitizer regeneration and electron collection from the bulk of TiO_2 .
- Electron-Electrolyte recombination (EER): Another possibility is the electron recombination with electron accepting agents in the electrolyte. This also influences the electron collection (Barnes et al., 2011) (Halme et al., 2010).

A PEC performance is strongly dependent on the yield of the driving processes (LH to ERG) and inhibitor phenomena (ED to EER). Although we present all mechanism independently, the complication of understanding a molecular device is that experimentally, some mechanisms are not completely isolated from the others such as photosensitizer regeneration.

These processes in PEC are illustrated in Figure 2.10. Hence for a DS-PEC producing electrical power (DSSC) or hydrogen the following equivalent circuit can be considered:

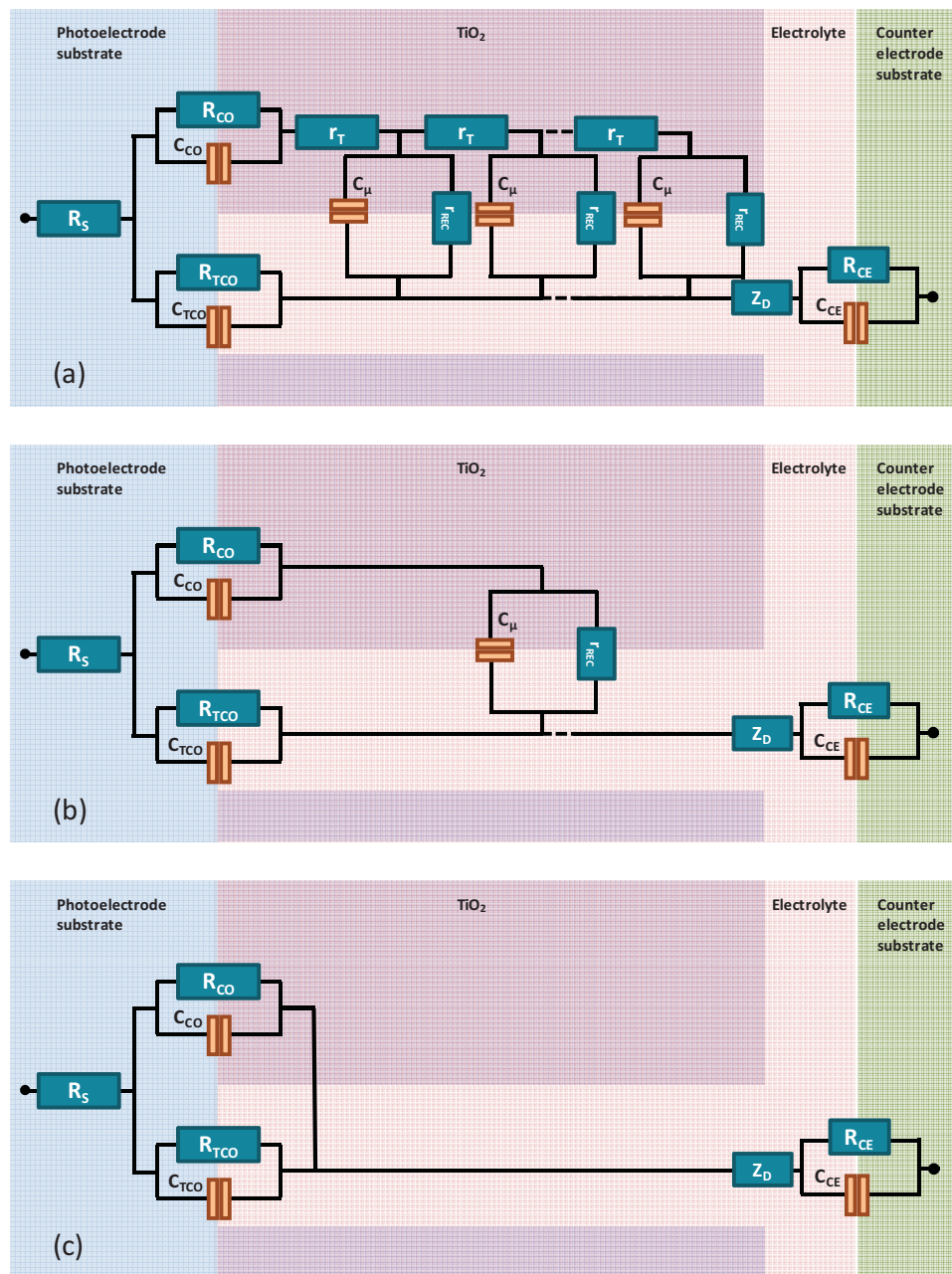


Figure 2.10 (a) General equivalent circuit model of PEC. (b) Simplified equivalent circuit model for high illumination intensities or high applied bias. (c) Simplified circuit for TiO₂ becoming conductive.

In these equivalent circuits of PEC we can see three main areas, distinguished by different colours. The photoelectrode substrate zone, the TiO₂ film, the electrolyte and counter electrode substrate parts. This model has been firstly developed by (Bisquert, 2002) and (Francisco Fabregat-Santiago, Bisquert, Garcia-Belmonte, Boschloo, Hagfeldt, 2005) for DSSC and it has been completed later by (Hoshikawa, Yamada, Kikuchi, Eguchi, 2005). The circuit components' description is as follow (Note that resistances and capacitance's units are $\Omega \cdot m^2$ and $F \cdot m^2$ respectively):

- All cell component ohmic resistances (substrate, electrolyte and electrical contacts) are introduced as R_S in electrical model.
- Contact resistance (R_{CO}) and capacitance (C_{CO}) have to be considered at the interface of photoanode TiO_2 film and conducting substrate (FTO).
- Photoelectrode resistance to electron transport within the TiO_2 film in particular (r_T). The total transport resistance of a film with thickness of d is: $R_T = r_T d$.
- Charge transfer resistance about electron recombination with electrolyte species at the interface of FTO, TiO_2 and electrolyte can be schematized as resistance at the photoelectrode-electrolyte interface (r_{rec}). The total recombination resistance of the film is: $R_{rec} = r_{rec}^{d-1}$.
- The chemical capacitance of photoanode film resulted from change of electron density as function of Fermi level per unit volume (c_μ), which comes to $C_\mu = c_\mu d$ for total film.
- R_{TCO} and C_{TCO} respectively represent charge transfer resistance and double layer capacitance at photoelectrode-electrolyte interface. Moreover R_{CE} and C_{CE} correspond likewise to charge transfer resistance and double layer capacitance at counter electrode-electrolyte interface.
- The circuit is closed by considering redox species diffusion impedance in the electrolyte (Z_D) which includes also the diffusion resistance of redox species R_D through the electrolyte.

As it is shown in the model (Figure 2.10) the impedance element of electrolyte species diffusion (Z_D) is the interconnector between photoanode and cathode parts. However in some literature (Halme et al., 2010) this impedance is considered as a limiting step for counter electrode functioning, so it comes into the counter electrode bloc in series with R_{CE} and in parallel with C_{CE} but according to (Kern et al., 2002) and (Fabregat-Santiago et al., 2002) it should be considered separately and in some cases for having a better fit it should be considered as a Constant Phase Element (CPE) which will be defined as Warburg or Q depending on the diffusive behaviour of electrolyte species.

The capacitive behaviour of the PEC which is measured by impedance spectroscopy is the equivalent of different capacitances. It is literally composed of chemical capacitance (C_μ) which is the result of electronic states, the space charge capacitance (C_{SC}) related to the space charge region of semiconductor, Helmholtz capacitance (C_H) resulted from capacitive behaviour in

double layer at the interface of TiO_2 and electrolyte and the ionic adsorption on the surface (C_{ad}) of electrode at the electrolyte side. Since C_{μ} and C_{SC} are related to the same region so they are in parallel together and in series with C_{H} and C_{ad} which are in parallel too, $C_{\mu} \parallel C_{\text{SC}} - C_{\text{H}} \parallel C_{\text{ad}}$. However the value of C_{SC} is negligible because the absence of space charge region in TiO_2 nanocrystalline structure (Wang et al., 2006). In the other hand the double layer capacitance ($C_{\text{H}} \parallel C_{\text{ad}}$) constitute a poor part of the total capacitance which is majorly conducted by C_{μ} under illumination or at higher bias potentials in the dark condition. The capacitance of FTO-electrolyte interface C_{TCO} contributes also to the photoanode capacitive behaviour and it is therefore placed in the same bloc as R_{TCO} which is the resistance of electron recombination between FTO and electrolyte. Another capacitance appearing in photoanode capacitance is FTO – TiO_2 contact C_{CO} which is associated to the R_{CO} resistance in this model (Halme et al., 2010). In other studies $R_{\text{CO}}, R_{\text{TCO}}, C_{\text{CO}}$ and C_{TCO} are all considered under $R_{\text{TCO}} \parallel C_{\text{TCO}}$ bloc, representing the resistance and the capacitance of FTO, TiO_2 in contact with electrolyte. Note that R_{S} is the sum of ohmic resistance corresponding to the plate of FTO and all contact resistances in the cell. On the other side, the capacitance of double layer (C_{CE}) and the charge transfer resistance (R_{CE}) at counter electrode should be also taken into account for while the impedance spectroscopy gives us the information about counter electrode at high frequency range (Wang et al., 2006).

a. Photoanode

- Capacitances

Chemical capacitance and electron trapping:

In order to have a complete understanding of EIS measurements we need to understand the chemical capacitance notion presented earlier. For this purpose, it is necessary to discriminate between bulk traps and surface states. Hence it has been considered three different zones of surface and trapping states. First are the conduction band states which permit to fast electrons transport and are defined by the energy (E_{C}) and effective density of conduction band (N_{C}). The electron density of electron in conduction band takes the form below as an exponential function of Fermi level energy (E_{F}):

$$n_{\text{c}} = N_{\text{c}} e^{[(E_{\text{F}} - E_{\text{C}})/k_{\text{B}}T]} \quad 2.17)$$

Second electronic states to consider are the bulk traps which are the states situated in band gap. Electrons trapped in these states will be only exchanged with conduction band. The density of these states stands as an exponential distribution function of states energy and T_0 characteristic parameter:

$$g_b(E) = \frac{N_b}{k_B T_0} \exp[(E - E_c)/k_B T_0] \quad (2.18)$$

While N_b is the total density of bulk traps per unit of volume.

The surface traps are the other electronic states which are also located in the band gap and are to trap and release electrons to the either of conduction band and electrolyte species. Surface traps are physically situated on the surface of nanocrystalline. The exponential distribution function of surface sates is:

$$g_s(E) = \frac{N_s}{k_B T_1} \exp[(E - E_c)/k_B T_1] \quad (2.19)$$

Where N_s , is the total density of surface traps per unit of volume and T_1 is the characteristic parameter.

Accordingly an evolution in Fermi level results to a variation in the electron densities and so formation of electronic states which are detailed by chemical capacitance represented separately for each of states.

For conduction band:

$$c_\mu^{(cb)} = e^2 \frac{\partial n_c}{\partial E_F} = e^2 \frac{n_c}{k_B T} \quad (2.20)$$

For bulk traps:

$$c_\mu^{(bt)} = e^2 \frac{\partial}{\partial E_F} \int_{E_V}^{E_c} g_b(E) f_b(E, E_F) dE \approx e^2 g_b(E_F) \quad (2.21)$$

And for surface traps:

$$c_\mu^{(st)} = e^2 \frac{\partial}{\partial E_F} \int_{E_V}^{E_c} g_s(E) f_s(E, E_F) dE \approx e^2 g_s(E_F) \quad (2.22)$$

Therefore we can introduce all trap capacitance as:

$$c_\mu^{(trap)} = c_\mu^{bt} + c_\mu^{st} = e^2 \frac{\partial n_L}{\partial E_F} \quad (2.23)$$

$$c_\mu^{(trap)} = e^2 \frac{N_L}{k_B T} \exp[(E_F - E_c)/k_B T_0] \quad (2.24)$$

$N_L = N_b + N_s$, is the total density of localized states. All capacitances of Equations 2.20 to 2.24 are exponentially dependent on Fermi level (Bisquert et al., 2004) (Bisquert, 2003).

We obtain therefore the chemical capacitance of PEC the sum of these three capacitances:

$$c_\mu = c_\mu^{cb} + c_\mu^{bt} + c_\mu^{st} = e^2 \frac{\partial(n_c+n_b+n_s)}{\partial\mu_n} \quad (2.25)$$

$$C_\mu = v_{eff}c_\mu = v_{eff}q^2 \frac{\partial n}{\partial E_{Fn}} \quad (2.26)$$

Where v_{eff} , is the effective volume of the film given by:

$$v_{eff} = dA(1 - p) \quad (2.27)$$

and A is the cell surface area and d is the film thickness and p is the porosity (Fabregat-Santiago et al., 2011).

Depletion capacitance (C_{SC}):

Beside the chemical capacitance there is a dielectric type of capacitance related to Schottky barrier in a cell at the interface of semiconductor and the electrolyte. The Schottky barrier is the origin of depletion layer also named space charge region in the semiconductor which shows a capacitive behaviour at its interface with the electrolyte. This phenomenon is characterised as depletion capacitance or also space charge capacitance (C_{SC}). Since, the C_{SC} is proportional to the depletion region thickness, in the presence of a reverse bias it becomes negligible because the space charge region is wider. In the other hand the capacitance will be no more negligible while a forward bias is applied and the depletion layer is reduced. The C_{SC} can be formulated from the depletion layer thickness which is a function of the voltage along the layer. By presenting the thickness as:

$$w = w_0 V_{DL}^{1/2} \quad (2.28)$$

and knowing that $w_0 = \sqrt{\left(\frac{2\varepsilon_r\varepsilon_0}{qN}\right)}$ where ε_0 and ε_r are the permittivity of free space and the material respectively and N is the total doping concentration of n and p regions in the material; so the C_{SC} can be presented as following:

$$C_{SC} = \frac{A\varepsilon_r\varepsilon_0}{w} \quad (2.29)$$

And to have a linear relation we can also write:

$$C_{SC}^{-2} = \frac{2}{A^2 q \epsilon_r \epsilon_0 N} (V_{bi} - V_{app}) \quad (2.30)$$

Note that the $V_{DL} = V_{app} - V_{bi}$ where V_{app} is the applied potential and V_{bi} is the potential built in between the materials in contact (semiconductor and electrolyte). The Equation 2.30 is also known as Mott-Schottky relation.

If we go back to the total capacitance of the cell measured by EIS, it can be concluded that at reverse bias applied to the cell the space charge capacitance C_{SC} is dominating the cell capacitance while at forward bias this role is majorly played by chemical capacitance C_{μ} as it becomes very large and represents almost the total the cell capacitance (Fabregat-Santiago et al., 2011).

Helmholtz capacitance (C_H):

About the Helmholtz capacitance C_H which is related to the thickness of double layer, the capacitance remains nearly constant until certain applied potential value. However applying higher potential to the film causes some displacement and shift to the edge of conduction band and consequently a large number of charge carriers leave this layer. It brings then more contribution of C_H to dielectric origin capacitance of cell. It should be considered that for the thicker films $C_H > C_{SC}$ because, regarding to the Equation 2.29 the C_{SC} become negligible (Wang et al., 2006) (Fabregat-Santiago et al., 2011).

- **Resistances**

The total resistance of the PEC at the steady state condition can be written as:

$$R_{CELL} = R_S + R_{PE} + R_D + R_{CE} \quad (2.31)$$

While the R_{PE} is the overall resistance of the photoelectrode and the substrate and it is formulated as:

$$R_{PE} = \frac{R_{TCO}(R_{CO} + R_{TiO_2})}{R_{TCO} + R_{CO} + R_{TiO_2}} \quad (2.32)$$

In the equation above R_{TiO_2} is the total resistance of the photoelectrode film inclusive of charge transport resistance in electrode film and charge transfer recombination resistance at the interface of photoanode-electrolyte. The jV curve can be subsequently explicated as a relation of differential cell resistance (R_{CELL}):

$$V_{CELL}(j_{CELL}) = V_{OC} + \int_0^{j_{CELL}} R_{CELL}(j) dj = V_0 + \int_0^{j_{CELL}} \sum_{k=S,PE,D,CE} R_k(j) dj \quad (2.33)$$

Where $R_{CELL} = \sum_{k=S,PE,D,CE} R_k$ and j is the current density (Halme et al., 2010).

Recombination resistance

If we consider the free electron density as explained by conversion equation below:

$$\frac{dn}{dt} = G - U_n + U_{n0} \quad (2.34)$$

Where G is the rate of carrier generation, while U_n is introducing the recombination rate and U_{n0} is a term that provides equilibrium at $G = 0$. If we consider that the recombination rate follows an empirical model given by:

$$U_n = k_{rec} n_c^\beta \quad (2.35)$$

As we take an expansion of Equation 2.34 according to (Fabregat-Santiago et al., 2011) from the main definition if we define the recombination resistance as a derivation of j_{rec} and V_F while $dE_{F_n} = qdV_F$; then we have:

$$R_{rec} = \frac{1}{qA} \left(\frac{\partial j_{rec}}{\partial E_{F_n}} \right)^{-1} = \frac{1}{A} \left(\frac{\partial j_{rec}}{\partial V_F} \right)^{-1} \quad (2.36)$$

From Equation 2.36 and regarding to the Equation 2.26 we reformulate the previous term as:

$$r_{rec} = \frac{1}{q^2} \left(\frac{\partial U_n}{\partial E_{F_n}} \right)^{-1} = \frac{1}{c_\mu^{cb}} \left(\frac{\partial U_n}{\partial n} \right)^{-1} = v_{eff} R_{rec} \quad (2.37)$$

Remembering the denotation of the electron lifetime we recognize the term $\left(\frac{\partial U_n}{\partial n} \right)^{-1} = \tau_0$ and the Equation 2.37 comes to:

$$r_{rec} c_\mu^{cb} = \tau_0 \quad (2.38)$$

This relation indicates the accuracy of putting recombination resistance and chemical capacitance in parallel in the same bloc as it has been presented in Figure 2.8.

According to (Fabregat-Santiago et al., 2011) as it is common to express the resistance as function of voltage, it is possible to present r_{rec} as follow:

$$r_{rec} = \frac{k_B T}{q\beta j_0} e^{-q\beta V_F / k_B T} \quad (2.39)$$

Charge transport resistance

The major resistance of the semiconductor film in photoanode is the charge transport resistance R_T . The charge transport resistance varies by the applied potential or light intensity.

To have an idea about parameters playing in transport resistance it has been formulated from the conductivity relation of semiconductor:

$$\sigma = e\mu n_{cb} \quad (2.40)$$

e is the elementary charge and n_{cb} is the electron density of conduction band as it has been already presented while μ is the mobility within the semiconductor which is related to the electron diffusion coefficient. Regarding to the Equation 2.17 and Equation 2.40 the charge transport resistance become:

$$R_T = R_0 \exp\left[-\frac{E_F - E_c}{k_B T}\right] \quad (2.41)$$

The Equation 2.41 is obtained under the condition we assume the mobility and the R_0 constant (Fabregat-Santiago et al., 2005). According to (Bisquert, 2008) we can also introduce the electron conductivity under the following form:

$$\sigma = \frac{q^2 n_c D_0}{k_B T} = D_0 c_\mu^{cb} \quad (2.42)$$

In which we recognize c_μ^{cb} and as a result R_T becomes:

$$R_T = \frac{d^2}{D_0 c_\mu^{cb}} \quad (2.43)$$

The latter relation confirms the presence of charge transport resistance R_T and c_μ^{cb} together with c_μ^{trap} and R_{rec} . Note that D_0 is the diffusion coefficient in the system with no trap. This will be discussed in detail during the section “c. Diffusion model relation to equivalent circuit”.

b. Counter Electrode (Cathode)

The two major phenomena participating at counter electrode are charge transfer resistance R_{CE} and the Helmholtz capacitance C_{CE} at the interface of counter electrode and the electrolyte. The mass transport resistance (R_D) related to the diffusion of ions in the electrolyte toward the counter electrode can be also considered as a limiting step for the counter electrode. The impedance arc appearing at high frequency is the result of R_{CE} and C_{CE} contribution while R_D appears in Z_D relation and emerges as an impedance arc at low frequency representing the charge diffusion within the electrolyte.

c. Diffusion model relation to equivalent circuit

Equations 2.38 and 2.43 frame that how the electron diffusion coefficient D , the electron life time τ and the diffusion length are related to the electron transport and recombination resistance (R_T and R_{rec}) through the chemical capacitance. However it should be considered that the presence of trap states makes a difference between measured kinetic parameters and trap free condition parameters, presented in Equations 2.42 and 2.43 (J Bisquert, 2004). If we assume the trapping parameter as:

$$\delta_L = \left(1 + \frac{\partial n_L}{\partial n_c}\right) \approx \frac{\partial n_L}{\partial n_c} = \frac{c_\mu^{trap}}{c_\mu^{cb}} \quad (2.44)$$

Then the measured diffusion coefficient change as:

$$D_n = \frac{D_0}{\delta_L} \quad (2.45)$$

and similarly the life time will be:

$$\tau_n = \delta_L \tau_0 \quad (2.46)$$

The D_n is known as chemical diffusion coefficient or also effective diffusion coefficient (Juan Bisquert, 2004), (Fabregat-Santiago et al., 2011), (Wang et al., 2006).

If we consider the semiconductor film with homogenous carrier charge distribution, the impedance relationship can be given as:

$$Z(\omega) = \left(\frac{R_T R_{rec}}{1 + \frac{i\omega}{\omega_{rec}}}\right)^{1/2} \coth \left[\left(\frac{\omega_k}{\omega_d}\right)^{1/2} \left(1 + \frac{i\omega}{\omega_k}\right)^{1/2} \right] \quad (2.47)$$

Where ω_k , is the constant recombination rate and ω is the angular frequency. Note:

$$\omega_k = \frac{1}{R_{rec} C_\mu} \quad (2.48)$$

and ω_d , is the characteristic frequency of diffusion in a finite layer:

$$\omega_d = \frac{D_n}{d^2} = \frac{1}{R_T C_\mu} \quad (2.49)$$

Note that the electron life time would be rewritten

$$\tau_n = \frac{1}{\omega_{rec}} = R_{rec} C_\mu \quad (2.50)$$

Consequently the electron diffusion length L is expressed as:

$$L = \sqrt{D_n \tau_n} = d \sqrt{\frac{R_{rec}}{R_T}} \quad (2.51)$$

Figure 2.11 illustrates theoretical Nyquist diagrams of impedance in the Equation 2.47.

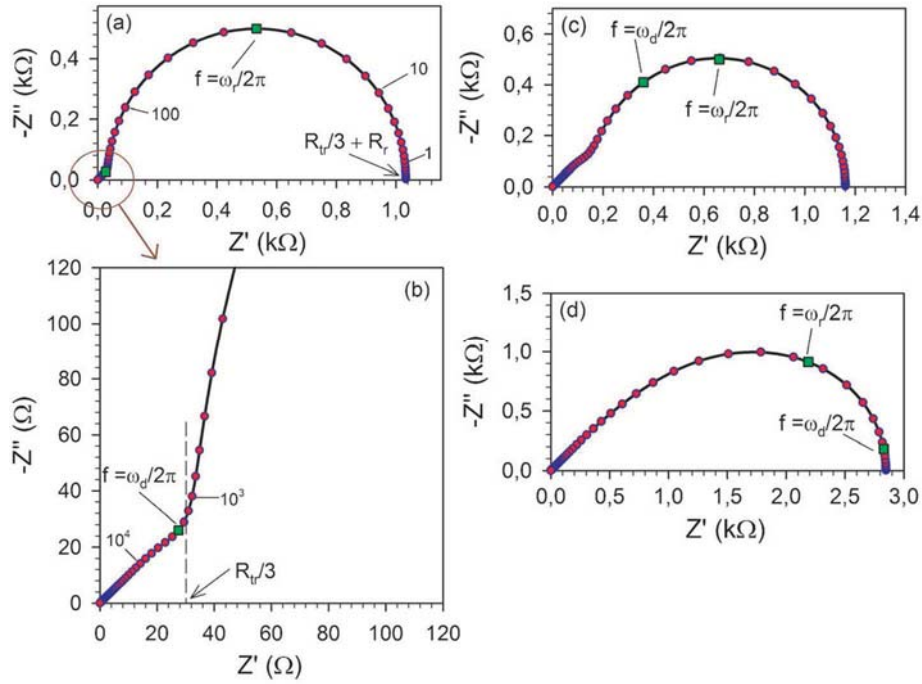


Figure 2.11 Different theoretical impedance spectra (Fabregat-Santiago et al., 2011).

When the recombination rate is low which means $R_T < R_{rec}$ or analogously $\omega_k < \omega_d$ the impedance relation in Equation 2.47 at low frequencies is summarized to:

$$Z = \frac{1}{3} R_T + \frac{R_{rec}}{1 + \frac{i\omega}{\omega_k}} \quad (2.52)$$

And for higher frequencies than ω_d to:

$$Z = R_T (i \frac{\omega}{\omega_k})^{1/2} \quad (2.53)$$

The previous relation is representing a Warburg impedance as a slope of 45° in high frequency zone of a complex impedance diagram (Figure 2.11(b)). The Warburg slop can be only observed at high frequency zone but with decreasing frequency an intermediate impedance arc appears due to the charge transfer resistance contribution with C_{tot} (Figure 2.11(a)).

According to Equation 2.52 the total resistance of the active layer of photoanode at low frequency ($R_T < R_{rec}$) is:

$$R_{al} = \frac{1}{3}R_T + R_{rec} \quad (2.54)$$

In the other hand in the opposite situation which means the recombination rate is large ($R_{rec} < R_T$) we reach the Gerisher impedance relation (Figure 2.11(d)):

$$Z = \left(\frac{R_T R_{rec}}{1 + \frac{i\omega}{\omega_{rec}}} \right)^{1/2} \quad (2.55)$$

In which R_{rec} and R_T , are not really recognizable and thereby we have:

$$R_{al} = (R_T R_{rec})^{1/2} \quad (2.56)$$

R_{al} is the active layer thickness resistance of the system without considering contacts, electrolyte and counter electrode resistances which are presented as series resistances in R_S (Fabregat-santiago et al., 2005), (Wang et al., 2005), (Wang et al., 2006).

For diffusion of ions in the electrolyte a Z_D element has been considered while the diffusion resistance of ions in the electrolyte is R_d . This effect is illustrated by following relation:

$$Z_D = R_d \frac{\tanh[(j\omega/\omega_d)^{1/2}]}{(j\omega)^{1/2}} \quad (2.57)$$

When the current flowing the cell is very small this element will be negligible (Fabregat-santiago et al., 2005; Fabregat-Santiago et al., 2011).

In the following we try to establish the R_{CELL} relationship which has been described generally in Equation 2.31, but this time by denoting more specifically each resistance after we introduced them in details earlier in this section. The total resistance R_{CELL} extracted from impedance in a real device has two major parts: first the part committed by R_{al} and the other part coming from all elements related to the active layer such as contacts, electrolyte and counter electrode (R_S, R_{CO}, R_{CE}, R_D) which are presented as series resistance R_S .

Regarding to R_{al} discussion here above for $R_{rec} \gg R_T$ we have:

$$R_{CELL} = R_S + R_{rec} + \frac{1}{3}R_T \quad (2.58)$$

While for $R_T \gg R_{rec}$ we obtain:

$$R_{CELL} = R_S + (R_{rec} R_T)^{1/2} \quad (2.59)$$

From the R_{CELL} we can write:

$$R_{CELL} = A \frac{dV}{dj} \quad (2.60)$$

And so on the current in the cell is obtained by:

$$j_{CELL} = j_{SC} - A \int_0^{V_{app}} \frac{dV}{R_{CELL}} \quad (2.61)$$

EIS is a major technique which provides a preliminary knowledge to discover the cause of the limitations to a PEC performance by determining the resistances in the system and revealing their evolution by varying different parameters such as frequency and applied potential. For example after photon injection by photoactive site of the cell the recombination resistance determines the open circuit voltage and maximum accessible efficiency. Moreover this value will be reduced by decreasing the fill factor (FF) by series resistances in the cell (Fabregat-Santiago et al., 2011; Wang et al., 2006).

2.4.2 SC-PEC equivalent circuit

Hematite $\alpha - \text{Fe}_2\text{O}_3$ became recently the centre of interest of PEC investigations for various reasons. First is that iron is a very abundant element in the earth and it can easily be oxidized to Fe^{+2} and Fe^{+3} while its oxide forms are available everywhere. Another important factor about iron oxides is their dyeing properties and because of their tinctorial characteristics they have photo sensibility features which make them interesting to PEC studies. Adding to all above their non-toxicity and chemical stability make iron based material and specifically hematite a very good option for photoelectrodes and particularly for photoelectrochemical water splitting (Sivula, Le Formal, Grätzel, 2011). Since this type of PECs and their functioning has been detailed in chapter 1, here we proceed directly to analogical modelling of Hematite ($\alpha - \text{Fe}_2\text{O}_3$) based PEC.

In case of hematite photoelectrodes ($\alpha - \text{Fe}_2\text{O}_3$) the model previously presented in Figure 2.10(a) will not completely cover the cell's behaviour since the photoanode material has been changed. As TiO_2 semiconductor is replaced by $\alpha - \text{Fe}_2\text{O}_3$ semiconductor, this change brings modifications to the electrical equivalent circuit for interpretation of EIS of the hematite based PEC. Referring to a classical sketch of semiconductor bulk-electrolyte interface presented by (Lopes et al., 2014), the Figure 2.12 illustrates the state of hematite electrode in contact with an electrolyte in a cell.

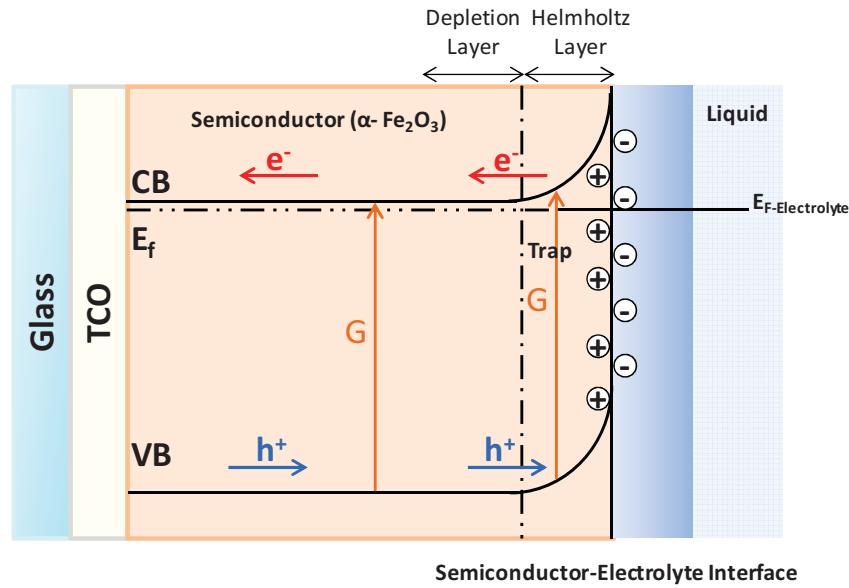


Figure 2.12 An n-type semiconductor in equilibrium with electrolyte.

Here we join the approach of (Klahr et al., 2012a, 2012c) presented as an equivalent circuit for general interpreting of the hematite photoanode impedance spectra is shown in Figure 2.13. This model covers all phenomena for both ranges of low and high frequency in EIS. It puts therefore the accent on surface trapping state contribution to recombination, by electrons and holes trapping from the conduction and valence band respectively under illumination. This phenomenon is presented by R_{trapping} in the model (Figure 2.13) while the charge transfer of holes from surface state to the electrolyte species is considered as $R_{\text{ct,trap}}$ and the charge transfer from the semiconductor bands to the electrolyte is represented under $R_{\text{ct,bulk}}$. Likewise the TiO_2 based PEC the important part of impedance spectra is attributed to the capacitances contribution. At low frequencies two capacitive elements in series appears; first is the depletion layer capacitance known as space charge capacitance (C_{SC}) and Helmholtz capacitance (double layer capacitance) at electrode-electrolyte interface C_{H} . The C_{SC} relation is driven from the Mott-Schottky (MS) statement:

$$\left(\frac{A_s}{C_{\text{SC}}}\right)^2 = \frac{2}{q\kappa\epsilon_0 N_D} \left(V_{\text{app}} - E_{\text{fb}} - \frac{k_{\text{B}}T}{q}\right) \quad (2.62)$$

This equation is same as Equation 2.30 for depletion layer capacitance. In fact space charge capacitance is same as depletion layer capacitance. Here the E_{fb} is the flat band potential, k_{B} is the constant of Boltzmann, k is the semiconductor dielectric constant (around 32 for hematite) and V_{app} is the applied potential.

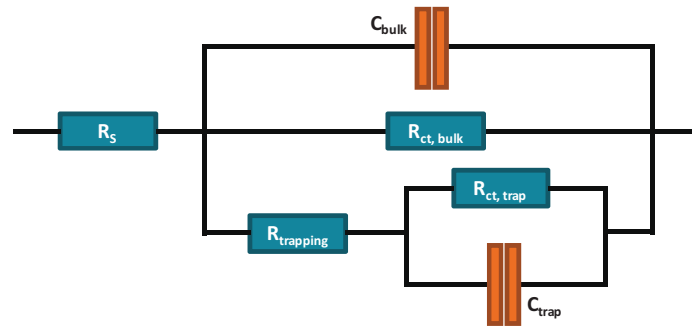


Figure 2.13 Equivalent circuit for hematite (α - Fe_2O_3) photoelectrode.

In the above equivalent circuit C_{SC} and C_H are compacted in C_{bulk} as an equivalent capacitance of these two elements. As we consider surface trapping states in the system, a chemical capacitance C_{trap} turns up in electrical circuit (EC). The origin of this capacitive behaviour has been detailed for TiO_2 so here we stand by previous explanation and we just mention that this capacitance has chemical origin and is different from C_{bulk} which has dielectric origin. The C_{trap} or also know as C_{SS} in literatures, is given by following relationship:

$$C_{SS} = A_S q N_{SS} \frac{\partial f_{SS}}{\partial E_{Fn}} = A_S \frac{N_{SS} q^2}{k_B T} f_{SS} (1 - f_{SS}) \quad (2.63)$$

With A_S attributed to electrode surface, N_{SS} to surface density, E_{Fn} to electron Fermi level of surface state while f_{SS} is fractional occupancy of surface state.

The modality of C_{trap} comes from state trapping state so it increases by decreasing of $R_{\text{ct,trap}}$. The trapping phenomenon can have two sides effects; one is causing electron-holes recombination which is shown under R_{trapping} but there is also hole transfer for water oxidation from surface state to the electrolyte. The fact that both values of C_{trap} and $R_{\text{ct,trap}}$ changes by changing illumination intensity indicates that this transfer comes to pass through the surface state. In addition the start of photocurrent is also related to the charging of surface states. Hence the more surface state is charged the more the C_{trap} increases and so the $R_{\text{ct,trap}}$ decreases. In fact the charge transfer from semiconductor to solution species can occur through the valence band and state surface channels but depending on the system characteristics one of $R_{\text{ct,trap}}$ or $R_{\text{ct,bulk}}$ dominates the charge transfer. Therefore in some cases either of $R_{\text{ct,trap}}$ or $R_{\text{ct,bulk}}$ can be simplified (K. Sivula M. Gratzel, 2011; Klahr, 2012). Following the mentioned simplifications the model would be rearranged as in Figure 2.14 (a), (b).

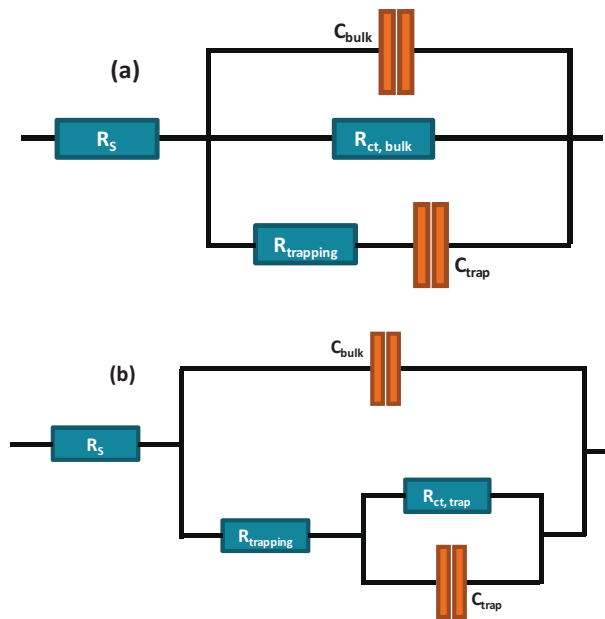


Figure 2.14 EC simplified by omitting $R_{ct, trap}$ (a), $R_{ct, bulk}$ (b).

But under dark condition in case the EIS gives us only one impedance arc according to (Lopes et al., 2014) the characteristics of hematite are different and apparently the simplification of C_{SC} and C_H to C_{bulk} does not fit properly the result. The author proposes to consider two RC circuits in series as below:

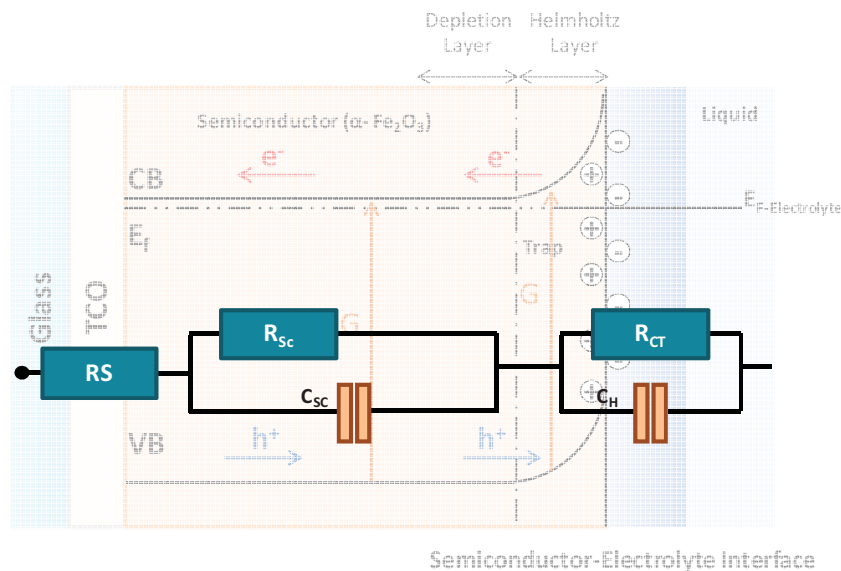


Figure 2.15 Hematite based photoelectrode EC under dark condition(Lopes et al., 2014).

This model is adequate to describe a thin layer photoelectrode in dark condition because by increasing the thickness the space charge capacitance C_{SC} decreases. In the other hand the

Helmholtz capacitance remains almost constant and bigger than C_{SC} in value because the Helmholtz double layer is thinner than the depletion region. Hence the model can be simplified to a circuit with C_{bulk} while the double layer capacitance is dominating the capacitive behaviour of photoelectrode. Here R_{SC} is the resistance represents the electron resistance in the bulk and the space charge of the semiconductor and is influenced by two factors: the applied potential and the thickness. Hence higher value of R_{SC} has been reported by increasing the thickness. Under dark condition and at low applied potential this resistance stays nearly constant while for high applied potential or under illumination the R_{SC} starts to decrease. This is because at high applied potential the Fermi level starts to bend toward the valence band and becomes more distanced from the conduction band which puts it near the surface and it gives result to the formation of an inversion band. This means that near the surface the holes become the major charge carriers. Therefore it creates a deep depletion layer and lower significantly the bulk resistance (R_{SC}). In this condition as the holes are near to the surface they are enable to easily react with the electrolyte ions so it becomes the beginning of water oxidation current under dark condition.

On the other hand contrary to the illumination condition, the R_{ct} value is enormous and rather constant which represents the water oxidation from valence band holes and with a slow kinetic. Basically the R_{ct} values are larger than R_{SC} and it is more or less independent from the thickness. But still for high values of applied potential the charge transfer resistance decreases (Lopes et al., 2014; Riha et al., 2013).

According to the models presented by (Klahr, Gimenez, Fabregat-Santiago, Bisquert, Hamann, 2012a; Lopes et al., 2014) the dark characteristics of hematite (Figure 2.15) are very different of its characteristics under illumination. Hence the R_{CELL} for hematite based PEC under illumination will be as:

$$R_{CELL} = R_S + R_{trapping} + R_{ct,trap} + R_{CE} \quad (2.64)$$

or

$$R_{CELL} = R_S + \frac{R_{trapping}R_{ct,bulk}}{R_{trapping} + R_{ct,bulk}} + R_{CE} \quad (2.65)$$

And for the dark condition it will be:

$$R_{CELL} = R_S + R_{SC} + R_{ct} + R_{CE} \quad (2.66)$$

Note that R_S is the series resistances as it has been mentioned in previous section.

We can consequently express the j and R_{CELL} relation as:

$$R_{CELL} = A_S \frac{dV}{dj} \quad (2.67)$$

2.5 First elements toward a knowledge model

This part aims to review the development of knowledge models of photoelectrochemical cells (PEC), by reviewing the literature in this field, and also by focusing on the experience gained in Institut Pascal during more than 20 years on modelling of photo-processes. The objective in particular, is to look for a model structure for the integration of knowledge at different levels of description and eventually reification of the model by ensuring its generic and predictive specifications. Only in this condition, it can be used as a tool for simulation, design, optimization and model based predictive control. The model will be established by taking into account the main controlling steps of the process, including the most important for photo-reactive systems, which is radiative transfer in the photo-electrodes (especially in photo-anode, with boundary condition corresponding to an artificial or incident solar radiation). It will then be necessary to couple thermokinetics of electron generation and transport with the radiation field $\mathcal{A}(\vec{x})$ to determine the current (or current density $\langle j_A \rangle$) flowing within the anode. Hence the kinetic and stoichiometric coupling will be formulated at the cathode in order to obtain the volumetric or surface rate of hydrogen production $\langle r_{H_2} \rangle$, $\langle s_{H_2} \rangle$ from the current density at the cathode $\langle j_C \rangle$. Other possible limiting steps such as catalysis, mass transfer and electrochemical processes will also be considered. As a final step, protons' transfer within the electrolyte, particularly through a membrane will be integrated in the knowledge model. Figure 2.16 summarizes the main variables and structure of the model in three compartments. In the following we discuss different types of PEC fabricated and tested in our laboratory for hydrogen production in future. These PECs are (i) based on the concept of Grätzel cells and use molecular photo-catalysts to absorb the radiation and titanium dioxide nano-particles to create specific surface area with a proper conduction band potential (DS-PEC for Dye Sensitized PEC) (ii) PECs based on semiconductor materials (SC-PEC for semi-conductor based PEC) with reduced band gap (hematite) and by using noble metals (iridium oxide or platinum) to catalyse the process.

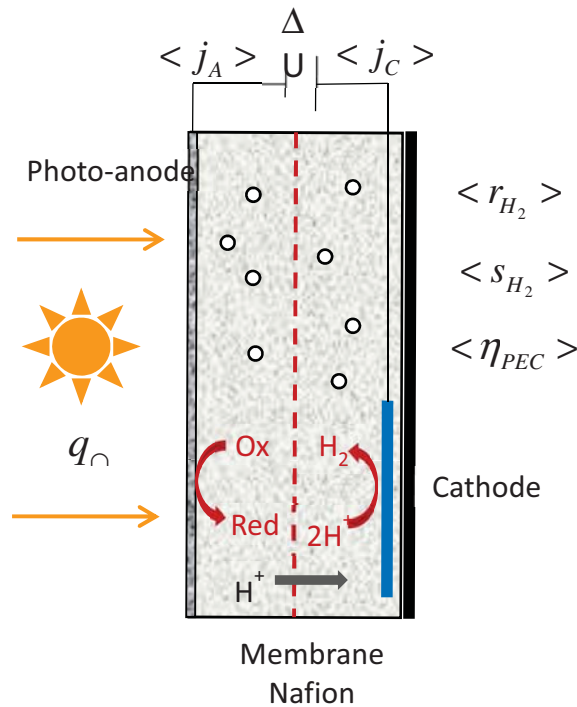


Figure 2.16 Schematic diagram of a photoelectrochemical cell (PEC) with the representation of the main variables of interest that can be measured and calculated by the model.

2.5.1 Radiative transfer in a photoanode (or photocathode)

The incident hemispherical flux density q_\odot and its angular distribution as rate determining steps are considered as the key parameters of radiative transfer modelling in a photoanode since it is the radiation field within photoanode which determines the PEC performance according to thermokinetic efficiencies used for calculation of current density and H_2 production rate.

a. Radiative transfer modelling in a multilayer thin film (quasi one-dimensional)

The modelling of radiative transfer in multilayer plane system is a relatively simple issue with several methods of resolution specially by accepting the one-dimensional approach. This step is crucial because it characterizes the physical limitation by radiative transfer in the process and so it will be a major source of future optimization for the engineer to fix the maximum performance of the PEC, once kinetic and energetic aspects are formulated at the whole process scale.

b. Bouguer law approach

To understand the subject, it is necessary to consider a non-polarized incidence of light, which can be artificial and constant over the time, or solar with natural fluctuations in angular

distribution, density and direction. The radiation field in the thickness of photo-electrode can be obtained by exact resolution of Maxwell's equations; or from radiative approximation (Bouguer law) by calculating the value of a dimensionless parameter (CORNET, 2005; Cornet, 2007):

$$\zeta = \frac{L}{d_c} = \frac{2\pi\kappa_\lambda L}{\lambda_0} \quad (2.68)$$

which represents the ratio of the characteristic dimension of the absorbing medium L (photo-electrode thickness), to the penetration distance of the wave d_c while κ represents the imaginary part of the refractive index of the considered equivalent medium (see infra). Therefore, the radiative Bouguer approximation will be only relevant if $\zeta \geq 2$. For example, based on average optical properties equivalent to the photoactive layer of DSSC (Grätzel cell) from the literature; we can estimate ζ parameter for different possible thicknesses (Wenger et al., 2011). The obtained results are shown in Figure 2.17:

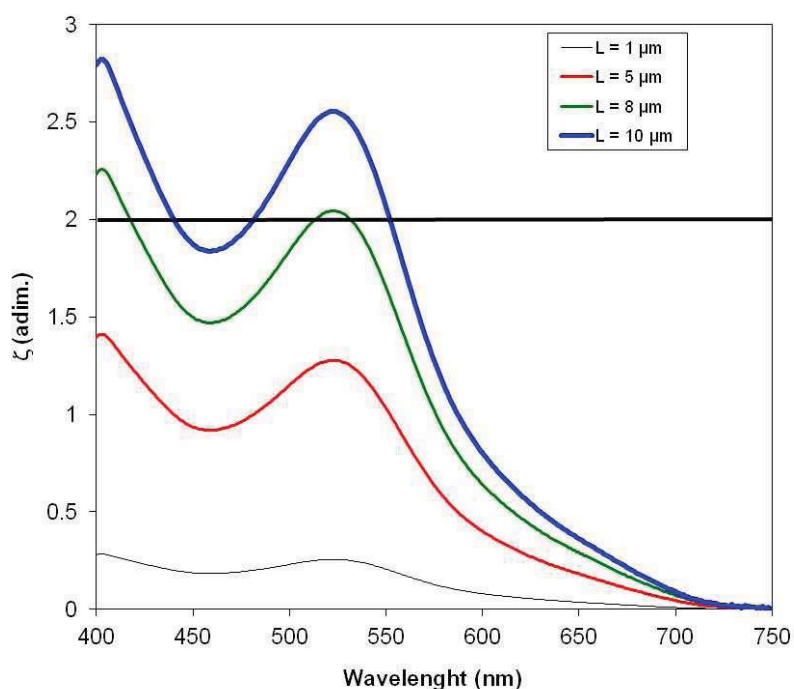


Figure 2.17 Estimated values of the parameter ζ (equation 2.68) for different thicknesses of the absorbing active layer. Optical properties of (Wenger et al., 2011).

Although these calculations need to be reconsidered based on optical properties of the compounds that have been tested in this project (catalytic complexes, bio-inspired chromophores, titanium dioxide and hematite electrodes), it is clear that for most wavelengths

of interest the thickness must be greater than to 10 μm to allow an adequate description of the radiation absorption by simplified radiative approach. In Wenger's work (Wenger et al., 2011), the active layer has a thickness of 8 μm . The conclusion is that electromagnetic approach will usually be necessary for a correct modelling of this phenomenon even though the optimization issue can bring to increase the thickness of active layer and promote the application of approximations.

Hence it is necessary to solve, from Maxwell's equations, the Helmholtz wave equation for multilayer system which is assumed homogenous, isotrope and linear:

$$\Delta \vec{E} + k^2 \vec{E} = 0 \quad (2.69)$$

Where k is the complex wave vector, from which we can determine the radiation field via the Poynting vector:

$$\vec{S} = \frac{1}{2} \text{Re} \left\{ \sqrt{\frac{\epsilon}{\mu}} \right\} |\vec{E}|^2 \vec{u} = \frac{1}{2} \text{Re} \left\{ \sqrt{\frac{\epsilon}{\mu}} \right\} |\vec{E}_0|^2 \exp\left(-\frac{4\pi\kappa_\lambda}{\lambda_0} z\right) \vec{u} \quad (2.70)$$

The connection with the radiative approach is given by the definition of luminance L_λ . Luminance is defined as the norm of the Poynting vector in the \vec{u} direction, as: $L_\lambda = |\vec{S}_\lambda|$.

This definition provides a theoretical basis for Bouguer relation by establishing:

$$L_\lambda = L_0 e^{-a_\lambda z} \quad (2.71)$$

where $a_\lambda = \frac{4\pi\kappa_\lambda}{\lambda_0}$ is the absorption coefficient.

Equation 2.69 can be solved by various methods. The literature mentions mainly the method of transition matrix which is well adapted to linear aspect of the electrical field propagation and the continuity of its tangential components (Burkhard, Hoke, McGehee, 2010; Monestier et al., 2007; Moulé et al., 2009; Pettersson, Roman, Inganas, 1999) . An example of resolution of Equation 2.69 from a case study in literature is given in Figure 2.18.

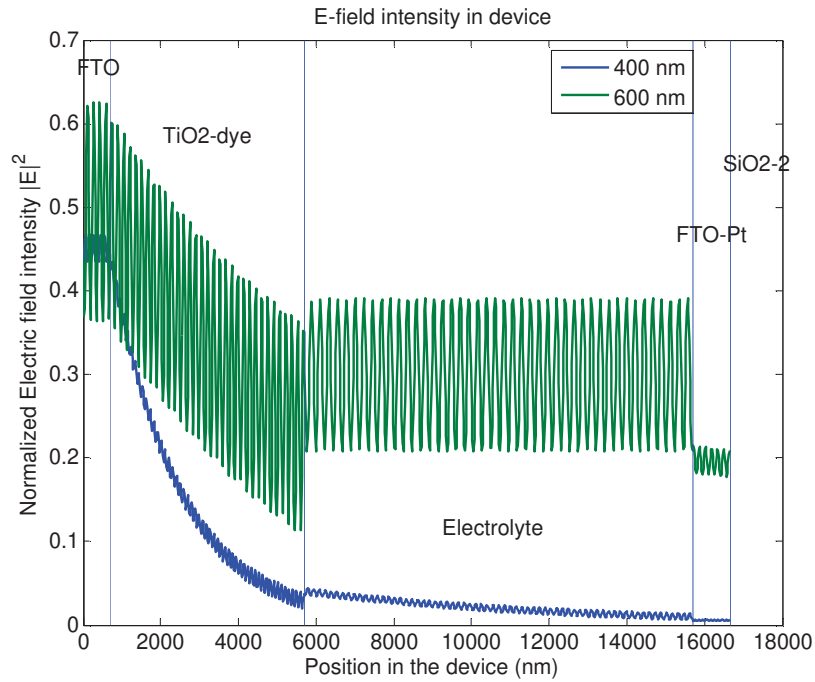


Figure 2.18 Example of radiation field obtained in the different layers of a DSSC (Grätzel cell type). The cell is illuminated from the left with non-polarized natural light and a collimated flux density with normal incidence. optical properties of Wenger et al. (2011).

This step permits to define the local volumetric density of absorbed radiative power:

$$\mathcal{A}(\vec{x}) = \int_{\lambda} \mathcal{A}_{\lambda}(\vec{x}) d\lambda \quad \text{W} \cdot \text{m}^{-3}$$

from local macroscopic field energy balance at pseudo-steady state:

$$\mathcal{A}_{\lambda}(\vec{x}) = -\text{div} \vec{S}_{\lambda} \quad (2.72)$$

This radiative variable can bring to a photonic variable $\mathcal{A}'(\vec{x}) \mu\text{mol}_{\text{h}\nu} \cdot \text{s}^{-1} \cdot \text{m}^{-3}$ more practical to understand kinetic formulations based on the photons flux and electrons (the number of photons can be counted regardless of their energy); however these two variables can be integrated on the photoanode volume V for calculating special variables which are important parameters in energetic analysis of PEC:

$$V \langle \mathcal{A}' \rangle = \int_V \mathcal{A}'(\vec{x}) d\vec{x} \quad (2.73)$$

This variable can be also obtained directly from measuring the density of input and output fluxes, because by integrating Equation 2.72 on a given volume (Cornet and Dussap, 2009) and inserting illuminated specific surface a_{light} (in one dimension) we obtain:

$$\langle \mathcal{A} \rangle = a_{light}[q_{in} - q_{out}] \quad \text{or also} \quad \frac{\langle \mathcal{A} \rangle}{\langle \mathcal{A}_0 \rangle} = 1 - T - R \quad (2.74)$$

Note that in the ideal case where we are able to limit transmittance to approach to 0 by absorbing all incident radiation (assuming that the overall optimization of the PEC by taking into account charge carriers loss in the thickness of the anode leads to this condition), Equation 2.74 shows that the optimum performance of PEC will be established as:

$$\langle \mathcal{A} \rangle_{max} = a_{light}(1 - \mathcal{R})q_{\cap} \quad (2.75)$$

Where the reflection of the anode can be calculated from the resolution of eq. 2.69 for incident unpolarized light.

c. Optical properties

If the numerical solution presented above does not impose major difficulties, it is because it has been assumed that the spectral optical properties of the multilayer medium are known. Defining the optical properties for photoelectrodes used in this work with complex constitution (FTO glass, TiO₂, dyes, molecular catalysts, semi-conductors) and nanostructuration is not a simple issue. At present state of work, the only possible way to work with predictive method is to estimate average equivalent properties, if and only if the optical properties of each single component and their volume fraction in the layer are known. Accordingly, we can use the composition relations, such as Maxwell-Garnett or Bruggeman relations which have also the usage limits that need to be verified. Otherwise, these optical properties can be obtained by experimental methods. For flat substrates, the contemplated method is ellipsometry (Flory, Escoubas, 2004; Moulé et al., 2009). This method is based on the measurement of the reflection of a plane wave at the surface of a flat substrate which enables the estimation of the n and κ parameters of the material (Harland G. Tompkins, 1999). In the case of mesoporous materials which have a particular surface roughness, it is more difficult to interpret the ellipsometry and requires additional processing. Other methods can be also considered with an optical bench available in the laboratory such as transmittance and reflectance measurements of small elementary samples and determination of optical properties by inversion results of (Chen,

(Rothenberger, Grätzel, 2008; Flory, Escoubas, 2004; Rothenberger, Comte, Grätzel, 1999). The possibility of coupling the two previously mentioned approaches can be also considered (Elalamy et al., 2004).

2.5.2 Coupling radiative transfer and thermokinetic of charge generation and transport in photo-anodes

As it has been presented in introduction, the main stages of the model which will be developed in this part try to analyse indifferently both of DS-PECs and SC-PECs which are two case studies of our laboratory with the same global sketch (See Figure 2.16 and 2.19) but with slight difference in structure and operating mode. A general scheme of a photoanode with main mechanisms which can take place in the electrode such as recombination and charge carrier loss are shown in Figure 2.19.

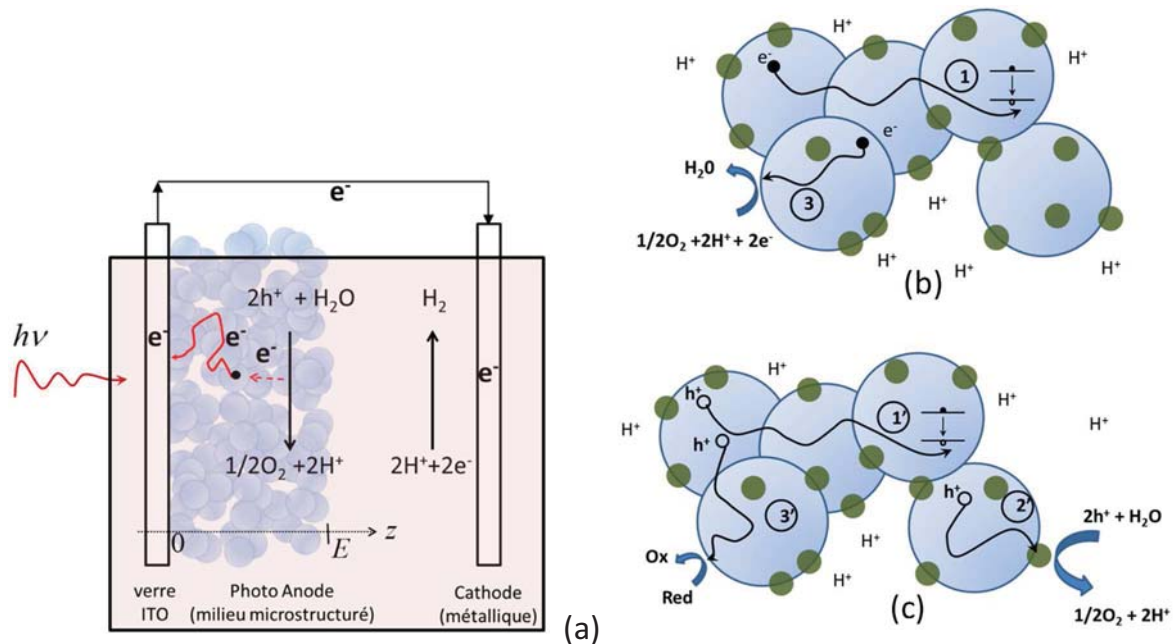


Figure 2.19 (a) Schematic type of a photo-electrochemical cell (PEC) with a focus on the photo-anode. Diagrams of electronic phenomena losses: (b) electrons from the conduction band, (c) the holes in the valence band. Phenomena 1 and 1' correspond to the volume recombination. 3, 2' and 3' to the recombination losses or electronic surface (case 2 would correspond to a reduction in the anode is not possible).

In this figure, if we study a DS-PEC, the grains represent TiO_2 particles and points, show the molecular photo-catalysts absorbing radiation. Otherwise, if we study a SC-PEC, the grains represent a short bandgap semiconductor (i.e. Fe_2O_3) which absorbs radiation and the points, are metal catalysts (Pt or IrO_2) having no photosensitive properties (or insignificant). This key

point, from which it is possible (or not) to make important assumptions for charge carrier transport will be discussed again in this chapter, each time the structure of the active layers interferes in the choice of assumptions for the model establishment.

The purpose of thermokinetic coupling formulation in photoanode is to calculate the current density $\langle j_A \rangle$ flowing out the anode by knowing from previous step the field \mathcal{A} based on optical properties of multilayer and the density of incident flux q_{in} .

Several phenomena can lead to a decrease of current density collected at photoanode from the density of incident flux (or precisely from the volumetric density of power absorbed locally in the thickness of the electrode). These phenomena will contribute to the reduction of useful electron flow and consequently the rate of hydrogen production (at the cathode). They can cause perturbation simply by the loss of electrons, or by adding additional resistance to the transfer of electrons or other related phenomena (i.e. mass transfer donors). Since the energy efficiency of the process is related to the current and the rate of hydrogen production, this means that any loss in "kinetic" efficiency (considered as mole of photons, electrons flux or current and moles of product) is related also to a loss of energy efficiency (expressing in absorbed joules, electrical power and produced chemical energy). For this reason, the term "thermokinetic coupling" is used, whenever it is considered that the phenomena contribute to reduction of both hydrogen production rate and the thermodynamic efficiency of the process. This will be the case for almost all the phenomena which will be discussed further in this document, except when we define (mostly for the cathode side of PEC) a stoichiometric quantum efficiency (similar to natural photosynthesis), because we seek to characterize them by energy efficiency ρ which should be derived from the detailed analysis of the relevant phenomena (reification). Hence, these efficiencies will be found normally while establishing a predictive formula, which gives the thermodynamic efficiency of photo-electrochemical cell $\langle \eta_{PEC} \rangle$.

Different ρ efficiencies may be classified into two distinct categories: those that do not depend on the local volumetric density of absorbed radiative power \mathcal{A} , and those which are dependent to. In first case, these yields will be constants in the area of interest (the volume of photo-anode) leading to a let's say, linear coupling with radiation. In second case, these efficiencies are not constant but they have local values which lead to a nonlinear coupling, what is the case in most photo-processes. Therefore, in the second case, the processes have a vast variety of behaviours and a strong dependency on the boundary conditions and geometry.

a. Variables independent of the radiation field (linear coupling)

These variables represent again two distinct categories of phenomena. First, the inevitable phenomena of energy dissipation because of light-material interaction (when a photon gives result to charge separation or to an exciton) which will be characterized by a maximum radiative conversion efficiency ρ_{max} . Also those phenomena that contribute to a loss of electrons, initially generated or to a reduction in production rate by adding resistance (mass transfer, electrical resistance) to the system. They will be characterized by efficiencies $\rho_{A,i}(T)$; where the index i refers to a particular phenomenon which will be modelled to specify its impact on the overall performance of the PEC.

I. Maximum conversion efficiency ρ_{max}

Maximum energy efficiency $\rho_{max}(\lambda, T, \mathcal{A}')$ can be seen in different ways (and therefore estimated by different theories) depending if we consider light as a wave or a particle (photon).

The theory shows that the maximum energy efficiency $\rho_{max}(\lambda, T, \mathcal{A}')$, corresponding to the conversion of radiation to usable physicochemical free energy (the maximum work that can be obtained from the solar radiation) is strictly a function of the field of volumetric density of absorbed power, \mathcal{A}' , and of the wavelength. However, the dependence of the efficiency on radiative quantities (density and wavelength) is very negligible. Moreover, at a first approximation we can consider that this efficiency is also poorly dependent on the temperature. Hence it can be written $\rho_{max}(\lambda, T, \mathcal{A}') \equiv \rho_{max}(T)$.

- Calculation from a radiative thermodynamic approach

This approach which involves both of the operating temperature and an equivalent temperature of solar radiation is still a scientific debate and three different relationships are used (Bădescu, 2000). However, the problem was studied by (Bejan, 2006, 1987) who showed that the three competing theories are actually only three forms of the same approach which difference is essentially in the definition of the radiating system and its use. Therefore (Cornet, 2007) used the relationship of Jeter-Duysens to estimate the value of ρ_{max} in natural photosynthesis from the wavelength and the definition of equivalent temperature of the radiation.

- Calculation from chemical potential of photon

Another approach, based on the Bose-Einstein statistics which permits to define the chemical potential of the photon out of equilibrium (it is zero at thermodynamic equilibrium of a black

body). It can also be considered as work of (Cook and Dickerson, 1995; Herrmann and Würfel, 2005; Ruppel and Würfel, 1980; Würfel, 1982). An important statistic study and theoretical work need to be conducted on this issue in order to develop the understanding of the involved phenomena and the relation between chemical potential of the photon and chemical potential of the exciton or electron-hole pair in transfer situations (out of equilibrium) and reaction. This item was discussed in the context of organic cells by (Meyer and Markvart, 2009).

II. Other conversion efficiencies, associated to possible limiting rates

Other limiting phenomena to $\rho_{A,i}(T)$ need also to be taken into account. These phenomena can take place in the solution or at the interface (by neglecting the ohmic losses or contact resistances, such as Schottky barrier at the interface of semiconductor/conductor glass), mainly as mass transfer near the anode when using a sacrificial electron donor. In this case, a classic model of transfer (double layer of Gouy-Chapman-Stern or Nernst thin layer) can be used to determine the resistance of additional transfer where an efficiency can be derived $\rho_{A, \text{mass}}(T)$.

b. Variables dependant of the radiation field (nonlinear coupling)

This part is about to describe and take into account all the processes that will lead to a loss of excitons created by the local photon absorption and determine the charge carriers flow. These phenomena generally depend on the temperature and also some of them on absorbed photon flux density \mathcal{A}' , which brings the problem to local scale.

The discussion in this paragraph is highly dependent on the structure (size, geometry, nanoscale) of the photoactive part of the anode and the differences depending on which one of DS-PEC or SC-PEC are the subject of study. This structure is presented very differently in the literature (see simplified diagram in Figure 2.20) with a direct impact on the assumptions considered for charge transport formulation (ballistic or diffusive transport, for example). In a classical approach of transport, these issues can be for example analysed in term of the average free path compared to characteristic thickness. In the following of this document, the described approaches are largely based on a structure which permits to assume the isotropy of the environment and work with an equivalent homogeneous medium. This is of course a restrictive choice (see Figure 2.20), in agreement with the patterns of Figure 2.19, which proves that to have an optimal performance within the cell it is necessary to have this type of nanostructuring (here we assume that the key factor is the specific surface, which may also has been called "antenna effect" in analogy with natural photosynthesis).

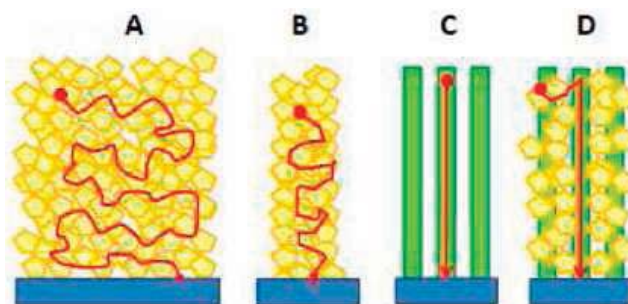


Figure 2.20 Diagrams showing different types of a photo-anode structure. Specially, the difference between a diffusive transportation (A) and ballistic transportation (C). This structure illustrates a competition between specific surface of absorption and charge transport.

Hence, it is possible to classify the phenomena related to possible dissipation and so kinetic efficiency loss (it is systematically excitons or electrons loss) into two categories. The first is about the mechanism of primary interaction between light and matter and therefore the primary conversion efficiency of an exciton into an electron that will actually be "injected" into the conduction band of a semiconductor to be transported to the conductive glass collector. Contrary to these electrons, this means that those excitons (from a photon) which have not been followed by an injection have been recombined or lost their energy to a non-photochemical activity. This common phenomenon is closely related to catalysis because the minimization of these recombinations requires a sufficiently efficient catalysis to allow the electron donor (the oxidation reaction) to travel and fill the gap, in a time less than the lifetime of the exciton. It will be characterized by an efficiency $\rho(\mathcal{A}', T, pH)$ which clearly depends on the radiation field (the more the absorbed radiant energy is high the more the catalyst becomes limiting and rate determining, as in natural photosynthesis). This efficiency $\rho(\mathcal{A}', T, pH)$, is related to the local absorbed radiant power \mathcal{A}' and to the local volumetric rate of charge carriers generation G by a nonlinear relationship $\rho(\mathcal{A}', T, pH) = \rho_{max} f(\mathcal{A}', T, pH) \times \mathcal{A}' = G(\mathcal{A}', T) f(\mathcal{A}', T, pH)$.

Establishing of a theoretical expression of $\rho(\mathcal{A}', T, pH)$ with the maximum value of ρ_{max} ; discussed earlier; is closely linked to catalysis model which is completely different in the case of a molecular catalysis (DS-PEC) or catalysis by precious metals (SC-PEC). Note that in the case of SC-PEC the recombination rate may be slightly influenced by the presence of a surface electric field related to chemical potential difference between species in each phase called band bending. This will depend on the value of the applied potential which can be exactly equal to that of oxidized redox couple.

The second phenomenon is the transport of charge carriers generated locally in the nano-composite structure (network) to their collection point to generate the current density $\langle j_A \rangle$. The description of this phenomenon in all cases, requires the resolution of a charge transport equation (electrons e^- and eventually holes h^+) for which the choice of the most appropriate scale has not been yet determined (today in most of published works, macroscopic diffusion equations have been used which unfortunately generate too many parameters in the model very difficult to reify). This choice is important because it commits to the model structure and leads (or not) to the reification of the parameters related to transport. We will see later in this chapter that some formulations allow identifying a collection efficiency $\rho_{col}(T)$ which will complete an integral formulation of the photo-anode model.

Various possibilities of loss of charge carriers during transport to the collector are summarized in Figure 2.19 (b) and (c). For a SC-PEC, it can correspond to **volume recombination** already known in the field of PV (Juan Bisquert, 2008; Gray, 2005; Grundmann, 2010; Landsberg, 1991; Tiedje, Yablonovitch, Cody, Brooks, 1984) (spontaneous or stimulated radiative recombination requiring the encounter of an e^- and a h^+ , Auger recombination with another charge or recombination Shockley-Read-Hall which is not intrinsic to the material but depends on defects in the crystal structure at intermediate energy levels) or **surface recombination** at the scale of the elementary grain (grain boundaries, defects, deficiencies, impurities, interaction of a h^+ with electrolyte). Note that the interaction between electrons which appear at high electronic density and lead to a nonlinear formulation of transport can probably be neglected in the PEC. In a DS-PEC, all phenomena described above may not exist because the semiconductor is not used to absorb the radiation, but for conducting electrons to the collector and create specific surface. The volumetric radiative and Auger recombinations which are already poorly possible, cannot really happen in a DS-PEC. The areal recombination (recombination at the surface), which is the interaction of the electron with the electrolyte (reduction) is also poorly possible, which give to the assumption that the Grätzel-type systems are certainly very efficient for charge transport.

I. Equation of macroscopic evolution

This scale of description for understanding the charge transport in the photo-anodes is recently very frequent in publications. Because it leads to establishment of an easily processable model, enabling us to understand different morphologies of internal structures. However, its

implementation is not very well supported. Specially the geometric assumptions based on physical dimensional analysis which takes average on statistical structuring of the semiconductor and positions of catalysts at its interface (Slattery, 1999; Whitaker, 1977) are rarely examined. Therefore, the main drawback of this approach is the failure in reifying many parameters of the model, which weaken the comprehensive and predictive characteristic of a model for design and optimization of large-scale PEC.

In general case, if we do not neglect the presence of electric field within the anode, the model leads to a drift-diffusion equation. No external electric field is applied, but there is an electric field induced by difference of electro-neutrality related to the local charge distribution. The Debye length which determines the characteristic dimension (beyond which, the effect of electrical field is not negligible) will be calculated case by case. If this length is very small (nanometre scale), as in plasmas, the charge carrier transport is strongly coupled and in this case, in macroscopic scale, only one type of carrier is considered and the effect of induced electrical field is included in a coefficient of an ambipolar diffusion (function of charge carriers' density and their electronic mobility). Based on (Jacoboni and Lugli, 1989; Jörg and Luther, 2001), the macroscopic equation can be briefly presented:

If we consider “n” the electronic density of electrons and “p” the electronic density of holes (N_D^+ , N_A^- represent the densities of dopants for electrons and holes respectively), the charge carriers flow densities can be obtained from the zero order moment of Boltzmann equation:

$$\begin{aligned}\vec{j}_n &= -en\mu_n\vec{E} + eD_n\overrightarrow{grad} n \\ \vec{j}_p &= ep\mu_p\vec{E} - eD_p\overrightarrow{grad} p\end{aligned}\tag{2.76}$$

The moment of first order of Boltzmann equation gives local balance for charge carriers:

$$\begin{aligned}G_n - R_n + \frac{1}{e}div\vec{j}_n &= \frac{\partial n}{\partial t} \\ G_p - R_p + \frac{1}{e}div\vec{j}_p &= \frac{\partial p}{\partial t}\end{aligned}\tag{2.77}$$

in which the flux relations of Equation 2.76 are rewritten as:

$$\frac{\partial n}{\partial t} = G_n - R_n - \mu_n n \text{div} \vec{E} - \mu_n \vec{E} \cdot \overrightarrow{\text{grad}} n + D_n \Delta n \quad (2.78)$$

$$\frac{\partial p}{\partial t} = G_p - R_p - \mu_p p \text{div} \vec{E} - \mu_p \vec{E} \cdot \overrightarrow{\text{grad}} p + D_p \Delta p$$

The model is completed by the relation between the electrical field and the electrostatic potential:

$$\text{div} \vec{E} = -\phi = \frac{\rho}{\varepsilon_{SC}} = \frac{e}{\varepsilon_{SC}} (N_D^+ + p - N_A^- - n) \quad (2.79)$$

This set of relations should be solved associated with boundary conditions which are not necessarily trivial to write. In particular, it may be necessary to consider the band bending phenomenon at the interface with the electrolyte as it has been mentioned above. In many situations (e.g. in the case of DS-PEC), it will not be necessary to solve the equation on holes (p) but only the evolution equation of the electrons that will lead to the expression of collected current density leaving the anode.

If we can neglect the effect of the induced field \vec{E} , which is often done in the publications about PEC, we obtain a simple diffusion-reaction equation, as presented today in Grätzel cells modelling (Barnes et al., 2011) which takes the general form (in the case of a one-dimensional writing, where the temperature dependence has been neglected to simplify):

$$(1 - \theta) \frac{\partial n}{\partial t} = \frac{(1 - \theta)}{\varpi^2} D \frac{\partial^2 n}{\partial x^2} + G(x, \mathcal{A}') - r_{\text{surface}}(x) - r_{\text{volume}}(x) \quad (2.80)$$

where n is the volumetric density of the considered charge carriers (m^{-3}) and D is the diffusion coefficient of charge carrier. In this writing, we intended to show the specific geometric variables of each system like the average porosity of the electrode θ or its tortuosity ϖ . In case of an electrochemical system operating in steady state, the left term is zero and the reaction terms of first order regarding involved reactive species (under certain assumptions which are again questionable). It will then be possible to determine an electronic density profile according to the thickness of the device (one-dimensional resolution) and by deducting a charge carrier density at a given direction x , (current density leaving the anode):

$$j_A = D \left. \frac{dn}{dx} \right|_{x=0} \quad (2.81)$$

II. Description of charge transport at smaller scales – Toward reification

As we have already mentioned above, previous approaches during their implementation lead to the determination of many parameters (for characterizing the diffusive phenomena and kinetics of recombination or charges loss- dozens in published models -) related to the considered electrochemical system and its geometry. These parameters are related to the phenomena that coming from transport physics, solid-state physics or even quantum physics at smaller scales. It seems impossible to reify all these parameters, which means, a predictive determination *ab initio*, giving the model a sufficiently predictive and generic characteristic for applications we envisage. In the same way as we have already achieved for photoreactors, the question is to find a description for smaller scales; considering that it is always possible to upgrade to the higher scales of process by integration (which can result to a complete integral formulation for which, today we have extremely efficient tools). We have already mentioned that the macroscopic equations presented above, are actually moments of Boltzmann transport equation, put to question the formulation of the problem during moving to mesoscopic scale, regarding the decrease in the parametric space and reification of parameters that appear on this scale.

A possible interesting approach consists in using a linear Boltzmann equation (under some assumptions in the collision term) for the description of charge carriers' transport. This presents at least two important advantages in our formulation of a mathematical knowledge model. First, we hope that solid quantum mechanics helps us to reify the main parameters appearing in the equation (Grundmann, 2010; Jacoboni and Lugli, 1989) such as the recombination rate, the charge diffusion rate and the phase function for diffusion. Second, in case of linear transport equation, it is possible to seek a solution by integral formulation finding the Green function of the problem $g(\vec{x}_0, \vec{v}_0)$. In this case, considering all our previous developments and definitions, one can rewrite the mean density current (where we set by definition $\varphi = 1$ mole of electrons per mole of photons) in the form:

$$\langle j_A \rangle = \frac{\varphi \mathcal{F}}{S_{light}} \rho_{max}(T) \int_{\mathcal{V}} d\vec{x}_0 \mathcal{A}' \rho_{col}(\vec{x}_0, T) f(\vec{x}_0, \mathcal{A}', T, pH) \quad (2.82)$$

where we inserted the so-called electron (or charge) collection efficiency ρ_{col} as a moment of Green function which does not depend on the radiation field (integral formulation of charge collection efficiency).

2.5.3 Stoichiometric and kinetic coupling at the cathode electrode.

At the cathode, by assuming that we know the current density $\langle j_C \rangle$, we can again reformulate the coupling between the current density and the surface rate of hydrogen production $\langle S_{H_2} \rangle$ by the efficiencies which only include this time, the kinetic limitations which are never coupled directly to the radiation field (so inducing a linear coupling).

Regardless of these phenomena, we must insert the molar stoichiometric coefficient $n_e = 2$ which is defined for any photo-electrochemical reaction by electrons balance and simply counting the number of moles of electrons to form one mole of desired product. In case of hydrogen, it requires two moles of electrons to produce one mole of hydrogen. Therefore; $n_e = 2$.

Other limitations that may decrease the rate of hydrogen production from the current density $\langle j_C \rangle$, belong to two distinct categories and can be so presented as efficiencies:

$$\rho_C(T) = \prod_i \rho_{C,i}(T) \quad (2.83)$$

Among the major phenomena to be considered, first is the catalysis of the protons reduction in hydrogen that will be characterized by efficiency $\rho_{cat}(T, pH)$ and can be limiting if the oxidation catalyst at the anode is very efficient. Note that in this case the anode runs at regime controlled by only radiative transfer and it is sufficient that the catalysis at the cathode be calibrated to work in this physical limitation regime. The second phenomenon (same as at the anode) is about possible limitations by mass transfer. In particular, the transfer of electroactive species (H^+ in this case) within the electrolyte happens generally through a membrane which may add resistance to the transfer of protons. Note that this phenomenon was initially listed as representing a third part of the model (outside of the anode and cathode), but it can be brought here a limiting step to the cathode presented as an efficiency $\rho_{C, mass}(T)$.

It is therefore possible to write the surface rate of hydrogen production from the current density at the cathode as a simple linear relationship:

$$\langle S_{H_2} \rangle = \frac{\rho_{cat}(T, PH)\rho_{C, mass}(T)}{n_e \mathcal{F}} \langle j_C \rangle \quad (2.84)$$

in which logically the coefficient $n_e = 2$ appears as each time that a relationship between reaction kinetics and electrical current will be given.

If necessary, it will be easy to pass the volumetric rate of hydrogen production by using the specific illuminated surface of the photoanode a_{light} that can be defined according to the desired interpretation, regarding the active thickness of the anode (as we have seen in previous paragraphs that an integral on volume will always appear in the model in the photo-active part of the anode) or the thickness of the entire cell:

$$\langle r_{H_2} \rangle = a_{light} \langle S_{H_2} \rangle = a_{light} \frac{\rho_{cat}(T, PH)\rho_{C, mass}(T)}{n_e \mathcal{F}} \langle j_C \rangle \quad (2.85)$$

2.5.4 A summary on a possible comprehensive formulation, of nonlinear coupling with the radiation field

Finally, it is possible to connect the superficial rate of hydrogen production $\langle S_{H_2} \rangle$ to the local volumetric spectral rate of photons absorption (in moles of photons) $\mathcal{A}'_{\lambda}(\vec{x})$ if we connect the two current densities values at the anode and the cathode to eliminate them. Indeed, by applying the conservation of charge we obtain $\langle j_C \rangle = \langle j_A \rangle$ where, from the relationships (2.82-2.84):

$$\frac{n_e \mathcal{F} \langle S_{H_2} \rangle}{\rho_{cat}(T, PH)\rho_{C, mass}(T)} = \frac{\frac{\varphi \mathcal{F}}{S_{light}} \rho_{A, mass}(T) \int_{\nu} d\vec{x}_0 \int_{\lambda} d\lambda \mathcal{A}'_{\lambda}(\vec{x}_0) \rho_{col}(\vec{x}_0, T) f(\vec{x}_0, \mathcal{A}', T, pH)}{\rho_{cat}(T, PH)\rho_{C, mass}(T)} \quad (2.86)$$

giving the integral formulation to calculate the surface productivity of a PEC in hydrogen:

$$\langle S_{H_2} \rangle = \frac{\varphi}{n_e} \rho_{cat}(T, PH)\rho_{C, mass}(T) \rho_{A, mass}(T) \frac{\rho_{max}(T)}{S_{light}} \int_{\nu} d\vec{x}_0 \int_{\lambda} d\lambda \mathcal{A}'_{\lambda}(\vec{x}_0) \rho_{col}(\vec{x}_0, T) f(\vec{x}_0, \mathcal{A}', T, pH) \quad (2.87)$$

Where $\frac{\phi}{n_e} \equiv \phi = \frac{1}{2}$ (in moles of hydrogen per mole of photons) is stoichiometric quantum efficiency. This is about, what we call the "stoichiometric conservative photons", which means the absorbed photons that resulted in the formation of the desired product with a given stoichiometry, and a photochemical ratio fixed to "one" electron per photon.

If the reduction catalysis is sufficiently efficient at the desired pH and if the mass transfer resistances are negligible (controlled), it can be written:

$$\langle s_{H_2} \rangle = \phi \frac{\rho_{max}(T)}{S_{light}} \int_v d\vec{x}_0 \int_\lambda d\lambda \mathcal{A}'_\lambda(\vec{x}_0) \rho_{col}(\vec{x}_0, T) f(\vec{x}_0, \mathcal{A}', T, pH) \quad (2.88)$$

Note that with the Equation 2.85, we can also write the volumetric rate of hydrogen production in which we see appearing the average volumetric rate at the photo-anode through by which we certainly obtain:

$$\langle r_{H_2} \rangle = \phi \frac{\rho_{max}(T)}{V_{light}} \int_v d\vec{x}_0 \int_\lambda d\lambda \mathcal{A}'_\lambda(\vec{x}_0) \rho_{col}(\vec{x}_0, T) f(\vec{x}_0, \mathcal{A}', T, pH) \quad (2.89)$$

2.5.5 Thermodynamic efficiency of PEC.

After processing thermo-kinetic aspect of coupling with the radiation field (which leads in this case to the predictive calculation of the surface or volumetric rate of hydrogen production), it is also important to be able to model energy conversion performance of PEC (and on a solid scientific basis which allows the comparisons with other solar technologies). Indeed, as any solar process for energy, the superiority of a technology over another is closely linked to its thermodynamic efficiency.

The thermodynamic efficiency of a PEC can be evaluated in two different ways which must be reconciled together. In one hand, it is possible to establish a rigorous relationship, from the initial establishment of the entropy dissipation function, for considered process. This relationship allows to calculate the average thermodynamic efficiency $\langle \eta_{PEC} \rangle$ of the cell from the input data (the density of incident light flux, the geometry of the system and possibly the bias value) and from the knowledge of the volumetric density of absorbed radiant power $\langle A \rangle$ and the volumetric rate of hydrogen production $\langle r_{H_2} \rangle$ (if we are able to calculate the electrochemical potentials at real conditions, which are involved in the calculation). Obviously, these two crucial variables can be defined experimentally (and so we can calculate $\langle \eta_{PEC} \rangle$)

accurately from measurements) or from the model that was developed earlier (and there is then a theoretical relationship which provides $\langle \eta_{PEC} \rangle$). On the other hand, by using all the thermodynamic efficiencies previously defined, and by adding exclusive energy conversion phenomena which have not been taken into account, it is possible to establish and calculate predictively a thermodynamic efficiency in form of a product of yields:

$$\langle \eta_{PEC} \rangle = \prod_i \rho_i \prod_j \eta_j.$$

a. Thermodynamic equilibrium, electrochemical potential, bias.

Before any discussion about the predictive calculation of thermodynamic efficiency of a PEC functioning out of equilibrium, it is essential to remember the basics of thermodynamic of electrochemical systems in equilibrium. Indeed, before generating any current or producing any hydrogen bubble, a photo-electrochemical cell must meet the thermodynamic conditions in terms of potential, in direct relation with the redox potentials of involved redox couples (typically in case of the water photolysis for H_2 production versus SHE at pH 7: $H^+/H_2 = -410$ mV and $H_2O/O_2 = +820$ mV). The potentials of the anode and cathode must be correctly positioned, otherwise the PEC will not work at all (see (Bak et al., 2002) and Figure 2.21 transcribed from this article). It seems pretty clear now that in most real systems, this position requires a bias (Bak et al., 2002) which therefore must absolutely be considered in the calculation of the thermodynamic efficiencies and formulas. Figure 2.21(a) to (d), also illustrates the positioning of the valence band of a semiconductor in case of SC-PEC in dark and presence of light versus electrochemical potentials of H^+/H_2 and H_2O/O_2 redox couples (it all shifts 59 mV per unit of pH at 25°C). The potential related to Fermi level are also indicated (Fig. 2.21a). At thermodynamic equilibrium, is conventionally defined:

- The Fermi level of electrons in the conduction band by:

$$E_F = E_C + mk_B T \ln \frac{n_C}{N_C} \approx E_{anode} \quad (2.90)$$

- The Fermi level of the electroactive species in the cathode compartment:

$$E_{Redox} = E_C + \frac{k_B T}{2} \ln \frac{a_{H_2}}{a_{H^+}} \quad (2.91)$$

lightened, there is often a sharp drop in anode potential versus the reference electrode), where the potentials are thermodynamically not adequate, which will require to use a bias (ΔU_{bias}) to operate the system (which obviously represents an additional energy cost to be considered in the analysis).

b. Thermodynamic efficiency of a PEC from observable experiments

The thermodynamic efficiency of a photo-electrochemical cell can be achieved globally, from knowing (experimentally or theoretically) the average rates of $\langle r_{H_2} \rangle$ or $\langle A \rangle$ (here inevitably presented in W/m^3 to process from energy point of view), presuming that we know how to calculate, at real conditions, the involved thermodynamic variables (especially electrochemical potentials). Based on the work already developed on photo-reactor (Cornet et al., 1994), it is possible to establish an accurate relationship giving thermodynamic efficiency (or energy yield) of a PEC $\langle \eta_{PEC} \rangle$ by knowing the average entropy dissipation function $\langle \sigma \rangle$ in the process. This was established by (Cornet, 2007) in a very general case, of a system in which electrostatics, radiation and chemical reaction are all considered.

This relationship will have to be first simplified in the case of electrostatic applications that we study and show the electrochemical potentials (Groot and Mazur, 1984; Salvador, 2001) and, secondly, be applied twice, at the anode and the cathode to show the current density $\langle j_A \rangle$ by integrating on the volume of the anode as we have done to formulate the thermo-kinetics coupling. The electrochemical potentials $\tilde{\mu}_i$ which appear in relationships giving η_{anode} and $\eta_{cathode}$ should be estimated under real conditions by using predictive thermodynamic models developed in our laboratory. It will be then possible to apply thermodynamic efficiency of the whole cell by writing:

$$\langle \eta_{PEC} \rangle = \langle \eta_{anode} \rangle \eta_{cathode} \quad (2.92)$$

This relationship has to contain the bias expression ΔU_{bias} , if it is necessary to the PEC functioning.

Meanwhile that this theoretical work be accomplished, it will be possible to use the following approximate relationship that should provide a good approximation of thermodynamic efficiency of the entire cell, reformulated from the analysis of (Parkinson, 1984):

$$\langle \eta_{PEC} \rangle \cong \frac{\langle r_{H_2} \rangle \Delta g'_0}{\langle A \rangle + \langle j \rangle a_{light} \Delta U_{bias}} \quad (2.93)$$

where $\Delta g'_0 = 237 \text{ kJ/mol}$ is the standard Gibbs free energy of water photolysis. If we characterize the current density $\langle j \rangle$ instead of hydrogen production rate, and assuming that we can neglect the limitations at the cathode (Equation 2.84), which comes to qualify performance of photo-anode we can alternately use (Faraday efficiency equal to 1):

$$\langle \eta_{PEC} \rangle \cong \frac{\frac{\langle j_A \rangle}{n_e \mathcal{F}} a_{light} \Delta g'_0}{\langle A \rangle + \langle j_A \rangle a_{light} \Delta U_{bias}}$$

Or from the Equation 2.74:

$$\langle \eta_{PEC} \rangle \cong \frac{\frac{\langle j_A \rangle}{n_e \mathcal{F}} \Delta g'_0}{q_{\odot}(1 - T - R) + \langle j_A \rangle \Delta U_{bias}} \quad (2.94)$$

It is obvious that these efficiencies are defined regarding the actual absorbed radiation in the cell $\langle \mathcal{A} \rangle$, according to the dissipation function, which allows to analyse the performances based on the quality of this absorption with the maximum value of $\langle A \rangle_{max}$ given by Equation 2.75. If instead we want to analyse the performance of the complete system, it is necessary to present the efficiency versus the incident flux density q_{\odot} by multiplying η_{PEC} by a radiation use efficiency we have:

$$\eta_{TOT} = \langle \eta_{PEC} \rangle \eta_{\tau} = \langle \eta_{PEC} \rangle \frac{\langle A \rangle}{q_{\odot} a_{light}}$$

Applied to relations (2.93-2.94) by using Eq. (2.74), we obtain:

$$\langle \eta_{TOT} \rangle \cong \frac{\frac{\langle j_A \rangle}{n_e \mathcal{F}} \Delta g'_0}{q_{\odot} + \langle j_A \rangle \Delta U_{bias}} = \frac{\langle S_{H_2} \rangle \Delta g'_0}{q_{\odot} + \langle j_A \rangle \Delta U_{bias}} \quad (2.82)$$

In case of interest to compare PEC performance to other solar systems (PV, solar thermal ...), it is preferable to use the variable η_{TOT} which corresponds to what is used in these areas. However, we cannot automatically fix the value of q_{\odot} to 1000 W/m^2 (AM 1.5); as it is often done in publications; because we should have the possibility to reduce this flux density to verify that the thermodynamic efficiency of a PEC increases when the incident flux reduces, which leads to the idea of radiation flux dilution (Cornet, 2010). If for consistency matters we define

only $\eta_{\tau} = \frac{\langle A \rangle}{q_{\text{light}}}$ in the actual absorbed spectral range (of 300 nm up to maximum [700 to 800 nm] for PEC), it then is needed to multiply the efficiency of Equation 2.95 by an integral over the entire solar spectrum, as:

$$\eta_{\text{sun}} = \frac{\int_{\lambda=0.3 \mu\text{m}}^{\lambda_{\text{max}}} W_{\lambda} d\lambda}{\int_{\lambda=0.3 \mu\text{m}}^{\lambda=4 \mu\text{m}} W_{\lambda} d\lambda} \quad (2.96)$$

This efficiency will be around 0.5 if the PEC works in complete UV-visible range (the most optimistic condition), which shows that the efficiency, compared to other solar technologies, will greatly reduce by need of using a bias (which seems inevitable until today) and the fact that at best, only half of the solar spectrum can be used. This leads to consider hybrid systems in which, associated with radiation dilution, captured infrared is used to provide mechanical work and bias to the complete system. This prospective solution permits to achieve easily to overall efficiencies 4 to 5 times higher (Cornet et al., 2015).

c. Predictive approach of thermodynamic efficiency of a PEC

Regardless of the above approach which requires to know by model or to measure the key observable variables of the cell, it is theoretically possible to establish and reify a relationship giving the thermodynamic efficiency of the PEC from a product of yields or efficiencies. As already mentioned, they will involve energy variables ρ_i already defined during establishing the thermo-kinetics coupling together with new purely energy variables η_j as:

$$\langle \eta_{PEC} \rangle = \prod_i \rho_i \prod_j \eta_j.$$

In publications about Grätzel cells, which are close to our matter of study, DS-PEC, we find frequently the use of η_{IPCE} yield (yield of incident photon to current efficiency) which integrates all the steps for achieving from q_{light} to generated current i in the cell. The elementary considered processes are generally (Barnes et al., 2011; Listorti et al., 2011; Villanueva et al., 2009):

- The absorption of photons (light harvesting) by dye molecules on the surface of substrate (semiconductor) with high specific surface and characterized by an efficiency η_{LH} .

- The injection of electrons into the conduction band of semiconductor specified by η_{INJ} (Halme et al., 2008).
- The collection of electrons by diffusion through the crystal structure denoted by η_{COL} .

which allows writing:

$$\eta_{IPCE} = \eta_{LH}(\lambda)\eta_{INJ}(\lambda)\eta_{COL}(\lambda)$$

These efficiencies are all considered dependent on the wavelength. It will be noted that the η_{LH} efficiency corresponds to an elementary description of radiative transfer which is not correctly modelled in this approach. However, η_{COL} and η_{INJ} efficiencies which consider the reaction-recombination-diffusion phenomena of electrons and the efficiency of injection in the conduction band of TiO_2 are close to the efficiencies that we called earlier $\rho(\mathcal{A}', T, pH) = \rho_M f(\mathcal{A}', T, pH)$ and $\rho_{col}(T)$ which seem to be defined better in a general way adequate for DS-PEC and SC-PEC which in our case do not depend on wave length during thermo-kinetic formulation (since they are derived from the coupling with a photonic density). Hence in this chapter, we will not follow the standardized definitions of IUPAC community in order to remain coherent with the thermo-kinetic coupling developed earlier.

To consider the wavelength in the calculation of energy efficiency, we define an energy yield η_{spec} considering the energy loss of photons which their wavelength is lower than the theoretical useful gap for water photolysis $\Delta V = 1.23 \text{ eV}$:

$$\eta_{spec} = \frac{\int_{\lambda_{min}}^{\lambda_{max}} w_{\lambda} \lambda \, d\lambda}{\lambda_{abs} \int_{\lambda_{min}}^{\lambda_{max}} w_{\lambda} \, d\lambda} = \frac{\lambda_{m,w}}{\lambda_{abs}} \quad (2.97)$$

In this general relation, the wavelength λ_{abs} is limited to the maximum thermodynamic value λ_{gap} if there is no limitation by absorption. However, if the process is limited by the absorption of a chromophore or a semiconductor, we consider this loss by a yield $\eta_{gap} = \lambda_{abs}/\lambda_{gap}$ (see further) in calculation of the overall efficiency of the cell.

Finally, as we have seen earlier, we need to take into account the loss of efficiency due to the use of a bias η_{bias} if it is necessary to use one. The accurate expression of this performance will be clearly defined while the entropic analysis presented in section 2.5.5.b will be formalized.

Hence, from Equation 2.87 in which we select only the thermo-kinetic yield ρ_i to which we simply add the thermodynamic efficiencies (purely energy conversion) η_j , we obtain a predictive expression of thermodynamic efficiency of a photo-electrochemical cell as:

$$\langle \eta_{PEC} \rangle = \eta_{spec} \eta_{bias} \eta_{gap} \rho_{cat}(T, pH) \rho_{c, mass}(T) \rho_{A, mass}(T) \rho_{max}(T) \langle \rho_{col}(\vec{x}_0, T) f(\vec{x}_0, \mathcal{A}', T, pH) \rangle \quad (2.98)$$

In which we have used $\langle \rangle = \frac{1}{v} \int_v d\vec{x}_0$.

Assuming that the resistances imposed by mass transfer are negligible or controlled and that the catalysis at the cathode is not limiting in the cell, we obtain a reduced expression which contains all the remaining not negligible physical phenomena (radiative transfer and charge transport) as well as photo-catalysis that we will probably never make it sufficiently efficient at high density of radiant absorbed energy absorbed (even the nature itself has failed to do):

$$\langle \eta_{PEC} \rangle = \eta_{spec} \eta_{bias} \eta_{gap} \rho_{max}(T) \langle \rho_{col}(\vec{x}_0, T) f(\vec{x}_0, \mathcal{A}', T, pH) \rangle \quad (2.99)$$

This relation can be used to introduce the ideal performances of photo-electrochemical cells by considering that at theoretical optimum $\eta_{bias} \rightarrow 1$ and $\langle \rho_{col}(\vec{x}_0, T) f(\vec{x}_0, \mathcal{A}', T, pH) \rangle \rightarrow 1$. Obviously, to compare the thermodynamic efficiencies with other solar processes, it is necessary to use a relationship that takes into account the optical losses in the device η_τ and the partial utilisation of the solar spectrum, with the efficiencies already defined as:

$$\eta_{th} = \eta_{TOT} \eta_{sun} = \langle \eta_{PEC} \rangle \eta_\tau \eta_{sun} = \langle \eta_{PEC} \rangle \frac{\langle A \rangle \int_{\lambda=0.3 \mu m}^{\lambda_{max}} W_\lambda d\lambda}{q_\odot a_{light} \int_{\lambda=0.3 \mu m}^{\lambda=4 \mu m} W_\lambda d\lambda} \quad (2.100)$$

d. Establishment of current-voltage relations in the PEC.

Although the current density $\langle j \rangle$ (or the current i) is the relevant data in a photoelectrochemical cell (directly related to the rate of hydrogen production), it is essential to connect via the model this current to electrode potentials. Indeed, on the one hand, numerous analogous information or knowledge can be derived from electrochemical studies, where the current is measured by imposing the voltage (voltammetry) or vice versa (amperometry), and on the other hand, we saw that the thermodynamics of the cell, at the equilibrium or out of equilibrium, requires knowing the potential of the anode and the cathode (which experimentally

demands a 3-electrode assembly) and also for estimation of bias in the calculation of the thermodynamic efficiency.

The maximum overall potential of the cell (by potential here we mean the potential difference) in the absence of current (open circuit) can be estimated from the Equations 2.90-2.91, providing the potential of the anode E_F and the cathode E_{redox} :

$$(\Delta U_{cell})_{max} = \Delta U_{OC} = \frac{1}{e} (E_F - E_{redox}) \quad (2.101)$$

Similarly, it is possible to estimate the maximum current density at short circuit from the theoretical expression giving the current at the anode from the spectral incident photon flux density on the cell $q'_{\gamma,\lambda}$ (real initial condition):

$$\begin{aligned} < j_{max} > = < j_{CC} > \\ &= \frac{\varphi \mathcal{F}}{S_{light}} \rho_{A, mass}(T) \rho_{max}(T) \int_v d\vec{x}_0 \int_{\lambda} d\lambda \mathcal{A}'_{\lambda}(\vec{x}_0) \rho_{col}(\vec{x}_0, T) f(\vec{x}_0, \mathcal{A}', T, pH) \end{aligned} \quad (2.102)$$

In general case, in real conditions out of equilibrium and under illumination, the current density and the potential are connected by theoretical relationships resulting from the Marcus-Hush theory which can, under certain simplifying assumptions be reduced to the law of Butler-Volmer in our case. Therefore, outside of equilibrium (electrode potential $\Delta U_{electrode} \neq 0$ comparing to the equilibrium), and if we work on each electrode with a low bias, the current density $< j >$ can be expressed as a function of the charge transfer overvoltage $\Delta U_{electrode}$ and a transfer coefficient α from (Bard and Faulkner, 2001):

$$< j > = < j_0 > \left[\exp\left(\frac{\alpha z_i \mathcal{F} \Delta U_{electrode}}{RT}\right) - \exp\left(\frac{(1 - \alpha) z_i \mathcal{F} \Delta U_{electrode}}{RT}\right) \right] \quad (2.103)$$

where $< j_0 >$ is the current density of exchange.

This relation is no longer applicable if the electrode functioning is limited by mass transfer (in that case we have direct proportionality between mass transfer and current).

The overall potential of the photo-electrochemical cell can be written in a more direct way (taking into account any possible overvoltage at each electrode, in particular for the proper positioning of the potential):

$$\Delta U_{cell}(i) = \Delta U_{anode}(i) - \Delta U_{cathode}(i) + R_{elec}i = U_{eq,anode}(i) - U_{eq,cathode}(i) + R_{elec}i + |\Delta U_{anode}(i) + \Delta U_{cathode}(i)| \quad (2.104)$$

Where R_{elec} is the resistance of the electrolyte.

2.5.6 Conclusions about knowledge model developments

Most of this chapter has helped to explain the structure of a knowledge model of PEC based on the calculation of the radiation field in a photo-anode as well as thermo-kinetics coupling with this field and the associated calculation of the thermodynamic efficiencies. We showed that the model could be written in the form of an elegant and concise integral formulation that allows a clear and appropriate definition of the model parameters on a physicochemical basis without any ambiguity. It also allows reconciliation between thermo-kinetic and energy approaches within a global coherence.

It obviously remains to refine a number of choices in the scales of limiting phenomena description. These choices will be made depending on the underlying capacity to reify the model parameters, an imperative step if we want to use it for the design and the optimization. This reification requires significant goings and comings with the experimental work in cells developed during the laboratory studies.

References

- Bădescu, V., 2000. Thermodynamics of Solar Energy Conversion into Work, in: Thermodynamics of Energy Conversion and Transport. Springer New York, New York, NY, pp. 14–48. https://doi.org/10.1007/978-1-4612-1286-7_2
- Bak, T., Nowotny, J., Rekas, M., Sorrell, C.C., 2002. Photo-electrochemical hydrogen generation from water using solar energy. Materials-related aspects. *Int. J. Hydrogen Energy* 27, 991–1022. [https://doi.org/10.1016/S0360-3199\(02\)00022-8](https://doi.org/10.1016/S0360-3199(02)00022-8)
- Bard, A.J., Faulkner, L.R., 2001. *Electrochemical Methods: Fundamentals and Applications*, Analytica Chimica Acta. <https://doi.org/10.1016/j.aca.2010.06.020>
- Barnes, P.R.F., Anderson, A.Y., Durrant, J.R., Regan, B.C.O., 2011. Simulation and measurement of complete dye sensitised solar cells : Including the influence of trapping , electrolyte , oxidised dyes and light intensity on steady state and transient device behaviour Example of cell showing similar non-ideality for trans 2–4.
- Barsoukov, E., Macdonald, J.R. (James R., 2005. *Impedance spectroscopy : theory, experiment, and applications*.
- Bejan, A., 2006. *Advanced Engineering Thermodynamics*, America.
- Bejan, A., 1987. Unification of Three Different Theories Concerning the Ideal Conversion of Enclosed Radiation. *J. Sol. Energy Eng.* 109, 46–51. <https://doi.org/10.1115/1.3268177>
- Bisquert, J., 2008. Interpretation of electron diffusion coefficient in organic and inorganic semiconductors with broad distributions of states. *Phys. Chem. Chem. Phys.* 10, 3175–94. <https://doi.org/10.1039/b719943k>
- Bisquert, J., 2004. Chemical diffusion coefficient of electrons in nanostructured semiconductor electrodes and dye-sensitized solar cells. *J. Phys. Chem. B* 108, 2332. <https://doi.org/10.1021/jp035397i>
- Bisquert, J., 2004. Chemical Diffusion Coefficient of Electrons in Nanostructured Semiconductor Electrodes and Dye-Sensitized Solar Cells. *J. Phys. Chem. B* 108, 2323–2332. <https://doi.org/10.1021/jp035397i>
- Bisquert, J., 2003. Chemical capacitance of nanostructured semiconductors: its origin and significance for nanocomposite solar cells. *Phys. Chem. Chem. Phys.* <https://doi.org/10.1039/b310907k>
- Bisquert, J., 2002. Theory of the impedance of electron diffusion and recombination in a thin layer. *J. Phys. Chem. B* 106, 325–333. <https://doi.org/10.1021/jp011941g>
- Bisquert, J., Zaban, A., Greenshtein, M., Mora-Seró, I., 2004. Determination of rate constants for charge transfer and the distribution of semiconductor and electrolyte electronic energy levels in dye-sensitized solar cells by open-circuit photovoltage decay method. *J. Am. Chem. Soc.* 126, 13550–13559. <https://doi.org/10.1021/ja047311k>
- Burkhard, G.F., Hoke, E.T., McGehee, M.D., 2010. Accounting for interference, scattering, and electrode absorption to make accurate internal quantum efficiency measurements in organic and other thin solar cells. *Adv. Mater.* 22, 3293–3297. <https://doi.org/10.1002/adma.201000883>
- Chen, P.C., Rothenberger, G., Grätzel, M., 2008. The Influence of Particle Sizes on the Optical

- Characteristics of Nanocrystalline TiO₂ Films for Dye-Sensitized Solar Cells. *Mater. Res.* 1101, 6.
- Cook, G., Dickerson, R.H., 1995. UNDERSTANDING THE CHEMICAL-POTENTIAL. *Am. J. Phys.* 63, 737–742. <https://doi.org/10.1119/1.17844>
- Cornet, J.-F., 2005. Theoretical Foundations and Covariant Balances for Chemical Engineering Applications with Electromagnetic Field. *Chem. Eng. Commun.* 192, 647–666. <https://doi.org/10.1080/009864490510635>
- Cornet, J.F., 2010. Calculation of optimal design and ideal productivities of volumetrically lightened photobioreactors using the constructal approach. *Chem. Eng. Sci.* 65, 985–998. <https://doi.org/10.1016/j.ces.2009.09.052>
- Cornet, J.F., 2007. Procédés Limités par le Transfert de Rayonnement en Milieu Hétérogène Étude des Couplages Cinétiques et Énergétiques dans les Photobioréacteurs par une Approche Thermodynamique. Université Blaise Pascal, Clermont-Fd II, Clermont-Ferrand.
- Cornet, J.F., Aukauloo, A., Gloaguen, F., Leibl, W., 2015. Ingénierie de la photosynthèse artificielle : verrous et perspectives - L'Actualité Chimique [WWW Document]. *L'Actualité Chim.* URL <http://www.lactualitechimique.org/Ingenierie-de-la-photosynthese-artificielle-verrous-et-perspectives>
- Cornet, J.F., Dussap, C.G., 2009. A simple and reliable formula for assessment of maximum volumetric productivities in photobioreactors. *Biotechnol. Prog.* 25, 424–435. <https://doi.org/10.1002/btpr.138>
- Cornet, J.F., Dussap, C.G., Gros, J.B., 1994. Conversion of Radiant Light Energy in Photobioreactors. *AIChE J.* 40, 1055–1066. <https://doi.org/10.1002/aic.690400616>
- Elalamy, Z., Drouard, E., Govern, T.M., Escoubas, L., Simon, J.J., Flory, F., 2004. Thermo-optical coefficients of sol-gel ZrO₂ thin films. *Opt. Commun.* 235, 365–372. <https://doi.org/10.1016/j.optcom.2004.02.043>
- Fabregat-santiago, F., Bisquert, J., Garcia-Belmonte, G., Boschloo, G., Hagfeldt, A., 2005. Influence of electrolyte in transport and recombination in dye-sensitized solar cells studied by impedance spectroscopy. *Sol. Energy Mater. Sol. Cells* 87, 117–131. <https://doi.org/10.1016/j.solmat.2004.07.017>
- Fabregat-Santiago, F., Bisquert, J., Garcia-Belmonte, G., Boschloo, G., Hagfeldt, A., 2005. Influence of electrolyte in transport and recombination in dye-sensitized solar cells studied by impedance spectroscopy. *Sol. Energy Mater. Sol. Cells* 87, 117–131. <https://doi.org/10.1016/j.solmat.2004.07.017>
- Fabregat-Santiago, F., Bisquert, J., Palomares, E., Otero, L., Kuang, D., Zakeeruddin, S.M., Gratzel, M., 2007. Correlation between Photovoltaic Performance and Impedance Spectroscopy of Dye-Sensitized Solar Cells Based on Ionic Liquids. *J. Phys. Chem. C* 111, 6550–6560. <https://doi.org/10.1021/jp066178a>
- Fabregat-Santiago, F., Garcia-Belmonte, G., Bisquert, J., Zaban, A., Salvador, P., 2002. Decoupling of transport, charge storage, and interfacial charge transfer in the nanocrystalline TiO₂/electrolyte system by impedance methods. *J. Phys. Chem. B* 106, 334–339. <https://doi.org/10.1021/jp0119429>
- Fabregat-Santiago, F., Garcia-Belmonte, G., Mora-Seró, I., Bisquert, J., 2011. Characterization of nanostructured hybrid and organic solar cells by impedance spectroscopy. *Phys. Chem.*

- Chem. Phys. 13, 9083–9118. <https://doi.org/10.1039/c0cp02249g>
- Flory, F., Escoubas, L., 2004. Optical properties of nanostructured thin films. *Prog. Quantum Electron.* 28, 89–112. <https://doi.org/10.1016/j.pquantelec.2003.09.002>
- Gray, J.L., 2005. The Physics of the Solar Cell, in: *Handbook of Photovoltaic Science and Engineering*. John Wiley & Sons, Ltd, Chichester, UK, pp. 61–112. <https://doi.org/10.1002/0470014008.ch3>
- Groot, S.R. de (Sybren R., Mazur, P. (Peter), 1984. *Non-equilibrium thermodynamics*. Dover Publications.
- Grundmann, M., 2010. *The physics of semiconductors: an introduction including nanophysics and applications (hardback)(series: graduate texts in physics)*, Science. <https://doi.org/10.1007/978-3-642-13884-3>
- Halme, J., Boschloo, G., Hagfeldt, A., Lund, P., 2008. Spectral characteristics of light harvesting, electron injection, and steady-state charge collection in pressed TiO₂ dye solar cells. *J. Phys. Chem. C* 112, 5623–5637. <https://doi.org/10.1021/jp711245f>
- Halme, J., Vahermaa, P., Miettunen, K., Lund, P., 2010. Device physics of dye solar cells. *Adv. Mater.* 22, E210–34. <https://doi.org/10.1002/adma.201000726>
- Harland G. Tompkins, W.A.M., 1999. *Wiley: Spectroscopic Ellipsometry and Reflectometry: A User's Guide - Harland G. Tompkins, William A. McGahan*. Wiley, New York.
- Herrmann, F., Würfel, P., 2005. Light with nonzero chemical potential. <https://doi.org/10.1119/1.1904623>
- Hoshikawa, T., Yamada, M., Kikuchi, R., Eguchi, K., 2005. Impedance analysis for dye-sensitized solar cells with a three-electrode system. *J. Electroanal. Chem.* 577, 339–348.
- Jacoboni, C., Lugli, P., 1989. *The Monte Carlo Method for Semiconductor Device Simulation, Computational Microelectronics*. Springer Vienna, Vienna. <https://doi.org/10.1007/978-3-7091-6963-6>
- Jörg, F., Luther, J., 2001. Modeling of Photovoltage and Photocurrent in Dye-Sensitized Titanium Dioxide Solar Cells. <https://doi.org/10.1021/JP002928J>
- K. Sivula M. Gratzel, F.L.F., 2011. Solar Water Splitting: Progress Using Hematite (α-Fe₂O₃) Photoelectrodes. *ChemSusChem* 4, 432–449. <https://doi.org/10.1002/cssc.201000416>
- Kern, R., Sastrawan, R., Ferber, J., Stangl, R., Luther, J., 2002. Modeling and interpretation of electrical impedance spectra of dye solar cells operated under open-circuit conditions. *Electrochim. Acta* 47, 4213–4225. [https://doi.org/10.1016/S0013-4686\(02\)00444-9](https://doi.org/10.1016/S0013-4686(02)00444-9)
- Klahr, B., 2012. Water oxidation at hematite photoelectrodes: The role of surface states. *J. Am. Chem. Soc.* 134, 4294–4302.
- Klahr, B., Gimenez, S., Fabregat-Santiago, F., Bisquert, J., Hamann, T.W., 2012a. Photoelectrochemical and impedance spectroscopic investigation of water oxidation with “co-Pi”-coated hematite electrodes. *J. Am. Chem. Soc.* 134, 16693–16700. <https://doi.org/10.1021/ja306427f>
- Klahr, B., Gimenez, S., Fabregat-Santiago, F., Bisquert, J., Hamann, T.W., 2012b. Electrochemical and photoelectrochemical investigation of water oxidation with hematite electrodes. *Energy Environ. Sci.* <https://doi.org/10.1039/c2ee21414h>

- Klahr, B., Gimenez, S., Fabregat-Santiago, F., Hamann, T., Bisquert, J., 2012c. Water oxidation at hematite photoelectrodes: The role of surface states. *J. Am. Chem. Soc.* 134, 4294–4302. <https://doi.org/10.1021/ja210755h>
- Koide, N., Islam, A., Chiba, Y., Han, L., 2006. Improvement of efficiency of dye-sensitized solar cells based on analysis of equivalent circuit. *J. Photochem. Photobiol. A Chem.* 182, 296–305. <https://doi.org/10.1016/j.jphotochem.2006.04.030>
- Landsberg, P.T., 1991. Recombination in semiconductors. Cambridge Univ. Press.
- Listorti, A., O'Regan, B., Durrant, J.R., 2011. Electron Transfer Dynamics in Dye-Sensitized Solar Cells. *Chem. Mater.* 23, 3381–3399. <https://doi.org/10.1021/cm200651e>
- Lopes, T., Andrade, L., Le Formal, F., Grätzel, M., Sivula, K., Mendes, A., 2014. Hematite photoelectrodes for water splitting: evaluation of the role of film thickness by impedance spectroscopy. *Phys. Chem. Chem. Phys.* 16, 16515–16523. <https://doi.org/10.1039/c3cp55473b>
- Loveday, D., Peterson, P., Rodgers, B., 2004. Evaluation of Organic Coatings with Electrochemical Impedance Spectroscopy Part 1: Fundamentals of Electrochemical Impedance Spectroscopy. *JCT coatings tech.*
- Memming, R., Wiley InterScience (Online service), 2001. Semiconductor electrochemistry. Wiley-VCH.
- Meyer, T.J.J., Markvart, T., 2009. The chemical potential of light in fluorescent solar collectors. *J. Appl. Phys.* 105. <https://doi.org/10.1063/1.3097328>
- Monestier, F., Pandey, A.K., Simon, J.J., Torchio, P., Escoubas, L., Nunzi, J.M., 2007. Optical modeling of the ultimate efficiency of pentacene: N, N'-ditridecylperylene-3, 4, 9, 10-tetracarboxylic diimide-blend solar cells. *J. Appl. Phys.* 102. <https://doi.org/10.1063/1.2767619>
- Mouí, A.J., Snaith, H.J., Kaiser, M., Klesper, H., Huang, D.M., Grätzel, M., Meerholz, K., 2009. Optical description of solid-state dye-sensitized solar cells. I. Measurement of layer optical properties. *J. Appl. Phys.* 106. <https://doi.org/10.1063/1.3204982>
- Parkinson, B., 1984. On the efficiency and stability of photoelectrochemical devices. *Acc. Chem. Res.* 17, 431–437. <https://doi.org/10.1021/ar00108a004>
- Pettersson, L.A.A., Roman, L.S., Inganas, O., 1999. Modeling photocurrent action spectra of photovoltaic devices based on organic thin films. *J. Appl. Phys.* 86, 487–496.
- Riha, S.C., Klahr, B.M., Tyo, E.C., Seifert, S., Vajda, S., Pellin, M.J., Hamann, T.W., Martinson, A.B.F., 2013. Atomic layer deposition of a submonolayer catalyst for the enhanced photoelectrochemical performance of water oxidation with hematite. *ACS Nano* 7, 2396–2405. <https://doi.org/10.1021/nn305639z>
- Rothenberger, G., Comte, P., Grätzel, M., 1999. Contribution to the optical design of dye-sensitized nanocrystalline solar cells. *Sol. Energy Mater. Sol. Cells* 58, 321–336. [https://doi.org/10.1016/S0927-0248\(99\)00015-X](https://doi.org/10.1016/S0927-0248(99)00015-X)
- Ruppel, W., Würfel, P., 1980. Upper Limit for the Conversion of Solar Energy. *IEEE Trans. Electron Devices* 27, 877–882. <https://doi.org/10.1109/T-ED.1980.19950>
- Salvador, P., 2001. Semiconductors' Photoelectrochemistry: A Kinetic and Thermodynamic Analysis in the Light of Equilibrium and Nonequilibrium Models. <https://doi.org/10.1021/JP0033869>

- Sivula, K., Le Formal, F., Grätzel, M., 2011. Solar water splitting: progress using hematite (α -Fe(2) O(3)) photoelectrodes. *ChemSusChem* 4, 432–449. <https://doi.org/10.1002/cssc.201000416>
- Slattery, J.C., 1999. *Advanced Transport Phenomena*.
- Tavernier, F., Steyaert, M., 2011. High-Speed Optical Receivers with Integrated Photodiode in Nanoscale CMOS. Springer. <https://doi.org/10.1007/978-1-4419-9925-2>
- Tiedje, T., Yablonovitch, E., Cody, G.D., Brooks, B.G., 1984. Limiting efficiency of silicon solar cells. *IEEE Trans. Electron Devices* 31, 711–716.
- Villanueva, J., Anta, J.A., Guillén, E., Oskam, G., 2009. Numerical Simulation of the Current–Voltage Curve in Dye-Sensitized Solar Cells. *J. Phys. Chem. C* 113, 19722–19731. <https://doi.org/10.1021/jp907011z>
- Wang, Q., Ito, S., Grätzel, M., Fabregat-Santiago, F., Mora-Seró, I., Bisquert, J., Bessho, T., Imai, H., 2006. Characteristics of high efficiency dye-sensitized solar cells. *J. Phys. Chem. B* 110, 25210–25221. <https://doi.org/10.1021/jp064256o>
- Wang, Q., Moser, J.-E., Grätzel, M., 2005. Electrochemical impedance spectroscopic analysis of dye-sensitized solar cells. *J. Phys. Chem. B* 109, 14945–53. <https://doi.org/10.1021/jp052768h>
- Wenger, S., Schmid, M., Rothenberger, G., Gentsch, A., Grätzel, M., Schumacher, J.O., 2011. Coupled optical and electronic modeling of dye-sensitized solar cells for steady-state parameter extraction. *J. Phys. Chem. C* 115, 10218–10229. <https://doi.org/10.1021/jp111565q>
- Whitaker, S., 1977. Simultaneous Heat, Mass, and Momentum Transfer in Porous Media: A Theory of Drying. *Adv. Heat Transf.* 13, 119–203. [https://doi.org/10.1016/S0065-2717\(08\)70223-5](https://doi.org/10.1016/S0065-2717(08)70223-5)
- Wurfel, P., 1982. The chemical potential of radiation. *J. Phys. C Solid State Phys.* 15, 3967–3985. <https://doi.org/10.1088/0022-3719/15/18/012>
- Zhang, Z., Yates, J.T., 2012. Band Bending in Semiconductors: Chemical and Physical Consequences at Surfaces and Interfaces. *Chem. Rev.* 112, 5520–5551. <https://doi.org/10.1021/cr3000626>

The Climbing



Hidden in the rocks, Van Gogh

Contents

Chapter 3	Materials and methods.....	99
3.1	Introduction	99
3.2	Optical devices and characterization methods.....	100
3.2.1	Light sources	100
3.2.2	Black Box.....	108
3.2.3	Transmission and reflection measurements with a high accuracy optical bench	109
3.3	Electrochemical materials.....	110
3.3.1	Commercial dye sensitized solar cell	111
3.3.2	Photo-electrochemical cell (Minucell)	112
3.4	System configuration	123
3.4.1	General presentation.....	123
3.4.2	Electrochemical instrumentation	124
3.5	Electrochemical measurement methods.....	127
3.5.1	jV (current-voltage) curve polarization	127
3.5.2	Open circuit voltage	128
3.5.3	Cyclic voltammetry	128
3.5.4	Chronoamperometry.....	129
3.5.5	Potentiostatic Electrochemical Impedance Spectroscopy (PEIS).....	129
3.6	Conclusion	131

Chapter 3

Materials and methods

3.1 Introduction

The comprehensive study of photo-electrochemical cells continues with experimental investigation accomplished by the fabrication of a complete photo-electrochemical cell in order to implement bioinspired molecular catalyst in photo-electrochemical experiments. In this present chapter we explain all the characterisation methods used during this thesis to understand all photo-devices which has been developed by our team or has been purchased due to their similarities to our system of study so that the obtained results could be used as a reference for our new developed prototype. Consequently, all these methods and devices have been divided in three categories by their domain of usage:

- optical devices and related methods,
- electrode deposition analysis,
- electrochemical techniques and devices.

Electrochemical experiment results will be specifically overviewed further in chapter 4 of this document.

3.2 Optical devices and characterization methods

Optical devices include all light sources used for illuminating during experiences. On the other hand, all metering and sensor devices to measure photon flux density are presented together with devices such as integrating sphere and spectrofluorometer used to measure transmittance and reflectance.

3.2.1 Light sources

Two types of light sources have been used in this work: a solar simulator which provides a lightening similar to sunlight with all range of solar spectrum and two light emitting diode panels, one providing blue monochromatic light and the other providing a white colour illumination.

3.2.1.1 Solar simulator

A solar simulator is designed to generate an illumination equivalent to a sun with the same energy and spectral distribution. In this thesis as we consider working at visible light, an arc lamp power supply has been utilized to make the possibility of working in visible spectrum. The «Universal Arc Lamp Power Supply» (model 69920, Oriel) 450 W solar simulator 4*4' Oriel ref: nr 91195) supplies the electric power to the solar simulator (model 91195, Oriel).



Figure 3.1 Arc lamp power supply model: 69920 and solar simulator with xenon lamps. It supplies constant and adjustable illumination. Several filters can be applied to obtain the illumination with or without a specified wavelength. A ventilation system is also considered for cooling system.

The regulation is possible through a computer interface (and optional IEEE-488), which permits to set the lamp parameters, to control the light output even before the start up the device.

During the use of the solar simulator, an important amount of infra-red radiation is emitted; we were facing fast temperature rises of the electrolyte used in the PEC. (as our cell is still not equipped with internal temperature regulation), we therefore decided to consider using solar simulator in further work but not during in this present thesis. As a result, the light emitting diode (LED) panels have been used as the light source in our experiments.

3.2.1.2 Light Emitting Diode panel (LED)

A LED is a p-n junction diode which dispatches light when an appropriate voltage is applied and subsequently a current overpass the junction. It produces a monochromatic collimated radiation as a consequence of the energy transformation by recombination of an electron and a hole in a semiconductor. The wavelength of the emitted radiation and so its colour is determined by the photonic band gap energy of the applied material. All values of the visible spectrum can be achieved with prevalent materials.

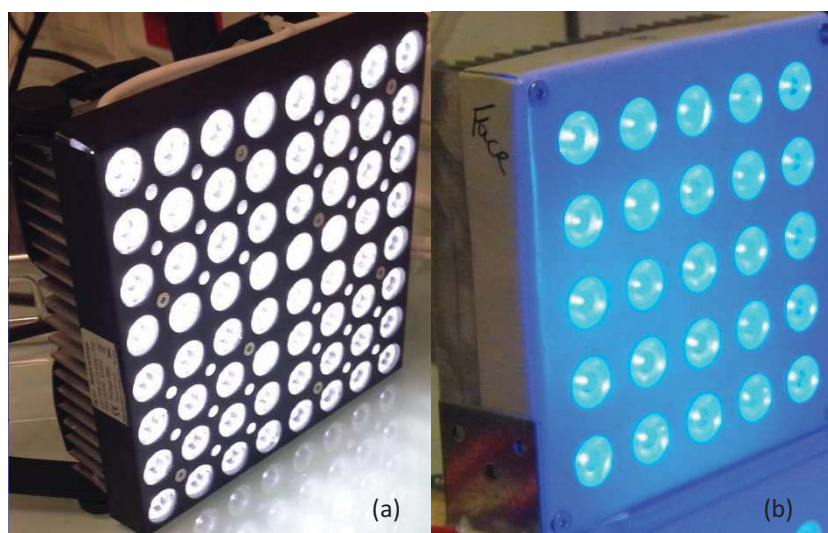


Figure 3.2 (a) White LED panel with 64 LEDs on the surface of $154 \times 154 \text{ mm}^2$ with emitting $500 \mu\text{mole}_{h\nu} \cdot \text{m}^{-2} \cdot \text{s}^{-1}$ at its maximum power. (b) Blue LED panel consisted of 25 LEDs spread out over the area of $114 \times 114 \text{ mm}^2$ with the maximum power of emitting $2864 \mu\text{mole}_{h\nu} \cdot \text{m}^{-2} \cdot \text{s}^{-1}$. All measurements have been carried out at the distance of 15 cm of each panel in order to have a homogeneous illumination on the area of interest.

In the course of this work two LED panels, emitting blue and white light, have been used. They were manufactured by the Sybilux company.

The white LED panel is composed of 64 LEDs distributed on a surface of $154 \times 154 \text{ mm}^2$. The white LED has been used in order to have a polychromatic emission spectrum in the visible spectrum (between 400 and 750 nm) with negligible temperature augmentation comparing to the use of the solar simulator. The emission spectrum of the white LED (see figure 3.3) indicates

it is composed of a blue LED and a yellow phosphor, these two complementary colours combine to form white light.

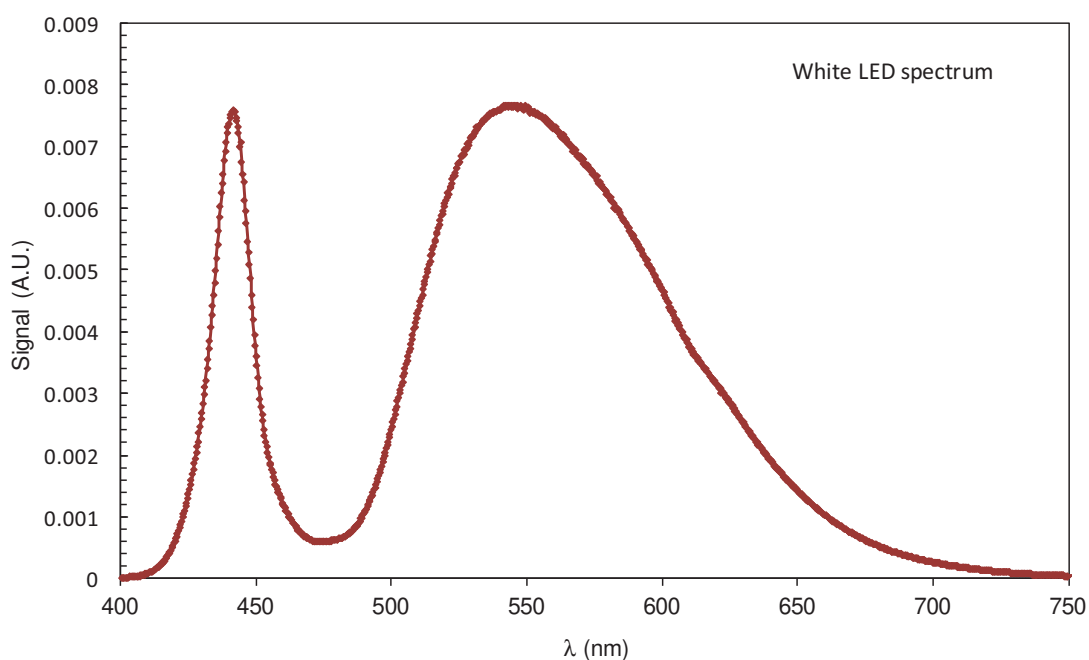


Figure 3.3 White LED panel spectrum. It provides white visible light between 400 and 750 nm. The graph is obtained by using a USB 2000+ spectrometer (Ocean Optics) associated by an optical fibre and cosine corrector.

Even the white LED provides quite the same photon flux density as the blue one, but all of these photons are not emitted at the wavelengths in which the best absorption by dye or chromophore molecules occurs.

So it has been interesting to test also a monochromatic blue LED since the spectrum results of chromophore and dye molecules show that their best absorption take place at 460 nm which corresponds to the blue region of visible spectrum; so using a blue LED permits to study other aspects of photo-process with considering that the light absorption of the system is optimal.

The blue LED panel is composed of 25 LED (Royal blue D42180, Seoul Semiconductor) equipped with lenses. It provides a blue light with an emission maximum at 457 nm wavelength (see figure 3.4), on a 12.5×12.5 cm surface.

Both white and blue LEDs provide a homogenous light at the surface of interest starting from the distance of 15 cm of the panel.

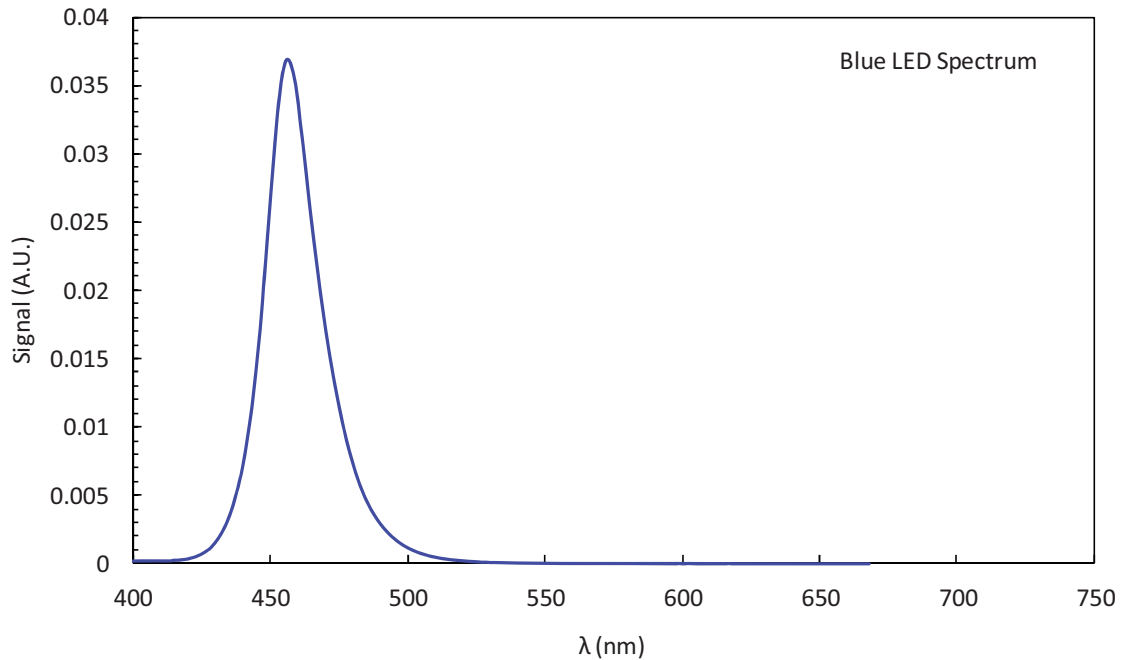


Figure 3.4 Blue LED panel spectrum. It provides blue visible light at around 460 nm. The graph is obtained by using an USB 2000+ spectrometer (Ocean Optics) associated by an optical fibre and cosine corrector.

Such light sources have been adopted for ease of use and post treatment. Indeed, the photon flux density can be easily and accurately controlled via an U9 USB DMX controller and the Easy Stand Alone software (Nicolaudie), including 256 different setting positions to modify the electric power supplied to the LED and thus the photon flux density.

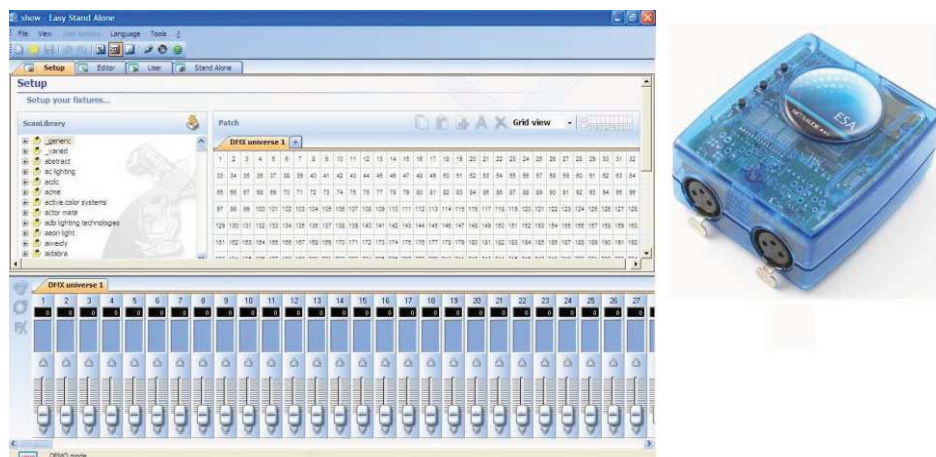


Figure 3.5. Picture of ESA Pro software and U9 Standalone controller. The software permits to adjust the light intensity. The controller box makes the connection between software and LED panel. The light intensity varies by displacing the cursor along the corresponding port (several ports are considered in the software, but one of them has action on the panel).

The software settings are not a correct measure to quantify the photon flux density. Hence several measurement methods have been used to quantify the photon flux density emitted by

the LED at each cursor placement. The simpler physical method is to use quantum sensor. Otherwise more complicated methods such as chemical actinometry can be utilized.

(a)- Spectrometer

We used the spectrometer USB 2000+ sold by Ocean Optics to obtain the spectral intensity diagram of the LED panels as they are presented in Figures 3.3 and 3.4 for white and blue panels respectively. It is associated with premium-grade optical fibre patch cords (QP400-2-SR, Ocean Optics) and an optical diffuser, Cosine Corrector (CC-3-UV-S, Ocean Optics) to collect signal from 180° field of view. Cosine correctors are configurations in which it is needed to redistribute the incident light, for example for measuring spectral irradiance of a plane surface in a specified media (Ocean optics, 2015).

(b)- Estimation of photon flux density by quantum sensors

A hemispherical quantum sensor (LiCor, Li-190SA as shown in Figure 3.6) linked to a Li-189 display has been used to measure the photon flux density arriving to the point of measurements.



Figure 3.6 Flat panel sensor, LiCor, Li-190SA is able to measure directly the micromole of photons. The measured micromole of photons with flat sensor corresponds to hemispheric photon flux.

We hence accomplished light intensity measurements at six different panel's intensity which corresponds to the cursor setting at 15, 50, 100, 150, 200, and 250 in the software. For each cursor setting the photon flux density (PFD) is quantified on a plane located at a 15 cm distance from the panel. An average value of PFD is subsequently presented in terms of cursor's placement at Figures 3.7 and 3.8 for blue and white panels respectively.

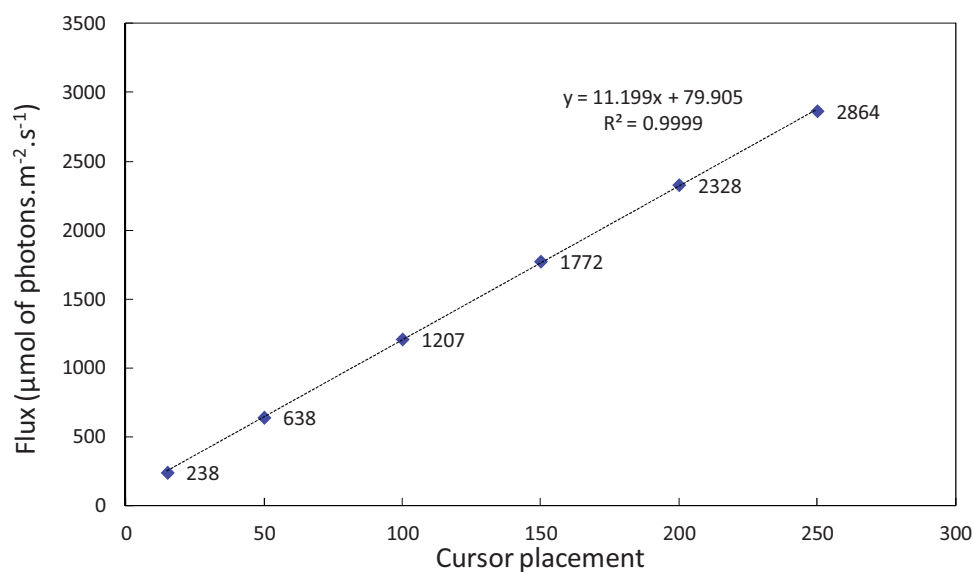


Figure 3.7 Blue LED photon emission measurements at the distance of 15cm of the LED panel at different photon flux densities by changing the LED intensity.

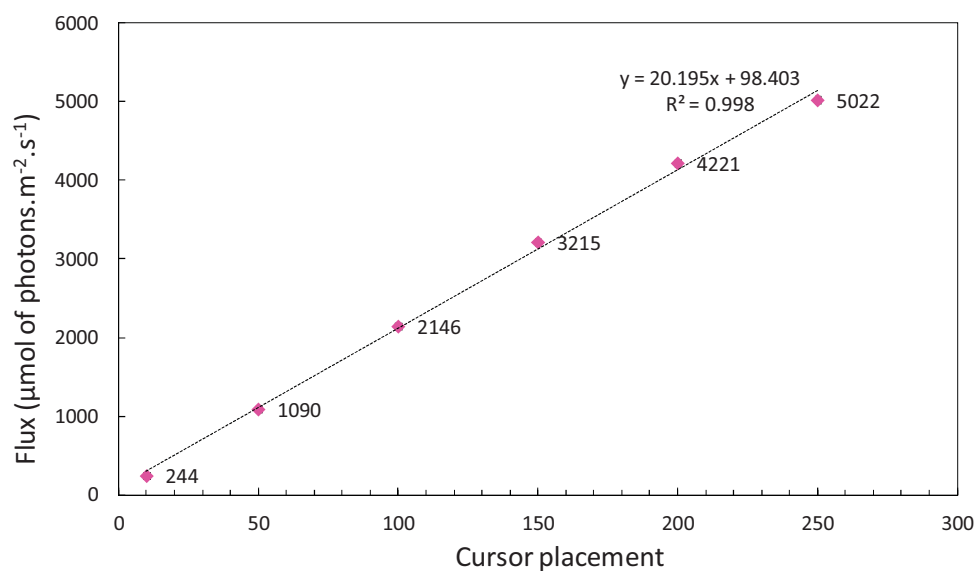


Figure 3.8 White LED photon emission measurements at the distance of 15cm of the LED panel at different photon flux densities by changing the LED intensity. The maximum panel intensity is higher than a sun ($\approx 2000 \mu\text{mol}_{\text{ph}}.\text{m}^{-2}.\text{s}^{-1}$).

With a fairly good approximation, the measured photon flux density changes linearly by changes in software. Note that we henceforth work only at these panel intensities for the rest of experiments during this thesis. It should also be considered that the white panel intensity is higher than blue panel but just a limited number of these photons with adequate energy will be involved in the reaction.

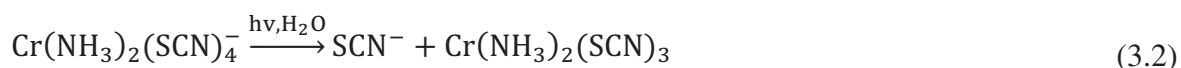
(c)- Estimation of photon flux density by actinometry

The actinometry is a chemical method to estimate photon flux densities, where a chemical actinometer undergoes a light-induced reaction (at a given wavelength λ) for which the quantum yield, Φ , as defined in equation 3.1, is accurately known. Measuring the reaction rate allows the direct estimation of photon absorption rate or of a mean integrated hemispherical photon flux density q_{ϕ} (instead of averaging measures obtained in several positions in the sensor method) or the calculation of the absorbed photon flux (Kuhn et al., 2004).

$$\Phi = \frac{\text{number of reacted molecules per time unit}}{\text{number of photons absorbed per time unit}} \quad (3.1)$$

It is important to use a monochromatic light source (the range in which the actinometer absorbs better) and an appropriate actinometer (Cornet et al., 1997).

The Reinecke's salt $[\text{Cr}(\text{NH}_3)_2(\text{SCN})_4]^-$ (supplied by Sigma Aldrich) has been chosen in this study as the actinometer as proposed by (Wegner and Adamson, 1966) and later modified by (Cornet et al., 1997). Its decomposition (Equation 3.2) with a constant quantum yield (equal to 0.31 in the blue LED emission spectrum), generates thiocyanate ions whose concentration can be determined spectrophotometrically, according to the protocol presented in (Cornet et al., 1997).



More details about the use of this actinometer can be found in the publication Rochatte et al. 2017. As already explained, the aim of this method is to accurately know the photons flux densities, this step allowed us to determine with confidence the boundary conditions of our system, i.e. the hemispherical photon flux density, $q_{\phi, \text{in}}$ (Rochatte et al., 2017).

Figure 3.9 gives a comparison of physic measurement by sensor and actinometry in a torus reactor for blue LED.

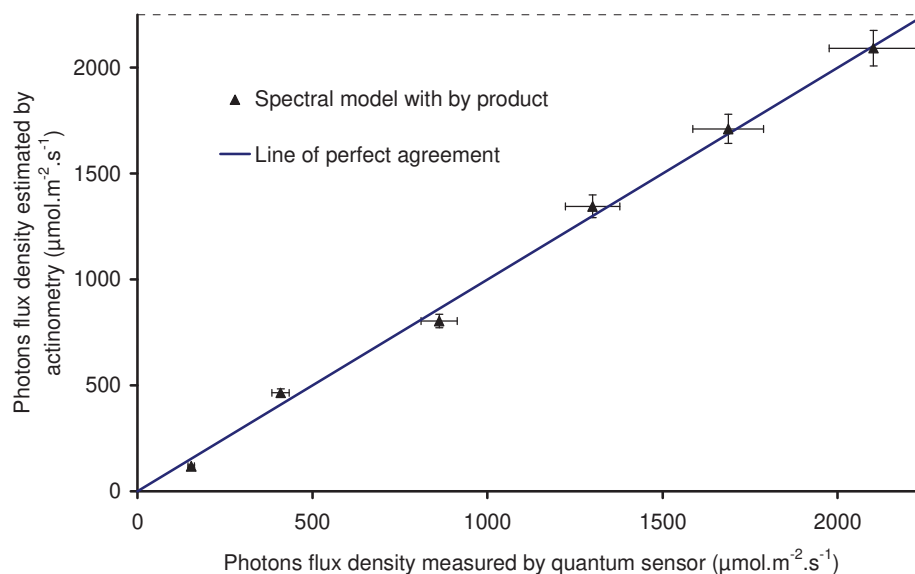
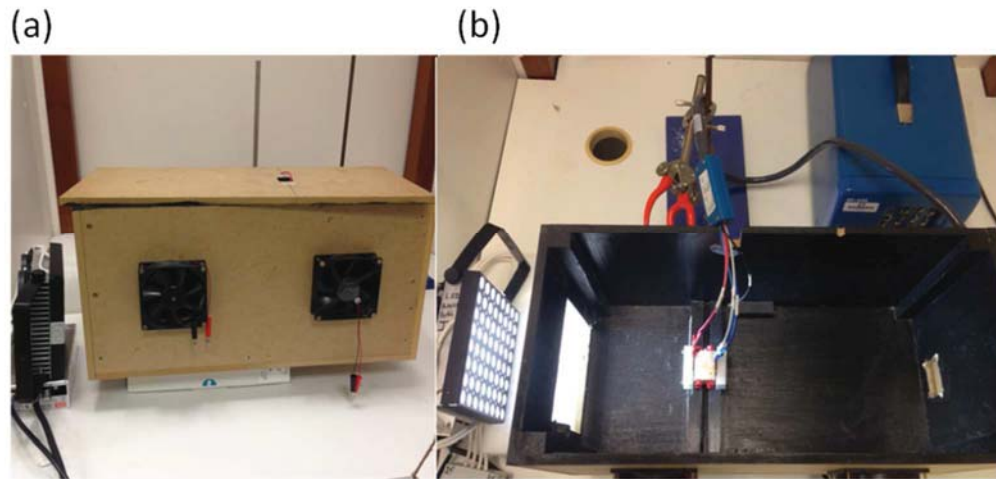


Figure 3.9 Parity chart of identified values of hemispherical photon flux density, q_{in} , obtained in actinometry and mean values measured by quantum sensor. The more the values from each method are close the trend line's slope has to approach to 1.

The values measured by sensor are presented on abscissa while the values quantified by actinometry are shown on ordinate (Parity plot). The results obtained by the two methods are in very good agreement. The slope, equal to 1.00 ± 0.04 , shows that the obtained values are close enough to say that both methods are reliable and that the photon flux density is accurately known. It gives us the confirmation to apply only the sensor method for white panel since the actinometry cannot be carried out in Minucell because of the small size of the cell.

3.2.2 Black Box

In order to avoid all stray lights from the environment, it was decided to position the PEC in an isolated compartment; we hence designed and constructed a box whose walls are painted in black (Figures 3.10).



Figures 3.10 The black box permits to protect the global system from stray illuminations. The temperature inside the box is regulated by ventilation system installed on the box. The light passage is also considered as well as camera path. The box has also a cover which completely isolates the system from its environment.

There are two fans embedded in the framework of the box on the opposite side for the LED and camera position (Figure 3.10(b)). A ventilation system (composed of two computer fans) has been installed on the box to keep the inner temperature equal to room temperature (Figure 3.10(a)). To check the efficiency of this cooling system, an experiment was carried out with temperature recording during one hour (Figure 3.11).

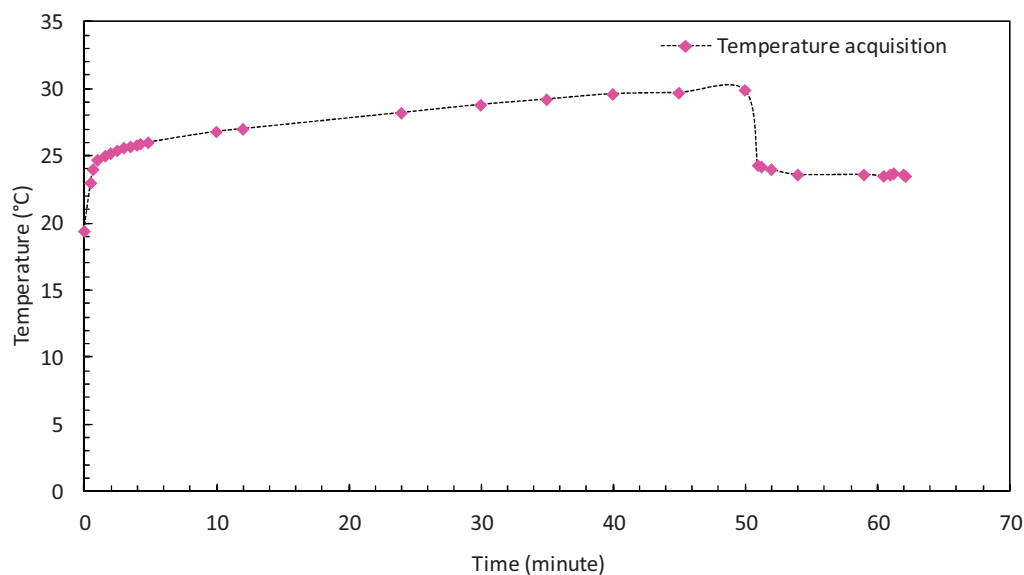


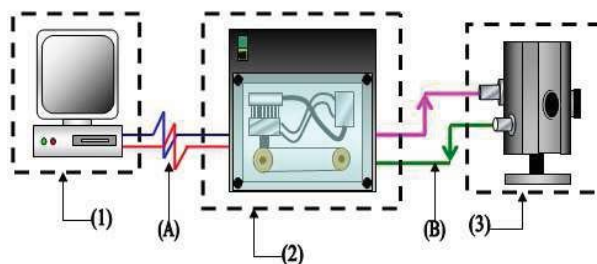
Figure 3.11 The first points are recorded while the LED is off. After one minute the LED panel is switched on and the inside temperature rises gradually. It reaches to an almost constant value of 30 °C. After turning on the ventilation system the inside temperature decreases to 23.5°C and then remains constant.

In Figure 3.11 we see the increment of temperature during 50 minutes when the LED panel is switched on; as soon as the ventilation system is started up (in the last 15 minutes of the experiment) the inner temperature dramatically drops. The temperature is stabilized at a 23.5°C value.

3.2.3 Transmission and reflection measurements with a high accuracy optical bench

To calculate the amount of absorbed radiation by electrode (electrodes composition and preparation are detailed in 3.3.2.1 of this chapter) we measured the transmittance and the reflectance of the electrodes by a high accuracy optical bench using an integrating sphere.

The integrating sphere is used in our experiments in order to specify the absorption coefficients which permit to identify optical properties of photoanode electrode. The device is developed by the SAFAS society (Monaco) and shown in Schema 3.1.



Schema 3.1 (1) The acquisition computer connected to (2) the spectrofluorometer FLX Xenius, consisting of a xenon lamp which supplies a collimated incident beam and send it to (3) the integrating sphere where it meets the sample and enter the sphere. The system provides the possibility of measuring the transmission and reflection of the beam for our electrodes. (A) is the connecting cable between the spectrofluorometer and acquisition PC. (B) the pink connection is the for sending the collimated incident beam into sphere and the green cable receives the beam after «nth» reflection and send it back to the spectrofluorometer and then to the acquisition PC.

The system consists of a spectrofluorometer FLX Xenius, with a high energy xenon lamp which provides a collimated incident beam through optical fibres and lenses. The beam afterward arrives to a sample which can be also placed directly on a metal support or in a special quartz case (width and height: 40 mm thickness: 3 mm or 10 mm, volume: 4.8 mL or 16 mL). The transmitted or reflected ray is totally captured by a large diameter integrating sphere (SAFAS, 2015).

An integrating sphere is an optical device composed of a spherical vacant cavity with several input and output ports. Its internal surface is covered with a white reflective coating so that the entering light beam hitting any point inside the sphere will be distributed homogeneously on the integral internal surface by numerous scattering reflections.

The integration sphere used in this work is provided by Labsphere with an internal diameter of 152 mm; coated with Spectralon[®] (pressed PTFE particles) that reflects over 99% of the incident radiation; it is equipped with a switch port for accurate measurement of reflection, with a trap by which it is possible to distinguish specular or diffuse reflection.

3.3 Electrochemical materials

In this part we present all electrochemical materials used in this work such as commercial DSSC prototype, Photo-electrochemical cell (Minucell) designed and fabricated by our laboratory team, electrodes preparation and also the whole methods used for photo-active layer deposition, analyse and understanding the structure and thickness of the electrode photoactive layer. Potentiostat and classic electrochemical methods are also described.

3.3.1 Commercial dye sensitized solar cell

Since dye-sensitized solar cell is a photo-electrochemical cell with a very similar concept to our envisaged prototype, it was logical to work with a commercial dye-sensitized solar cell before developing our laboratory pattern. Characterization of such a device by electrochemical methods can be considered as an example; to validate and compare the obtained results in similar systems used in this project.

This cell that can be seen in Figure 3.12 is a DSSC fabricated by Solaronix (Model PICTO 1010DEMO 114 mm × 114 mm; Ref 52101/Red; total thickness \approx 1cm); composed of transparent and conductive glass substrate coated with fluorine tin oxide (FTO; $\text{SnO}_2\text{:F}$) with a surface resistivity of 15 ohm/square. The set is achieved by sealing the two electrodes together and the medium is filled with an electrolyte. For simplicity in DSSC fabrication, it is common to use premade electrolytes based on redox couples which their adequacy is highly approved. For instance Iodolyte[©] is a ready to use electrolyte type composed of iodide and tri-iodide redox couple (Solaronix SA, 2014).



Figure 3.12 Commercial Dye-sensitized solar cell; fabricated by Solaronix PICTO 1010DEMO 114 mm × 114 mm; Ref 52101/Red; total thickness \approx 1 cm). It is composed of FTO electrodes with a surface resistivity of 15 ohm/square. This DSSC is used as a reference for our DSSC experiments in our prototype (Minucell).

The solar cell can be directly connected to an external device through two ports which link the cathode and anode electrodes to the other device's ports. Further details about Solaronix dye-sensitized solar cell, its electrochemical characteristics will be discussed in chapter 4.

3.3.2 Photo-electrochemical cell (Minucell)

This thesis groundwork starts with studying all aspects of fabrication and modelling of a photo-electrochemical cell (PEC). The design specifications of the prototype should cover our conceptual considerations about radiative transfer in a flat system and also the operational criteria of bioinspired catalysts. The cell should be easy to fabricate, separable and easy to assemble as well. Our photo-electrochemical cell, also called Minucell, has therefore been constructed on a miniature scale. It includes two separated anodic and cathodic compartments, which gives the chance to work in either complete or half-cell mode. The integral cell is composed of four thin parts assembled together by two threaded rods shown in Figure 3.13. The two internal parts with the dimension of 38 mm × 38 mm × 12 mm constitute the volume of the cell while they are shut by two FTO glassy electrodes (Figure 3.13c). Note that in each part a headspace has been considered for gas collection. The two external parts join to the internal parts to stabilize the electrodes and close the system (Figure 3.14 c & d). Each external part has a dimension of 48 mm × 38 mm × 12 mm while the dimension of liquid compartment is 14 mm × 14 mm × 12 mm. The cell volume will be achieved by gathering the two middle parts and is 4.7 mL which is 2.35 mL for each compartment. These two compartments could be separated by a Nafion membrane (please refer to part 3.2.2.3 of this chapter). It should be also noted that the exposed surface of each electrode to the illumination is 1.96 cm².

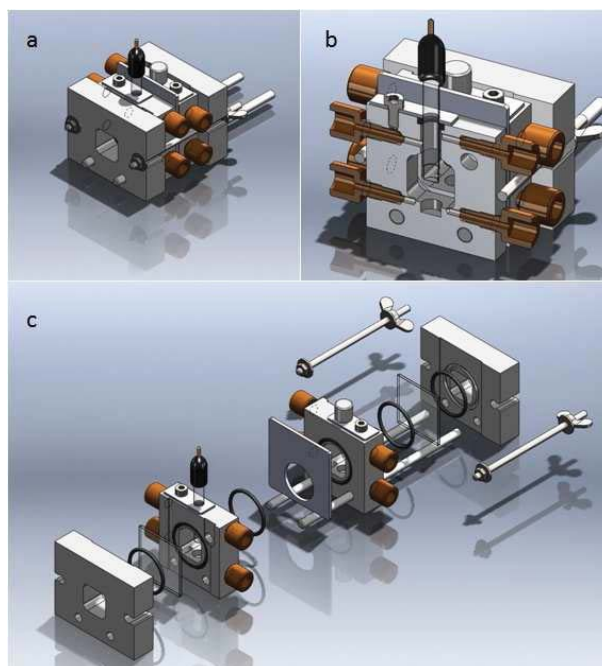


Figure 3.13 CAD of the miniature photo-electrochemical cell, Minucell. (a) Complete cell assembly with the reference electrode presentation. (b) Cross-sectional view of Minucell, in which inlet/outlet are visible. (c) Widespread view of each cell compartments with ring-seals which guarantee the cell sealing.

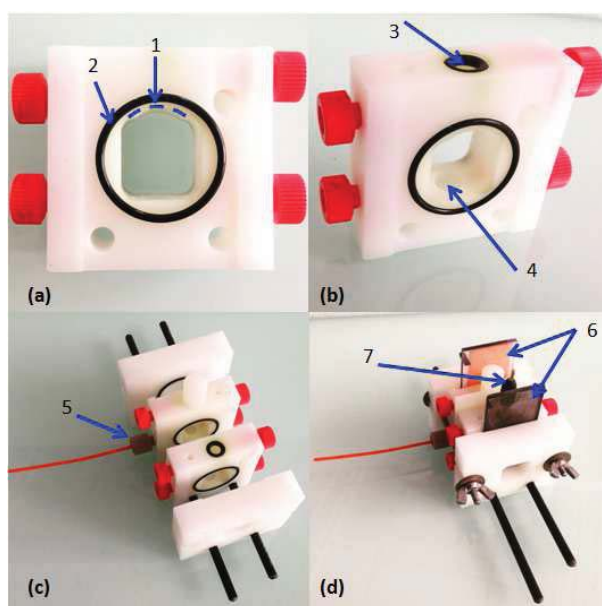


Figure 3.14 (a) Picture of an internal part of the cell in which we can see (1) the headspace for gas collection and (2) the ring-seal. (b) We can see the reference electrode entry (3) and the cavity considered for magnetic stirrer in order to have the possibility of agitating the electrolyte. (c) This picture illustrates the connection with Peek fitting for taking samples or gas circulation in the system. All the four parts for cell assembly are shown. (d) The complete Minucell with (6) photoanode and Pt cathode and (7) the reference electrode.

In addition, on the sides of each middle part, four holes can be found. Depending on the operating conditions, they could be either closed by plugs (Supelco, PE ref: 59031) or fitted with open-end plugs (Supelco, ref: 55067-U) for other operation modes: for example operating

with blanketing gas to inert the cell (using inert gas such as argon), or connecting directly the cell to a gas chromatograph or even to renew the electrolyte.

The important concern of cell design is sealing. Although the advantage of the system is that it can easily be disassembled so it can be easily cleaned or work in different operation modes (complete cell or half-cell) however it is a challenge to make it impermeable. The embedded grooves are filled with NBR (nitrile butadiene rubber) toric joints (Ring-seal, ref: 119104) to seal the system, and also to reduce the friction between the electrodes and framework during the cell compacting. Since some electrolytes can cause inflation in ring-seals which risk breaking the electrodes, we have chosen NBR and EPDM materials which are both resistive to a large range of electrolytes.

3.3.2.1 Photoanode components and preparation

Conductive glasses are produced in large variety and are very commonly used in photo-electrochemical cell fabrication because of their specific electrical and optical properties. We used the same type of glasses to prepare our electrodes.

(a)- DS-PEC photoanodes preparation

The electrodes are made up of 10 cm × 10 cm, 2.2 mm thick conductive substrate, coated with FTO (fluorine tin oxide) on one side with a surface resistivity of 7 ohm/square (Solaronix; TCO30-8). To customize the size according to our usage; we cut the substrate sheets into smaller laminae (50 mm × 25 mm) appropriate for using in Minucell.

The most important part of photoanode preparation corresponds to TiO₂ paste deposition. There are several methods for laminating TiO₂ paste on FTO substrate; including screen printing and Doctor Blading thin film which are the most prevalent methods. Doctor Blading method is simple and quick; furthermore the adequate TiO₂ paste for this method is available commercially. The preliminary step is to start by defining the conductive side of the substrate by a multimeter. The next step is fixing the FTO electrode on the laboratory bench (see Figure 3.15) by an adhesive tape (FIDUCIAL, Ref: 110154, adhesive Polypropylene, dimension: 66 m × 55 mm, thickness 35 μm). This avoids the electrode moving during the paste deposition and so permits to have a homogeneous layer, but the substantial point is that the thickness of TiO₂ layer is very dependent to the thickness of the tape we use. As it was previously brought up in Chapter 2, the thickness of TiO₂ layer on the FTO substrate is a crucial point in radiative transfer modelling. So in order to have an enough thin layer, the thick adhesive taps should be avoided.

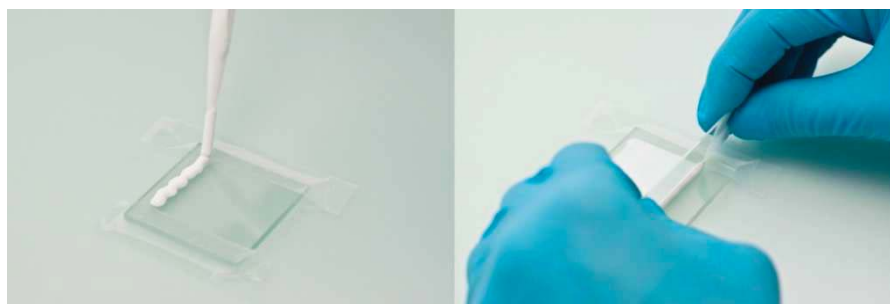


Figure 3.15 Doctor blade method of TiO_2 paste deposition on the conductive side of FTO electrodes. The electrode is fixed by adhesive tape on the table. The tap's thickness is important because it defines the thickness of TiO_2 layer on the electrode. The electrode after drying in free air should be heated to $450\text{ }^\circ\text{C}$ in the furnace or on a heating plate. Image is from Solaronix notice for DSSC (Solaronix SA, 2014).

Eventually it is sufficient to apply some TiO_2 paste and flatten it on the slide and give it few minutes to dry. Depending on the type of TiO_2 paste we use, the paste will be white or transparent after drying. We have used TiO_2 paste type T (Solaronix, ref: 11411) which is at first a white paste and becomes transparent after drying. While TiO_2 paste type D (Solaronix, ref: 14111) gives an opaque white layer after drying. Having a transparent layer of TiO_2 allows more photons to reach the photoactive molecules grafted on TiO_2 . Henceforth each time we mention TiO_2 paste, it is the TiO_2 type T.

To finish the preparation of TiO_2 electrode it will be heated at 450°C for 30 minutes. This step is necessary to eliminate probable impurities and evaporate the solvent of the TiO_2 paste; what remain are TiO_2 particles on the substrate and continuing heating establishes the electrical contact between TiO_2 particles and the FTO substrate. Note that at first TiO_2 changes the colour to brown but by completing the heating process it becomes again neutral.

The photo-electrode at the next step shall be impregnated with a dye or chromophore molecule. During this study, we prepared two different types of photoanode. The first type is made by using the synthetic dye molecules (Ruthenizer 535-bis TBA, Solaronix) to perform dye-sensitized solar cell (DSSC) experiments in Minucell. In this case we aim at producing electricity by using Minucell as DSSC with known performance. It gives us the possibility to validate the Minucell performance in a well-known photo-electrochemical process and compare its performance to the commercial type (PICTO 1010DEMO). The second photoanode is prepared with the bioinspired catalyst-chromophore molecules manufactured by our chemist colleagues in CEA Saclay.

The synthetic dye molecule used for making DSSC photoanode is an extremely efficient ruthenium sensitizer (Figure 3.16) commercially named Ruthenizer 535-bis TBA (supplied by

Solaronix). It is affiliated to the ruthenium dyes group, which is very commonly used in dye-sensitized solar cells. This group of complexes are also known as N719 in the literature. Ruthenizer 535-bisTBA sensitizes with remarkable efficiency wide band-gap oxide semiconductors, like titanium dioxide, up to 750 nm wavelength.

The procedure continues with soaking the TiO₂ electrode in a 0.3 mM solution of Ruthenizer 535-bis and ethanol (100%) for 4 to 8 hours.

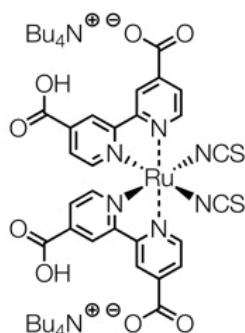


Figure 3.16 Ruthenizer 535-bis TBA molecule is a high performance ruthenium sensitizer for Dye Solar Cell applications from the ruthenium dye family.

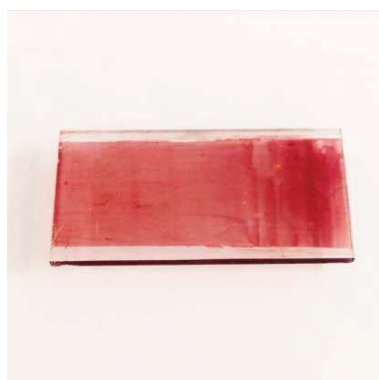
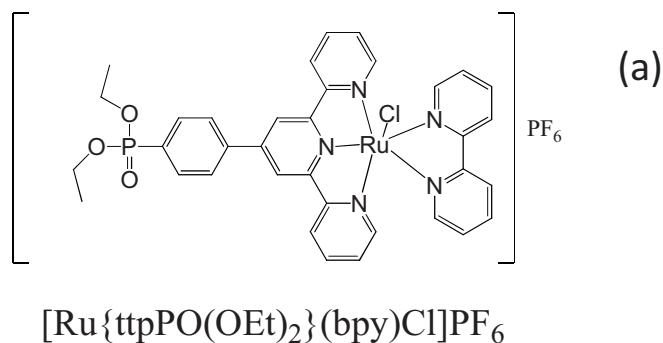


Figure 3.17 An example of stained electrode of TiO₂ with Ruthenizer 535-bis TBA. The electrode remained 12 hours in the impregnation solution. It should be rinsed with absolute ethanol before be used.

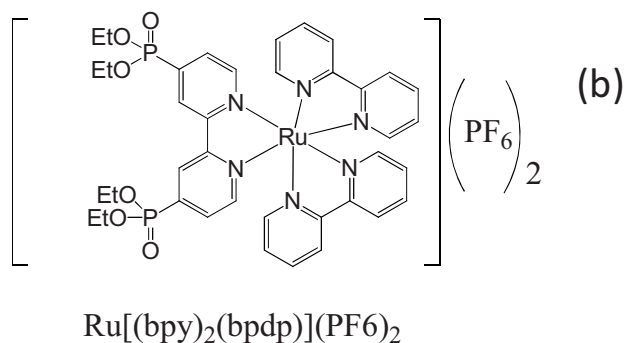
The coloured electrode (Figure 3.17) should be rinsed by the same solvent of impregnation solution, here absolute ethanol, after removing from the staining vessel. Technically after removing the electrode, it should be quickly used; otherwise it is better to conserve it in the container. The staining bath can even be re-used for several times.

To prepare the bioinspired ruthenium photoanode with catalyst (Ru_{cat}) and chromophore (Ru) or a mixture of both compounds (Ru-Ru_{cat}), a complete protocol of preparation has been developed. The macro molecular chromophores and catalysts (Figures 3.18) shall be dissolved in deionised water with the concentration of 0.2 mM. The electrode will be soaked for 12 hours

and it should be washed lightly by deionised water. The ratio of catalyst and chromophore within the impregnation solution is 1:1. Note that the ratio of adsorbed catalyst and chromophore on the electrode layer might be different than in impregnation solution and it needs to be defined. The simplest method is to rinse the impregnated electrode with a solvent which washes the adsorbed species from the electrode and then the transmittance of this solution containing washed chromophore and catalysts can be measured (by using integrating sphere) and then the ratio of catalyst/chromophore can be defined by a simple calculation.



ttpPO(OEt)₂=diethyl (4-([2,2':6',2''-terpyridin]-4'-yl)phenyl)phosphonate



bppp=Diethyl 4-(2,2'-Bipyrid-4-yl)phenylphosphonate,

Figure 3.18 (a) the catalyst and (b) chromophore molecules are presented as well as their IUPAC name.

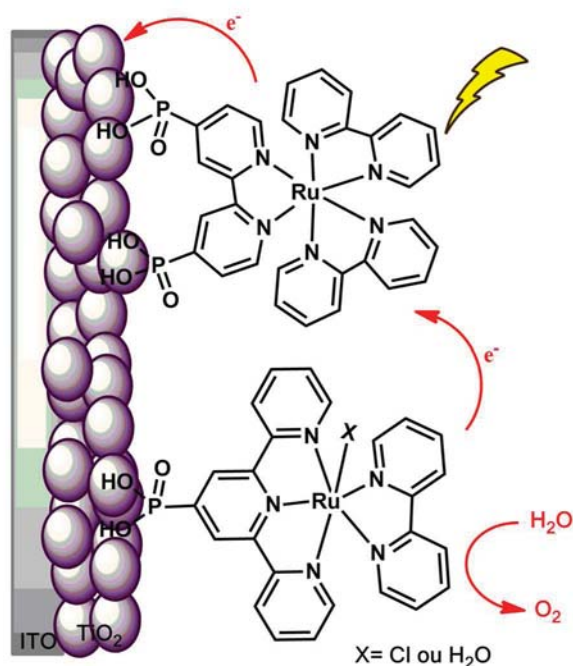


Figure 3.19 Explicit schema of chromophores and catalysts molecules transplanted on the TiO_2 surface. Electronic exchange between catalyst and chromophore molecules (reduction of chromophore by catalyst) and water oxidation is shown in this picture (Leibl, personal communication).

The impregnation solution can be used several times for further electrodes. The important point is that the electrode after impregnation should be rinsed only with the same solvent have been used for preparing the impregnation solution, if not the deposition on the electrode will be partially or thoroughly removed.

(b)- Film thickness estimation

Electrode thickness measurement is an important preliminary step because of its direct relation with radiative transfer within the electrode layer as discussed in chapter 2 while developing the knowledge model. For this reason, we should have an accurate estimation of the thickness of TiO_2 layer on the FTO electrode. Hence TiO_2 electrodes samples were prepared by the same method explained in section 3.3.2.1.a with considering that we have to increase the number of adhesive tape layers on each electrode's sides in order to obtain different thickness of semiconductor. Accordingly, when we mention single layer TiO_2 electrode, we have only used one layer of adhesive tape. Similarly a double layer TiO_2 electrode has been obtained by doubling adhesive tape layers on each electrode's side and likewise for any thicker layer of deposition that we wish to achieve.

(I)- Scanning electron microscope (SEM)

As a first step we used the scanning electron microscopy (SEM) technique to have an estimation of the electrode thickness, by scaling the pictures taken by SEM of TiO_2 electrodes with different thicknesses (Figure 3.21). For preparing samples we put TiO_2 electrodes in resin. Once they are incrustated in resin, we polish the resin, removing the resin gently of the cross section surface of the samples.

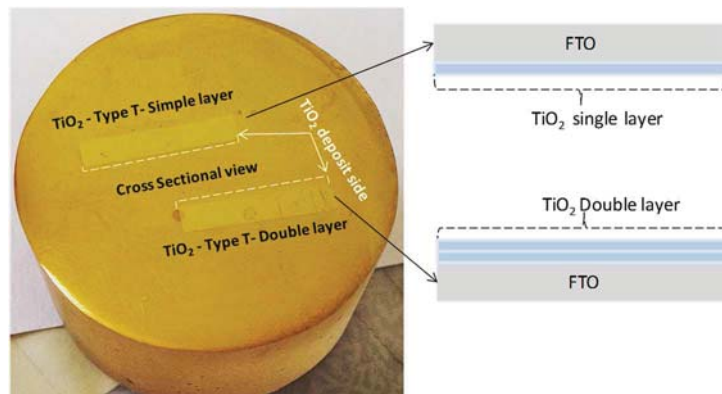


Figure 3.20 FTO electrode with single and double layer of TiO_2 have been incrustated in resin so that we see the cross sectional view. The samples have been next polished and coated by gold to provide a conductive surface for SEM analysis.

The polished resin surface should be next coated with gold by pulverization method to have a conductive surface. Figure 3.20 shows a processed sample for SEM analysis.

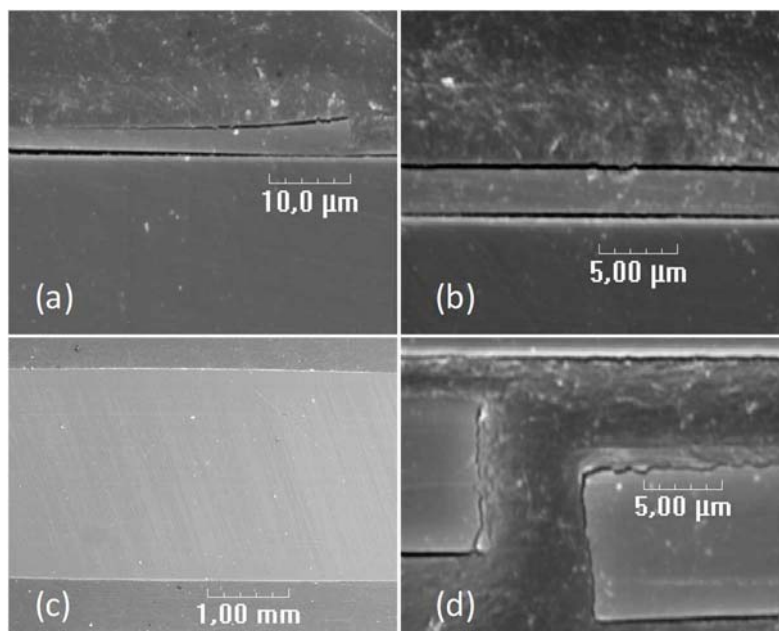


Figure 3.21 (a) Cross sectional view of TiO_2 single layer electrode near the edge of layer. (b) The image shows another part along the deposition. (c) Cross sectional view of TiO_2 double layer electrode. (d) The image of fracture in TiO_2 double layer deposit. From the scales estimated by SEM, the thickness of TiO_2

single layer is around 2.5 μm while it gives a value of 7 μm . These values will be cross-checked with results obtained by profilometer.

Pictures of Figure 3.20 present the TiO_2 -Type T, single and double layers. Considering the scales on the images given by SEM, the thickness of single layer of TiO_2 type T, is estimated around 2.5 μm . We have similarly around 7 μm for double layer of TiO_2 . Since estimating the thickness through scales on the pictures, is not very accurate and also during sample preparation we may cause some changes on the deposit surface we decided to cross-check our measurements by using profilometer.

(II)- Profilometer device

A KLA-Tencor Alpha-Step IQ Profilometer has been used. It is basically a device for measuring the surface profile in order to evaluate its roughness. The sample's surface is traversed by a needle along a determined distance. Profilometer is able to record very small variation of surface according to vertical displacement of stylus. We tested three samples with single, double and triple layer of TiO_2 deposited on FTO by the same method we explained in section 3.3.2.1.a.

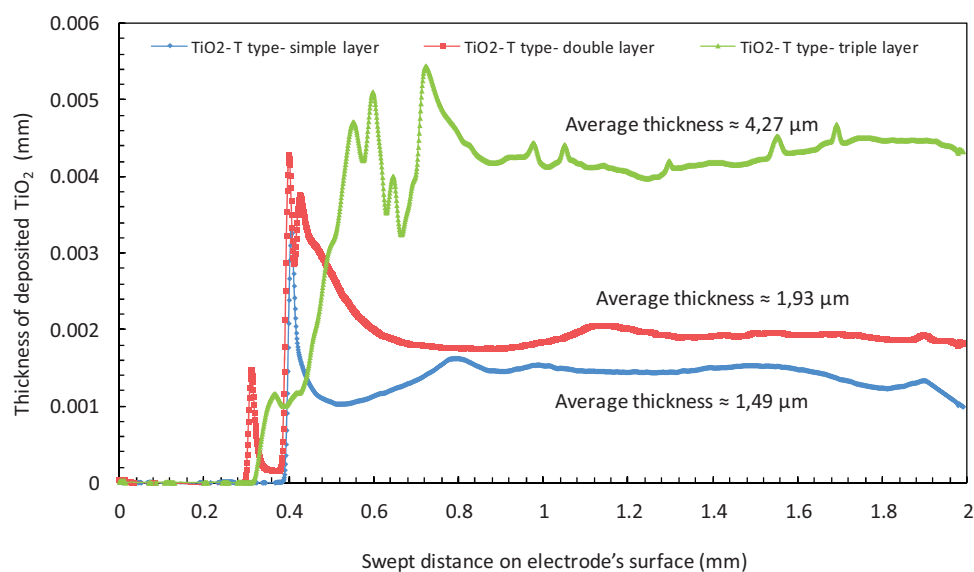


Figure 3.22 Profilometer results are shown for three different samples. The blue line illustrates the thickness of TiO_2 single layer measured 1.49 μm . The red and green lines represent 1.93 μm and 4.27 μm for double and triple layer of TiO_2 respectively. The major difference between the beginning and the final measured points is because the layers near the edges are thicker than the middle parts which are more homogenous. So the values given for thickness are based on the data obtained from these parts.

Since there is always a margin between the edges of the electrode and TiO_2 layer (because the trace of the tapes used for deposition) it is preferable to start from a point on FTO without TiO_2 covering and then to sweep over the layer of interest. The result as it is illustrated in Figure 3.22

shows clearly the place at which the TiO₂ layer starts (starts from 0.3 mm on the electrode). It is inevitable to have a thicker and non-homogeneous deposition of TiO₂ near the edges (between 0.4 and 0.8 mm). After a distance of nearly 0.8 mm from the edges we have a homogenous layer, whereupon the average considered for each sample, has been only calculated on the homogenous part. From profilometer result we obtain an average of 1.49 μm for single layer of TiO₂, while for double and triple layers we obtain 1.93 and 4.27 μm respectively. It should be noticed that these values are by far smaller than the adhesive tape thickness. The reason is the TiO₂ paste thickness will reduce after drying and heating process. The difference between profilometer and SEM results can come from the fact that SEM (at least the device we used for measurements) gives only an approximate of the thickness (as it is explained before we have to estimate the thickness of the layer by using the scales given by the SEM). Besides there can be also some deviations in profilometer measurements. For example, the needle which move through the layer gets really close to the sample but do not touch it to avoid scratches on the layer. But after all, we consider profilometer results are more accurate for our further study.

(c)- SC-PEC photoanode preparation (Hematite photoanode)

To continue with photoanode preparation, here we introduce hematite photoanode that we used in our tests in SC-PEC system (Refer to Chapter 2 for SC-PEC introduction). In general, hematite films are deposited on a transparent electrode of FTO. It is important to control the morphology of the film in order to increase the number of photo-generated holes reaching the semiconductor/electrolyte interface. Grätzel's team managed to produce nanostructured films using a technique called Atmospheric Pressure Chemical Vapour Deposition (APCVD) (Tilley et al., 2010).

In this project, hematite electrodes have been fabricated by our colleagues of the CEMCA, UMR 6521, CNRS, Université de Bretagne Occidentale, Brest. It has been decided to use an electrochemical method (Wang et al., 2013) less expensive and easier to implement than the APCVD technique. As a first step, it is necessary to coat a FTO glass on the conductive side by an anodic deposition of FeOOH from a slightly acidic solution (pH 4) of Fe²⁺ ions. Then the deposited layer of FeOOH is heated in air between 520°C for 30 min to obtain the α – Fe₂O₃ film. By adjusting the deposition time of FeOOH and the heating temperature, it is possible to vary the final thickness and morphology of the hematite film.



Figure 3.23 Hematite electrode, fabricated by anodic deposition of FeOOH from solution of Fe^{2+} , (pH 4). The final film is obtained after heating the electrode up to 520°C . The thickness of deposition can be varied by regulating the time of FeOOH deposition and the annealing temperature.

In the next step we test water oxidation by using platinum particles as catalyst on hematite layer. We used Platisol T (Platinum Catalyst Precursor Paint, purchased from Solaronix), a liquid paste which can be applied easily by using a brush on the hematite electrode. After giving enough time to Platisol to dry in ambient condition it should be heated afterward to 450°C for at least 10 minutes to be transformed into activated platinum. Usually the iridium oxide (IrO_2) is the most efficient electro-catalyst in terms of activation over-potential for the water oxidation into oxygen; but due to problems in IrO_2 synthesis we replaced IrO_2 by activated platinum which is assumed to be efficient as well.

3.3.2.2 Cathode

(a)- Platinum cathode

Platinum has always shown a satisfying catalytic activity in electrochemical reduction reactions, thereby it is a good option for its use in cathode electrode. The counter-electrode is composed of a FTO plate coated with a platinum paste. Our procedure relies on using Platisol T (by Solaronix); a typical transparent paste including a precursor of platinum. A portion of Platisol was applied by a brush on the conductive side of FTO plate and immediately heated at 450°C for at least 10 minutes in order to fix the Platisol layer on the plate.

The heat treatment procedure shall be repeated each time before using the electrode to eliminate probable impurities and reactivate the platinum layer.

(b)- CoTAA cathode

Even if platinum is a promising material for H^+ reduction at cathode, recent researches inquire about new catalytic materials with more abundance and cheaper price (Rioual et al., 2015). As a result, molecular complexes of transition metals have been recognized to be reasonable

catalytic materials if the central metal has been chosen properly. Hence the studies carried on cobalt complexes show that, the tetraazaanulene of Co(II), COTAA, has two advantages: (i) it is stable in acidic aqueous solution, and (ii) the TAA ligand can be polymerized by electrochemical oxidation to form an insoluble film on the electrode. COTAA electrodes synthesis have been accomplished as reported by (Convert et al., 2001; Hiller et al., 1968; Rioual et al., 2015) by using glassy carbon tips and the rotating disk electrode. COTAA electrodes have been synthesised by our colleagues of the CEMCA, UMR 6521, CNRS, Université de Bretagne Occidentale, Brest, for more details on the fabrication procedure see (Convert et al., 2001; Hiller et al., 1968).

3.3.2.3 Nafion© membrane

To separate the two, anodic and cathodic, compartments of Minucell (we can even use different electrolytes with different pH in each compartment) and also have a ionic exchange between two parts we need to use a membrane. Nafion© is a perfluorinated ion-exchange membrane enables us to operate as such.

We have used the Nafion© 117 (ref: 292567-1EA) membrane with a thickness of 0.007 inch. It is insoluble in water and it has been purchased from Sigma-Aldrich. Nafion© needs pre-treatment before being used in electrochemical experiment. It is commonly prepared with the method of (Zawodzinski et al., 1993) which is about to boil it slightly (~80°C) in 3% H₂O₂ in for 1 hour following with boiling two hours in deionised water. It should be once boiled in a 0.5 M H₂SO₄ solution and finally rinsed and stored in deionised water.

3.4 System configuration

3.4.1 General presentation

The complete system is composed of the Minucell in the black box, exposed to the LED panel, and associated to a potentiostat. The Figure 3.24 illustrates the complete experimental setup of the cell with all necessary devices for electrochemical experiments.

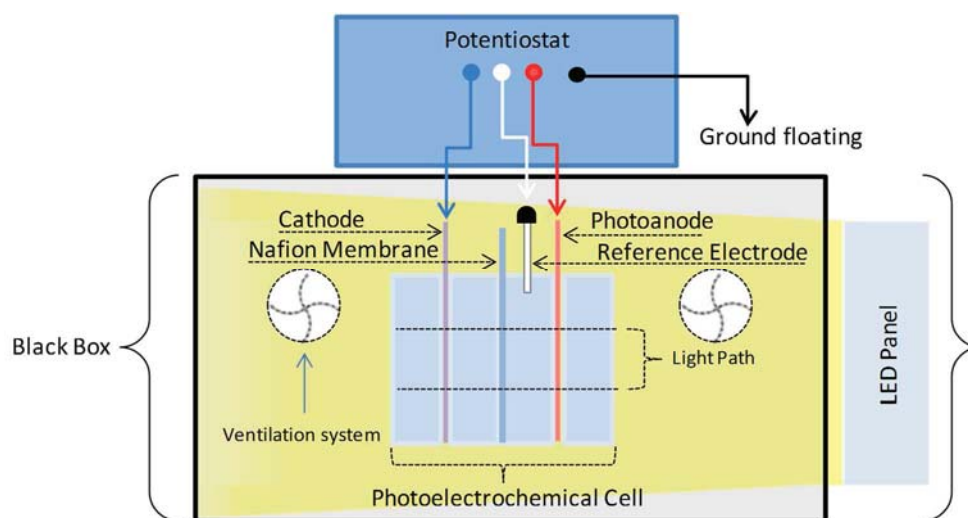


Figure 3.24 The comprehensive schema of the complete systems setup with all essential components including: Minucell, reference electrode (depends on operating connection mode), potentiostat, LED panel and the black box.

In the following the potentiostat functioning and different possibilities of connections will be detailed.

3.4.2 Electrochemical instrumentation

A potentiostat is an electronic device which permits to control an electrochemical cell in different operation modes; two, three, or four electrodes assembly during executing electrochemical measurements. Generally, a potentiostat measures the current circulating between the two electrodes in measurement; work electrode and counter electrode (Bard and Faulkner, 2001).



Figure 3.25 SP-240 potentiostat, 4A research grade, distributed BioLogic can work at the voltage range of -3V up to 14V and provides the current between the ranges of 1 μ A – 4 A. It permits to carry out the data acquisition which will be then interpreted and traced by EC-Lab software. Several electrochemical techniques are provided and supported by EC-Lab such as general voltamperometric (Cyclic Voltammetry, Chronopotentiometry) techniques, impedance techniques, and a technique builder including modular potentiostat and galvanostat.

In other words, it controls the potential of the work electrode and regulates the current at counter electrode. There are few tests like open circuit measurement in which the current value is null and so the test is based on the open circuit voltage variation during the time. The potentiostat used in Institute Pascal for TechBioPhyp project is a SP-240, supplied by Bio-Logic. SP-240 is compact portable form of potentiostat with excellent specifications.

This potentiostat can provide a current range from 1 μA up to 4 A with current resolution of 760fA and the voltage range of -3V to 14V. Furthermore it has the possibility to be controlled from the PC by USB or Ethernet connections. It has also two analogue inputs and one analogue output which can be used to connect instruments, such as electrodes. Data interpretation and analysis is executed by EC-Lab software, a software supplied also by Bio-Logic which provides variant range of analysis tools for different measurements together with equivalent circuit modelling for impedance measurements (Zoski, 2007). It is also equipped with an impedance port which provides the option of Electrochemical Impedance Spectroscopy (EIS) measurements.

3.4.2.1 Complete system setup

The study of electrochemical system is possible through several system setups. We can use two electrode setup for the system to define the general behaviour of the PEC (see Figure 3.25). It means that we connect the photoanode to the work electrode port (the red connection) and the cathode to the counter electrode port (the blue connection). The potentiostat measures the difference of electric potential between two electrodes. It is also common to use the term of complete cell setup.

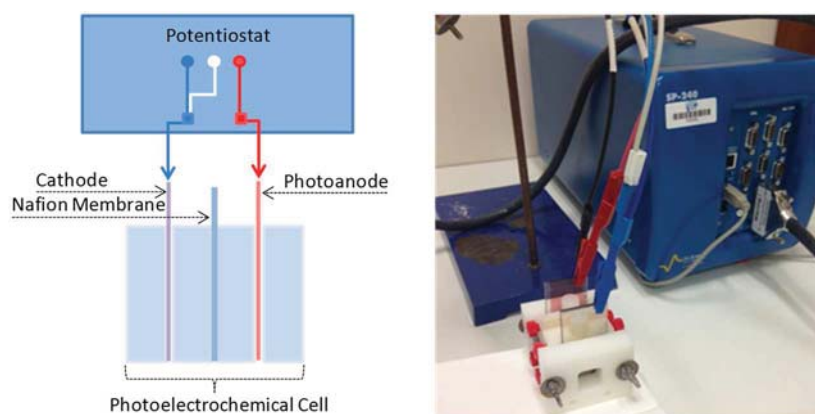


Figure 3.26 The scheme on the left illustrates the two electrodes setups. The red electrode represents the photoanode connected to the red connection (work electrode) and the violet electrode is the cathode (Pt in our setup) connected to the blue connection and the white connection related to the reference electrode

is associated to counter electrode connection in two electrodes setup. On the right we find the image of this setup with Minucell connected to the potentiostat.

It is obvious that the potential difference measured in this case is a relative value. It means we have no information about each electrode's potential but we know the global electric potential difference of the cell. Two electrode setup measurements can provide general information about the cell operating point but it does not give any details about each electrode's potential.

Two-electrode configuration is the simplest cell setup and allows measuring the whole cell potential difference variation. More studies about each electrode characterisation are carried out by three electrodes configuration in which, the third electrode is a reference electrode. It makes possible to identify each electrode potential as we measure the potential difference between the working electrode (photoanode or photocathode) and the reference electrode while the potential of reference electrode is already known and constant, we can therefore define the working electrode potential. On the other hand, we have also the possibility of recording the counter electrode potential (this option is possible with or potentiostat device and may not be possible with old models). It is important as well to study the generation of photocurrent at photoanode by limiting the effect of counter electrode.

In three electrode setup the reference electrode should be connected to the white connection (Figure 3.26). This connection has been assembled with counter electrode's connection during two electrodes setup.

(a)- Reference electrode

A reference electrode is an important device in electrochemical measurements. There are many variants of reference electrodes for different mediums; for example, organic or non-organic solvents. It is very important to choose the appropriate reference electrode to acquire proper results. Here we use a silver chloride reference electrode (RE-1S silver, OD 4.5 mm, L 50 mm) for aqueous solutions, purchased from BioLogic. This reference electrode has been chosen because of its small dimensions which are adapted to the small size of Minucell.



Figure 3.27 RE-1S silver, silver chloride reference electrode, OD: 4.5mm \times L: 50 mm. The Ag electrode is submerged in 3 M NaCl solution. The electrode is appropriate to be used in aqueous solutions.

It is composed of a Ag wire covered with an AgCl deposit. The wire is immersed in a 3M NaCl solution. Its potential is +0.195 V/ENH at 25°C. The reference electrode passage into the Minucell is arranged on the top of the cell.

3.5 Electrochemical measurement methods

For an electrochemical system characterisation, several methods can be used to get information.

3.5.1 jV (current-voltage) curve polarization

A current-voltage measurement is a test which describes the ability of energy conversion of a solar device for a constant illumination and temperature condition. In other words, it gives an evaluation of produced current and power of the system resulting from an applied potential to the system.

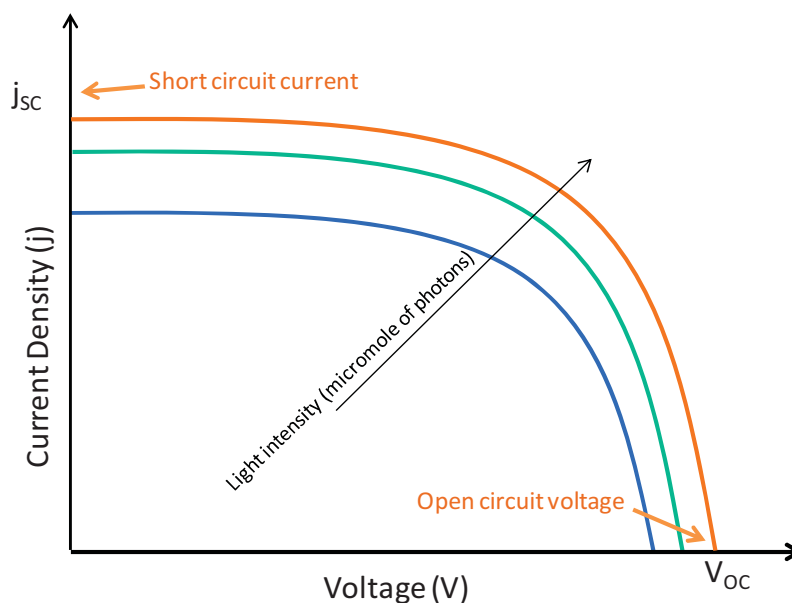


Figure 3.28 Typical jV curve of PEC for different light intensities. The open circuit potential V_{OC} increases by increasing the light intensity. By moving toward lower potential differences the current flowing within cell connections increases and when the total potential difference of the cell approaches to zero the current reaches to its maximum amounts. This current is called short circuit current in which the cell resistance is nearly zero.

jV curve gives information about electrical characteristics of the cell such as the maximum current value (short circuit point; j_{sc}), the maximum obtainable voltage value (open circuit voltage V_{OC}) and maximum nominal power of the system (P_{max}).

3.5.2 Open circuit voltage

The open circuit is a state of the cell in which no current flows within the cell and the potential difference between the two electrodes is open circuit voltage (V_{OC}). This voltage corresponds to the maximum different potential procurable in a cell (Figure 3.28).

However, in a photo-electrochemical device it is important to record the evolution of open circuit voltage induced by variation of light intensity. So during open circuit acquisition, the potentiostat measures the variation of the potential difference between the working electrode and a reference electrode (for 3 electrode configuration) or a counter electrode (for two electrode configuration) during a specific time.

3.5.3 Cyclic voltammetry

Voltammetry is category of electrochemical analysis in which the system is analysed by measuring the current through the system by potential variation. Cyclic voltammetry (CV) is a

potentiodynamic measurement during which the potential of working electrode will vary linearly during the time to a set potential and once the set potential is achieved the working electrode potential will be ramped back in opposite direction to reach the initial potential. During a CV experience the current of the cell is measured and traced versus working electrode potential and it gives the cyclic form of the graph. This technique is usually used to study the electrochemical properties of redox couples in a solution. The cyclic voltammetry tests were accomplished for Minucell in three electrodes montage. The test was repeated for each TiO₂ photoanode with commercial dye photo-sensitizer and TechBioPhyp chromophore-catalyst and Pt counter electrode and Ag/AgCl as reference electrode.

3.5.4 Chronoamperometry

Chronoamperometry is another electrochemical method in which the working electrode potential is be stepped and the faradic current resulted from stepped potential is traced versus time. Some analytical information about electrolyzed species can be understood from oxidation and reduction peaks of current but the drawback is that chronoamperometry causes high charging currents which exponentially decay with time as in all RC circuit. Here, chronoamperometry measurement was employed to evaluate the photocurrent generation for a specific time duration in the cell, under illumination or in obscurity (Bard and Faulkner, 2001).

3.5.5 Potentiostatic Electrochemical Impedance Spectroscopy

(PEIS)

As it has been described in detail earlier in chapter 2, during an electrochemical impedance spectroscopy test, the potentiostat applies an AC signal (sinusoidal) to the cell. The response of the cell is analysed by the potentiostat in order to define the resistive, capacitive or diffusive behaviour of the medium as a function of frequency. Each phenomenon has a different time constant response and therefore they show up at different frequencies. The test can be practiced in two modes: potentiostatic or galvanostatic. In potentiostatic mode the potentiostat applies a sinusoidal signal around a given potential value or even the open circuit potential, and scans the impedance of the system. The concept of the test is similar for galvanostatic mode but the difference is that the current is controlled rather than potential.

Equivalent circuit modelling is a method of representation of results based on an electrical analogy which is mostly appropriate to explain our system since our experiment variables are current and potential.

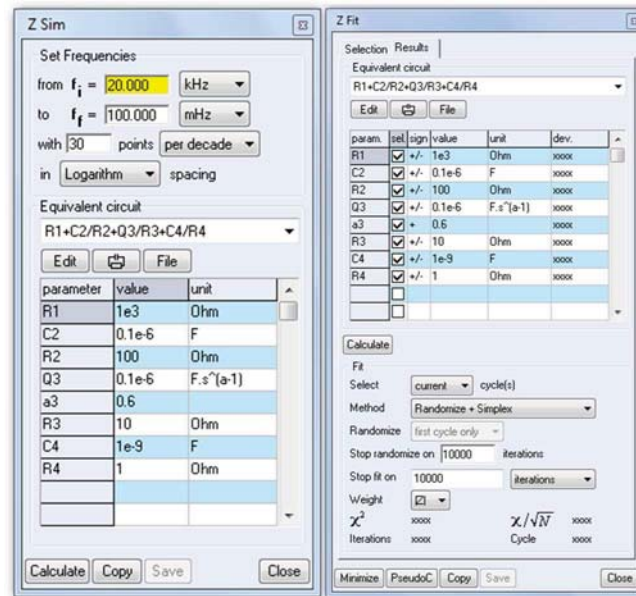


Figure 3.29 Zfit and ZSim menu in the EC lab software. ZSim gives the possibility to define an appropriate equivalent circuit according to experimental data. This equivalent model can be next fitted to experimental points by Zfit and each components value will be identified. Using ZSim would not be necessary if we have enough knowledge about the adequate equivalent circuit for our system.

With this method we can attribute an electrical element and an explanation to the impedance data obtained from an electrochemical system. We need to establish the appropriate electrical circuit and fit this model (for a specified frequency range) to the experimental data (presented in a Nyquist diagram). EC lab software has a Zfit simulator giving the possibility to define the appropriate electrical circuit and fit it to the experimental diagram. Zfit gives also an estimation of the defined electrical parameters (resistors and capacitors).

EIS method with a complete set of electrical modelling by equivalent circuit method has been used as an alternative modelling method in this work.

3.6 Conclusion

In this chapter we presented all optical methods used for our light sources characterisation. The results of this characterisation have been also introduced and we concluded by using first, the blue LED panel at the beginning of the work because of good absorption at green-blue range by dye molecules. However, we further preferred to work with all range of light spectrum to have more realistic operating conditions. To that, after testing solar simulator and observing several complications that our actual design for Minucell was not ready to meet such as high temperature increase (despite the external ventilation system) which could harshly impact the system behaviour and electrochemical analyses. So we decided to use the white LED panel which would enable us to work at more range of solar spectrum and also the impact of temperature increasing would be controllable by external ventilation.

A complete analysis of TiO_2 electrodes with different thicknesses by two different methods was presented.

The results of electrochemical measurements on commercial DSSC and Minucell tested with different photo-electrodes (TiO_2 and hematite photoanodes) and cathodes are discussed in chapter 4.

This chapter helps to follow our methodology of characterisation step by step. Indeed, some finer points might not be totally cleared within the text, which can be discussed and shared during practice.

References

- Bard, A.J., Faulkner, L.R., 2001. *Electrochemical Methods: Fundamentals and Applications*, Analytica Chimica Acta. <https://doi.org/10.1016/j.aca.2010.06.020>
- Convert, P., Coutanceau, C., Crouigneau, P., Gloaguen, F., Lamy, C., 2001. Electrodes modified by electrodeposition of CoTAA complexes as selective oxygen cathodes in a direct methanol fuel cell. *J. Appl. Electrochem.* 31, 945–952. <https://doi.org/10.1023/A:1017596408165>
- Cornet, J.-F., Marty, A., Gros, J.-B., 1997. Revised Technique for the Determination of Mean Incident Light Fluxes on Photobioreactors. *Biotechnol. Prog.* 13, 408–415. <https://doi.org/10.1021/bp970045c>
- Hiller, H., Dimroth, P., Pfitzner, H., 1968. 5.14-Dihydro-dibenzo[b,i][5.9.14.18]tetraaza[14]annulen, ein makrocyclischer Chelat-Bildner. *Justus Liebig's Ann. Chem.* 717, 137–147. <https://doi.org/10.1002/jlac.19687170115>
- Kuhn, H.J., Braslavsky, S.E., Schmidt, R., 2004. Chemical actinometry (IUPAC Technical Report). *Pure Appl. Chem.* 76, 2105–2146. <https://doi.org/10.1351/pac200476122105>
- Ocean optics, 2015. Technical Documents - Ocean Optics [WWW Document].
- Rioual, S., Lescop, B., Quentel, F., Gloaguen, F., 2015. A molecular material based on electropolymerized cobalt macrocycles for electrocatalytic hydrogen evolution. *Phys. Chem. Chem. Phys.* 17, 13374–9. <https://doi.org/10.1039/c5cp01210d>
- Rochatte, V., Dahi, G., Eskandari, A., Dauchet, J., Gros, F., Roudet, M., Cornet, J.F., 2017. Radiative transfer approach using Monte Carlo Method for actinometry in complex geometry and its application to Reinecke salt photodissociation within innovative pilot-scale photo(bio)reactors. *Chem. Eng. J.* 308, 940–953. <https://doi.org/10.1016/j.cej.2016.08.112>
- SAFAS, 2015. SAFAS -Spectrofluorometer [WWW Document]. <http://www.safas.com>.
- Solaronix SA, 2014. Solaronix materials. Switzerland. <https://doi.org/Rev.050514DM>
- Tilley, S.D., Cornuz, M., Sivula, K., Grätzel, M., 2010. Light-induced water splitting with hematite: Improved nanostructure and iridium oxide catalysis. *Angew. Chemie - Int. Ed.* 49, 6405–6408. <https://doi.org/10.1002/anie.201003110>
- Wang, L., Lee, C.-Y., Schmuki, P., 2013. Influence of annealing temperature on photoelectrochemical water splitting of α -Fe₂O₃ films prepared by anodic deposition. *Electrochim. Acta* 91, 307–313. <https://doi.org/10.1016/j.electacta.2012.12.101>
- Wegner, E.E., Adamson, A.W., 1966. Photochemistry of Complex Ions. III. Absolute Quantum Yields for the Photolysis of Some Aqueous Chromium(III) Complexes. *Chemical Actinometry in the Long Wavelength Visible Region. J. Am. Chem. Soc.* 88, 394–404. <https://doi.org/10.1021/ja00955a003>
- Zawodzinski, T.A., Derouin, C., Radzinski, S., Sherman, R.J., Smith, V.T., Springer, T.E., Gottesfeld, S., 1993. Water-Uptake by and Transport through Nafion(R) 117 Membranes. *J. Electrochem. Soc.* 140, 1041–1047. <https://doi.org/10.1149/1.2056194>
- Zoski, C.G.C., 2007. *Handbook of Electrochemistry*, Khimiya Leningrad. <https://doi.org/10.1016/B978-044451958-0.50000-8>

The view from the Highland

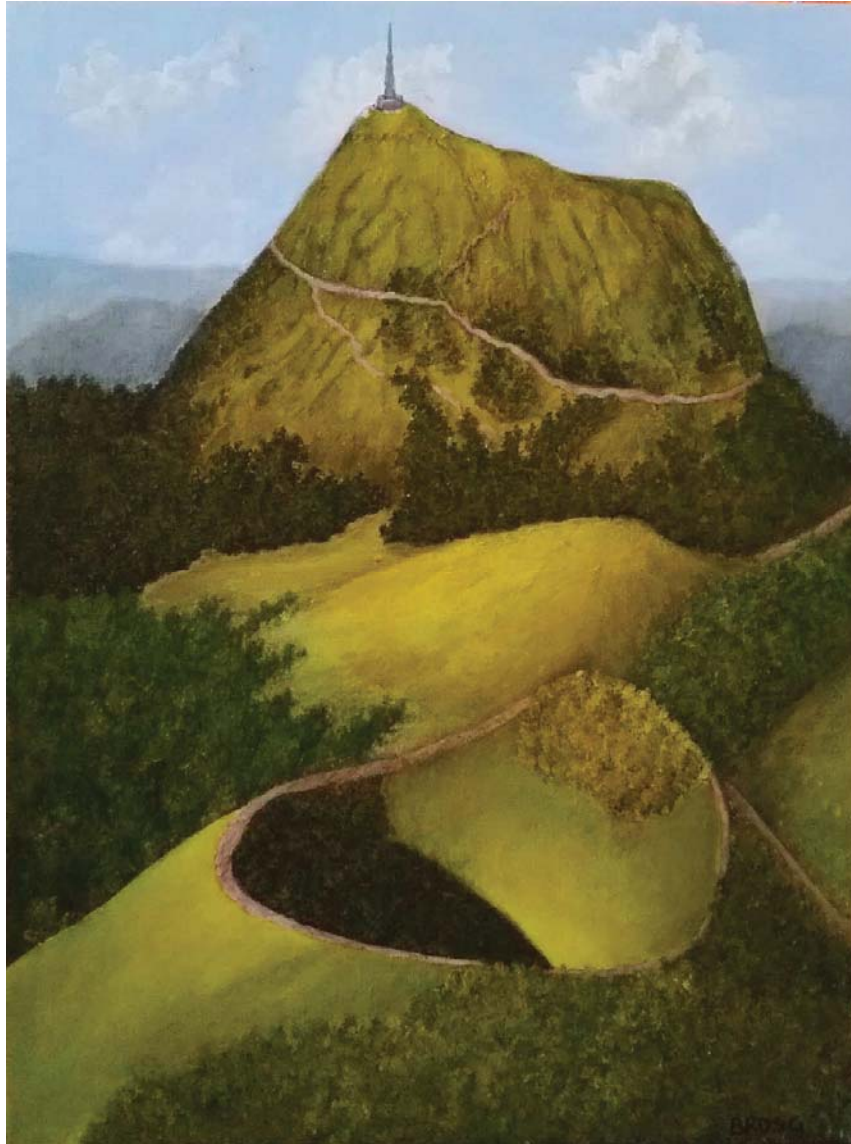


Table of Content

Chapter 4	Experimental characterization of photoelectrochemical cells	133
	Introduction	133
4.1	Titanium dioxide (TiO₂) electrode characterization	135
4.1.1	Transmittance measurements	135
4.1.1.1	Influence of the paste type on transmittance	135
4.1.1.2	Transmittance measurements: effect of deposit thickness	136
4.1.2	Electrochemical measurements	138
4.1.2.1	Characterization by cyclic voltammetry	138
(a)-	Influence of scan rate at dark	138
(b)-	Influence of photon flux density	140
(c)-	Influence of thickness	141
4.1.2.2	Impedance spectroscopy measurement	142
4.2	Dye-Sensitized solar cell (DS-PEC)	146
4.2.1	DSSC Solaronix characterization	146
4.2.1.1	DSSC Solaronix current density-voltage	146
4.2.1.2	DSSC Solaronix EIS study	149
(a)-	Photon flux density effect	149
(b)-	Cell operating tension	153
4.2.2	DS-PEC implementation with Minucell	154
4.2.2.1	DS-PEC photoanode characterisation	154
(a)-	Transmittance measurements of the dyed photoanode	154
(b)-	Polarization under illumination conditions	155
(c)-	Comparison between Solaronix and Minucell DS PEC on an energetic point of view	157
(d)-	Electrochemical Impedance Spectroscopy	158
4.3	DS-PEC characterization (molecular ruthenium based)	163
4.3.1	Ru chromophore photoanode	163
4.3.1.1	Transmittance measurements with chromophore (Ru) impregnation	163
4.3.1.2	Electrochemical characterization of Ru chromophore photoanode	165
4.3.2	Ru _{Cat} catalyst photoanode	167

4.3.2.1	Transmittance of catalyst Ru _{Cat} impregnation	167
4.3.2.2	Electrochemical characterisation of Ru _{Cat} catalyst photoanode.....	168
4.3.3	Ru-Ru _{Cat} chromophore-catalyst photoanode	170
4.3.3.1	Transmittance of Ru-Ru _{Cat} chromophore-catalyst impregnation.....	170
4.3.3.2	Electrochemical characterisation of Ru-Ru _{cat} chromophore-catalyst photoanode.....	171
(a)-	Characterisation of the photoanode by cyclic voltammetry	171
(b)-	Characterisation of the photoanode by impedance.....	172
4.3.4	Ru-Ru _{Cat} PEC complete system (two electrodes setup).....	177
4.3.4.1	PEC using platinum coated cathode.....	177
(a)-	jV results.....	177
(b)-	EIS study of Minucell in two electrodes configuration:.....	178
4.3.4.2	PEC using CoTAA cathode.....	182
(a)-	Linear and cyclic voltammetry of CoTAA electrode	182
(b)-	Implementation of CoTAA cathode in a PEC.....	183
4.4	Hematite PEC characterization (SC-PEC)	186
4.4.1	Hematite photoelectrode characterization without catalyst.....	186
4.4.1.1	Transmittance measurements	186
4.4.1.2	Electrochemical characterization	187
(a)-	Photocurrent measurements.....	187
(b)-	Potentiostatic Electrochemical Impedance Spectroscopy	189
4.4.2	Hematite electrode characterisation with catalyst (Pt) coating.....	194
4.5	Conclusions.....	197

Chapter 4

Experimental characterization of photoelectrochemical cells

Introduction

As explained in the previous chapters, PhotoElectrochemical Cells can be divided in two distinct groups according their purpose, the first one with cells close to photovoltaics where only electricity is generated (Grätzel cells are included) whereas the second category includes photoelectrosynthetic cell to carry out water splitting as a final purpose. However their conceptions are rather close with the use of a photoanode and a cathode (the only difference lies in the electrode reactions).

By developing the Minucell device, we intended to easily study these two groups of photoelectrochemical cells with the final purpose of hydrogen production. The scientific approach chosen was progressive. Hence it was decided to implement a similar dye sensitized system as commercial DSSC in Minucell in order to validate the electrochemical and photoelectrochemical aspects of our prototype. Appropriate electrodes were fabricated with the same materials or compounds as used in commercial features. A dye-sensitized solar cell similar to Grätzel cell was obtained. The same electrochemical tests were run for both of commercial DSSC and Minucell-DSSC application (DS-PEC category)¹. These aspects and related results are presented in section 4.2 with a focus (in section 4.1) on electrochemical analysis of fabricated TiO₂ electrodes as a basic element with which we unroll all further tests in Minucell. The section 4.3 is devoted to of Ruthenium-Phosponate PEC system (which belongs to DS-

¹ Refer to Chapter 2 Modelling for the acronym.

PEC category) and the last part of this chapter (4.4) will be focused on Hematite PEC system (also a SC-PEC feature)¹. Both of these PECs have been developed and studied for hydrogen production purpose.

4.1 Titanium dioxide (TiO₂) electrode characterization

This section is devoted to the characterisation of the TiO₂ electrodes without sensitizer impregnation as it is a major component of the photoanode and it influences the general behaviour of the anode. These characterizations include optical properties as well as electrochemical characteristics.

4.1.1 Transmittance measurements

Focusing on the two different and available types of TiO₂ pastes and also on film thickness, different samples were prepared; simple layer and double layer electrode for each type of TiO₂.

4.1.1.1 Influence of the paste type on transmittance

Typical results of monolayer transmittances can be seen in Figure 4.1. It enables the comparison of single layer samples of both types (T and D).

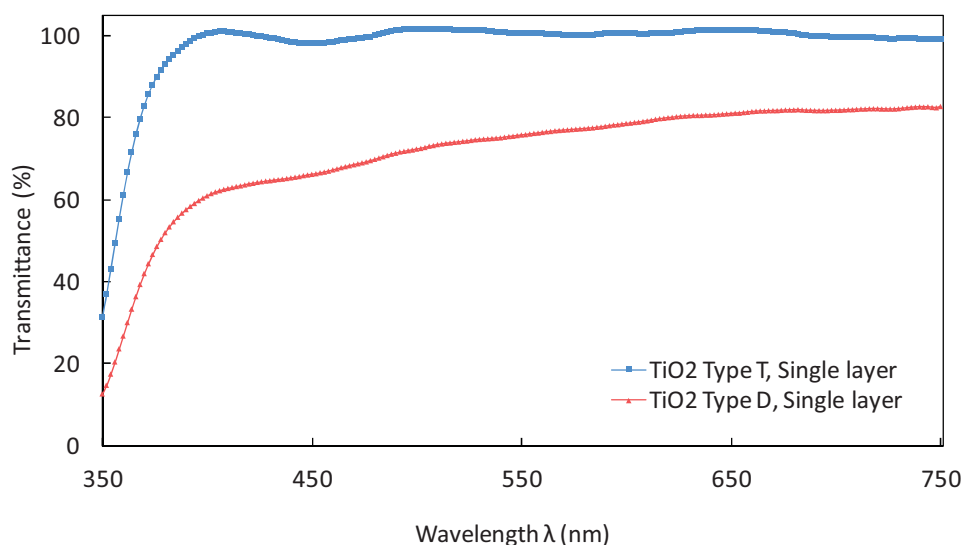


Figure 4.1 Transmittance measurements of TiO₂ type T and D. The measurements baselines were made from a FTO electrode without TiO₂ deposition. Both samples have nearly the same thickness.

For both samples, two different behaviours can be noticed. Below 400 nm wavelength, the TiO₂ layer absorbs the photons, whereas above 400 nm TiO₂ type T transmittance is higher and can be considered as transparent compared to TiO₂ type D. This latter kind of deposit is white opaque and exhibits predominant scattering due to the mixing of large and small nanoparticles that imply light diffusion. As the opaque layer transmits fewer photons (fewer photons would reach the sensitizer molecules), the performances will be impacted; we hence prefer to use the

transparent TiO₂ type T for our photoanodes fabrication for both DSSC and Ruthenium Phosphonate (Ru-Ru_{cat}) photoanodes.

Another benefit of type T deposit is that it experimentally shows more persistency for thicker deposit layers than type D. Hence a double layer film of type D shows less consistency than type T and it should be mentioned that we encountered the same problem for type T for thicker deposition ($\geq 2\mu\text{m}$). Attempts were made to obtain triple layer film for the T type but the result showed a modest consistency. Therefore, electrochemical tests haven't been carried out for triple layer electrodes, these experiments were limited to single (T1) and double (T2) layer electrodes of TiO₂ type T only.

The weak light absorption in the range 400-700 nm of the TiO₂ paste obviously implies the use of photosensitizer to widen the absorption range.

4.1.1.2 Transmittance measurements: effect of deposit thickness

Focusing only on T type paste, the transmittance and reflectance measurements for single and double layer TiO₂ electrodes (note that hereinafter when we mention TiO₂, it stands for TiO₂ type T), to evaluate the influence of thickness on transmittance. The results are presented in figures 4.2 and 4.3.

The baseline in these measurements is once again blank FTO electrode ($T > 83\%$ in the visible wavelength range) without any deposit. This means all transmittances and reflections are given based on assuming FTO transmittance and reflection are 100 and 0 % respectively.

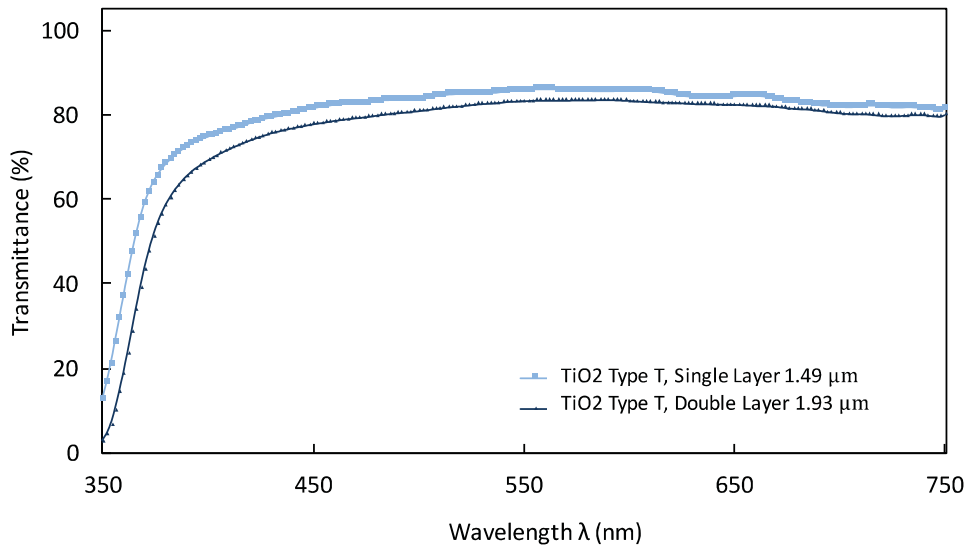


Figure 4.2 Transmittances of single and double layer electrodes of TiO_2 . The double layer electrode transmits less than the single layer because of higher thickness.

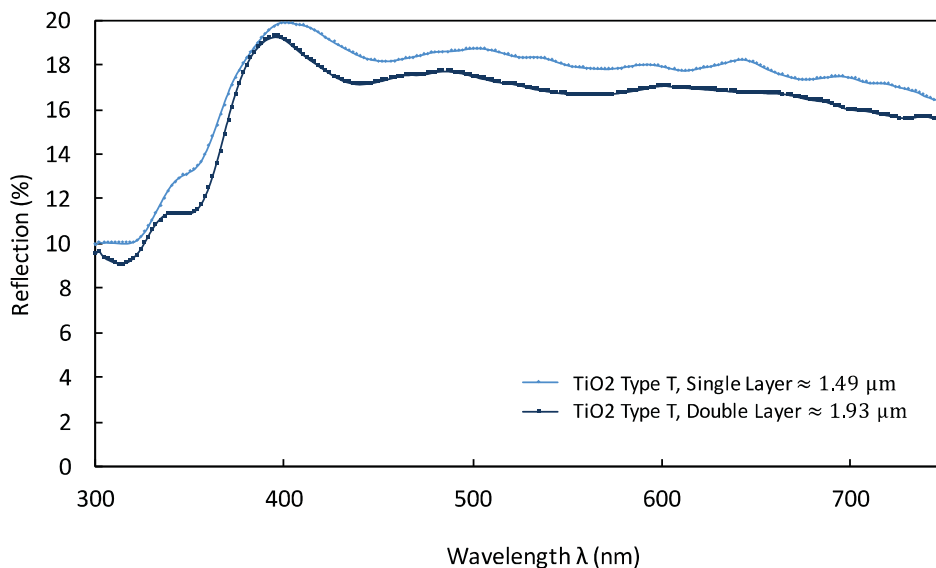


Figure 4.3 Reflectance results for the same electrodes presented in Figure 4.2. The single layer electrode reflects more than the double layer.

Figures 4.2 and 4.3 illustrate a tiny difference between single and double layer. This is because T paste in both cases becomes completely transparent after drying. So before dye impregnation on the semiconductor film the difference between single and double layer electrodes is not very significant although their performance might be different during electrochemical measurement. Having the transmittance and reflectance data permits us to calculate the exact part of radiation entering the cell and participating in reaction.

4.1.2 Electrochemical measurements

Different electrochemical and photoelectrochemical tests were run on the bare (without any coloration) TiO₂ electrodes: cyclic voltammetry and electrochemical impedance spectroscopy. In each experiment we have varied one of the scan rate, the incident photon flux density or the thickness factors while keeping the other parameter constant.

4.1.2.1 Characterization by cyclic voltammetry

(a)- Influence of scan rate at dark

We present a selection of Cyclic Voltammetry (CV) results, obtained for a single layer TiO₂ electrode at different scan rates with a tin oxide platinum covered counter electrode (Platisol on FTO glass). These measurements in 0.5 M degassed (oxygen has been removed) Na₂SO₄ electrolyte (pH ≈ 6) are shown in Figure 4.4.

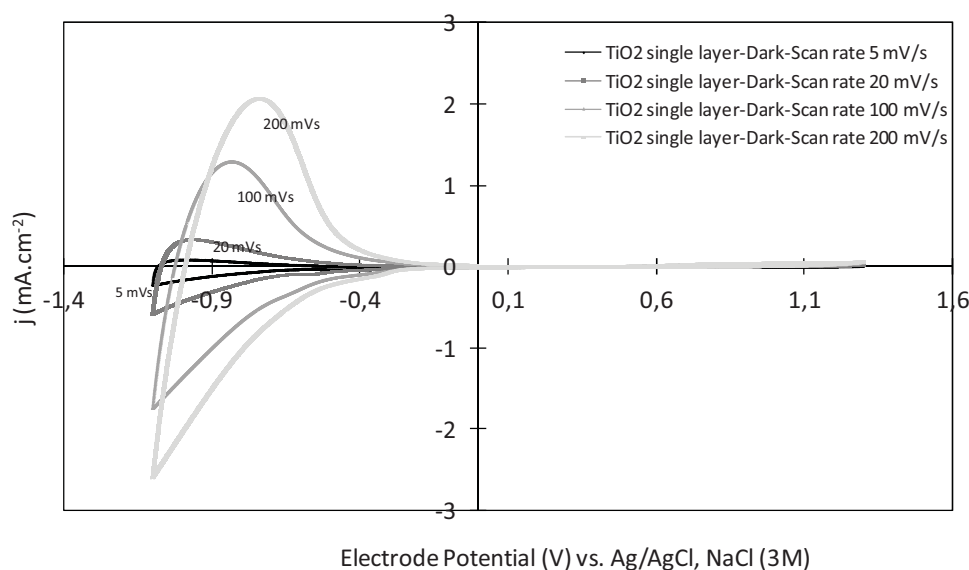


Figure 4.4 CV results of single layer TiO₂ electrode at different scan rate. The experiments were carried out at in aqueous electrolyte (pH ≈ 6).

The electrolyte was kept permanently under Argon atmosphere during the experience. The electrode was polarized in the potential range of -1.1 to 1.3 V vs. Ag/AgCl reference electrode. By varying the scan rate we see that the CV feature changes and the cathodic current shows a more or less linear increase by increasing the scan speed. The anodic peak at reversal current is not very distinguishable at low scan rates (5 mV.s⁻¹). This phenomenon is attributed to current loss even though there is some charge accumulation in the film. For higher scan rate the charge accumulation becomes more prevalent and so the anodic peak increases with the scan rate, the

film shows a more capacitive behaviour. According to (Francisco Fabregat-Santiago et al., 2003) under some assumptions we can simplify the relation of CV current to:

$$I = \frac{dQ}{dt} = C \cdot s \quad (4.1)$$

Where $s = dV/dt$, is the scan rate and C is the film capacitance. This relation is only reliable if the electron transfer between nanoparticles and electrolyte is negligible.

We can conclude that by increasing the scan rate the reversibility of the cycle increases as well as the total charge involved in the process by polarization. However, the small peak at low potential region may refer to surface states charging. This will be discussed further in this chapter.

Figure 4.5 presents the evolution of the peak current as a function of the scan rate for solution at given pH.

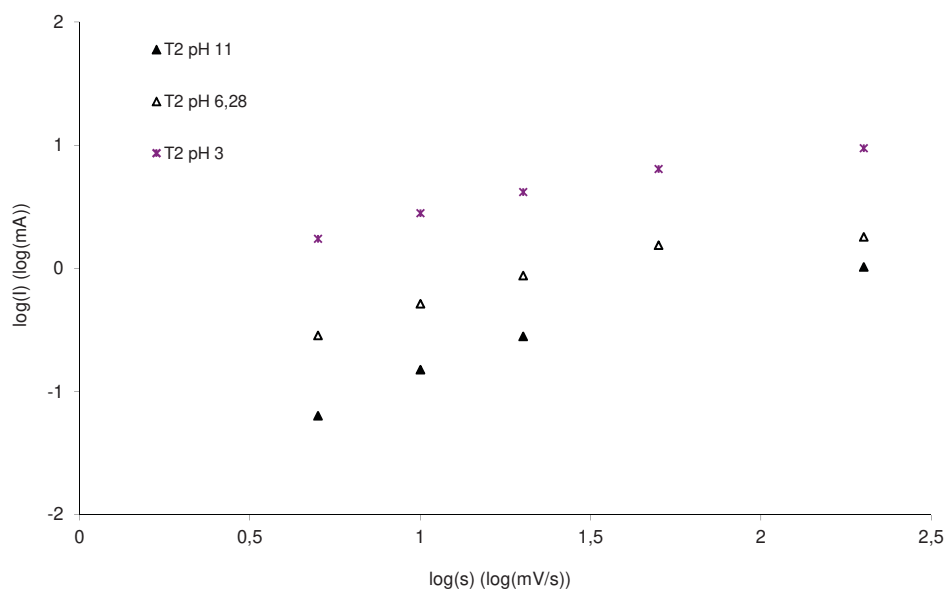


Figure 4.5 Experimental peak currents vs. scan rate at different pH Solution.

As can be seen in figure 4.5, the current peak increases as a function of scan rate. This conclusion has already been drawn from experiments in figure 4.4. The most interesting point is the evolution of current peak according to pH at a given scan rate. In fact, the capacitive aspect of the TiO_2 film is partly given by extended states and band gap localized states. A pH modification imply a change in the states of the electrode (either extended or band gap localized), altering the current peak.

(b)- Influence of photon flux density

The TiO₂ film under sufficient energetic illumination (photons whose energy is higher than the TiO₂ band gap) generates electron hole pairs. The holes could diffuse to the surface of TiO₂ and oxidize electrolyte's species at TiO₂/electrolyte interface. On the other hand the electrons travel the film bulk to the TiO₂-FTO interface where they will be collected at positive anodic bias. Hence if the photons are absorbed by the TiO₂ layer, the open circuit potential of the electrode will be different from the one measured in dark condition. Open circuit potentials measured at different photons flux densities (from 0 to 5000 $\mu\text{mol}\cdot\text{m}^{-2}\cdot\text{s}^{-1}$) appear to diminish non linearly (or even lognormally) from 0,18 to -0,08 and 0,18 to -0,28 V/(Ag/AgCl) for T1 and T2 electrodes respectively, hinting at a small photoactivity of the TiO₂ electrode in the visible range. The decrease of the open circuit potential according to photon flux density indicates that the synthesized TiO₂ layer is a n-type semiconductor as expected. Given this small photoactivity, the cyclic voltammeteries of the layer would be different from the one obtained at dark.

Figure 4.6 compares the CV results of a single layer TiO₂ electrode for different illumination intensities. Generally, at a constant operating temperature, by increasing the incident photon flux density the number of electron-holes pairs in film increases. Therefore, the film become more charged comparing to the dark condition for the same applied potential range.

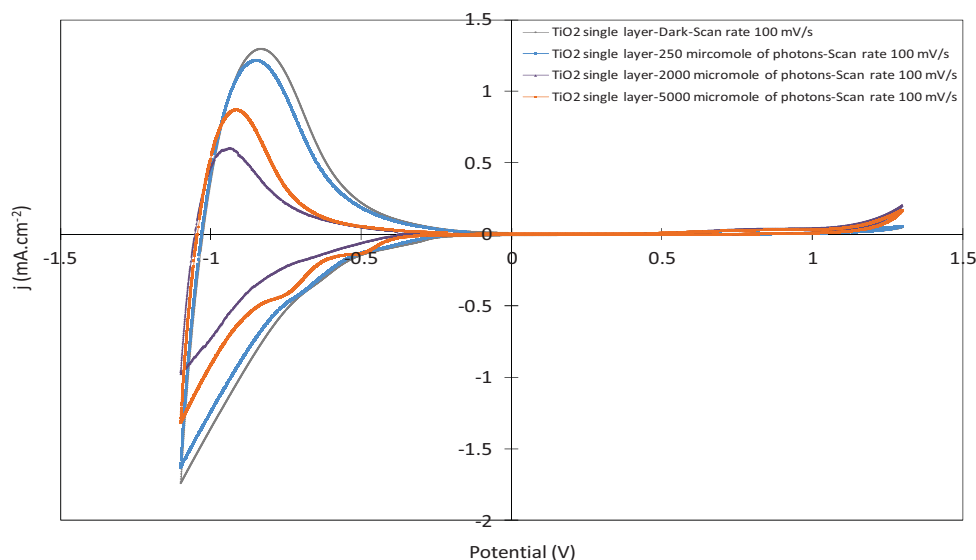


Figure 4.6 The effect of incident photon flux density on single layer TiO₂ electrode in 0.5 M Na₂SO₄ support electrolyte (pH≈6).

However, since we do not use an internal temperature regulation within the cell, by increasing the illumination intensity we certainly have a temperature variation within the cell (less than

10°C, at highest LED panel intensity). Although this variation is not very significant but it still can accelerate the interfacial charge transfer between TiO₂ film and electrolyte. This phenomenon as it has been discussed earlier in this chapter contributes to diminution of charge transfer resistance R_{rec} . Hence the film shows less capacitive behaviour and the anodic peaks decrease by temperature increasing.

(c)- Influence of thickness

TiO₂ electrodes with single and double layer thicknesses (1.49 and 1.93 μm) were tested. The cyclic voltammetry response of TiO₂ in 0.5 M aqueous degassed Na₂SO₄ (always under argon atmosphere) electrolyte at pH = 6 was recorded (Figure 4.7).

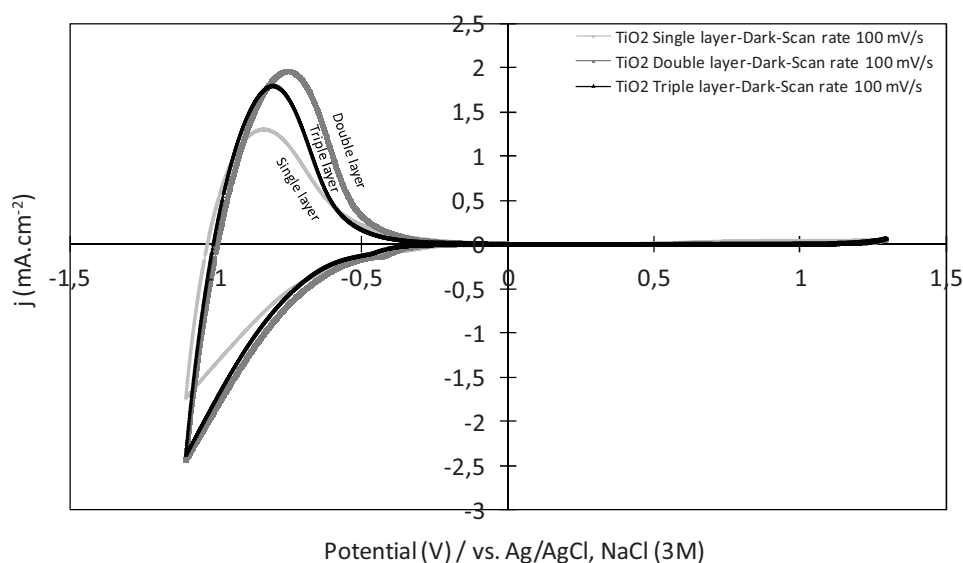


Figure 4.7 Effect of thickness variation for TiO₂ film in dark condition and at 100 mV/s scan rate. The cathodic current around -0.3V vs. Ag/AgCl corresponds to redox reaction of Ti ions on the surface.

According to (Kityakarn et al., 2012), the faradic current observed under -0.3 V vs. Ag/AgCl can be recognized as reduction of Ti⁴⁺ to Ti³⁺ under the reaction of:

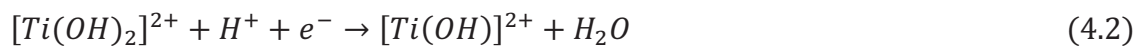


Figure 4.7 shows that this cathodic current changes with the number of TiO₂ layers. One strong assumption is the inner surface of the film and so the surface in contact with the electrolyte is proportional to the amount of TiO₂ deposited on the electrode and so the charge density per mass could be assumed constant or the total charge within the film grows almost linearly by increasing thickness of TiO₂ layer.

Note: Thicker layer of TiO₂ in this work (triple layer and more) might show a deviation of linear behaviour since the ideal behaviour of semiconductor layer is highly dependent upon the type

of semiconductor and also the film morphologies. Since our triple layer electrode does not present a homogenous feature of TiO_2 we may exclude the nonlinear result of this electrode from the rest of our study.

4.1.2.2 Impedance spectroscopy measurement

Impedance spectroscopy measurements were carried out in addition to cyclic voltammetry in order to characterize the TiO_2 layer without any photosensitisation at dark or under illumination conditions, at rest potential or with a given applied potential.

As explained in the third chapter, the experimental set-up is quite simple. Electrochemical impedance spectroscopy (EIS) tests were run on a system consisting of TiO_2 anode (TCO glass with a single thin layer of TiO_2), an Ag/AgCl reference electrode and a platinum cathode (Platisol brushed on TCO glass). The electrical equivalent model used to fit Nyquist impedance curves consists of:

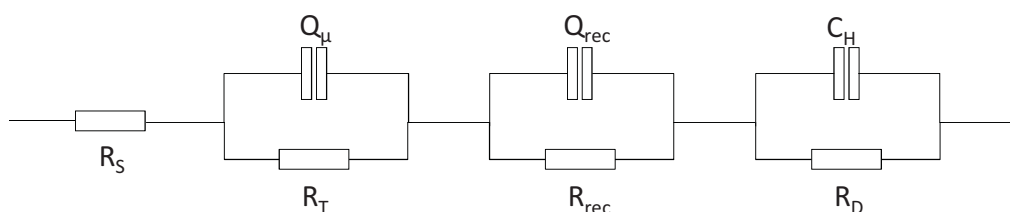


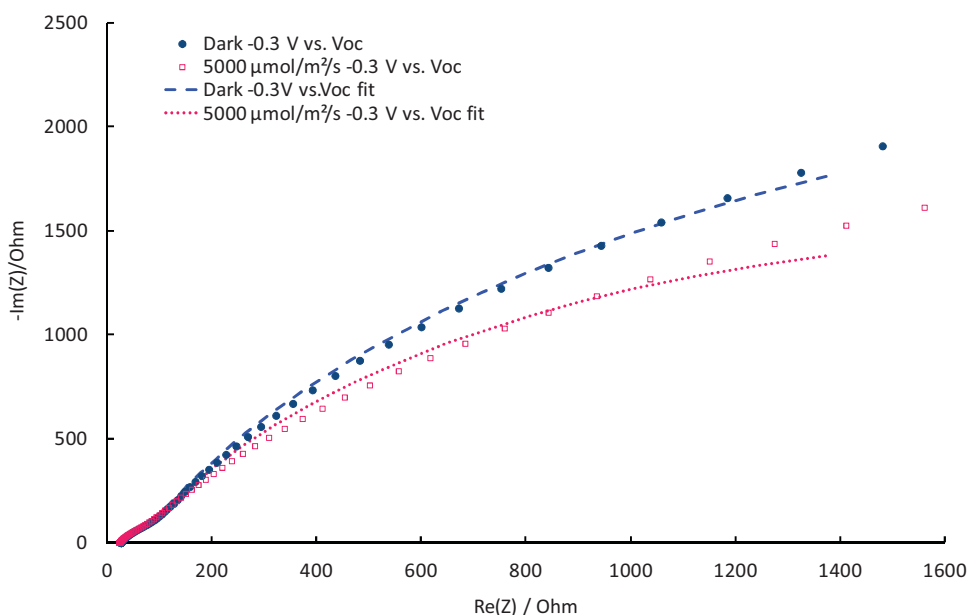
Figure 4.8 Electrical equivalent model of the TiO_2 electrode.

Where the parameters stand for:

R_S	Ohmic resistance of the system including glass ohmic resistance, wires, etc.
R_T	Charge transfer resistance within the TiO_2 electrode.
R_{rec}	Associated with R_T , represents the charge recombination resistance of TiO_2 electrode.
Q_μ	Constant phase elements (CPE) used as imperfect capacitor to model space charged capacitive behaviour of TiO_2 layer which also presents the capacitive behaviour of charge recombination.
Q_{rec}	
C_H	Helmholtz capacitor of double layer.
R_D	Diffusion resistance of electrolyte.

Figure 4.9 presents the impedance measured in dark and under illumination at 0.3 V vs V_{oc} . No drastic changes have been observed between two curves. The slight difference between two

arcs would be because of illumination and charging TiO₂ layer. Red and blue lines present the fitting curves issued from equivalent circuit (Figure 4.8).



4.9 Impedance and fitting results of T1 TiO₂ electrode without dye under dark and illumination conditions with 0.3 V vs V_{OC} applied potential in order to bring the electrode into oxidation (working zone).

Table 4.1 presents the equivalent circuit fitting results for EIS tests under dark (first row) and 5000 μmole of photons.m⁻² (second row) at applied potential of 0.3 V vs. V_{OC}. The ohmic resistance R_S remains quite constant.

Incident photon flux density (μmol/m ² /s)	R _S (Ω)	Q _μ	Q _{rec}	C _H (F)
0	2.56E+01	3.85E-05	9.87E-04	2.76E-04
5000	2.58E+01	7.26E-05	1.83E-04	1.24E-04
		R _T (Ω)	R _{rec} (Ω)	R _D (Ω)
		3.74E+05	1.40E+02	1.08E+03
		2.17E+05	4.02E+04	7.93E+03

Table 4.1 Fitting results of equivalent circuit for non photosensitized TiO₂ electrode under dark and illumination at 0.3 V applied bias vs. V_{OC}.

CPEs (shown as Q) model the behaviour of imperfect capacitors (the nanoporous semiconductors do not behave as ideal double-layer capacitor), yet it is possible to convert them to a pseudocapacitance. The value of the pseudocapacitance C for the R/C circuit giving the same characteristic frequency than that of the (R/Q) circuit is obtained from²:

² Note that $\alpha = 1$ describes an ideal capacitor while $\alpha = 0$ describes a pure resistor.

$$\omega_c = \frac{1}{(RQ)^{1/\alpha}} = \frac{1}{RC} \Rightarrow C = Q^{\frac{1}{\alpha}} R^{\frac{1}{\alpha}-1} \quad (4.3)$$

Table 4.2 shows calculated equivalent capacitance for charge transfer capacitance for both dark and illumination conditions which shows that under illumination we have a higher estimated value for charge transfer this is due to excitation at TiO₂ conduction band but since there is no photosensitization under both condition the value keeps the same magnitude, which is the same for charge transfer resistance.

Incident photon flux density (μmol/m ² /s)	R _s (Ω)
0	2.56E+01
5000	2.58E+01

C _{μ-pseudo}	C _{rec-pseudo}	C _H
4.12E-05	4.86E-04	2.76E-04
9.38E-05	2.00E-04	1.24E-04
R _T	R _{rec}	R _D
3.74E+05	1.40E+02	1.08E+03
2.17E+05	4.02E+04	7.93E+03
Z _μ	Z _{rec}	Z _D
2.60E+01	2.62E+03	1.71E+03
6.62E+01	2.40E+02	2.06E+02

Table 4.2 The same fitting results of equivalent circuit for non photosensitized TiO₂ presented in Table 4.1. C_{μ-pseudo} and C_{rec-pseudo} are estimated equivalent pseudo capacitances representing Q_μ and Q_{rec} if they were ideal linear capacitances. Z (impedance) values calculated impedances from C and R according to equation (4.4).

However, as capacitance increases, the resistance and so impedance reduces, regarding:

$$\frac{1}{Z} = \frac{1}{R} + j\omega C \quad (4.4)$$

the equivalent impedance value for charge transfer is calculated from:

$$Z_{eq} = Z_{\mu} + Z_{rec} \quad (4.5)$$

Incident photon flux density ($\mu\text{mol}/\text{m}^2/\text{s}$)	R_S
0	2.56E+01
5000	2.58E+01

C_μ	C_H
3.80E-05	2.76E-04
6.38E-05	1.24E-04
R_{TiO_2}	R_D
3.74E+05	1.08E+03
2.57E+05	7.93E+03
Z_{eq}	Z_D
2.65E+03	1.71E+03
3.06E+02	2.06E+02

Table 4.3 Equivalent circuit fitting results for TiO_2 cell with Pt cathode. $C_{\text{eq-pseudo}}$ is calculated equivalent capacitance representing space charge surface capacitance of TiO_2 layer in parallel with equivalent TiO_2 resistance, including charge transfer and recombination resistances.

4.2 Dye-Sensitized solar cell (DS-PEC³)

In this part the results obtained in the characterization of a commercial DSSC and the implementation of DSSC concept with Minucell will be detailed. The classical electrochemical experiments will be once again used to get information on the influence of operating parameters (dyeing, layer thickness, photon flux densities...) on the overall performances of the cell. At last, an energetic analysis of the cell performances will be carried out.

4.2.1 DSSC Solaronix characterization

The characterized device is the pre-assembled PICTO 1010 DEMO by Solaronix (*cf.* 3rd chapter) unequipped by a reference electrode; hence the electrochemical tests were limited to two electrode configuration. The tests were run on DSSC Solaronix are polarization, impedance spectroscopy.

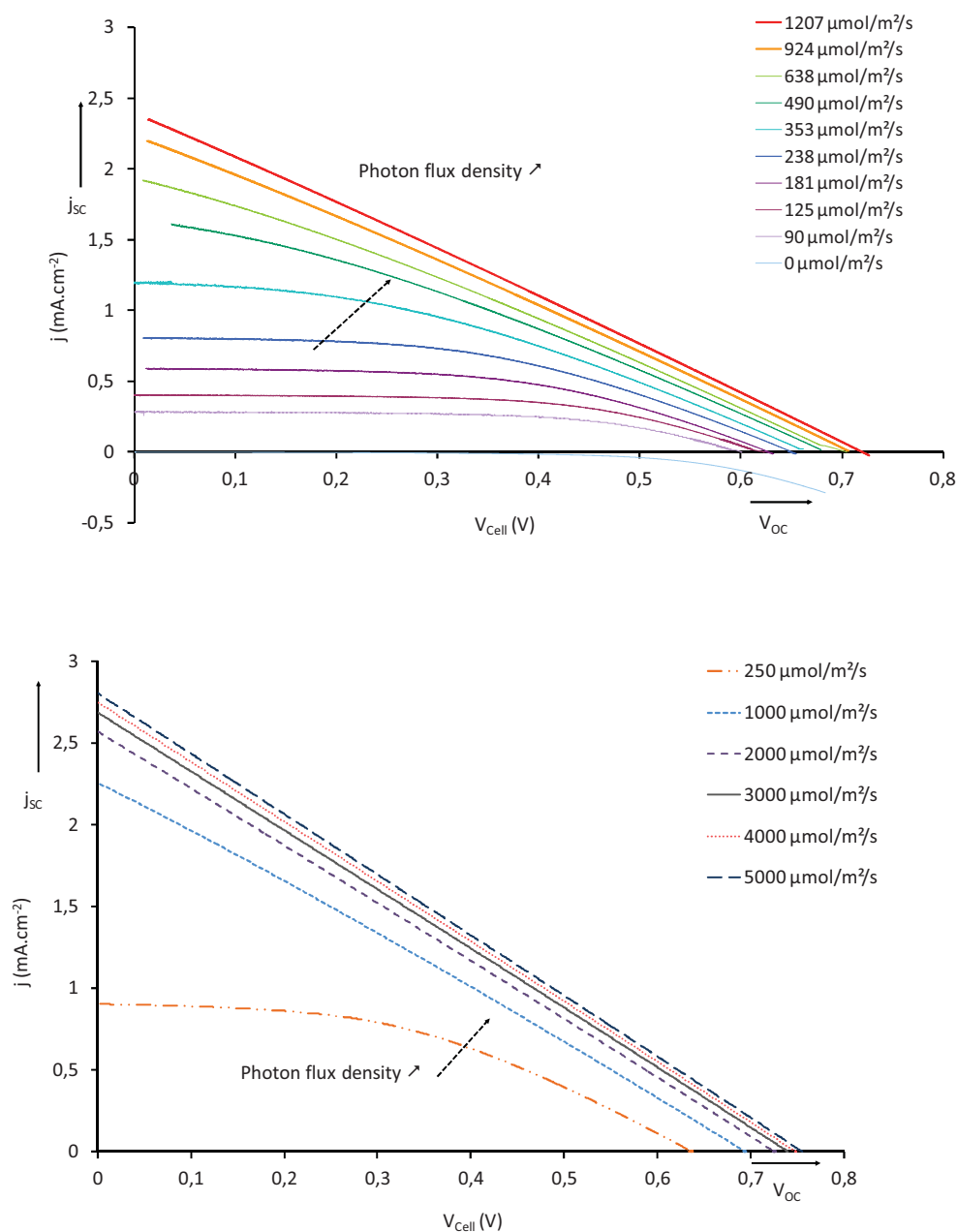
4.2.1.1 DSSC Solaronix current density-voltage

At the outset, current density voltage (jV) characterisations have been contemplated to acquire the necessary information about (a) short circuit current j_{SC} which is the maximum current circulating within the cell while the cell potential approaches to $V_{cell} = 0$; (b) open circuit voltage V_{OC} indicating the maximum potential difference of the cell when no current flows through the system ($j = 0$); (c) the theoretical surfacic electrical power of the system given by $P_T = j_{SC} \times V_{OC}$ as well as (d) maximum real surfacic electrical power ($P_{MAX} = \max(j \times V)$) and (e) the fill factor (FF) which is the ratio of P_{MAX} to P_T . The operating temperature can vary due to radiation and the ambient temperature fluctuation.

Since the temperature variation can highly influence the system response, the temperature was kept constant by ventilation during experiments to investigate only the effect of incident photon flux density⁴. Hereby we present jV curves of commercial DSSC for different photon flux densities in Figure 4.10. The illumination sources used during the experiments could be either a blue LED panel or the white LED panel. The emitted photon flux densities are adjustable by control software.

³ Refer to Chapter 2 Modelling.

⁴ Indeed, by ventilation the temperature around the cell constant is kept almost constant.



Figures 4.10 The commercial DSSC j/V results for different photon flux densities ($\mu\text{mol}\cdot\text{m}^{-2}\cdot\text{s}^{-1}$) of blue (a) and white (b) LED panels. We observe the development of V_{OC} to higher values as well as j_{SC} augmentation.

Three clear trends can be seen in figures 4.10. Firstly, the potential difference at open circuit, V_{OC} , decreases as the photon flux density increases. By increasing the incident photon flux density from 90 to 5000 $\mu\text{mol}\cdot\text{m}^{-2}\cdot\text{s}^{-1}$ (whatever the LED panel used), V_{OC} augments from 0.6 V to 0.72 V. The effect of illumination intensity becomes clearer when we compare V_{OC} values of DSSC under illumination to the open circuit potential in dark ($V_{OC} = 0.003$ V). This observation corresponds to the potential difference between the Fermi level electrons in the TiO_2 photoanode and the equilibrium potential of the redox couple used as a mediator, the latter parameter being slightly impacted by the photon flux density, the variation of the potential

difference at zero current is imputed to a modification of the Fermi level of the electrons in the photoanode under the effect of a larger number of excited dye molecules injecting their electrons into the conduction band of the semiconductor. As the electron density increases, the energy level, E_{CB} , of the conduction band is then modified until it reaches a constant value corresponding to a configuration of flat-band in the n-type semiconductor, which is TiO_2 . The overall shape of the current response corresponds to the behaviour electrochemical state of a single n-type semiconductor electrode (the potential of cathode being little influenced by a variation of the current density), with a photocurrent almost nil in the dark and an oxidation current depending on the photon flux density.

The second notable point is the increase in the current density, at a given potential, depending on the incident photon flux density. This phenomenon is easily explained by a greater flux of electrons collected, following a larger number of injections in the TiO_2 conduction band. Beyond a given value of the photon flux density, the characteristic curve of the cell $j = f(V_{cell})$ no longer changes, the dyes are no longer able to inject electrons into the conduction band at a higher rate (this saturation phenomenon is, to a certain extent, comparable to what appears in natural photosynthesis).

The third aspect is the visible change in the shape of the cell characteristic. With a low photon flux density (and therefore with a low current value), the curve $j = f(V_{cell})$ corresponds to characteristics usually encountered on laboratory photoelectrochemical cells. Then gradually, we observe a linearization, the current evolving proportionally according to the potential difference imposed on the cell. This can be explained by taking inspiration from the diode model conventionally developed in the photovoltaic literature as presented in the second chapter (figure 2.2). This model involves a series resistance, R_{serie} , dependent on the conductivities and thicknesses of the materials used, and a shunt resistance, R_{sh} , function of the phenomena recombination of the charge carriers (e^-) before their collection. Our results indicate that this latter resistance decreases strongly according to the density of flow of incident photons. This finding is consistent; indeed an increase of photon flux density implies a higher charge carrier density in the photoanode and therefore higher recombination rates.

As a consequence of the polarization curve, it is possible to calculate the surfacic power obtained when operating the cell with different photon flux densities. Figure 4.11 presents these results with the typical bell curve ranging from V_{OC} to 0 V. The maxima of the curves P_{max} appears to continuously rise with the photon flux density.

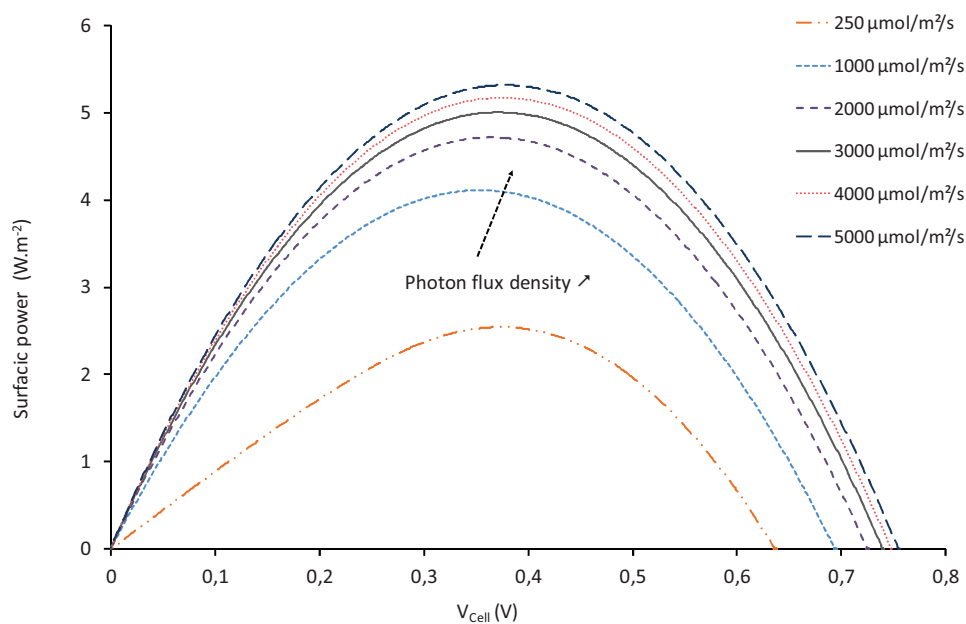


Figure 4.11 Surface power of the cell according to cell voltage for different photon flux densities with white LED panel

This first schematic representation of the photoelectrochemical cell in the form of an equivalent electrical circuit (diode model) allows us to make the transition to the very useful electrochemical technique, the electrochemical impedance spectroscopy (EIS). It will enable us to get more information about resistive and capacitive behaviour of the DSSC under illumination and/or with an applied bias.

4.2.1.2 DSSC Solaronix EIS study

(a)- Photon flux density effect

The electrochemical impedance spectroscopy (EIS) tests were carried out at the same photon flux densities as jV plots and for different applied potential on the cell. Figure 4.12 presents equivalent circuit that will be used for the analysis of the Nyquist plots.

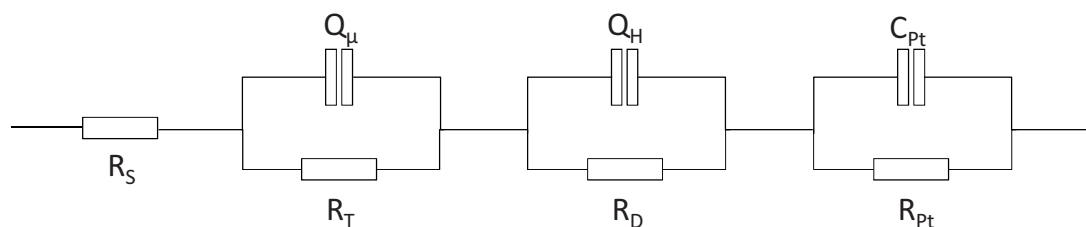


Figure 4.12 Electrical equivalent model of the DSSC.

The electrical elements stand for:

R_S	Ohmic resistance of the system including glass ohmic resistance, wires, etc .
R_T	Charge transfer resistance of the photoanode in which there is also the charge recombination resistance within the photoanode but they are modelled within the same resistance.
R_D	Diffusion resistance at the interface of photoanode and electrolyte.
Q_μ	Constant phase elements (CPE) used as imperfect capacitor to model space charged capacitive behaviour of photoanode.
Q_H	Constant phase elements (CPE) used as imperfect capacitor to model the capacitive behaviour of charge recombination
C_{Pt}	Helmholtz capacitor of double layer at cathode side.
R_{Pt}	Cathode resistance.

Figure 4.13 presents Nyquist plots of EIS results only under dark condition. Because of high values of impedance under dark condition, other impedance results obtained under illumination are not visible in this figure 4.13, so data are reported in figure 4.14 that illustrates a comparative zoom in the low impedance region.

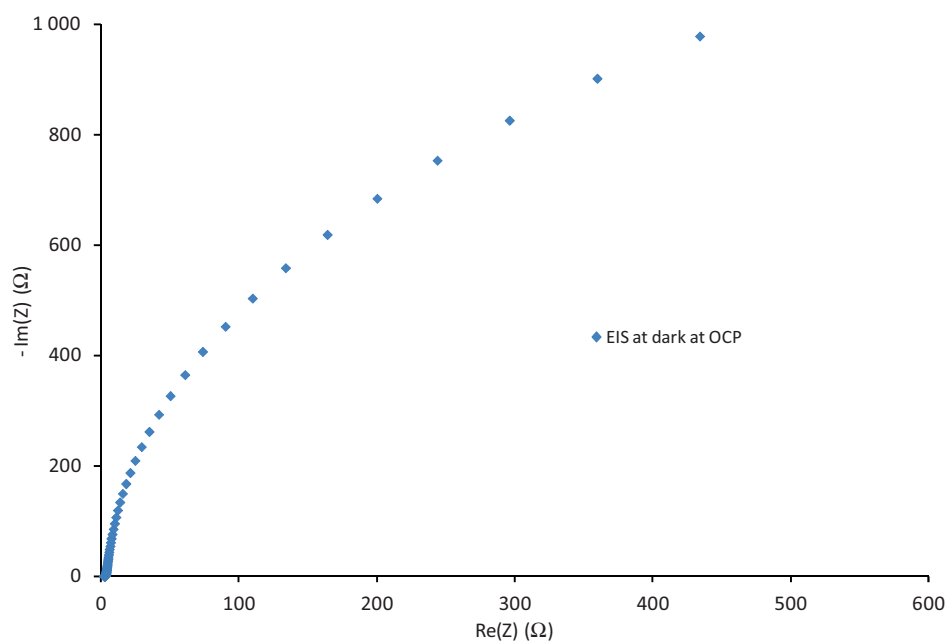


Figure 4.13 Commercial DSSC impedance spectra in the dark at V_{OC} . One semi circle with high impedances (real and imaginary part) appears.

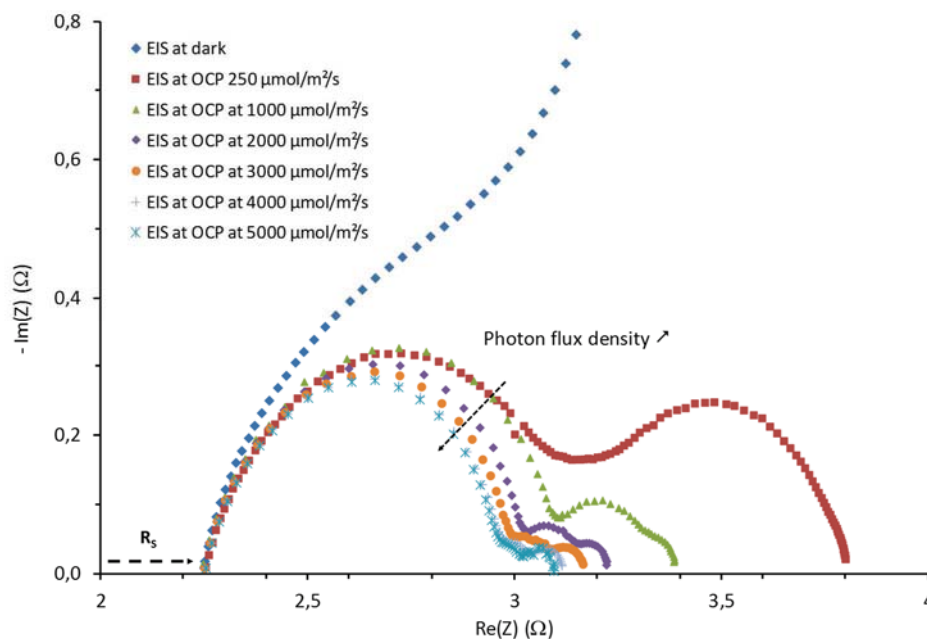


Figure 4.14 Impedance spectra of commercial DSSC at V_{OC} at dark and for different photon flux densities for the white LED panel. The shift from origin on abscissa axis corresponds R_s .

The results shown in Figure 4.13 and Figure 4.14 are obtained with a two electrode setup without a reference electrode. Accordingly, the results correspond to the overall impedance of the Solaronix DSSC. We observe a reduction in both real and imaginary parts of impedance values. Also, in low frequency range, the impedance feature changes by increasing the photon flux density; means diffusion and charge transfer phenomena are more visible at such fluxes.

The results show that series resistances, R_s , remain constant with photon flux density. Note that series resistances do not change the shape of the EIS spectra but they make a shift in the Nyquist diagram along the horizontal axe (see Figure 4.14).

Incident photon flux density ($\mu\text{mol}/\text{m}^2/\text{s}$)	R_s (Ω)
0	2.33
250	2.26
2000	2.26
5000	2.27

Table 4.4 Equivalent circuit of series resistances for commercial DSSC commercial under either of dark or illumination conditions. The series resistances remain rather constant during the whole experience (dark and illumination conditions).

If we consider one of the Nyquist diagram in Figure 4.14, the first semicircle appearing at high frequencies (beginning of the curve at low impedance value) represents the resistance of counter electrode and the capacitance of double layer at the counter electrode-electrolyte interface. The

low frequency semicircle (high impedance) corresponds to the diffusion of I_3^- ions within the double layer at anode-electrolyte interface. At intermediate frequencies; a second semicircle which appears between the counter electrode and double layer diffusion arc is attributed to charge transport resistance within anode electrode TiO_2 film with sensitizer (the electrode is dyed). For low photon flux densities ($250 \mu\text{mol}/\text{m}^2/\text{s}$) this arc is merged with diffusion arc. At higher densities, all semicircles decrease significantly especially the TiO_2 film semicircle which now becomes completely discriminated from diffusion arc. The resistance of counter electrode reduces slightly with illumination increment and subsequently the capacitance increases because of increasing interfacial charge transfer.

Incident photon flux density ($\mu\text{mol}/\text{m}^2/\text{s}$)	C_{Pt} (F)	R_{Pt} (Ω)	Q_{dl}	R_T (Ω)	C_H (F)	R_D (Ω)
0	7.45E-05	9.08E-01	3.08E-03	1.52E+00	5.97E-04	2.70E+03
250	3.24E-04	7.40E-01	1.22E-01	5.44E-01	7.83E-02	2.73E-01
2000	2.99E-04	7.70E-01	2.32E-01	1.14E-01	8.08E-02	9.48E-02
5000	3.07E-04	7.22E-01	1.77E-01	5.27E-02	2.82E+00	6.35E-02

Table 4.5 The results of equivalent circuit of commercial DSSC under either dark or illumination conditions. The counter electrode impedance values (both imaginary and real parts) changes between dark and illumination because of current circulation from photoanode and remains quite constant for different illumination intensities. Charge transfer resistance within the photoanode reduces by increasing the photon flux density and the space charge capacitance increases due to the charging the space charges after photon absorption and electron injection in the conduction band. There is also more charge exchange at the photoanode and electrolyte interface between so the diffusion resistance decreases but also Helmholtz capacitance corresponding to the double layer capacitance increases by presence of more charge accumulation at the interface.

The effect of illumination according to (F. Fabregat-Santiago et al 2007) can be related firstly to the temperature increasing which increases the charge transfer at the interface. Considering Equation 2.39, the charge transfer resistance (recombination resistance) in TiO_2 is inversely proportional with the temperature. It can be also considered as the reason of increasing charge transfer at counter electrode-electrolyte interface. It is also reported by the same author that the temperature augmentation can also diminish the viscosity of the electrolyte which can affect the diffusion resistance due to an increase in the diffusion coefficient of electroactive species. However in our experiments we tried to avoid temperature variation by using ventilation system (but it is still not negligible); the decrease of semicircles in size can be the consequence of increasing triiodide (I_3^-) ion concentration locally in the pores under illumination and following the dye oxidation. Having more triiodide ions present at the interface increases the rate of recombination between electrolyte and TiO_2 conduction band which means the charge recombination resistance R_{rec} decreases. This phenomenon is visible in Figure 4.14.

Illumination reduces also the charge transport resistance of TiO_2 and it becomes completely insignificant comparing to the dark condition (Francisco Fabregat-Santiago et al 2005).

(b)- Cell operating tension

Another parameter that could be investigated in the case of a DSSC is the operating tension of the cell from V_{OC} to a potential corresponding to j_{SC} . Such an evolution in the case of can be seen in figure 4.15 at a low photon flux density ($250 \mu\text{mol}\cdot\text{m}^{-2}\cdot\text{s}^{-1}$).

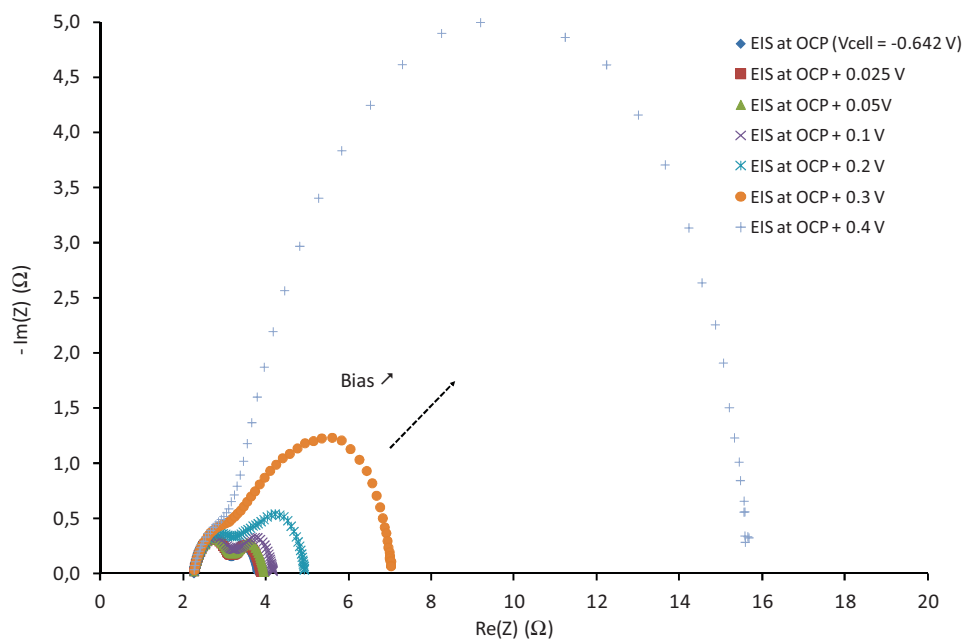


Figure 4.15 Impedance spectra of commercial DSSC at a given photon flux density ($250 \mu\text{mol}/\text{m}^2/\text{s}$, with white LED) for different bias compared to V_{OC} .

In that case, the cell was under reverse bias to carry out oxidation at the photoanode. It can be noticed that the higher the bias, the bigger is the semi circle corresponding to the photoanode and ion diffusion. This could be explained by a variation in the electron Fermi level of the electron generating a variation of the capacitance of the photoelectrode and in the modification of ion concentration profile in the cell.

4.2.2 DS-PEC implementation with Minucell

Based on the commercial DSSC, we fabricated the same photoanode and cathode (using almost the same material) on smaller size⁵ adequate to be used in Minucell. The same characterization tests, such as transmission, polarization or EIS, were run.

4.2.2.1 DS-PEC photoanode characterisation

The photoanode of DSSC consisted in an electrode with TiO₂ film, impregnated in a 300 μ M solution of sensitizer (Ruthenizer 535-bis TBA) solubilised in absolute ethanol. The electrode should be rinsed before use, with the same solvent as the impregnated solution. Two electrodes with single and double thickness T paste type were prepared.

(a)- Transmittance measurements of the dyed photoanode

Before using electrodes in the cell, the transmittance for each electrode was measured for further thermodynamic efficiency calculation. Figure 4.16 compares these values for different thicknesses. The difference of transmittance values between single and double layer films becomes more significant after coloration with dye.

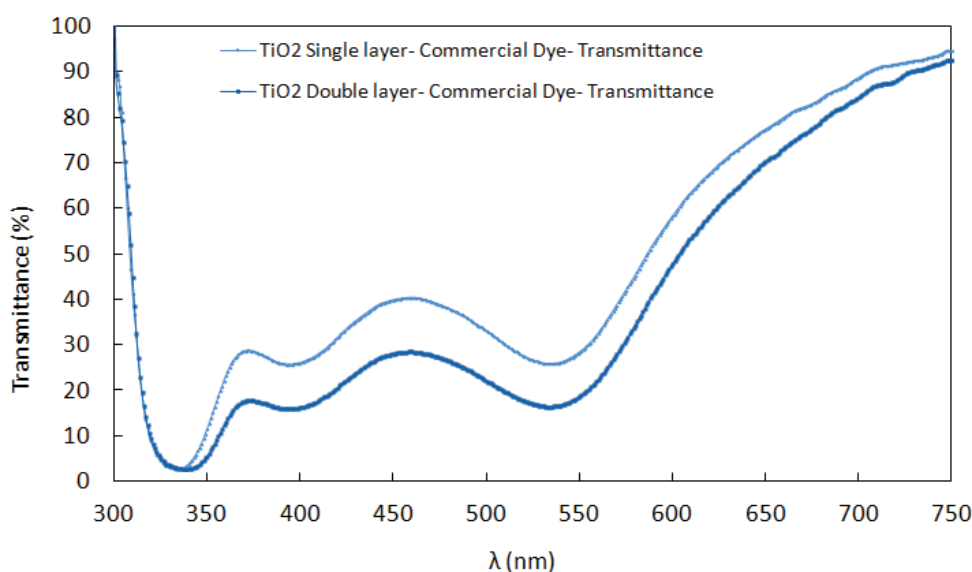


Figure 4.16 Transmittance of single and double layer TiO₂ film impregnated with Ruthenizer 535-bis TBA dye molecules. Measurements accomplished with FTO blank electrode as base line.

We observe that a double layer film transmits less and reflects (not shown here) more than a monolayer film. The Ruthenizer 535-bis TBA molecules absorption spectrum presents 3

⁵ For further information please refer to Chapter 3 Material and Methods.

absorption peaks at 312 nm, 395 nm and 535 nm wavelength, which can be seen in figure 4.16 in comparison with figure 4.1.

(b)- Polarization under illumination conditions

The implementation of DSSC within Minucell includes polarization tests and electrochemical impedance spectroscopy under dark and illumination conditions. These tests are similar to Solaronix DSSC experiments and the results will be compared together. However, by adapting DSSC cell in Minucell we had also the possibility to run the tests for different photoanode thicknesses or dyes which was not possible to investigate in the commercial version of Solaronix.

In the next figure (Figure 4.17), Minucell device was used with a single layer, T1, TiO₂ photoelectrode as photoanode and a platinum pasted FTO electrode as a counter electrode. The support electrolyte was Iodolyte⁶. The measurements were accomplished in two electrode setup without using a reference electrode.

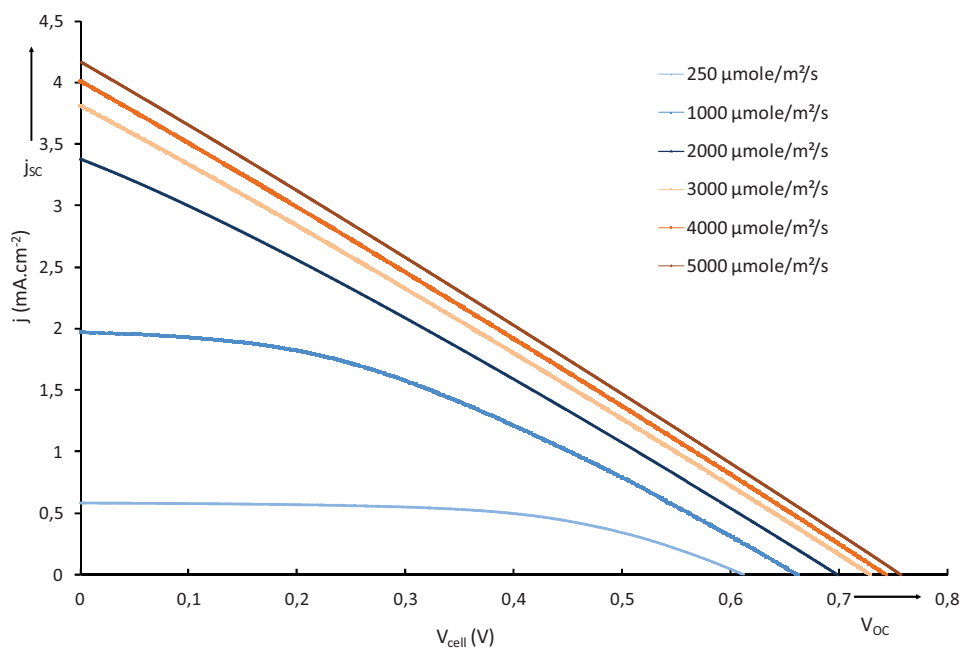


Figure 4.17 Current- potential difference (jV) curve of a DSSC using T1 TiO₂ photoanode dyed with Ruthenizer 535-bis TBA, for different photon flux densities (white LED panel). Tests are accomplished at two electrode setup.

In the same way as for Solaronix DSSC, the three previous clear trends (V_{OC} and j_{sc} increases and jV shape modification) can be seen in figure 4.17. Hence the potential difference at open circuit, V_{OC} , decreases with an increase in the photon flux density. By increasing the light

⁶ For more information refer to Chapter 3 Material and Methods.

intensity from 250 to 5000 $\mu\text{mol}\cdot\text{m}^{-2}\cdot\text{s}^{-1}$ with white LED panel, V_{OC} rises (in terms of absolute value) from -0.61 V to -0.76 V for the same reason (potential difference evolution between the Fermi level electrons in the TiO_2 photoanode and the equilibrium potential of the redox couple used) as in Solaronix cell. The current density, at a given potential, once again increases from 0.5 to 4.15 $\text{mA}\cdot\text{cm}^{-2}$ (a higher current density value than in Solaronix DSSC) depending on the incident photon flux density. The saturation phenomenon still appears but to a lesser extent.

The same kind of experiments was repeated using a double layer (T2) dyed photoanode. A comparison between cells respectively equipped with T1 or T2 dyed photoanode is given in figure 4.18.

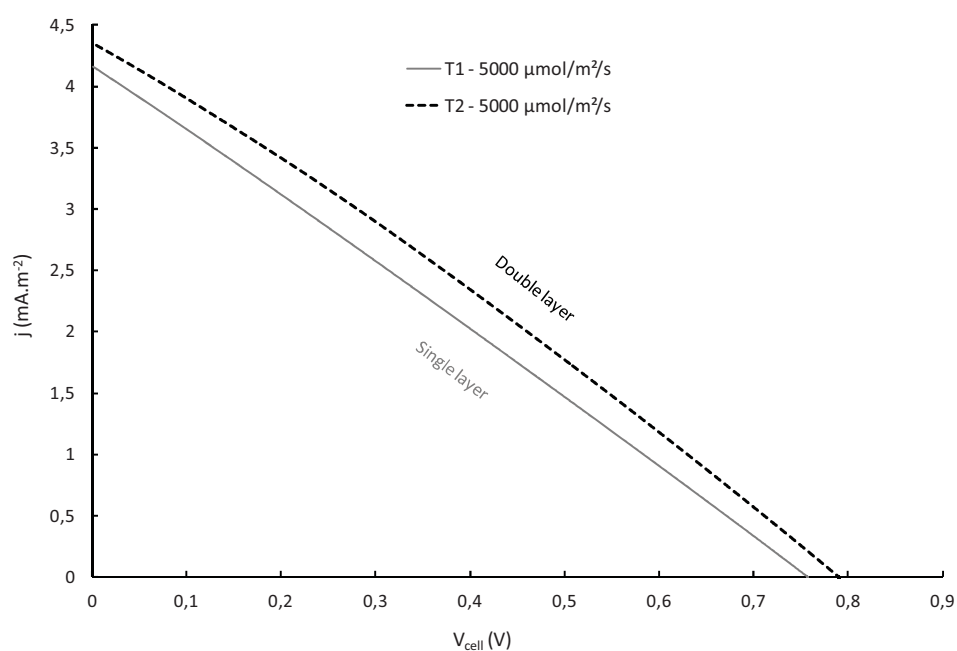


Figure 4.18 Comparison of polarization results for single, T₁, and double, T₂, layer photoelectrodes. All experiment parameters including the photon flux density were kept constant during both experiences.

Whatever the photon flux density, the double layer electrode presents a higher V_{OC} and j_{sc} . Referring to the previous discussion about thickness variation of TiO_2 electrode we might relate this observation to the fact that the inner surface of film and so the surface in contact with the electrolyte for double layer electrode is larger than the inner surface of single layer film. Beside, according to the transmittance results a thicker layer of TiO_2 adsorbs more dye molecules. Hence the photocurrent density increases by increasing the film thickness.

In the same way as in figure 4.11 (for Solaronix PEC), the surfacic power density for DS-PEC using Minucell is calculated; the results are presented in figure 4.19.

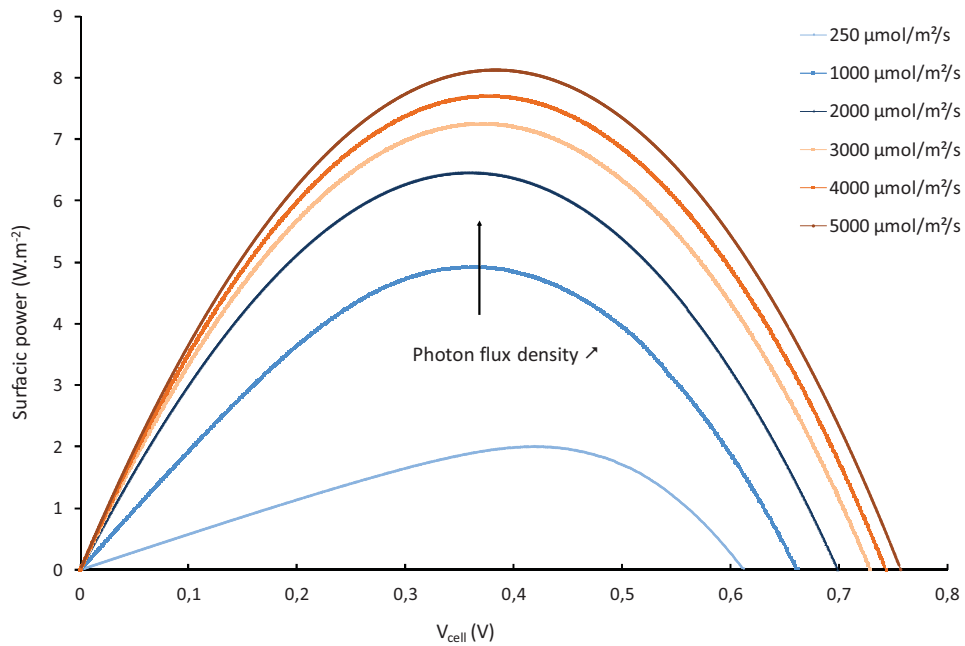
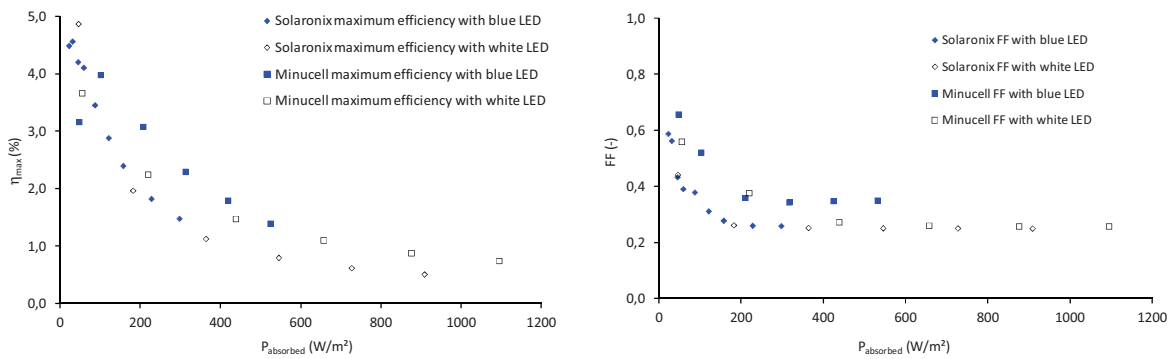


Figure 4.19 Surfacic power density of the Minucell DSSC (using T1 TiO₂ photoanode dyed with Ruthenizer 535-bis TBA) according to cell voltage for different photon flux densities using white LED panel.

(c)- Comparison between Solaronix and Minucell DS PEC on an energetic point of view

The next figures (Figures 4.20 a and b) present respectively the evolutions of the cell efficiency and fill factor (FF) according to the absorbed surfacic power (either for Minucell or Solaronix DS PEC).



Figures 4.20 a) Maximum efficiency of the cells; b) Fill factor (FF) of the cells according to the surfacic power absorbed.

By observing Figure 4.20 a), one can notice a clear decrease of the maximum efficiency according to the surfacic power absorbed. This can be related with the saturation phenomenon observed when the photon flux density increases: the voltage of the cell, V_{cell} , doesn't change

although the photon flux density rises. The current density evolving linearly with V_{cell} the maximum efficiency kept on decreasing.

Related to this efficiency diminution, the fill factor FF decreases and then remains constant as the absorbed power rises. The plateau that is reached corresponds to a DS PEC behavior purely resistive.

(d)- Electrochemical Impedance Spectroscopy

Once again the EIS technique is used to gain further information on the different phenomena which take place in the photoelectrochemical cell. The objective is hence to test our photoelectrochemical cell (Minucell) with EIS and to compare it with the Solaronix DSSC as a reference.

The experimental set up system consists Minucell with a photoanode made of TiO_2 electrode covered with a layer of sensitizer (the electrode is red) and a cathode made of tin oxide glass electrode covered by a platinum deposit (Platisol)⁷. The electrolyte is Iodolyte, the same as in commercial DSSC. The measurements were set with two electrode configuration with no reference electrode to have the same measurement conditions as for DSSC Solaronix. The EIS tests were carried out at dark and different illumination intensities at V_{OC} (without applied bias) as shown in Figure 4.21 (presenting Minucell EIS with T1 TiO_2 photoanode). The frequency range is between 200 kHz and 1 mHz, with an applied amplitude of 30 mV around V_{OC} . The equivalent electrical circuit used is the same as previously (*cf.* figure 4.12)

The EIS results obtained in dark condition are not shown in this graph because of high impedance values which flatten other curves but the identified parameters are presented in Tables 4.6 and 4.7.

⁷ For more information about the electrodes compositions and methods of fabrication, refer to Chapter 3.

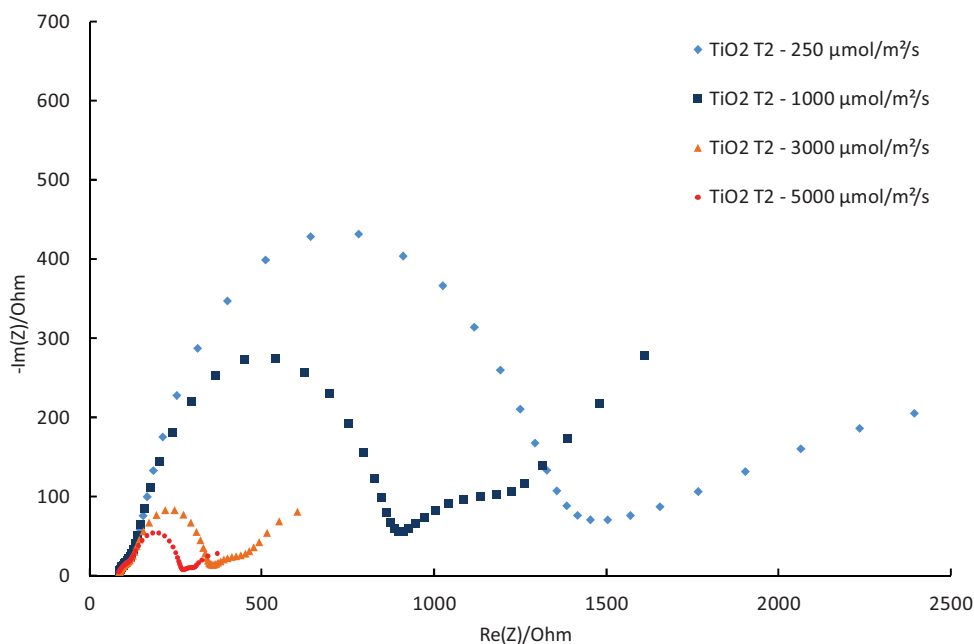


Figure 4.21 Nyquist diagrams of DSSC implementation in Minucell at V_{OC} , $1 \text{ mHz} < f < 200 \text{ kHz}$ and at different photon flux densities.

By comparing the EIS results with Solaronix DSSC, the offset at the abscissa, R_s , corresponding to ohmic resistance of the system including glass and wire resistance is higher (far above the 2Ω observed previously). In addition to this first statement, we could highlight in the high frequency zone (not very visible in Figure 4.21) the occurrence of a small semi circle which corresponds to R_{Pt} contribution in parallel with Helmholtz capacitance of counter electrode double layer C_{Pt} . The size of this semicircle is smaller comparing to the impedance results of Solaronix DSSC in Figure 4.14. The intermediate frequency arc is attributed to the charge transport resistance, R_T , of the photoanode film in parallel with the space charge capacitance C_μ . The last part resistance of diffusion of I_3^- and I^- ions at the interface, R_D , in parallel with Helmholtz capacitance at photoanode-electrolyte interface C_H .

Tables 4.6 and 4.7 present the values of these parameters. The series resistances, R_s , remain roughly constant during the whole experience (dark and illumination conditions).

Incident photon flux density ($\mu\text{mol}/\text{m}^2/\text{s}$)	R_s (Ω)
0	87.9
250	80.6
1000	78.8
5000	77.9

Table 4.6 Equivalent circuit of series resistances for DS-PEC with Minucell under either of dark and illumination conditions.

Incident photon flux density ($\mu\text{mol}/\text{m}^2/\text{s}$)	Q_{Pt}	$R_{\text{Pt}} (\Omega)$	Q_{dl}	$R_{\text{T}} (\Omega)$	$C_{\text{H}} (\text{F})$	$R_{\text{D}} (\Omega)$
0	2.74E-03	6.41E+00	5.02E-05	2.13E+04	5.49E-05	4.66E+04
250	7.22E-05	1.36E+00	4.82E-03	4.72E+01	3.80E-04	5.65E+01
1000	2.92E-04	9.32E-01	1.73E-03	1.22E+01	1.95E-03	3.16E+00
5000	1.56E-03	9.62E-01	1.15E-03	1.18E+00	1.10E-03	3.32E+00

Incident photon flux density ($\mu\text{mol}/\text{m}^2/\text{s}$)	$C_{\text{Pt-Pseudo}} (\text{F})$	$R_{\text{Pt}} (\Omega)$	$C_{\text{dl-Pseudo}} (\text{F})$	$R_{\text{T}} (\Omega)$	$C_{\text{H}} (\text{F})$	$R_{\text{D}} (\Omega)$
0	1.86E-03	6.41E+00	5.34E-05	2.13E+04	5.49E-05	4.66E+04
250	7.37E-01	1.36E+00	3.68E-03	4.72E+01	3.80E-04	5.65E+01
1000	0.00E+00	9.32E-01	8.50E-04	1.22E+01	1.95E-03	3.16E+00
5000	1.04E+00	9.62E-01	3.41E-04	1.18E+00	1.10E-03	3.32E+00

Table 4.7 Identified parameters for the equivalent circuit of DS-PEC with Minucell under either of dark and illumination conditions.

As can be noticed in table 4.7, a significant decrease is observed in TiO_2 film resistance by increasing photon flux density. Consequently the surface states get charged and chemical capacitance of the film increases. The reason of decreasing TiO_2 film resistance by illumination has been given earlier during Solaronix DSSC discussion. Charge transfer resistance within the photoanode reduces by increasing the photon flux density and the space charge capacitance increases because of charging the space charges by more photons and so electron flux from conduction band. There is more charge exchange at the photoanode and electrolyte interface. It can also be seen that Helmholtz capacitance corresponding to the double layer capacitance increases by presence of this charge accumulation at the interface. The low frequency semicircle (high impedance) corresponding to the diffusion of I_3^- ions within the double layer at anode-electrolyte interface is more visible in Minucell DSSC comparing to Solaronix because the larger electrolyte compartment and so the mass transport resistance due to tri-iodide diffusion increases.

Implementing DSSC in Minucell gives us the possibility to study the thickness variation effect on the impedance spectra which has been largely neglected in the literature. To this purpose, in figures 4.22 and 4.23, are presented the Nyquist diagrams of PEC at open circuit for two thicknesses and two different photon flux densities. As can be seen, the features of the spectra are different.

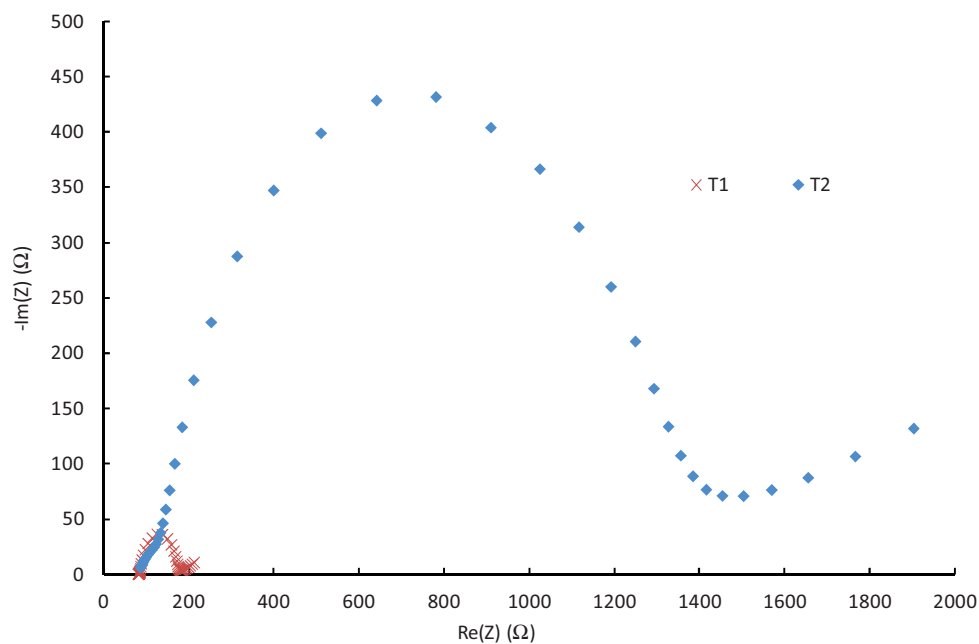


Figure 4.22 Nyquist diagram of DSSC implementation in Minucell at V_{OC} for single (T1) and double (T2) layer photoanodes at low photon flux density ($250 \mu\text{mol}/\text{m}^2/\text{s}$).

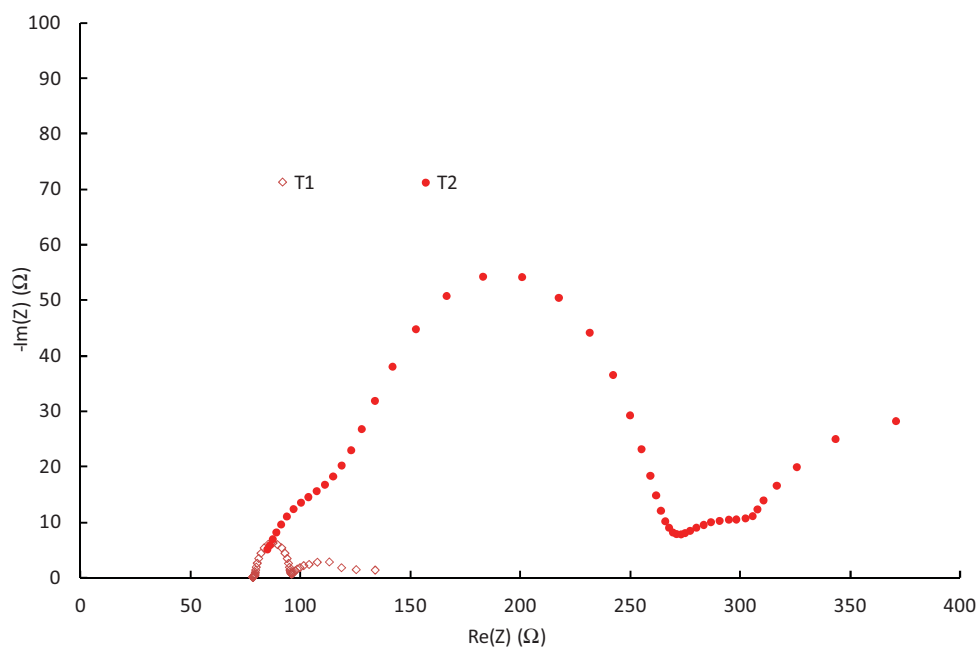


Figure 4.23 Nyquist diagram of DSSC implementation in Minucell at V_{OC} for single (T1) and double (T2) layer photoanodes at high photon flux density ($5000 \mu\text{mol}/\text{m}^2/\text{s}$).

There is a small difference between the first arcs of the two features in Figure 4.22. Since the platinum cathode did not change during the experience this may come from the Helmholtz dielectric capacitance of photoanode which overlaps with the counter electrode arc at the limit of 100 kHz frequency regions. However, the significant change appears in the semiconductor film and the intermediate semi-circle increases with thickness. We may take a look to model

parameters presented in chapter “Modelling” where charge transfer resistance, electron transport resistance and chemical capacitance are related to the film thickness regarding their formulation: $R_{\text{rec}} = r_{\text{rec}}^{-1}L$, $R_{\text{T}} = r_{\text{T}}L$, $C_{\mu} = c_{\mu}L$ where L is the film thickness. We also notice that the recombination resistance increase exponentially with thickness. Hence generally the impedance of the PEC will rise by increasing the thickness of the photoanode. It is then preferable to work with thin layer of deposit on the photoanode to minimize recombination and charge transfer resistance within the photoanode, provided it ensures efficient photon absorption.

4.3 DS-PEC⁸ characterization (molecular ruthenium based)

After implementing DSSC within Minucell and approving its use for photoelectrochemical measurement, photoanodes impregnated by ruthenium chromophores (Ru) and catalyst (Ru_{cat}) were tested. However, for better understanding the effect of each molecule (chromophore and catalyst), the tests were divided in 3 steps: firstly with a photoanode impregnated only with chromophore with its characterizations. Secondly the photoanode was prepared with only catalyst, its properties are determined. Finally the photoanode was impregnated with both chromophore and catalyst molecules.

4.3.1 Ru chromophore photoanode

First of all we tested the electrode with only Ru chromophore molecules engrafted on TiO₂ film. The results of this part correspond to the transmittance measurements of impregnation solutions as well as impregnated photoanodes together with the electrochemical characterisation of Ru chromophore photoanode.

4.3.1.1 Transmittance measurements with chromophore (Ru) impregnation

The impregnation solution of chromophore was prepared by solvating the chromophore in deionised water (concentration 200 µM). The transmittance of the solution was measured before impregnating TiO₂ electrodes (Figure 4.23; black line). Single and double layer TiO₂ electrode (T1 and T2) were separately impregnated with the same solution volume. Afterward the transmittance of the solution of each container was quantified. These measurements are presented and compared in Figure 4.23.

⁸ Refer to Chapter 2 Modelling.

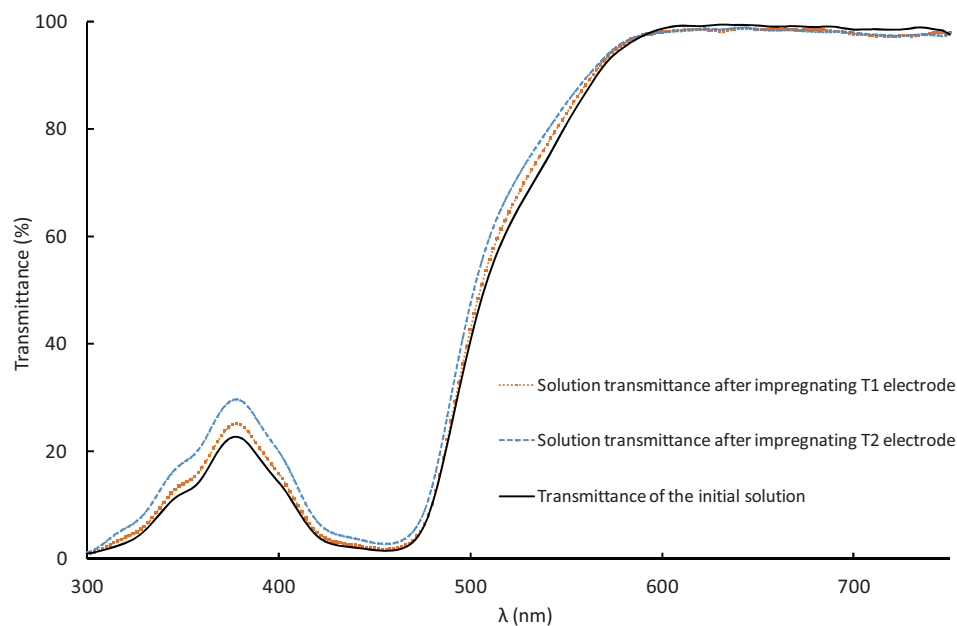


Figure 4.23 Transmittances of chromophore impregnation solution before and after impregnating T1 and T2 TiO_2 electrodes. Measurements done with deionised water as base line.

As expected (considering its chemical formula) the dye has a broad absorption band in the range [300-550 nm]. The absorption band around 455 nm corresponds to a transition of metal-ligand charge transfer type (MLCT), the one of low intensity around 350 nm may be caused by an intrametal transition (orbital d-d). The band around 300 nm is attributed to a transition $\pi\text{-}\pi^*$ intraligand. The use of this dye will therefore allow photon absorption well beyond the 380 nm associated with TiO_2 . The exploitation of the transmission spectrum of the initial solution (in black) allows the determination of the dye absorption coefficient.

Both solutions after impregnation show higher transmittance values comparing to the initial solution (before the impregnation). The solution used for T2 electrode transmits slightly more than the solution of single layer electrode. The amount of adsorbed chromophore is therefore higher on a thicker electrode.

It should be mentioned that, as a result of impregnation, a clear visual difference can be noticed between the electrodes. They are coloured to bright red and the double layer electrode is more chromatic than single layer. The electrode transmittances were subsequently measured, the figure 4.24 presents the obtained results.

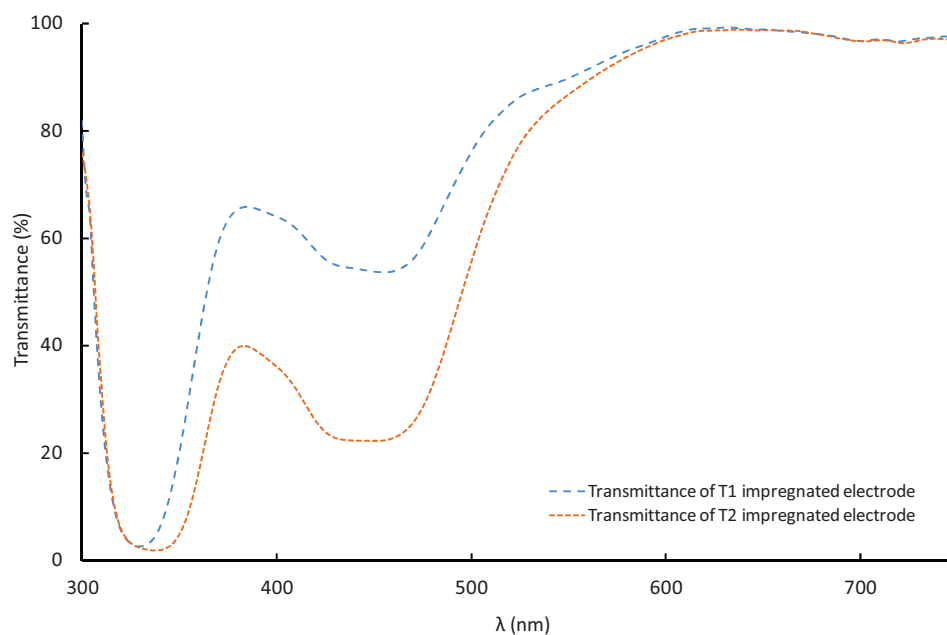


Figure 4.24 Transmittance of T1 and T2 TiO_2 electrodes impregnated with Ru chromophore. Measurements accomplished with FTO blank electrode as base line.

The results presented in Figure 4.24 are in agreement with the impregnation solution transmittances: the single layer electrode displays more transparency in comparison with double layer electrode. The double layer electrode contains more chromophore molecules than single layer electrode. Moreover the spectrum shapes are typically influenced by the presence of the chromophore adsorbed on the surface (low transmission at 350 nm, plateau at 450 nm...).

Transmittance measurements of the impregnation solution after impregnation enable (via a mass balance and the knowledge of the absorption coefficient) the estimation of the amount of adsorbed dye. This parameter that is dependent of the solution concentration is around $2\text{-}3 \cdot 10^{-4} \text{ mol.m}^{-2}$.

4.3.1.2 Electrochemical characterization of Ru chromophore photoanode

Electrochemical tests were accomplished for single and double layer electrodes impregnated with Ru chromophores under dark and illumination conditions. A solution containing a support electrolyte (Na_2SO_4 0.1 M at pH 6.08) was used. Figure 4.25 shows T1 electrode with Ru chromophore characterized by cyclic voltammetry in dark. The electrode was polarised between -0.5 and 1.7 V vs. Ag/AgCl NaCl 3M. The photoelectrode does not show any oxidation peak under dark condition and the current density is almost negligible ($10^{-7} \text{ mA.cm}^{-2}$) regarding the polarisation range. The hysteresis loop obtained is typical of CV experiments; its amplitude depends on the scan rate, as seen for TiO_2 electrodes.

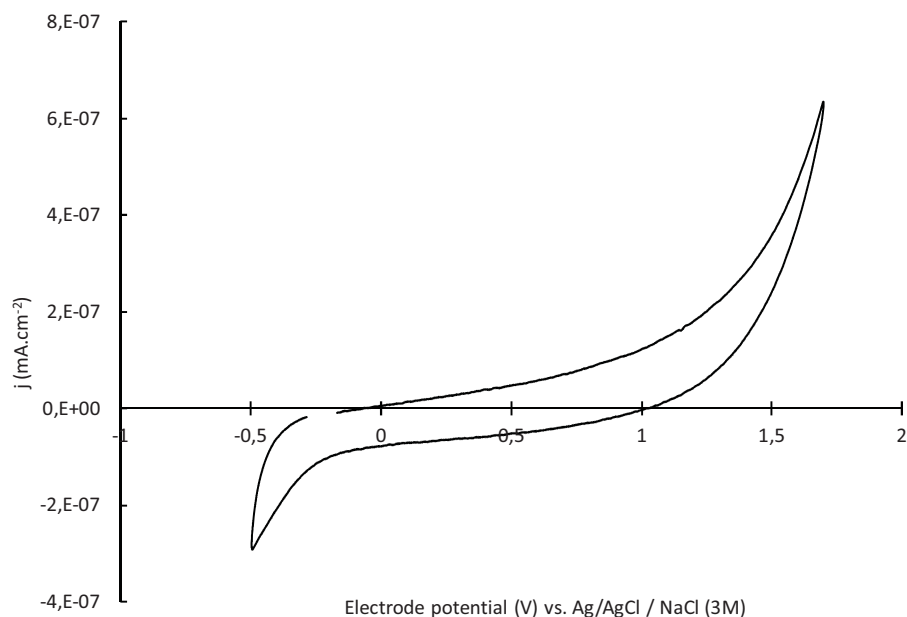


Figure 4.255 Cyclic voltammety of T1 anode with Ru chromophore in dark and aqueous electrolyte at a 100 mV/s scan rate. The T2 photoanode presents the same behavior at dark

Figure 4.26 shows CV results of double layer Ru electrode for two given photon flux densities where photocurrent reaches to 0.83 mA.cm^{-2} at maximum LED power ($5000 \mu\text{mol/m}^2/\text{s}$).

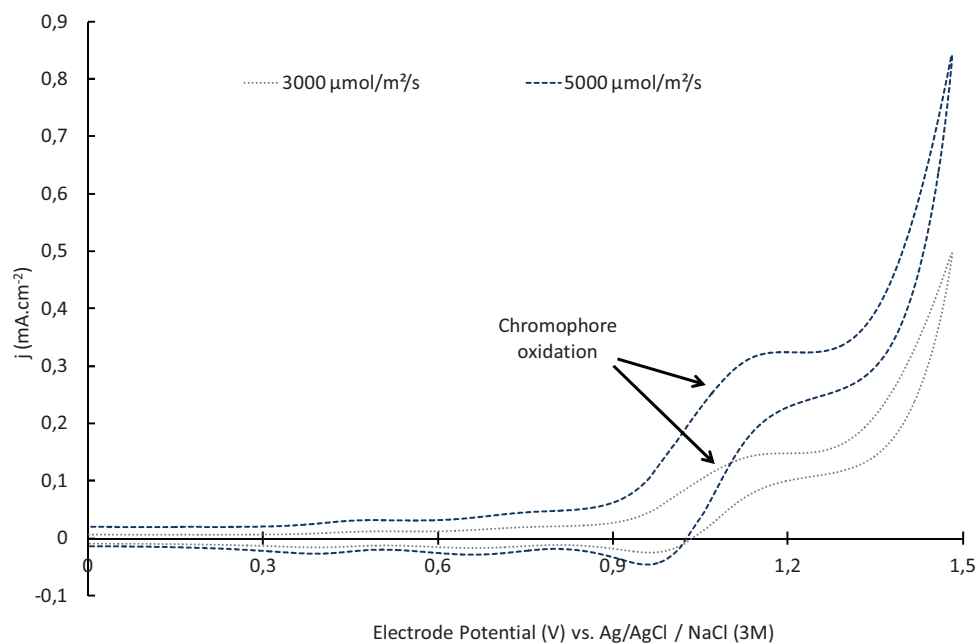


Figure 4.26 Cyclic voltammety of T2 Ru electrode for different illumination intensities. the photoelectrode was polarised between 0 to 1.5 V vs. Ag/AgCl NaCl (3M) at a 100 mV/s scan rate.

Under illumination the results are significantly different (Figure 4.26). Thus, the open circuit potential of the electrode is shifted towards negative value (-0.17 to -0.21 V/ref); the current density at a given potential increases according the photon flux density. We observe an

oxidation peak corresponding to Ru chromophores around 1.1 V vs. Ag/AgCl where we reach to plateau of 0.34 mA.cm^{-2} at anodic biasing and maximum incident photon flux density. The numbers of experiments were limited because the chromophores are consumed after some experiments and since there is no regenerating system (or sacrificial donor) the photoanode suffers the lack of stability over the time.

4.3.2 Ru_{Cat} catalyst photoanode

To understand the optical and electrochemical characteristics of Ru_{Cat} catalyst molecules we prepared the electrodes by using only Ru_{Cat} molecules. The results of transmittance and electrochemical measurements are presented in the following paragraphs.

4.3.2.1 Transmittance of catalyst Ru_{Cat} impregnation

An impregnation solution with Ru_{Cat} catalyst was prepared with similar procedure to the electrode with chromophore. The solution was prepared with deionised water and Ru_{Cat} molecules with the concentration of $200 \mu\text{M}$. Figure 4.27 presents the transmittance results of the Ru_{Cat} solution before and after impregnation process.

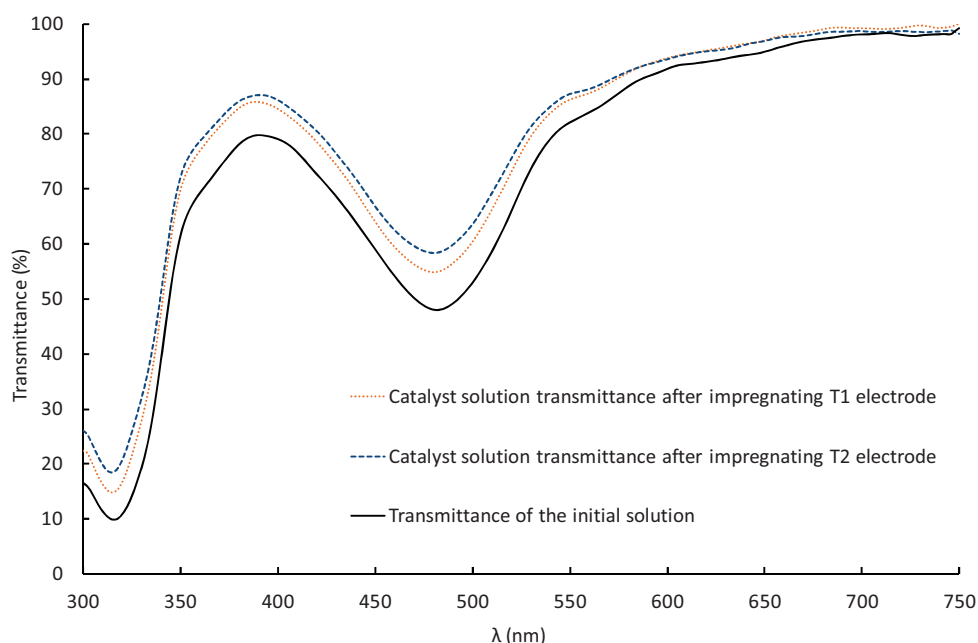


Figure 4.27 Transmittance of catalyst impregnation solutions before and after impregnating single (T1) and double (T2) layer electrodes. Measurements accomplished with deionised water as baseline.

Thanks to figure 4.27, it is possible to compare the results of single and double layer electrode solutions and it confirms that a higher amount of catalyst is adsorbed on the T2 TiO₂ film than on T1.

After dyeing, the electrodes of Ru_{Cat} are coloured to bright pink. However the colouration is less remarkable compared with Ru electrodes. It can be seen in figure 4.28 that presents the transmittance of T1 and T2 TiO₂ electrodes with Ru_{Cat} adsorbed.

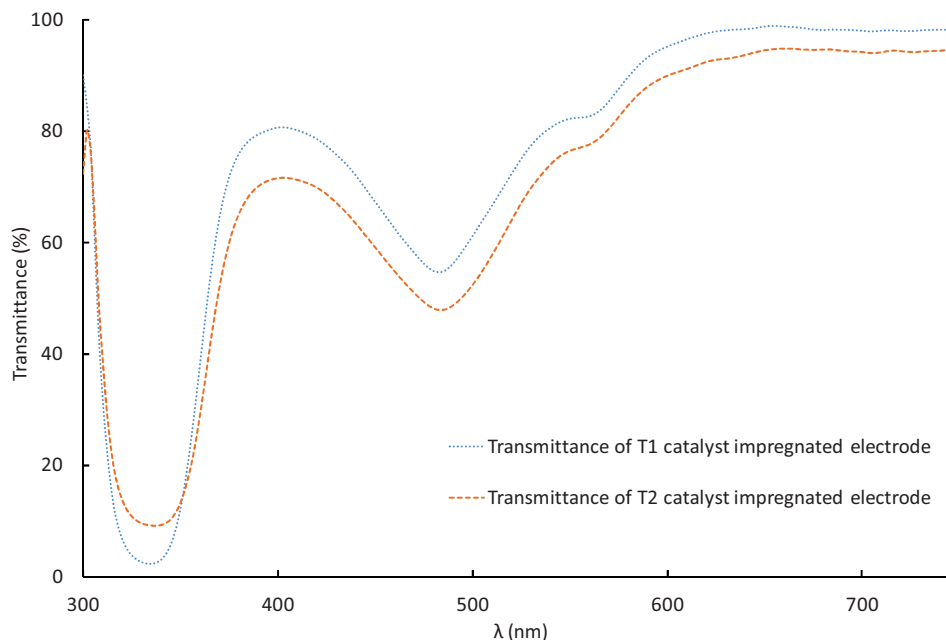


Figure 4.28 Transmittance of single and double layer electrodes impregnated with Ru_{Cat} catalyst. Measurements accomplished with FTO blank electrode as baseline.

As suggested by the solution transmittance measurement, the T1 electrode transmits more than the T2 (6 points of transmittance). This cannot only be explained by a thicker deposit. We can conclude that there is more Ru_{Cat} molecules present on the surface of double layer electrode than the single layer electrode.

4.3.2.2 Electrochemical characterisation of Ru_{Cat} catalyst photoanode

The T1 and T2 electrodes impregnated with Ru_{Cat} catalyst were characterized under dark and illumination conditions. The support electrolyte was Na₂SO₄, 0.1 M and pH 6.08. The results of CV tests are shown in Figure 4.29 for a T1 Ru_{Cat} electrode. The electrode was polarised between 0 and 1.5 V vs. Ag/AgCl 3 M in dark, and in the range 0-1.2 V under illumination. Despite the potential ranges are different, we indeed observe a difference between illumination and dark CV results but we do not gain too much difference in photocurrent density. It approves that using only catalyst will not make a complete photoelectrochemical system and it needs to be coupled with chromophore molecules which show stronger chromatic properties. In contrast by using only chromophores without catalysts we realized that the electrodes show less stability

and the film is not durable because after some number of experiences the film on the photoanode in contact with the electrolyte is removed.

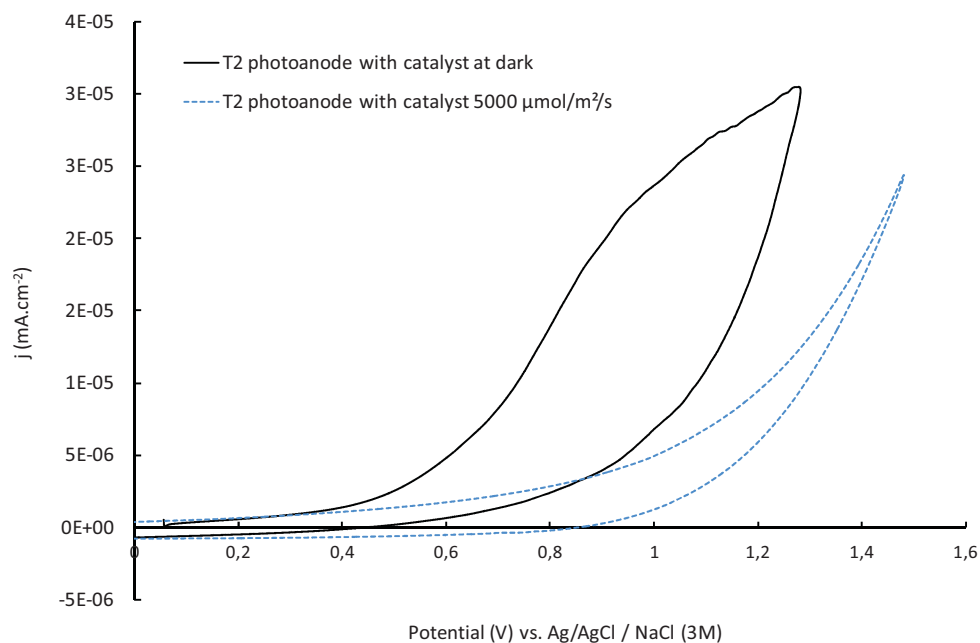


Figure 4.29 Cyclic voltammetry of double layer Ru_{Cat} electrode under dark and illumination condition. Scan rate 100 mV/s

This observation may be due to an electrode evolution during the whole tests. By polarising the photoanode, adsorbed chromophore may have evolved as we do not have the possibility to regenerate them. Hence as it was contemplated we made photoanodes impregnated in a solution containing both Ru chromophores and Ru_{Cat} catalysts.

4.3.3 Ru-Ru_{Cat} chromophore-catalyst photoanode

The following sections are devoted to exchange views on results of optical properties of electrodes (transmittance, reflectance) and electrochemical characterisation.

4.3.3.1 Transmittance of Ru-Ru_{Cat} chromophore-catalyst impregnation

The impregnation solution was prepared with a mixture of Ru chromophore and Ru_{Cat} catalyst molecules with the ratio of 1:1 (at initial solution concentrations equal to 200 μM) in deionised water. The solution transmittances before and after impregnation are presented in figure 4.30.

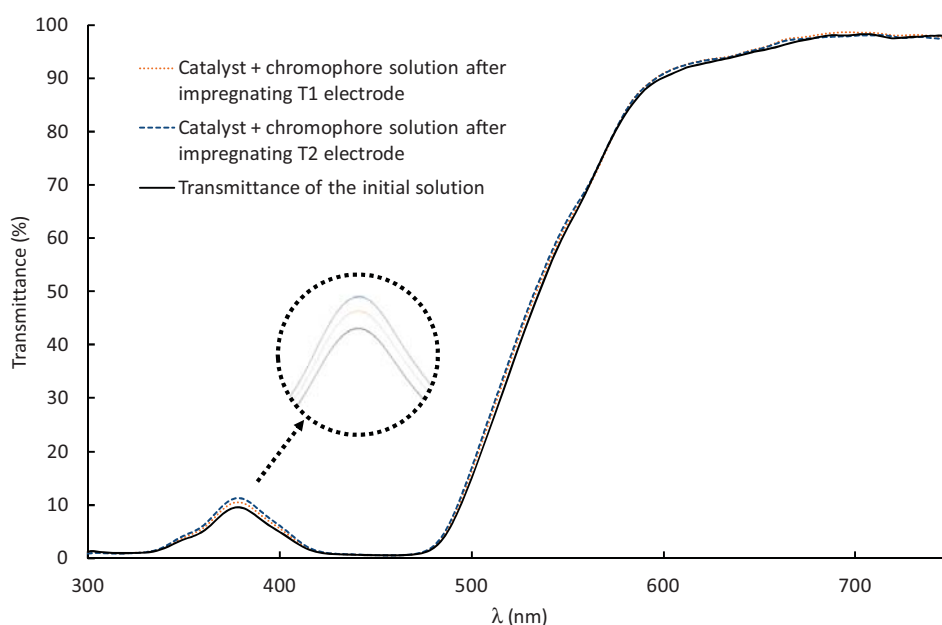


Figure 4.30 Transmittances of chromophore-catalyst impregnation solutions before and after impregnating of T1 and T2 layer electrodes. Measurements accomplished with deionised water as base line.

Only a small difference can be seen in the transmission spectra in the 350-450 nm range of wavelength indicating a small difference in the quantity of chromophore and catalyst adsorbed. On the contrary, as shown in figure 4.31, the transmittance measurements of T1 and T2 impregnated photoanodes are slightly different.

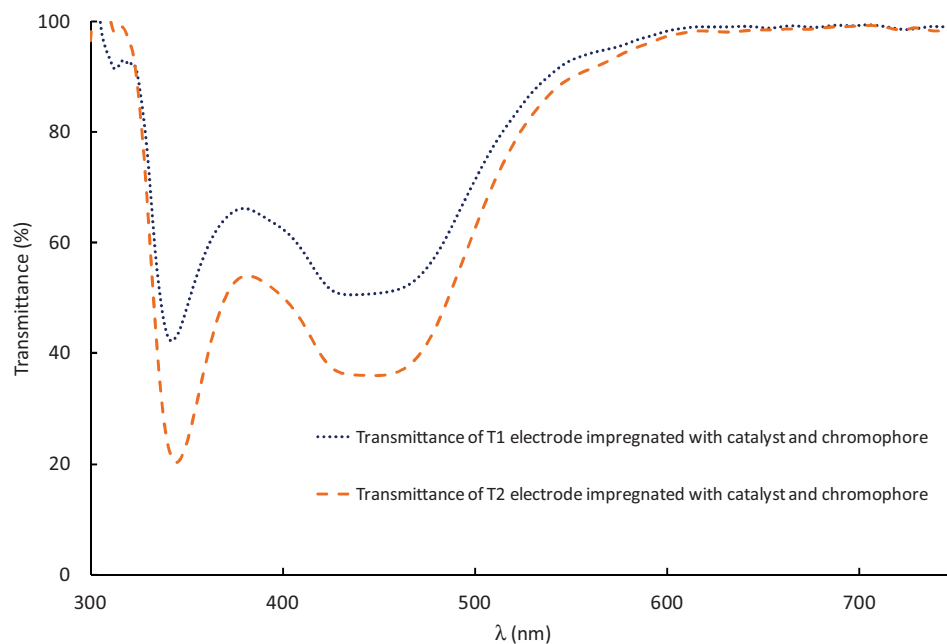


Figure 4.31 Transmittances of T1 and T2 electrodes impregnated with Ru-Ru_{Cat} chromophore and catalyst molecules. Measurements accomplished with FTO blank electrode as base line.

4.3.3.2 Electrochemical characterisation of Ru-Ru_{cat} chromophore-catalyst photoanode

(a)- Characterisation of the photoanode by cyclic voltammetry

In this section, the electrochemical characterisation of Ru-Ru_{Cat} photoanodes will be presented in order to be compared with Ru and Ru_{Cat} electrodes. The experiments conditions are carried out using the same electrolyte as previously: 0.1 M Na₂SO₄ electrolyte, pH 6.08. Cyclic voltammetry tests were run in dark and under different photon flux densities. The electrode was polarised between 0 V vs. V_{OC} and 1.5 V vs. Ag/AgCl NaCl 3M.

The oxidation peak of chromophore always happen around 1.1 V vs. Ag/AgCl NaCl 3M but the photocurrent density is reduced to 0.2 mA.cm⁻² at maximum incident photon flux compared to the double layer Ru electrode at the same potential (Figure 4.32). It seems that the presence of catalyst on the photoanode film reduces the amount of chromophore absorbed into the TiO₂ film. This might reduce the photosensibility of the electrode and so the produced photocurrent for the same potential is less than in the case we have only chromophores on the film. In contrast the Ru chromophores can be regenerated by Ru catalysts and so the photoanode film lasts longer.

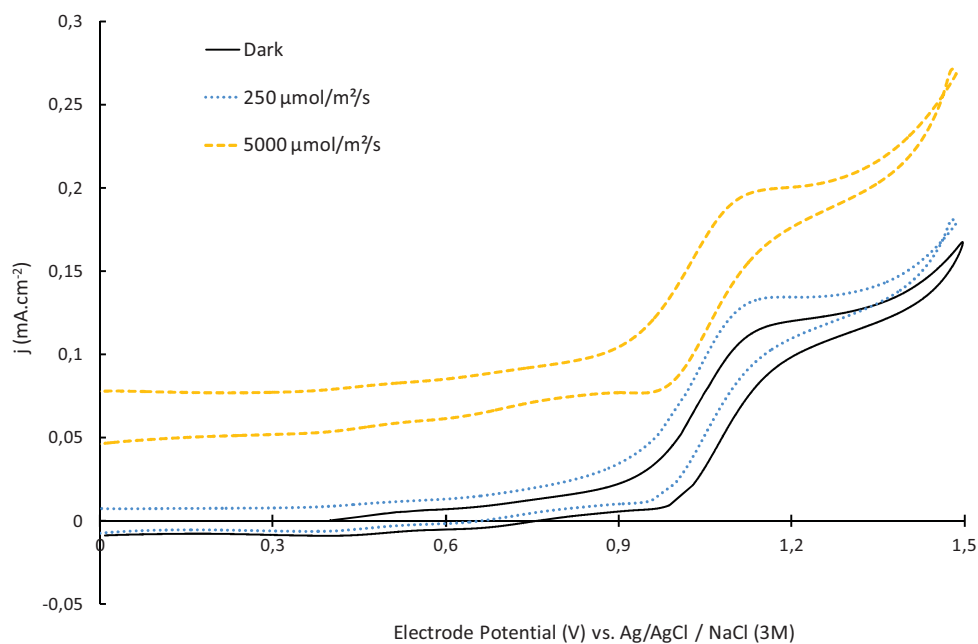


Figure 4.32 Cyclic voltammetry of Ru-Ru_{cat} photoanode in dark and under different photon flux densities. The photoelectrode was polarised between 0 to 1.5 V vs. Ag/AgCl NaCl (3M).

Having persistence photoanode gives us the possibility to go further and do EIS tests on the same electrode of previous experiment.

(b)- Characterisation of the photoanode by impedance

Impedance tests were then run on the photoanode under dark and illumination at V_{OC} in order to compare it to similar tests when Minucell DSSC was put into use. To examine only the photoanode behaviour a three electrode setup with Ag/AgCl NaCl (3M) as reference electrode and a platinum coated cathode. The support electrolyte was Na₂SO₄, 0.1 M and pH 6.08. The electrical equivalent model used to fit Nyquist impedance curves consists of:

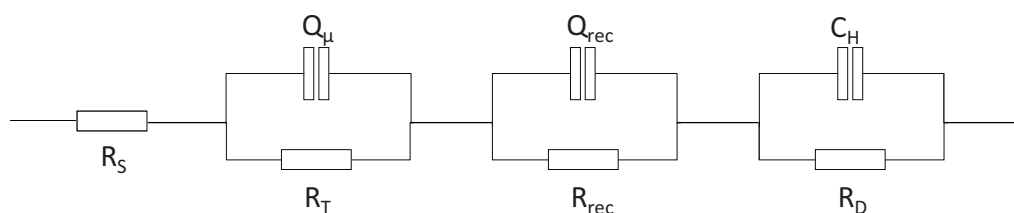


Figure 4.33 Equivalent electrical model of the photoanode.

Where the elements stand for:

R_S	Ohmic resistance of the system including glass ohmic resistance, wires, etc .
R_T	Charge transfer resistance within the photoanode. It should be noted that in this case R_T sum up the charge transfer resistances of catalyst to chromophore, chromophore to TiO_2 and charge transfer within the TiO_2 film. We call the sum of these resistances the charge transfer of photoanode.
R_{rec}	R_{rec} covers charge recombination resistance, especially at high radiation intensities it competes with R_T and gives the photoanode non ohmic resistance.
Q_μ	Constant phase elements (CPE) used as imperfect capacitor to model space charged capacitive behaviour of photoanode.
Q_{rec}	CPE presenting the capacitive behaviour of space charged recombination
C_H	Helmholtz capacitor of double layer at photoanode/electrolyte interface.
R_D	Diffusion resistance within the double layer at photoanode/electrolyte interface.

Note: Since the Ru-Ru_{Cat} photoanodes are not very resistant during electrochemical experiments, the tests are limited to two different illumination intensities.

Figure 4.34 shows the electrochemical impedance of Ru-Ru_{Cat} photoanode in dark. It has been presented separately due to high values of impedance comparing to impedance at illumination condition.

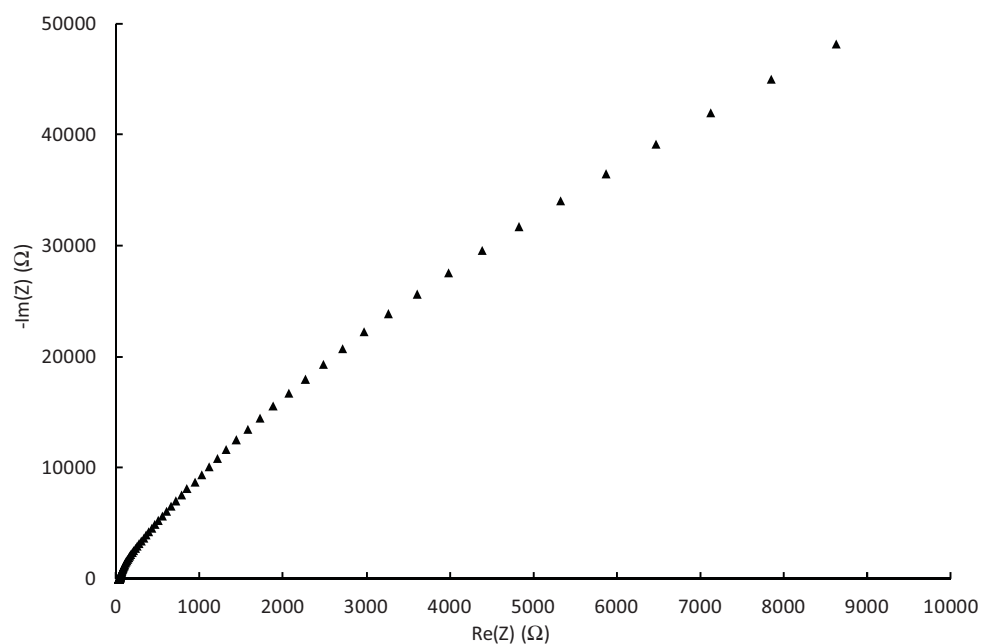


Figure 4.346 Impedance spectra double layer Ru-Ru_{Cat} photoanode at V_{OC} in dark.

The obtained impedance feature corresponds to the photoanode and the electrode-electrolyte interface impedance because the experiments were carried out in 3 electrode configuration. In dark condition and at V_{OC} we obtained only one semi circle and the impedance value is relatively high because of TiO_2 acting as an isolator without chromophore activity (the chromophore is not active without illumination). This semicircle can be fitted with a simple Randles (Figure 4.35) circuit which is the association of R_{TCO} and C_{TCO} in series with R_s .

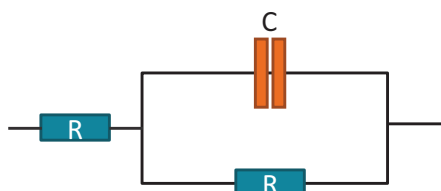


Figure 4.35 Randles circuit, simple electrical model which can be used as an equivalent circuit to fit a single semi-circle of impedance.

The impedance results of double layer Ru-Ru_{Cat} photoanode at V_{OC} under low and high radiation intensities (250 and 5000 $\mu\text{mol}/\text{m}^2/\text{s}$ respectively) are illustrated in Figure 4.36. At high frequency region we have the charge transfer resistance in parallel with chemical capacitance which reduces notably at high radiation intensities because of increasing the conductivity of semiconductor film and space charging.

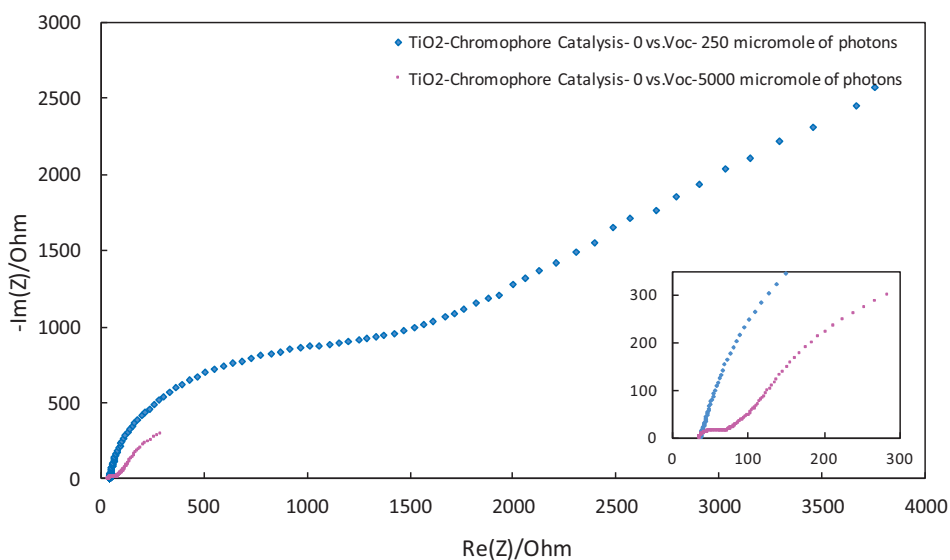


Figure 4.36 Impedance spectra of double layer Ru-Ru_{Cat} photoanode at V_{OC} for different photon flux densities.

The low frequency impedance corresponds to mass transport resistance of electrolyte ions into the double layer at the interface of photoanode electrolyte associated with Helmholtz capacitance. Figure 4.37 shows the impedance fitting curve at intensity of 5000 $\mu\text{mol}\cdot\text{m}^{-2}\cdot\text{s}^{-1}$.

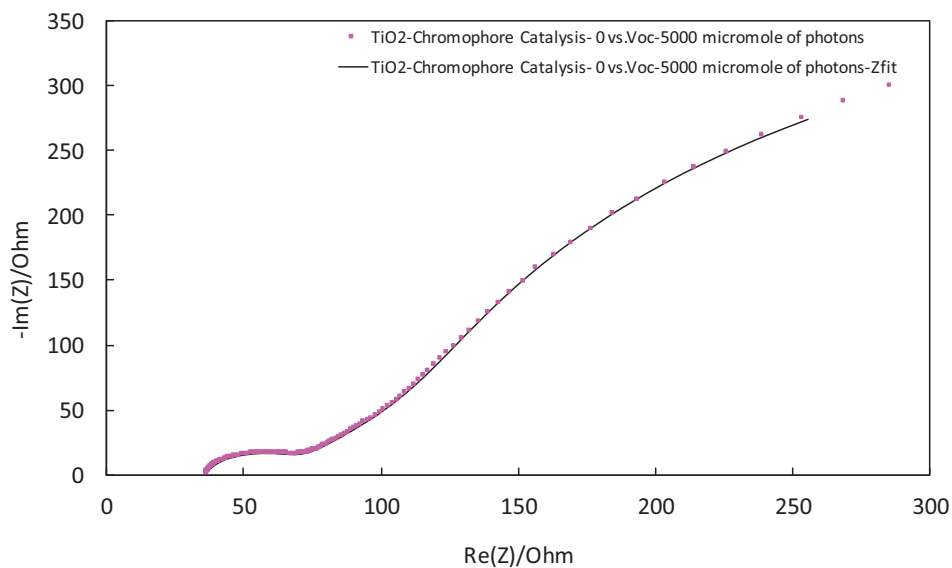


Figure 4.37 Impedance result and fitted curve for Ru-Ru_{cat} photoanode at 5000 $\mu\text{mol}\cdot\text{m}^{-2}\cdot\text{s}^{-1}$.

The analysis of equivalent circuit shows that there is no change in ohmic resistances, R_s , as shown in Table 4.8.

Incident photon flux density ($\mu\text{mol}/\text{m}^2/\text{s}$)	R_s (Ω)
0	33.9
5000	36.0

Table 4.8 Equivalent circuit of series resistances for DS-PEC with Minucell and Ru-Ru_{cat} photoanode under either of dark and illumination conditions. The series resistances remain roughly constant during the whole experience (dark and illumination conditions).

Other equivalent circuits elements change with illumination are illustrated in Table 4.9. Please note that some of elements are not necessary for fitting the impedance spectra under dark condition but they are presented in Table 4.9 as a matter of comparison on how illumination could change these values representing charge transfer resistance and space capacitances charging.

Incident photon flux density ($\mu\text{mol}/\text{m}^2/\text{s}$)	Q_T	R_T (Ω)	Q_{rec}	R_{rec} (Ω)	C_H (F)	R_D (Ω)
0	3.12E-05	3.76E+04	1.05E-04	1.03E+01	2.47E-04	1.02E+03
5000	2.91E-03	5.52E+01	1.03E-04	3.53E+01	4.06E-03	6.63E+02

Incident photon flux density ($\mu\text{mol}/\text{m}^2/\text{s}$)	$C_{\mu\text{-pseudo}}$	R_T (Ω)	$C_{rec\text{-pseudo}}$ (F)	R_{rec} (Ω)	C_H (F)	R_D (Ω)
0	3.13E-05	3.76E+04	5.67E-05	10.3	2.47E-04	1.02E+03
5000	1.89E-03	5.52E+01	4.49E-05	35.3	4.06E-03	6.63E+02

Table 4.9 The results of equivalent circuit of DS-PEC with Minucell and Ru-Ru_{Cat} photoanode under either of dark and illumination conditions. Charge transfer resistance within the photoanode reduces by increasing the incident photon flux and the space charge capacitance increases because of charging the space charges by more photons and so electrons flux from conduction band. There is also more charge exchange at the photoanode and electrolyte interface between the catalyst/electrolyte. So the diffusion resistance decreases but also Helmholtz capacitance corresponding to the double layer capacitance increases by presence of more charge accumulation at the interface. At the intermediate frequency zone, the ohmic recombination resistance remains constant with slight increase by illumination.

The charge transfer resistance reduces significantly under illumination and the space charge capacitance increases which means space surfaces in semiconductor get charged due to charge transfer from chromophores to semiconductor. On the other hand, R_{rec} increases very little. The R_{rec} corresponds to the recombination resistance in the photoanode. At high illumination intensities chromophores inject charges into semiconductor conduction band and the space surfaces get charged, this reduces the charge transfer resistance but it also increases the rate of recombination which resists to the charge transfer. Therefore, we consider an equivalent resistance for both R_T and R_{rec} which reduces under illumination since charge transfer resistance decreasing is dominant.

The last part of impedance spectra (low frequency area) corresponding to double layer at photoanode and electrolyte interface, shows more a diffusive behaviour. Because of short duration of acquisition, the double layer thickness does not change very much so the Helmholtz capacitance does not vary significantly⁹ but the diffusion resistance of charge transfer between electrolyte and catalyst reduces also significantly between dark and illumination conditions. It proves that under illumination the catalysts transfer the charges between chromophores and electrolyte which reduces the diffusion resistance value while under dark condition there is no charge transfer between electrolyte and catalyst which leads to high value of diffusion resistance at this point.

⁹ As mentioned Ru-Ru_{Cat} photoanode is not very stable in aqueous solution (water based) after few hours the deposit (chromophore-catalyst) can get detached from the electrode. Hence to run the maximum variant tests with the same photoanode the acquisitions are quick and ran just for dark and few different illuminations intensities. Then in some cases the double layer does not change significantly between two series EIS under dark and illumination.

4.3.4 Ru-Ru_{Cat} PEC complete system (two electrodes setup)

When the system is set up in two electrodes configuration the objective is to study the whole system including the photoanode, the cathode and the electrolyte. It will therefore not give us information about each electrode separately such as their potential but the measured potential by the potentiostat corresponds to the potential difference of the cell, $E_{\text{CELL}} = E_{\text{WE}} - E_{\text{CE}}$. Hence E_{CE} plays an important role in defining the potential difference of the cell and so in interpreting the jV curve provided in two electrodes mode. In this work we always used FTO platinum coated cathode while we were studying the photoanode in three electrodes setup (using a reference electrode) but we also needed to integrate the cathode defined by TechBio'Phyp project named CoTAA. The interest of using CoTAA will be explained further in this chapter but in order to understand how the cathode would affect the cell behaviour we also accomplished the tests with platinum (Pt) cathode without using a reference electrode (two electrodes configuration) to have a comparison with CoTAA performance.

4.3.4.1 PEC using platinum coated cathode

(a)- jV results

The platinum coated electrode was used as cathode with a double layer Ru-Ru_{Cat} photoanode. Figure 4.38 presents the result of cell polarisation in dark and under illumination. The difference between the current density in dark condition and under radiation is clearly shown in this figure. The cell was polarised from V_{OC} to the potential equivalent to 0 V. The measurements are hence carried out in two electrode configuration in dark and under different photon flux densities. The electrolyte is a 0.1 M Na₂SO₄ solution (pH \approx 6.08). A Nafion membrane was used to separate the cathodic and anodic compartments.

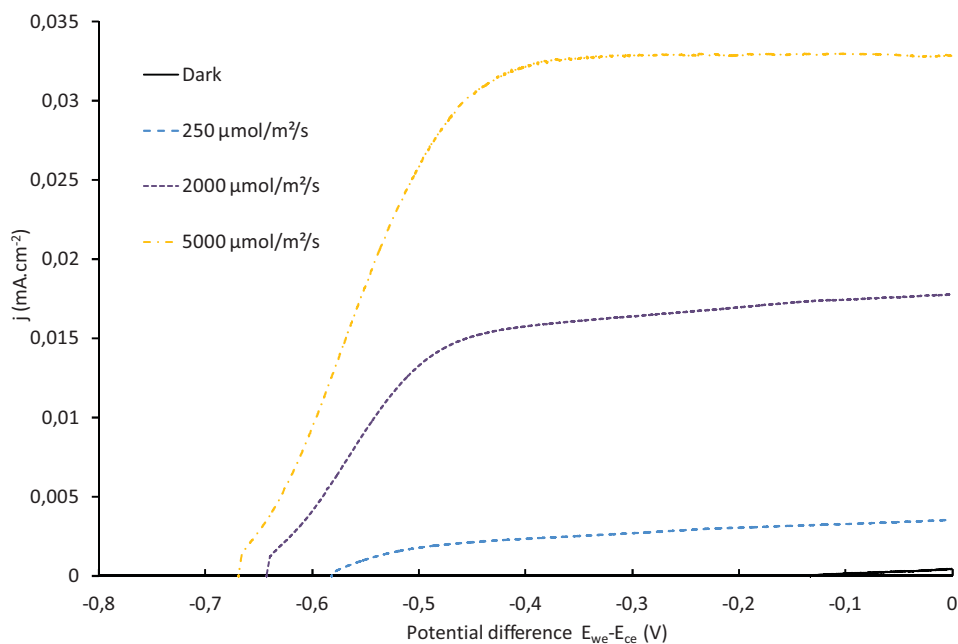


Figure 4.38 The polarisation (jV) curves of PEC with double layer Ru-Ru_{cat} photoanode and platinum cathode.

By comparing the curves in Figure 4.38 to a general jV curve we observe that for higher photon flux density value, the curves are convex at starting point and then they reach a constant value of current density and continue gradually to reach j_{SC} value. This sharp slope might be attributed to a rapid charge injection process.

(b)- EIS study of Minucell in two electrodes configuration:

Tests for complete cell with Ru-R_{cat} photoanode were also run at two electrodes configuration to measure the whole cell impedance and give us the possibility to have a comparison between PEC with Ru-R_{cat} photoanode cell and DSSC. Although the purpose of Minucell with photoanode is to produce hydrogen while DSSC produces only electrical current and basically we cannot compare rationally two different systems but due to similarities between them we can analyse both systems in term of photo activities and their response to variation of photon flux densities.

The electrical equivalent model used to fit Nyquist impedance curves is the same as previously used (figure 4.12):

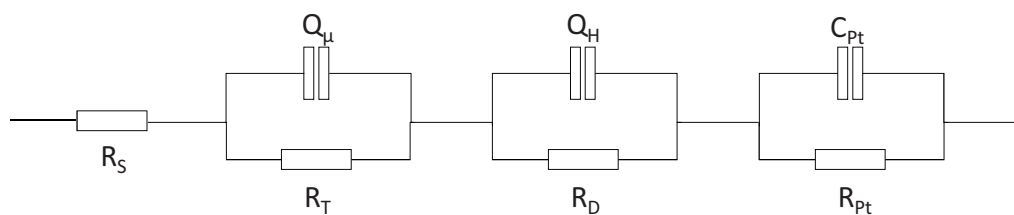


Figure 4.12 Electrical equivalent model of the DSSC.

With, for reminder, the following elements:

R_S	Ohmic series resistances of the system including glass ohmic resistance, wires, etc.
R_T	Sum of all charge transfer resistances within photoanode, from catalyst, chromophore to TiO_2 conduction band, recombination and electron transfer from TiO_2 to TCO glass.
Q_μ	Constant phase elements (CPE) used as imperfect capacitor to model space charged capacitive behaviour of TiO_2 layer.
R_D	Electrolyte double layer diffusion impedance at photoanode/electrolyte interface.
Q_H	Helmholtz capacitor of double layer at photoanode/electrolyte interface.
R_{Pt}	Double layer diffusion resistance of cathode.
C_{Pt}	Helmholtz capacitor of double layer at cathode/electrolyte interface.

Figure 4.39 presents the results of Minucell with Ru- Ru_{cat} photoanode and platinum cathode in two electrode configuration (measurement performed between photoanode and cathode) under illumination, and also compares the same measurement with three electrode configuration means cell potential is measured between the photoanode and the reference electrode (for a given photon flux density) at V_{OC} .

In Figure 4.39 the impedance results in red crosses corresponds to photoanode impedance and its interface with electrolyte and the blue losanges presents the whole cell impedance including cathode, photoanode and electrolyte impedances.

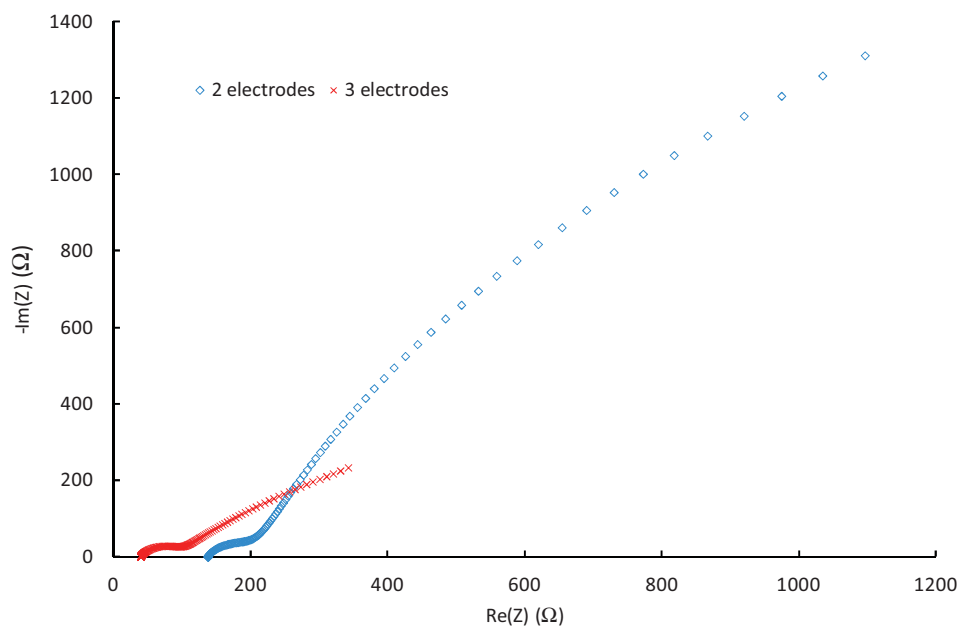


Figure 4.39 EIS result of PEC in two electrode and three electrode configurations using T2 Ru-Ru_{cat} photoanode and Pt cathode. The frequency range corresponds to 100kHz-100mHz and the perturbation voltage was 10 mV.

Table 4.10 and 4.11 compare the equivalent circuit results of Figure 4.33 (for Minucell for H₂ production at 2 electrodes setup), to DSSC Minucell at the same configuration.

Application	Incident photon flux density (μmol/m ² /s)	R _s (Ω)
DSSC	5000	77.9
PEC for H ₂	5000	138

Table 4.10 Equivalent circuit results of series resistances for DS-PEC with Minucell with Ru-Ru_{cat} photoanode for H₂ production application and DSSC application (with TiO₂ photoanode and dye molecules)¹⁰ under illumination (5000 μmol.m⁻².s⁻¹). The series resistances have higher value for Ru-Ru_{cat} PEC than DSSC which completely normal because of different basic materials of each application (photosensitizers, electrolyte, etc.).

¹⁰ Refer to section 4.2.2 of this chapter.

Application	Incident photon flux density ($\mu\text{mol}/\text{m}^2/\text{s}$)	C_{μ} (F)	R_T (Ω)	C_H (F)	R_D (Ω)	C_{Pt} (F)	R_{Pt} (Ω)
DSSC	5000	1.04E+00	9.62E-01	3.41E-04	1.18E+00	1.10E-03	3.32
PEC for H ₂	5000	5.82E-05	64.7	1.49E-03	4.48E+03	1.63E+02	2.75E-02

Table 4.11 The results of equivalent circuit of DS-PEC with Minucell and Ru-Ru_{cat} photoanode for H₂ production application and DSSC application (with TiO₂ photoanode and dye molecules) under illumination ($5000 \mu\text{mol}\cdot\text{m}^{-2}\cdot\text{s}^{-1}$). Charge transfer resistance is higher for Ru-Ru_{cat} photoanode than DSSC photoanode and consequently the surface states get less charged so space charge capacitance C_{μ} has smaller value for Ru-Ru_{cat} photoanode. Also the double layer diffusion resistance is higher in Ru-Ru_{cat} photoanode. This can be also because of less exchange between photoanode and the electrolyte due to catalyst oxidation limits while dye molecules and Iodolyte electrolyte in DSSC seems to have more efficient oxidation system.

We can say that generally the Minucell with H₂ production application is a more resistive system than Minucell with DSSC application, which is understandable because each system has been designed with different basic materials (photosensitizer, catalyst, electrolyte etc.) and for different purposes. Series resistances are more important in H₂ production system, in which electrolyte and cathode have an important part, if we compare R_S of photoanode (Table 4.8) in which half of electrolyte contributes also in R_S , we have 36Ω vs. 138Ω for complete cell (2 electrodes setup) with the whole electrolyte series resistance included.

The cathode resistance corresponds to the resistance of charge transfer R_{Pt} from electrode to the electrolyte and reduction of oxide species in the electrolyte while C_{Pt} is the Helmholtz capacitance at cathode. They both appear at high frequencies means at the beginning of impedance spectra which is not visible due to very small value of resistance comparing to other phenomena. The first visible semicircle at intermediate frequencies corresponds to photoanode impedance consisting of charge transfer resistance in photoanode and space charged surfaces capacitances; which has the same shape and size in both 2 and 3 electrodes setups because it presents the same phenomenon for the same part. However comparing to the DSSC application the charge transfer resistance is more important in H₂ production system so surface states are less charged and C_{μ} is smaller. The diffusion impedance of 0.1 M Na₂SO₄ electrolyte in H₂ production mode is higher than Iodolyte. This can be also because of less exchange between photoanode and the electrolyte due to catalyst oxidation limits while dye molecules and Iodolyte electrolyte in DSSC seems to have more efficient oxidation system.

Naturally we observe that both graphs have the same shape with slight deformation at the end but also the blue graph is shifted to right comparing to the red curve. This is because of ohmic

resistance which is higher for the whole cell because the cathode ohmic resistance is also measured and added to the photoanode ohmic resistance. The photoanode resistance does not change very much (slight difference because the photoanodes are different in each experiments). The rest of impedance spectra difference is due to cathode and electrolyte diffusion impedance contribution.

4.3.4.2 PEC using CoTAA cathode

(a)- Linear and cyclic voltammetry of CoTAA electrode

To complete the development of the photo-electrochemical cell using non noble metal, we decided to utilize a cathode made of a transition metal complex, the tetraazaanulene Co (II) (CoTAA). According to literatures (Convert et al 2001) this complex has two advantages: firstly, it is stable in acidic aqueous solution, and secondly the TAA ligand polymerizes by electrochemical oxidation to form an insoluble film on the electrode. To estimate electrochemical characteristics of the CoTAA electrode it was tested as a cathode using a platinum coated counter electrode in presence of reference electrode (Ag/AgCl, NaCl (3M)) in aqueous acidic electrolyte (Na₂SO₄, 0.1 M) at different pH. Linear sweep voltammetry experiments were then carried out in the range [0; -1V] vs. ref electrode (figure 4.40).

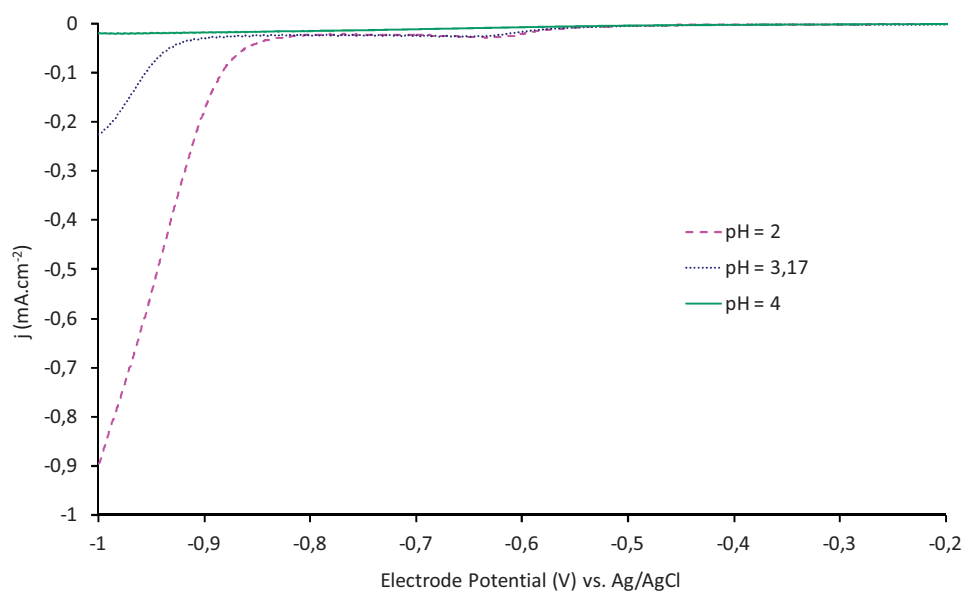


Figure 4.40 Linear sweep voltammetry of CoTAA electrode at different pH

As can be noticed in figure 4.40, the cathodic current density increases as the electrode potential goes towards negative value. The pH influence on current density is highlighted, the lower the pH the higher the current density is. A comparison with platinum coated FTO electrode

indicates a necessary 0.5 V overpotential for the CoTAA electrode to reach the same current density. Another study carried with cyclic voltammetry (figure 4.41), with different scan rates, shows that the cathodic peaks change linearly by increasing the scan rate which confirms the capacitive behaviour of insoluble CoTAA film.

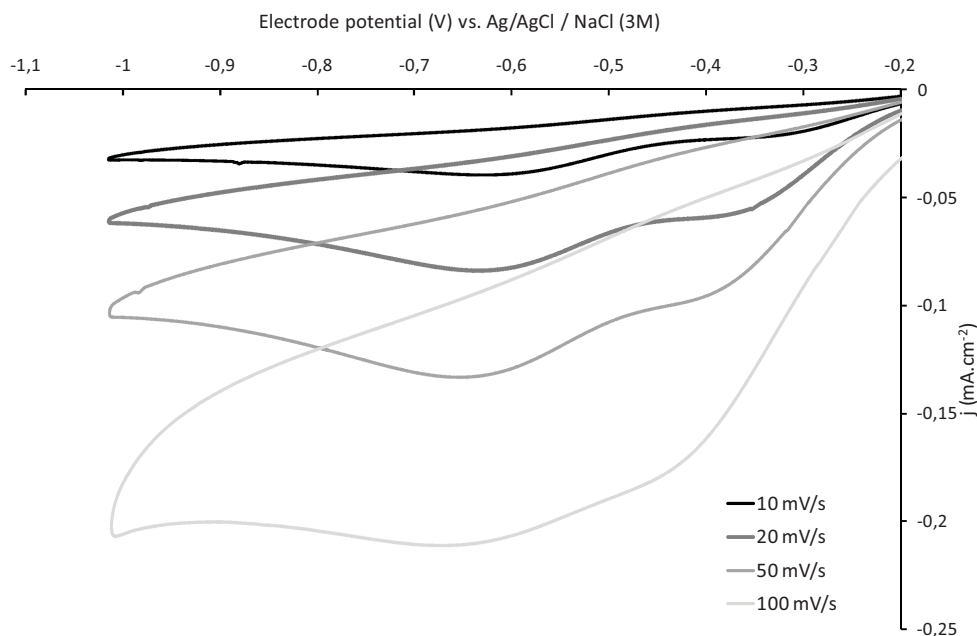


Figure 4.41 Cyclic voltammetry of COTAA in aqueous electrolyte (Na_2SO_4 .1 M, pH 3.4) for different scan rates. A Pt electrode was used as counter electrode.

(b)- Implementation of CoTAA cathode in a PEC

After having characterized the CoTAA electrode as a cathode for proton ion reduction, it has been implemented a cathode with a Ru-Ru_{cat} photoanode. The results are presented in figure 4.42, where we could notice the influence of the photoanode on the general aspect of the jV curves: the open circuit potential is shifted according to photon flux density and the current density increase with photon flux density at a given potential difference.

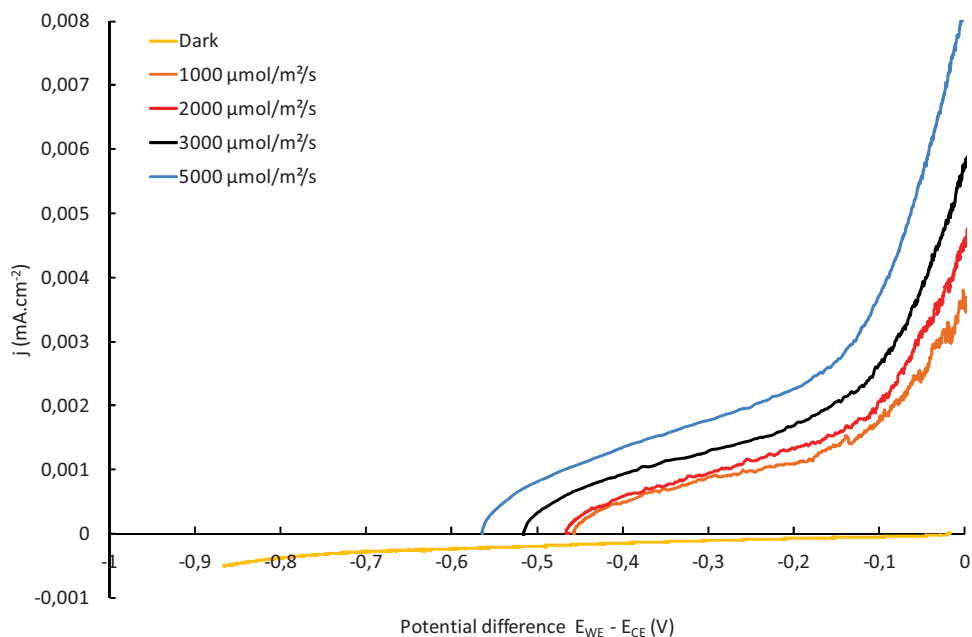


Figure 4.42 The polarisation curves of a PEC with Ru-Ru_{cat} photoanode (double layer) and CoTAA cathode.

However, the current densities remains low compared to a two electrode set-up using a platinum coated cathode, as can be seen in figure 4.43, where data of figure 4.38 are partially plotted.

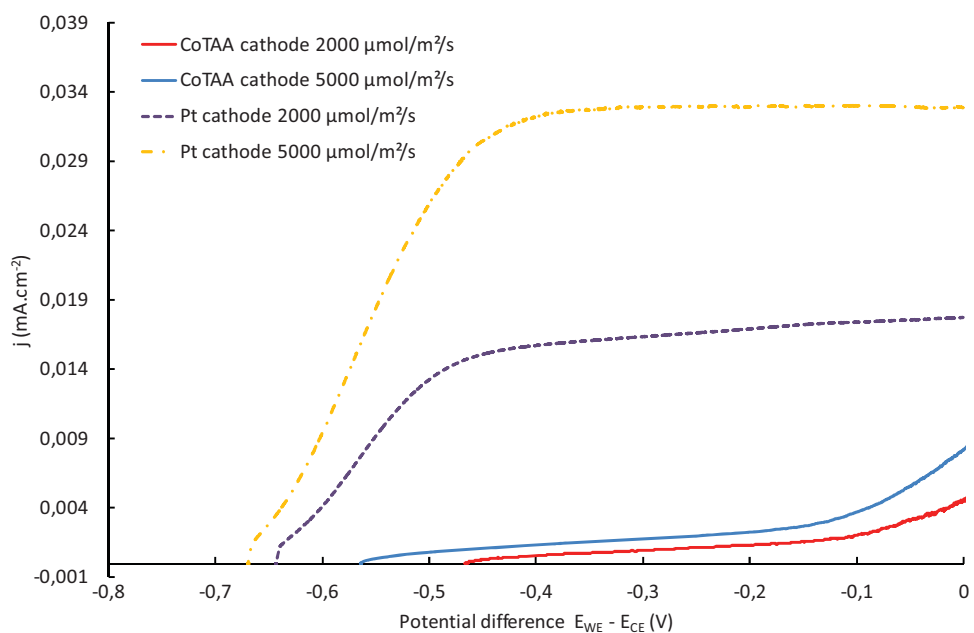


Figure 4.43 Comparison of jV results of PEC using CoTAA or Pt coated cathode as for a given photon flux densities.

Such a difference in potential difference and current density values may be explained by the substitution of a rather efficient cathode (Pt coated cathode) by a less efficient one (the

CoTAA). To reach equivalent current densities, the potential difference should be increased; the reduction step at the CoTAA cathode could be considered as another limiting step.

To complete the study on the cell using CoTAA as cathode, electrochemical impedance spectroscopy was carried out (figure 4.44) on the cell. A comparison on the identified parameters (in the case of a Pt cathode) is done in table 4.12.

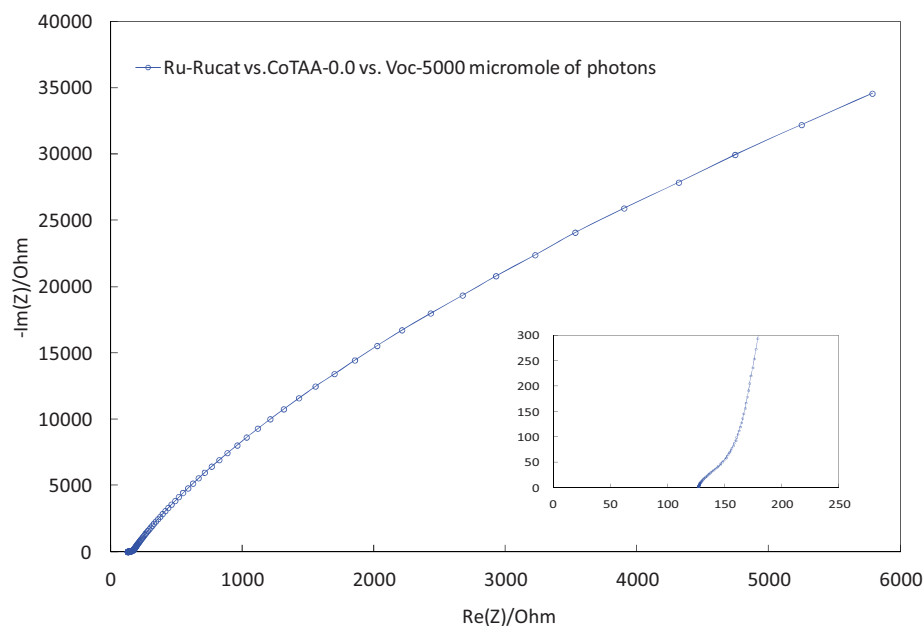


Figure 4.44 EIS result of PEC in two electrodes configuration with Ru-Ru_{cat} photoanode and CoTAA cathode. The result is obtained at V_{OC} for a $5000 \mu\text{mol}\cdot\text{m}^{-2}\cdot\text{s}^{-1}$ (white LED panel) photon flux density. The frequency ranges is 100kHz-100mHz and the a perturbation of 10 mV was applied. The zoomed out part corresponds to the high frequencies region and counter electrode contribution.

The high frequency semicircle corresponding to the photoanode impedance remains in the same magnitude as the cell with the same photoanode and platinum cathode. However, the change of impedance spectra happens at intermediate frequency where diffusion through the electrolyte and majorly the diffusion of electrons from cathode into electrolyte occurs. So globally in the system with CoTAA the reduction reaction is limiting.

Cathode	R_S (Ω)	C_μ (F)	R_T (Ω)	C_H (F)	R_D (Ω)	C_{cathode} (F)	R_{cathode} (Ω)
CoTAA	207	3.20E-05	65.6	3.82E-04	1.18E+03	4.14E-03	4.06E+03
Pt	138	5.82E-05	64.7	1.49E-03	4.48E+03	1.63E+02	2.75E-02

Table 4.12 Equivalent circuit results of Ru-Ru_{cat} PEC with CoTAA and Pt cathode impedance test.

As can be noticed in table 4.12 series resistance, R_S , remains at the same magnitude for both cells. The charge transport resistance and associated surface states capacitance are also very

close this observation is coherent as the same photoanode was used in both systems. By the same reasoning, Helmholtz capacitance, C_H , and diffusion resistance, R_D , are also very close in both systems. The only difference that we can observe is between resistance of cathodes, R_{cathode} , and associated double layer capacitances, C_{cathode} , these values are higher for CoTAA than Pt. This fact confirm a less efficient charge transfer from cathode to protons in the electrolyte, the reaction is slower with CoTAA.

4.4 Hematite PEC characterization (SC-PEC)

Alternative to dye sensitized photoelectrode, hematite can be also used to split water as photoanode. Several electrochemical tests have been performed for hematite electrode characterization such as Linear Sweep Voltammetry (LSV) and EIS measurements. The tests carried out in two phases. Phase one is concentrated on hematite photoanode without catalyst deposition and the second phase investigates the characteristics of hematite electrode with platinum paste (Platisol) deposited on the electrode. Each phase includes optical measurements (transmittance, reflectance) and electrochemical characterization. Electrochemical measurements were accomplished in three electrodes assembly versus Ag/AgCl 3M NaCl reference electrode. The complete cell characterization in two electrode setup is also presented at the end.

4.4.1 Hematite photoelectrode characterization without catalyst

The hematite electrode as it is shown in Figure 3.23 has a bright red colour. So before electrochemical characterisation it is necessary to measure the transmittance of the photoelectrode.

4.4.1.1 Transmittance measurements

Since our hematite photoelectrode (Figure 3.23) was not homogenously coloured, only a well coloured zone of the electrode was exposed to the xenon beam. We measured the transmittance of the electrode within the range of 350 to 700 nm. The electrode was kept in a quartz cuvette containing NaOH, the same electrolyte used for electrochemical tests. The objective was to carry out optical measurements in the same condition as electrochemical measurements and have the same interfaces.

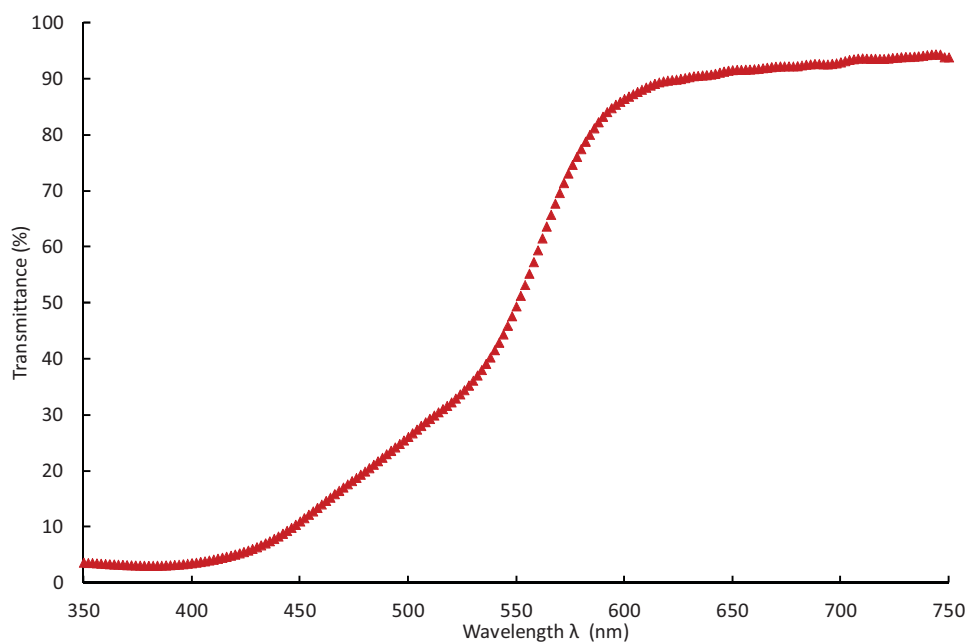


Figure 4.45 Transmittance spectra of hematite electrode in NaOH solution. Measurements were accomplished with FTO blank electrode in NaOH solution as base line.

The hematite photoelectrode absorbs between 350 and 600 nm (Figure 4.45) which is also reported for similar material by (Riha et al 2013). The band gap of the hematite can be estimated around 2.3 eV.

4.4.1.2 Electrochemical characterization

The hematite electrode was polarised in dark and under different photon flux densities. Afterward the results of dark and illumination are compared and the contribution of cathode is discussed. Moreover, for more profound study about the photoanode EIS measurements were run for the PEC in three electrode setup.

(a)- Photocurrent measurements

Photoelectrochemical current density measurement of hematite photoanode has been performed in NaOH 1M electrolyte ($\text{pH} \approx 13.5$) vs Ag/AgCl reference electrode. A platinum electrode prepared with Platisol deposition on FTO has been used as counter electrode. The polarisation results (jV curves) are presented in Figure 4.46 and show an evolution of V_{OC} as well as the current density by increasing incident photon flux density.

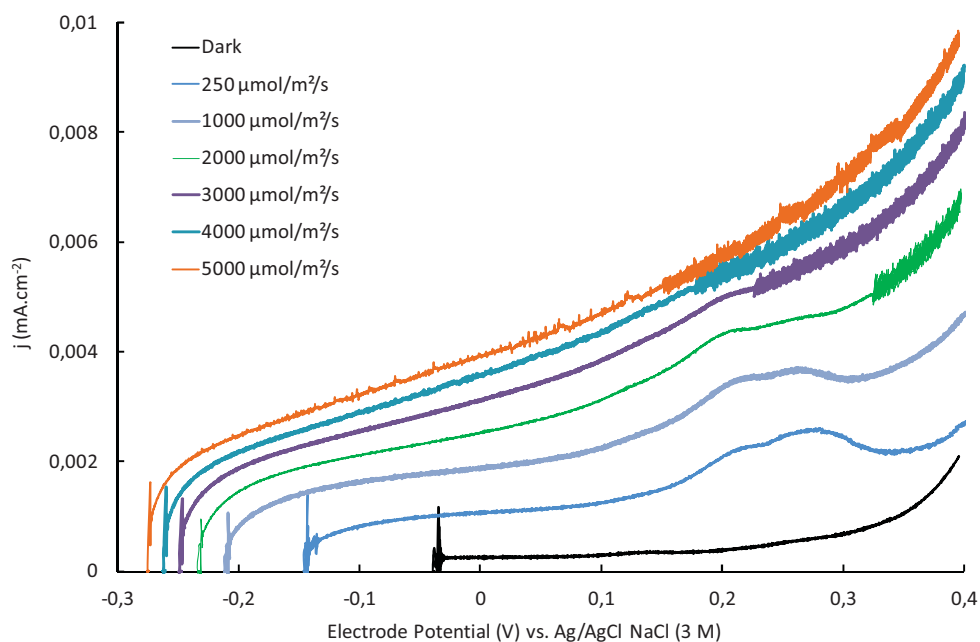


Figure 4.46 Evolution of current density PEC hematite photoanode as a function of electrode potential. The measurements are carried out in three electrode configuration in dark and under different photon flux densities (white LED).

The open circuit potential decreases (from -0.03 V to -0.27 V/ reference electrode) as the photon flux density increases hinting at a photoactivity of the hematite electrode. A wider electrode potential range was also tested up to 1.5 V vs. Ag/AgCl NaCl (3 M). The results are presented in figure 4.47.

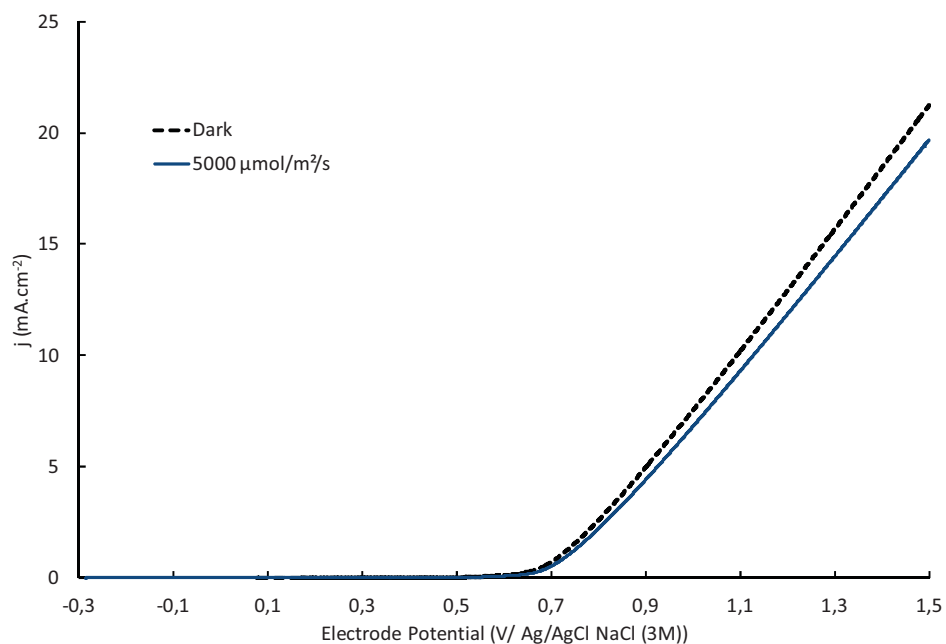


Figure 4.47 Evolution of current density PEC hematite photoanode as a function of electrode potential in a wider potential range.

The current density reaches $20 \text{ mA}\cdot\text{cm}^{-2}$ but the photocurrent represents only a small part. After 0.5 V the system turns into the electrolysis phase and the current density corresponds to the electrolysis current. Although the shift between V_{OC} under dark and illumination confirms the photo-sensibility of hematite electrode but the photocurrent is barely higher than the dark current and remains far from the photocurrent values reported in literature (e.g. $0.4 \text{ mA}\cdot\text{cm}^{-2}$). According to (Chou et al 2013) the ability of hematite photoanode depends strongly on the method of deposition. Figures 4.48 from the same authors compare the results of two methods of deposition: anodic electrodeposition and iron oxidation. Figure 4.48 (a) shows the results of electrodeposited hematite in dark and illumination whereas Figure 4.48 (b) presents the polarisation results of hematite electrode made from iron oxidation. Clearly there is no photocurrent for the hematite film prepared from electrodeposition method while the iron oxidated film shows very remarkable values of photocurrent. A strong assumption is that in the sample prepared with anodic electrodeposition the effect of the film thickness has been excluded whereas in the case of electroplating the film thickness decreases with the operation duration. As a result no photocurrent was generated even for the samples with presenting light absorption.

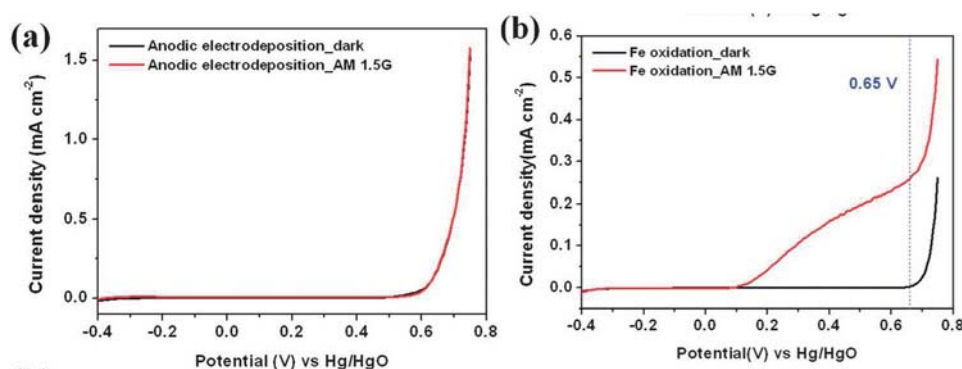


Figure 4.48 Photocurrent voltage characteristics of the hematite films in the dark and under illumination. (a) Anodic electrodeposition. (b) Fe oxidation (Chou et al 2013).

(Sivula et al 2011) have been investigated the increasing photocurrent density through morphology control. Hence we assume that our problem of not observing enough high photocurrent might probably come from our anodic method of deposition.

(b)- Potentiostatic Electrochemical Impedance Spectroscopy

Electrochemical impedance tests were carried out under different illumination condition for hematite photoanode versus Ag/AgCl reference electrode with platinum counter electrode. The tests were accomplished at V_{OC} (system is at relaxing state) under illumination and dark condition and also at applied potential under illumination. Impedance curves shown in Figure

4.49 have been measured at V_{OC} under different illumination conditions without biasing the PEC. The blue curve corresponds to the impedance measurement in dark while the two other curves are presenting the impedance under 250 and 5000 $\mu\text{mole}/\text{m}^2/\text{s}$ respectively.

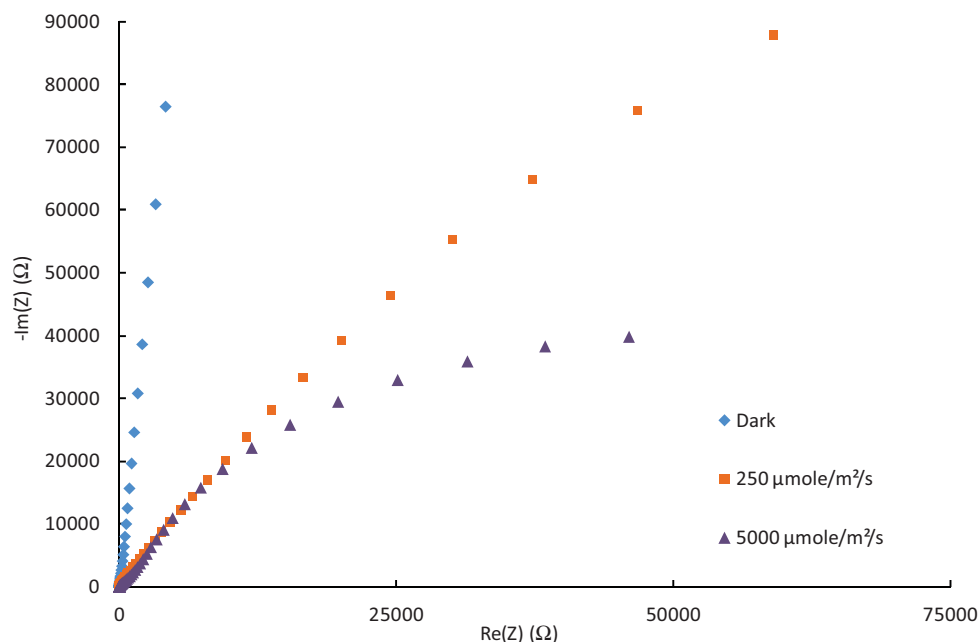
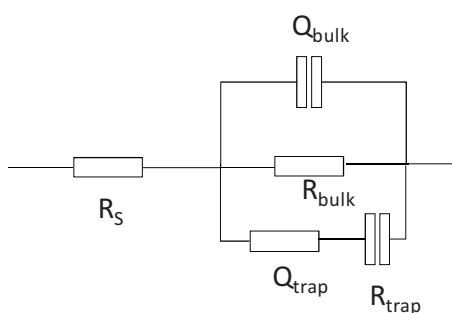


Figure 4.497 The impedance of PEC in three electrode configuration with hematite photoanode and Pt cathode. The result is obtained at V_{OC} and under dark and illumination conditions. The electrolyte was NaOH 1M.

The electrical equivalent model used to fit Nyquist impedance curves is the same as presented in the chapter 2:



R_s	Ohmic series resistances of the system including glass ohmic resistance, wires, etc.
R_{bulk}	Double layer diffusion impedance at photoanode/electrolyte interface.
Q_{bulk}	Constant phase elements (CPE) used as imperfect capacitor to model space charged capacitive behaviour of hematite layer.
R_{trap}	Charge transfer resistance within photoanode including recombination resistance.
Q_{trap}	Helmholtz capacitor of double layer at photoanode/electrolyte interface.

As can be seen in figure 4.49, the impedance values, particularly the imaginary part reduces by increasing the illumination intensity. The sample at V_{OC} in dark condition produces only one capacitive semicircle while we can barely observe a second semicircle for the same electrode under illumination at high frequency region. The small deformation at high frequency region

can be assigned to the charge transfer resistance and the double layer capacitance of TCO-electrolyte interface. The main arc corresponds to the charge transfer resistance of hematite from surface states R_{trap} and C_{trap} . By increasing the incident photon flux density, the absorbed photon amount increases, the surface states become charged hence the values of C_{trap} increase; the imaginary part of impedance is reduced.

Incident photon flux density ($\mu\text{mol}/\text{m}^2/\text{s}$)	R_s (Ω)
dark	16.8
250	16.7
5000	16.6

Table 4.13 Series resistances during remain unchanged for different experiments under dark and different illumination intensities for the same Hematite electrode.

The semicircles particularly at high frequency region become more separable at more positive applied potential when a photocurrent flows within the illuminated sample. The figure 4.50 illustrates the Nyquist plots measured under two different illumination intensities at an applied potential of 0.4 V vs. reference electrode. The photoanode shows two semicircles for both photon flux densities. Referring to the developed model for hematite photoelectrode in chapter 2 (figure 2.13), the high frequency semicircle corresponds to the capacitance of $\alpha\text{-Fe}_2\text{O}_3$ and electrolyte (C_{bulk}) in parallel with the trapping/detrapping resistance (R_{trapping}) of holes from the valence band and electrons from the conduction band to or from the surface states. The low frequency semicircle is therefore related to the charge transfer process from surface states (we have already assumed that the charge transfer occurs within the surface states) (Chou et al 2013).

Incident photon flux density ($\mu\text{mol}/\text{m}^2/\text{s}$)	Q_{bulk} ($\text{F}\cdot\text{s}^{(a-1)}$)	R_{bulk} (Ω)	Q_{trap} ($\text{F}\cdot\text{s}^{(a-1)}$)	R_{trap} (Ω)
dark	1.58E-05	1.77E-05	9.16E-21	2.43E+07
250	2.38E-05	4.66E+03	3.05E-05	5.17E+05
5000	4.84E-05	2.07E+03	6.64E-05	1.17E+05

Table 4.13 Identified parameters for the equivalent electrical circuit of hematite electrode.

The bulk capacitance and resistances changes slightly with photon flux density. However the state traps (surface states) get charged and so the Q_{trap} increases and consequently the charge transfer resistance R_{trap} is reduced. The bulk resistance is negligible under dark due to the lack of exchange between the electrolyte and electrode. Its value increases under low photon flux densities ($250 \mu\text{mole}/\text{m}^2/\text{s}$) and then decreases at higher photon flux density because of more

exchange between the photoanode and the electrolyte. In general, the impedance value reduces by increasing photon flux density.

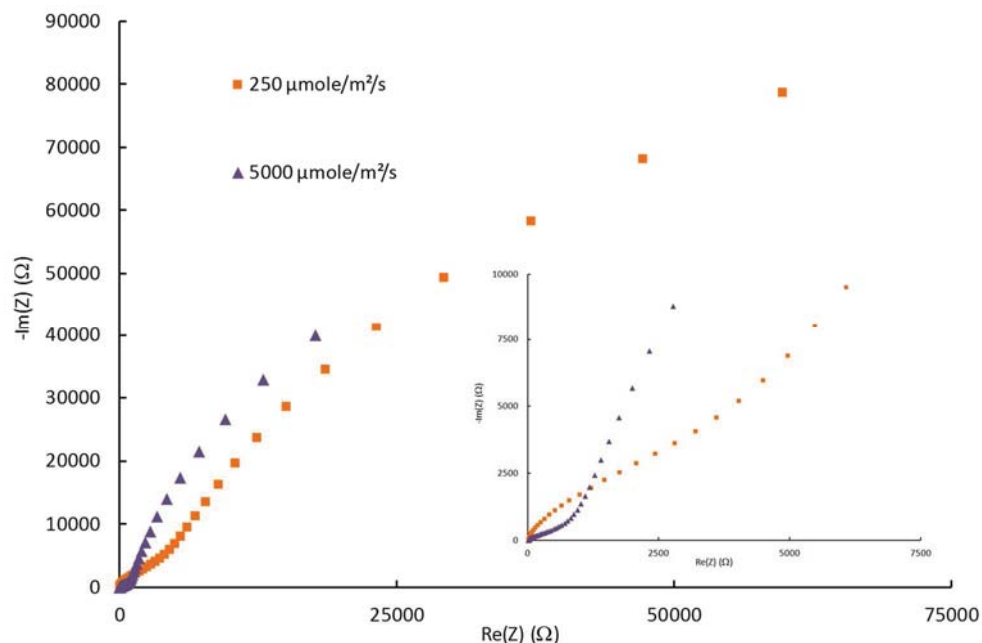


Figure 4.50 Hematite photoanode impedance under different photon flux densities at a reverse bias of + 0.4 V vs. Ag/AgCl reference electrode. The focused part shows the impedance feature at high frequencies.

By applying a positive potential compared to open circuit potential, the high frequency semicircle slightly increases because R_{trapping} reduces as the Fermi level bends and approaching the valence band it implies C_{bulk} charging. However the low frequency semicircle decreases significantly with bias. This is assigned to the capacitance of surface states. By applying a bias the surface states become charged and consequently the charge transfer resistance from surface states ($R_{\text{ct,trap}}$) reduces as well; coinciding with the photocurrent onset (0.4 V vs. Ag/AgCl NaCl (3M)). For higher bias value (not shown) the second semicircle become very small and in some cases disappears because of rapid charge transfer from oxidised surface states and cannot be easily resolved. In some literature it has been neglected and the equivalent circuit reduces to a simple Randles model but since the one semicircle at high frequency is attributed to C_{bulk} which is the contribution of C_{SC} and C_{H} it is also recommended to use the equivalent model represented in figure 2.13. Similarly when impedance measurement is carried out in dark condition we may use the same equivalent circuit but with different interpretation. Because under dark condition R_{trap} is no more negligible. In contrast it shows large and rather constant values which indicate low progressive water oxidation kinetics by transferring holes through valence band to the electrolyte. To fit this very single semicircle we can simply proceed with a single RC Randles circuit or fitting model of figure 2.13.

As a comparison with the same experiment without bias, the equivalent circuit results are:

Incident photon flux density ($\mu\text{mol}/\text{m}^2/\text{s}$)	R_s (Ω)
250	16.6
5000	16.1

Table 4.14 Series resistances remain unchanged for different photon flux densities. There is also not much difference between the values without and with bias potential.

Incident photon flux density ($\mu\text{mol}/\text{m}^2/\text{s}$)	Q_{bulk} ($\text{F}\cdot\text{s}^{(a-1)}$)	R_{bulk} (Ω)	Q_{trap} ($\text{F}\cdot\text{s}^{(a-1)}$)	R_{trap} (Ω)
250	2.26E-05	4.57E+03	6.97E-05	2.98E+05
5000	4.46E-05	7.24E+02	2.39E-04	2.95E+05

Table 4.15 The bulk capacitance and resistances change slightly with photon flux density increase. In the other hand the state traps (surface states) get charged and so the Q_{trap} increases but the charge transfer resistance does not change very much and it can be because of the applied bias which dominates the charge transfer over illumination changes. The bulk resistance decreases by increasing the radiative intensity and so the double layer capacitance increases.

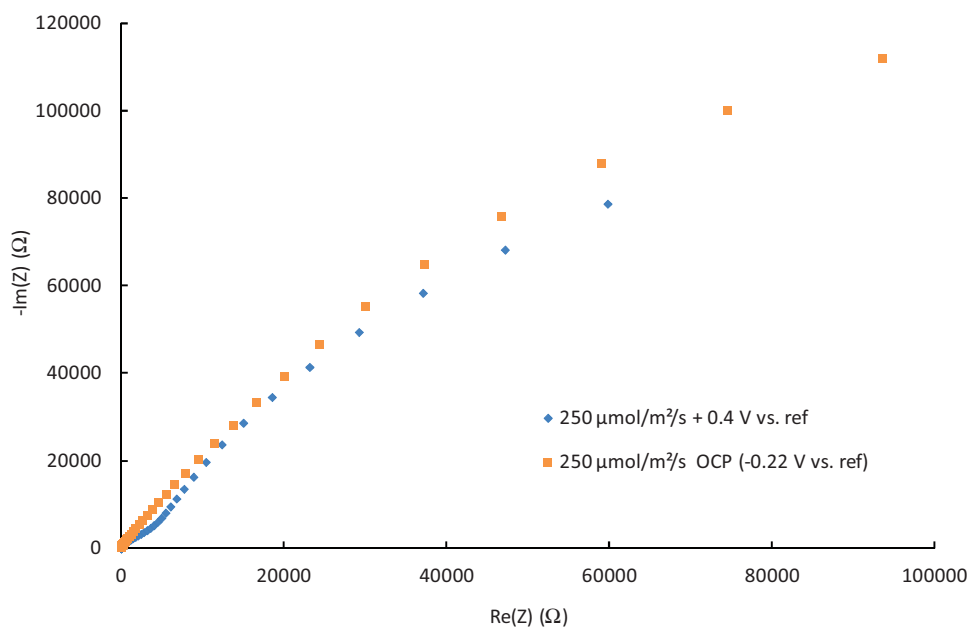


Figure 4.51 The effect of bias on hematite photoanode impedance under illumination.

Comparing the Nyquist plots of photoanode at V_{OC} and 0.4 V bias (Figure 4.51) confirms that applying bias reduces both high and low frequency semi circles but it clearly influences more Q_{bulk} appearing at high frequency region.

4.4.2 Hematite electrode characterisation with catalyst (Pt) coating

The development of a system able to efficiently use sunlight to split water into hydrogen and oxygen is hindered mainly by the lack of performance of the photoanode. Hence the objective is to characterise the performance of a system composed of catalyst deposited on hematite. The iridium oxide attached on hematite film is known to be one of the most effective for the photo oxidation of water and it is widely discussed in literature. It has been reported that IrO₂ nanoparticles linked to the hematite film surface can reduce the photocurrent onset by 0.2 V but the catalyst faces stability problem over the time (Tilley et al., 2010). Other catalysts such as cobalt based materials (cobalt ions, cobalt phosphate, Co-Pi, Co₃O₄) and also nickel oxides have been considered as interesting catalyst because of their low cost comparing to IrO₂ and ruthenium based catalysts (Le Formal et al., 2011, Kay et al., 2006). Furthermore they equally reduce the required bias and improve the photocurrent. Using a sufficiently efficient photoanode which is not majorly limiting to the system provides the possibility of developing a predictive model of the operating conditions controlled by the radiation transfer. This model can subsequently be used for design and optimization of PECs fabricated with other components, once their intrinsic characteristics are taken into account.

In this work due to the timing of project and problems with fabrication of IrO₂- α -Fe₂O₃ photoanode, we decided to test platinum as catalyst. Since we had already fabricated platinised FTO with Platisol as cathode electrode and because of well compatibility and functionality of Platisol on FTO, we decided to put a layer of Platisol on the same hematite electrode which was tested previously. Figure 4.52 shows the polarisation results of Hematite-Platisol photoanode, in a 1 M NaOH electrolyte, between V_{OC} and 0.8 V vs. reference electrode.

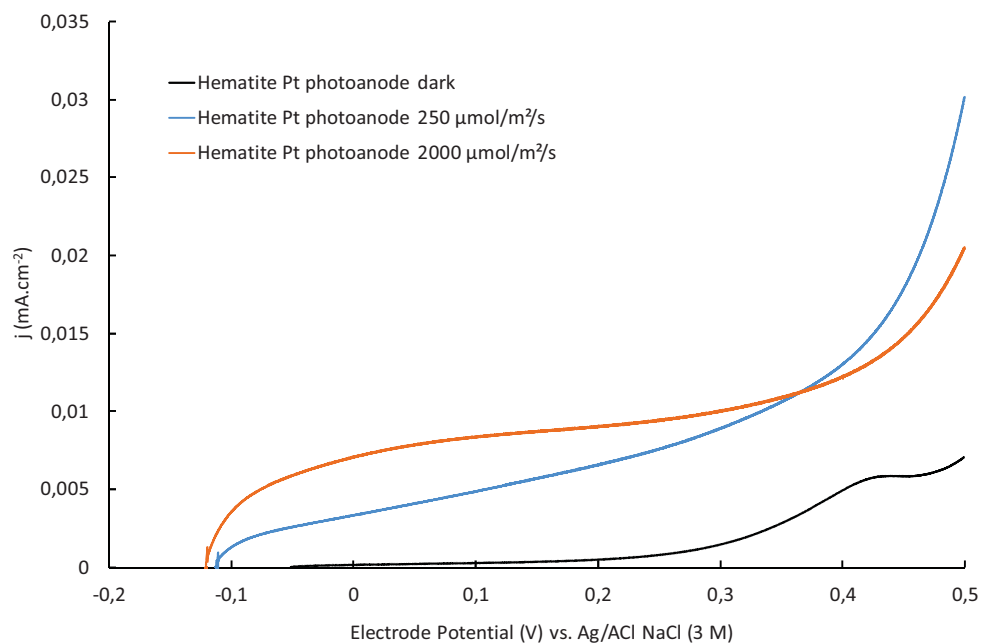


Figure 4.52 Evolution of current density PEC hematite - platisol photoanode as a function of electrode potential.

Depositing platinum on the hematite electrode changes its photoactivity. Indeed the open circuit potential, V_{OC} , of the electrode is less sensitive to the incident photon flux density. It only evolve from -4 mV to -117 mV/reference electrode from dark to $5000 \mu\text{mol.m}^{-2}.\text{s}^{-1}$. A part of the photons may be absorbed by the the platinum deposit instead of hematite. Figure 4.52 also shows that the photocurrent shows significant improvement compared to the hematite photoanode and it reaches a 0.01 mA.m^{-2} at 0.3 V vs. reference electrode for $2000 \mu\text{mol.m}^{-2}.\text{s}^{-1}$ photon flux density while for hematite electrode without Platisol a value of 0.0047 mA.m^{-2} was only obtained under the same condition (Figure 4.46). At higher electrode potential (1.5 V/ref), the current density increase is about 3 mA.cm^{-2} compared to the hematite electrode.

EIS results show also decrease in impedance values after Platisol deposition. Figure 4.53 compares the EIS results of hematite photoanode before and after of Platisol deposition in dark and under illumination. The impedance spectra are composed of two partial semicircles as before but both semicircles are strongly reduced.

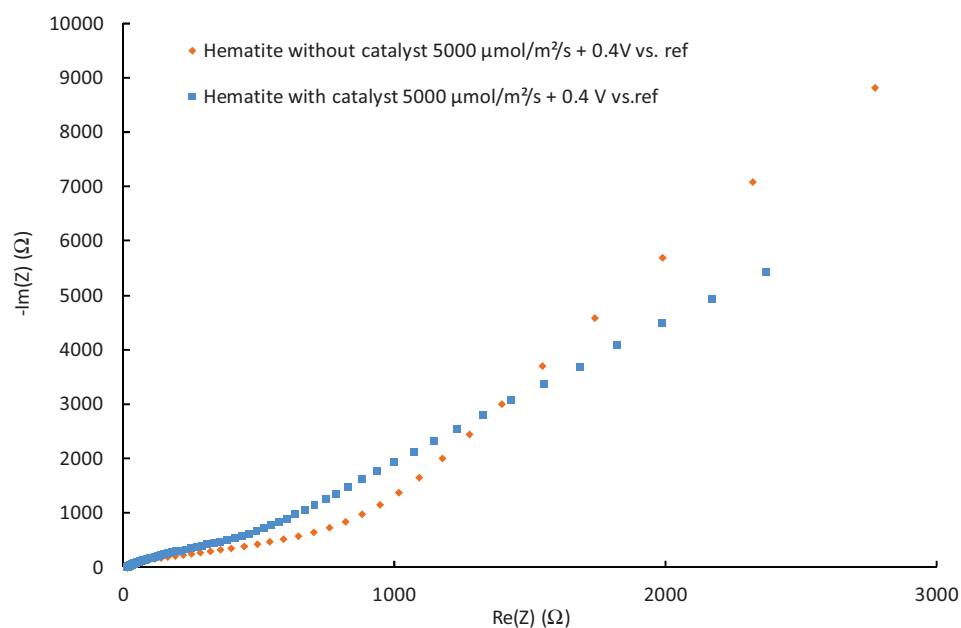


Figure 4.53 Comparison of impedance spectra before and after Platisol deposition under illumination and at 0.4 V bias vs. ref.

This is in agreement with the fact that the charge transfer from the surface states of the modified photoanode is faster than charge transfer from the surface states of hematite photoanode. Indeed, fast hole transfer will lead to a lower steady-state hole concentration in the surface states and thus a lower capacitance and lower charge transfer resistance. This suggests that the role of catalyst layer is to accelerate charge transfer kinetics, that is, act as a true water oxidation electrode.

4.5 Conclusions

The essence of this fourth and last chapter of this thesis manuscript consisted in the implementation of photoelectrochemical cells presented in the previous chapters. Different electrochemical systems were used and characterized through experiments. Starting from the simple one, i.e. the commercial Solaronix cell, to cells using a photoanode made of hematite and aimed at water splitting, it enabled us to gain insights in the operation of such solar energy conversion devices in relation with developed models.

References

- Chou J-C, Lin S-A, Lee C-Y and Gan J-Y (2013) Effect of bulk doping and surface-trapped states on water splitting with hematite photoanodes. *Journal of Materials Chemistry A* 1(19): 5908. Available at: <http://xlink.rsc.org/?DOI=c3ta00087g>.
- Convert P, Coutanceau C, Crouïgneau P, Gloaguen F and Lamy C (2001) Electrodes modified by electrodeposition of CoTAA complexes as selective oxygen cathodes in a direct methanol fuel cell. *Journal of Applied Electrochemistry* 31(9): 945–952.
- Fabregat-Santiago F, Bisquert J, Garcia-Belmonte G, Boschloo G and Hagfeldt A (2005) Influence of electrolyte in transport and recombination in dye-sensitized solar cells studied by impedance spectroscopy. *Solar Energy Materials and Solar Cells* 87(1–4): 117–131.
- Fabregat-Santiago F, Bisquert J, Palomares E, Otero L, Kuang D, Zakeeruddin SM and Grätzel M (2007) Correlation between Photovoltaic Performance and Impedance Spectroscopy of Dye-Sensitized Solar Cells Based on Ionic Liquids. *Journal of Physical Chemistry C* 111(17): 6550–6560.
- Fabregat-Santiago F, Garcia-Belmonte G, Mora-Seró I and Bisquert J (2011) Characterization of nanostructured hybrid and organic solar cells by impedance spectroscopy. *Physical chemistry chemical physics : PCCP* 13(20): 9083–9118.
- Fabregat-Santiago F, Mora-Seró I, Garcia-Belmonte G and Bisquert J (2003) Cyclic voltammetry studies of nanoporous semiconductors. Capacitive and reactive properties of nanocrystalline TiO₂ electrodes in aqueous electrolyte. *Journal of Physical Chemistry B* 107(3): 758–768.
- Le Formal F, Tétreault N, Cornuz M, Moehl T, Grätzel M and Sivula K (2011) Passivating surface states on water splitting hematite photoanodes with alumina overlayers. *Chemical Science* 2(4): 737.
- Kay A, Cesar I and Grätzel M (2006) New benchmark for water photooxidation by nanostructured α -Fe₂O₃ films. *Journal of the American Chemical Society* 128: 15714–15721.
- Kityakarn S, Pooarporn Y, Songsiriritthigul P, Worayingyong A, Robl S, Braun AM and Wörner M (2012) (Photo)Electrochemical characterization of nanoporous TiO₂ and Ce-doped TiO₂ sol-gel film electrodes. *Electrochimica Acta* 83: 113–124.
- Riha SC, Klahr BM, Tyo EC, Seifert S, Vajda S, Pellin MJ, Hamann TW and Martinson ABF (2013) Atomic layer deposition of a submonolayer catalyst for the enhanced photoelectrochemical performance of water oxidation with hematite. *ACS Nano* 7(3): 2396–2405.
- Sivula K, Le Formal F and Grätzel M (2011) Solar water splitting: progress using hematite (α -Fe(2) O(3)) photoelectrodes. *ChemSusChem* 4(4): 432–449.
- Tilley SD, Cornuz M, Sivula K and Grätzel M (2010) Light-induced water splitting with hematite: Improved nanostructure and iridium oxide catalysis. *Angewandte Chemie - International Edition* 49(36): 6405–6408.
- Wang Q, Ito S, Grätzel M, Fabregat-Santiago F, Mora-Seró I, Bisquert J, Bessho T and Imai H (2006) Characteristics of high efficiency dye-sensitized solar cells. *The journal of physical chemistry. B* 110(50): 25210–25221.

Chapter 5

Conclusions and perspectives

This manuscript summarizes the first work of the laboratory on the matter of photo-electrochemical cells. This topical extension, engaged by the lab in 2006 with the decision to work on the solar photo-reactive hydrogen production processes, has been achieved in 2011 in the field of PEC engineering with the ANR project Tech'BioPhyp (2011-15) in which this work is part of.

In a first chapter the context of a future economy for the hydrogen energy has been analyzed and discussed from the up-to-date literature and many different renewable processes for hydrogen production have been presented. The study was then focused on the photo-electrochemical processes for water oxidation and protons reduction, defining the main key process variables of such systems. Then, different kinds of PEC were presented, with a special attention for Dye-sensitized PEC (DS-PEC) at the centre of this work. Finally, the main choices governing the organization of this manuscript were explained.

The second chapter, one of the key parts of the thesis was devoted to modeling of PEC. Two different complementary approaches were discussed for that. The first approach, classically used in electrochemistry, relies on analogical equivalent-circuit modeling of the photo-electrochemical device. It appears extremely fruitful to analyze, understand the limiting steps in the photo-electrochemical process and all the main variables and models were presented and

discussed. Unfortunately, this approach is not suitable for conception, scale-up and optimization of highly efficient PEC, such objectives being only achievable from predictive knowledge models of PEC. On the basis of the previous knowledge and skills of our photo-reactive engineering research group, the foundations of a multi-scale model were laid out. Focusing either on electromagnetic wave propagation or charge carrier transport (at meso-scale) in the photo-anode, the chosen approach is robust enough to guarantee its genericity, thus to be transposed to many kind of PEC systems (the literature abounds). A particular attention has been paid on the structure of the model in writing the coupling between radiation absorption, charge carrier generation rates and surface or volumetric hydrogen production rates or electric current densities, in order to reconcile kinetics and thermodynamics aspects in the final formulation.

The third chapter was devoted to a sound description of materials and methods used for this study, requiring extremely rigorous procedures. One of the main originality of this part relies in the conception, development and realization from A to Z (with the help of colleagues from Polytech' Clermont) of a small PEC at lab-scale (MinuCell) equipped with many features (ports, separators...) which guarantee its future sustainable use. Identical devices have been provided to all the partners of the ANR project. Besides another key point of this work was the elaboration and physical characterization of photoelectrodes. These skills were not originally present in the laboratory, and this thesis contributed to the mastery of these peculiar points. After the elaboration came the implementation of the photoelectrodes into the different configurations (DS-PEC, SC-PEC for current generation or electrosynthesis) using electrochemical techniques. This extension toward the electrochemical process engineering adds another string to the bow of the laboratory and could give interesting tools or information for the future.

Finally, chapter four summarized all the important results obtained in this work. First, home-made and commercial DS-Solar Cells have been analyzed properly. Second, at the heart of the project, very interesting and new results have been obtained with bio-inspired and cheap photo-anode (using Ru-Ru_{cat} catalyst) and cathode (using CoTAA instead of platinum) in a photo-reactive supra-molecular system. Then, a first attempt to build a SC-PEC with hematite as semiconductor and Pt as co-catalyst was reported. For all these systems, the results obtained were analyzed in the framework of classical analogical models of electrochemistry and a first tentative to use some parts of the proposed knowledge model was discussed. It must be noticed also that a part of my work during this PhD thesis, not presented in this manuscript, involved

hydrogen production in photoreactors with bio-inspired reduction catalyst of hydrogenases which revealed impossible to graft at the cathode of the PEC and led to the publication of two articles in *Chemical Engineering and Processing* and *Chemical Engineering Journal*.

Among the numerous perspectives that open after this preliminary work, one can present hereafter some challenging tasks that will be tackled in the future by the GePEB team of Institut Pascal.

- *Finalize modeling at each scale and reify parameters to increase genericity*

The original work (regarding the current literature) on the development of knowledge models of PEC must be reinforced, improved, and numerous parameters remain to be reified.

Regarding first the DS-PEC, many improvements will be achieved by working experimentally and theoretically on Grätzel DSSC. Original work remains to be performed in writing, with an adapted formulation, a model of thermokinetic coupling in case of supra-molecular catalysts for water oxidation. Second, SC-PEC modeling with charge carrier transport and link to nano-structuration (transport in complex geometry) needs to be improved. In the same manner, structure and formulation of the thermokinetic coupling for (doped) semi-conductor type photo-anodes used as catalysts for water splitting and its reification is still a long-term challenge.

- *Scale-up, light dilution and operation in real solar conditions*

One of the results presented in chapter 4 is that the photo-electrochemical cells outputs (potential, current density, thermodynamic efficiency) are very dependent on the incident photon flux. Higher efficiencies are hence obtained at low photon flux density demonstrating that the key concept of dilution of solar radiation (conceptualized in our lab) could be applied here in the same manner as for natural photosynthesis in photobioreactors. Besides, for sake of production and cost, photo-processes are supposed in the future to operate with natural solar light. Considering the variability and intermittency of the sun as the light source will imply the temporal evolution of incident photon flux will lead to temporal performance evolution. This aspect should be thoroughly studied both on modeling and experimental points of view.

For this last point, a platform is intended to be developed at the Institut Pascal, the solar Eco-PAVIN Platform. This technical set was a first set up to allow to test on a reduced scale and in a safe way autonomous vehicles circulating in an urban environment. It includes a set of streets and intersections of different natures. Located next to our laboratory, it is the ideal place (up

and away from existing buildings) to implement a series of photo-reactive processes on a pilot scale operating in natural light, in particular photo-electrochemical cells, with an active surface area of 100 cm² (remaining to date to be conceived and realized). This project, extending the original scope of the PAVIN platform is strongly supported by the Labex IMobS³, Clermont Auvergne Métropole and UCA. An architect's view presents the future implantation of the technical room of the solar Eco-PAVIN platform, at the heart of which will be implanted different pilots and demonstrators, in particular our hybridization-dilution pilot plant of photo-reactive processes and the DiCoFluV photobioreactor.



Figure 5.1 Architect's view of the Pavin solar platform.

- *Hybridization of the photo-electrochemical cell*

The concept of light dilution developed at the Institute Pascal that consists in spatially separating the steps of collection of the incident solar radiation (via a sun tracking system), concentrating (by means of adapted optical devices) the photon beam, implementing photoreaction (by the use of photoreactors/cell with internal lighting emitting surfaces larger than that of radiation collection) seems possible to put into use in the case of photo-electrochemical cells. In order to increase the overall efficiency of the photoprocess, it will be compulsory to collect and separate the usable visible fraction from the infrared part of the solar spectrum (that couldn't be absorbed by the PEC). This last valuation can be done in two different ways:

- either through the use of a Stirling engine (converting the thermal energy of photons into mechanical energy) to provide work for the installation,
- or with a concentrated photovoltaic module (CPV), coupled with batteries, which would supply the system with electricity.

Hence considering this thesis as a starting point, many new doors are opening at the Institut Pascal on the study of photo-electrochemical cells.

- *Carbon dioxide reduction*

While photo-generated electrons were used to reduce protons from water, it would be conceivable to use these electrons (and the protons generated by the photo-oxidation of water) to reduce CO₂ to CO, or simple hydrocarbon molecules such as formic acid, HCO₂H or other liquid fuels (more easily manipulated and storable than hydrogen), such as CH₃OH or more complex fuels from syngas. While CO₂ is mainly produced by the combustion of fuels containing carbon, its utilization by artificial photosynthesis could constitute a virtuous cycle, compatible with a large autonomy of vehicles and thus significantly reduce the carbon footprint of the production process. The energy required for the reactions (≈ 1.5 eV) is close to that required for the photolysis of the water molecule, so it can be provided by means of photons in the spectral band of the visible light. It would be possible to achieve this CO₂ reduction of carbon dioxide in particular in photo-electrochemical cell with the advantage of the spatial separation of the oxidation zones of water and the reduction of carbon dioxide. Photo-electrochemical cell performances could be however affected by water photolysis and/or gas/liquid transfer overall limitation.

Résumé : Afin de relever le défi énergétique et climatique du 21^{ème} siècle qui s'annonce, une solution consiste, pour valoriser la ressource solaire, à mettre au point des procédés de production de vecteurs énergétiques stockables par photosynthèse artificielle permettant la synthèse de carburants solaires, en particulier l'hydrogène. La compréhension de ses procédés et l'obtention de performances cinétiques et énergétiques élevées nécessitent le développement de modèles de connaissance génériques, robustes et prédictifs considérant le transfert de rayonnement comme processus physique contrôlant le procédé à plusieurs échelles mais aussi les différents autres phénomènes intervenant dans la structure ou la réification du modèle.

Dans le cadre de ce travail de doctorat, le procédé photo-réactif au cœur de l'étude était la cellule photo-électrochimique. D'un fonctionnement plus complexe que le simple photoréacteur, avec une photo-anode et une (photo)cathode, la cellule photo-électrochimique dissocie spatialement les étapes d'oxydation et de réduction. En se basant à la fois sur la littérature existante (essentiellement dans le domaine de l'électrochimie) et en déployant les outils développés par l'équipe de recherche sur le transfert de rayonnement et la formulation du couplage thermocinétique, il a été possible d'établir des indicateurs de performance des cellules photo-électrochimiques.

En parallèle de l'établissement de ce modèle, une démarche expérimentale a été entreprise en se basant tout d'abord sur une cellule commerciale de type Grätzel (DS-PEC) indiquant les tendances générales de tels convertisseurs de l'énergie des photons avec en particulier une chute de l'efficacité énergétique en fonction de la densité incidente de flux de photons. Un dispositif expérimental modulable (Minucell) a aussi été développé et validé afin de caractériser des photo-anodes de différentes compositions comme des électrodes de TiO₂ imprégnées de chromophore pour un fonctionnement en cellule de Grätzel ou bien des électrodes d'hématite Fe₂O₃ (SC-PEC) où le semiconducteur joue à la fois les fonctions d'absorption des photons et de conduction des porteurs de charges. Surtout, le dispositif Minucell a permis de tester, caractériser et modéliser le comportement d'une cellule photo-électrochimique de type bio-inspiré pour la production d'H₂ utilisant à la photo-anode un catalyseur moléculaire Ru-RuCat (développé par ICMMO Orsay/CEA Saclay) et à la cathode un catalyseur CoTAA (développé par LCEMCA Brest). Minucell a été utilisé pour caractériser chaque élément constitutif d'une cellule photo-électrochimique puis la cellule dans son ensemble, confirmant les tendances et observations obtenues sur les efficacités énergétiques.

Ce travail préliminaire ouvre de très nombreuses perspectives de recherche, il pose des bases communes entre électrochimie et génie des systèmes photo-réactifs et donne des pistes quant à la conception et l'optimisation cinétique et énergétique des cellules photo-électrochimiques pour la production d'hydrogène et de carburants solaires.

Mots clés : Cellule photo-électrochimique, hydrogène solaire, électrochimie, transfert de rayonnement, couplage thermocinétique, catalyseurs moléculaires bio-inspirés.

Summary: In order to meet the energy and climate challenge of the coming 21st century, one solution consists of developing processes for producing storable energy carriers by artificial photosynthesis to synthesize solar fuels, in particular hydrogen, in order to valorize the solar resource. The understanding of these processes and the achievement of high kinetic and energetic performances require the development of generic, robust and predictive knowledge models considering radiative transfer as a physical process controlling the process at several scales but also including the various other phenomena involved in the structure or reification of the model.

In this PhD work, the photo-reactive process at the heart of the study was the photo-electrochemical cell. More complex than the simple photoreactor, with a photo-anode and a (photo)cathode, the photo-electrochemical cell spatially dissociates the oxidation and reduction steps. Based both on the existing literature (mainly in the field of electrochemistry) and by deploying the tools developed by the research team on radiative transfer and thermokinetic coupling formulation, it was possible to establish performance indicators of photo-electrochemical cells.

In parallel to the establishment of this model, an experimental approach was undertaken based first on a commercial Grätzel-type cell (DS-PEC) indicating the general trends of such photon energy converters with in particular a drop in energy efficiency as a function of the incident photon flux density. A modular experimental device (Minucell) has also been developed and validated in order to characterize photo-anodes of different compositions such as chromophore impregnated TiO₂ electrodes for operation in Grätzel cells or Fe₂O₃ hematite electrodes (SC-PEC) where the semiconductor plays both the functions of photon absorption and charge carrier conduction. Above all, the Minucell device allowed to test, characterize and model the behavior of a bio-inspired photo-electrochemical cell for H₂ production using at the photo-anode a Ru-RuCat molecular catalyst (developed by ICMMO Orsay/CEA Saclay) and at the cathode a CoTAA catalyst (developed by LCEMCA Brest). Minucell was used to characterize each constituent element of a photo-electrochemical cell and then the cell as a whole confirming the trends and observations obtained on energy efficiencies.

This preliminary work opens up a wide range of research prospects, lays common ground between electrochemistry and photo-reactive systems engineering, and provides insights into the design and kinetic and energy optimization of photo-electrochemical cells for the production of hydrogen and solar fuels.

Keywords: Photoelectrochemical cell, solar hydrogen, electrochemistry, radiative transfer, thermokinetic coupling, bio-inspired molecular catalysts